Sites NGHP-01-19

By T. Collett, M. Riedel, J. Cochran, R. Boswell, J. Presley, P. Kumar, A. Sathe,
A. Sethi, M. Lall, and the National Gas Hydrate Program Expedition 01 Scientists

Scientific Investigations Report 2012–5054

U.S. Department of the Interior
U.S. Geological Survey

Contents

Background and Objectives....1119
Operations....1119
Hole NGHP-01-19A....1119
Hole NGHP-01-19B....1125
Lithostratigraphy....1125
Lithostratigraphic Units....1125
Lithostratigraphic Unit I....1125
Lithostratigraphic Unit II....1126
Subunit IIa....1139
Subunit IIb....1139
Subunit IIc....1139
Subunit IId....1139
Sedimentary Environment....1141
Correlation between Sites NGHP-01-18 and NGHP-01-19....1141
Gas-Hydrate Occurrence....1141
Inorganic Geochemistry....1145
Interstitial Water Chloride and Salinity....1145
Sulfate and Alkalinity Concentrations: Characterization of the SMI....1147
Bromide Concentrations....1154
Organic Geochemistry....1154
Microbiology....1155
Hole NGHP-01-19A....1155
Physical Properties....1155
Infrared Imaging....1155
Environmental Conditions....1155
Infrared Images....1161
Core-End Temperature Readings....1169
Estimate of Gas Hydrate Concentration Based on IR Temperature Change....1169
Index Properties....1169
Strength....1172
Electrical Resistivity....1179
P-Wave Velocity....1179
Magnetic Susceptibility....1179
Thermal Conductivity....1191
Downhole Temperature Measurements....1191
Pressure Coring....1191
Pressure Core Operations and Measurements....1192
Gas-Hydrate Concentration, Nature, and Distribution from Pressure Coring....1203
Downhole Logging....1205
Operations....1205
Logging Data Quality....1206
Logging Units....1210
Gas-Hydrate and Free Gas Occurrence....1210
References Cited....1212

Figures

1. Bathymetric map showing the area of the Mahanadi Basin and Site NGHP-01-19 1120
2. Map of the area in the Mahanadi Basin showing available seismic data and Site NGHP-01-19 1121
3. Detailed map of the area of Site NGHP-01-19 in the Mahanadi Basin showing available seismic data 1122
4. Seismic line crossing Site NGHP-01-19 1123
5. Map showing all holes occupied at Site NGHP-01-19 1124
6. Lithostratigraphic summary of Hole NGHP-01-19A 1126
7. A, Major lithologic components in smear slide and coarse fraction plotted from percent visual estimation. B, Calcareous components, pyrite, other iron sulfides, and glauconite observed in smear slides and coarse fractions; C, Biosiliceous components observed in smear slides and coarse fractions 1135
8. Visible foraminifera and shell fragments observed throughout Unit I 1138
9. Terrestrial organic debris recovered in Section NGHP-01-19A-05H-2 1139
10. Thick ash bed, possibly the Toba ash in Section NGHP-01-19A-02H-2 and NGHP-01-19B-02H-1 1140
11. Dolomite concretions in A, Sections NGHP-01-19A-11H-3 and B, NGHP-01-19A-20X-1 1144
12. Visible glauconite grains in Section NGHP-01-19A-38X-6 1146
13. Concentration-depth profiles of A, chloride and B, salinity at NGHP-01-19A 1151
14. Concentration-depth profiles of A, alkalinity; B, sulfate; and C, sulfate, methane, and alkalinity at Hole NGHP-01-19A 1152
15. Concentration-depth profile of dissolved bromide at Hole NGHP-01-19A 1153
16. Plot of headspace methane gas concentration with depth for Hole NGHP-01-19A 1158
17. Plot of headspace carbon dioxide gas concentration with depth for Hole NGHP-01-19A 1159
18. Plot of methane to carbon dioxide gas ratio with depth for headspace, free/void gas, and PCS gas for Hole NGHP-01-19A 1160
19. Plot of free/void gas and PCS methane to ethane gas ratio with depth for Hole NGHP-01-19A 1162
20. Catwalk temperature and humidity measurements as a function of time during drilling operations at Site NGHP-01-19 1165
21. Infrared imaging and the derived downhole temperature profile for Hole NGHP-01-19A 1168
22. Comparison of core end infrared images and cross-core temperature profiles from two different parts of Hole NGHP-01-19A 1170
23. Down-core temperature profile for Hole NGHP-01-19A 1171
24. Estimate of gas-hydrate abundance based on downcore temperature anomalies for Hole NGHP-01-19A 1176
25. Profiles of core recovery, index, and strength properties for Site NGHP-01-19 1177

26. Profiles of infrared images, core recovery, electrical resistivity, acoustic *P*-wave velocity, magnetic susceptibility, and thermal conductivity for Site NGHP-01-19 1178
27. Shear strengths normalized by the effective vertical stress versus sub-bottom depth for Hole NGHP-01-19A....1182
28. Peak and remolded vane shear strengths and sensitivity for Hole NGHP-01-19A....1182
29. Apparent formation factor versus sub-bottom depth for Hole NGHP-01-19A....1191
30. Geothermal gradient and estimated depth to the BSR from *in situ* temperature measurements for Hole NGHP-01-19A....1193
31. Temperature and pressure versus elapsed time for each pressure corer deployment as recorded by the corer's internal data logger....1194
32. Temperature versus pressure for each successful pressure-corer deployment, showing trajectories relative to gas hydrate stability at 30 ppt and 35 ppt salinity....1195
33. Data collected at near *in situ* pressure and at 7 °C for Cores NGHP-1-19A-17E and -27E, including X-ray images, gamma density, and *P*-wave velocity....1196
34. Summary of data taken from successful pressure cores before, during, and after depressurization, including gamma-density profiles collected before and after depressurization, X-ray images collected before and after depressurization, and line-scan images collected after depressurization....1198
35. Pressure versus volume for successful pressure cores, also showing placement of gas samples....1201
36. Pressure versus time for successful pressure cores....1202
37. Methane phase diagram for Site NGHP-01-19, with total methane concentration measured from the three successful pressure cores at Site NGHP-01-19 1204
38. Summary of the wireline logs recorded during the two triple combo runs in Hole NGHP-01-19B 1207
39. Sonic waveform amplitude and coherence data and velocity logs measured by the DSI in Hole NGHP-01-19B....1208
40. Preliminary stacks derived from the waveforms recorded during the VSP survey in Hole NGHP-01-19B 1209
41. Water saturations from Archie's equation and wireline porosity and resistivity logs in Hole NGHP-01-19B....1211

Tables

1. Smear-slide data for Hole NGHP-01-19A....1130
2. Smear-slide data for Hole NGHP-01-19B....1134
3. Coarse-fraction sieve data for Hole NGHP-01-19A....1142
4. Interstitial-water data for Hole NGHP-01-19A....1148
5. Interstitial-water data corrected for drill-water contamination based on sulfate concentration, for Hole NGHP-01-19A....1150
6. Headspace gas composition for Site NGHP-01-19....1156
7. Void gas composition for Site NGHP-01-19....1161
8. Pressure Core Sampler gas composition for Site NGHP-01-19....1162
9. List of microbiological samples taken for Site NGHP-01-19....1163
10. List of infrared images collected from Hole NGHP-01-19A....1166

11. List of infrared image files collected on section ends from Hole NGHP-01-19A....1167
12. List of temperature-probe data collected at bottom of cores from Hole NGHP-01-19A....1172
13. Moisture and density (MAD) physical properties for Hole NGHP-01-19A....1173
14. Vane shear strength results for Hole NGHP-01-19A....1179
15. Pocket Penetrometer strength results for Hole NGHP-01-19A....1180
16. Wenner array electrical resistivity and formation factor results for Hole NGHP-01-19A....1183
17. Contact *P*-wave velocity results determined on split cores sections from Hole NGHP-01-19A....1191
18. Thermal conductivity results for Hole NGHP-01-19A....1192
19. *In situ* temperature estimates for Hole NGHP-01-19A....1193
20. Summary of pressure-coring operations at Site NGHP-01-19....1193
21. Methane-hydrate volume and concentration in pore space for successful pressure cores at Site NGHP-01-19....1203

Site NGHP-01-19

By T. Collett, M. Riedel, J. Cochran, R. Boswell, J. Presley, P. Kumar, A. Sathe, A. Sethi, M. Lall, and the National Gas Hydrate Program Expedition 01 Scientists

Background and Objectives

Site NGHP-01-19 (Prospectus Site MNGH-Gap) is located at 18° 58.6568'N, 85° 39.5202'E in the Mahanadi Basin (figs. 1, 2, and 3). The water depth is ~1,422 m. All seismic data were made available through Reliance Ltd., and were extracted from a larger 3D seismic volume.

The objectives of the work carried out at this site follow the general objectives of the India NGHP Expedition 01:

- Determine if gas hydrate is indeed present at this site and if the seismic reflection is a gas-hydrate-related BSR;
- Study the occurrence of gas hydrate and establish the background geochemical, geological, geophysical, and microbiological baselines for gas hydrate proxy-studies;
- Define the relationship between the sedimentology and structure of the sediments and the occurrence and concentration of gas hydrate;
- Calibrate remote sensing data (such as seismic data) by acquiring wire-line log data.

The location for Site NGHP-01-19 in the Mahanadi Basin was chosen as it shows a gap in the otherwise regionally continuous BSR (fig. 4). This site provided the opportunity to core a background location in an area adjacent to, but lacking, high amplitude reflectors below the interpreted BSR that most likely indicates the presence of free gas. The nearby BSR is marked by an abrupt increase in reflection strength of the sediments underlying the horizon. Inside the gap, however, the sediments are of similar reflection strength above and below the projected depth of the BSR. The seismic data at this site show complex structures and geometries suggestive of channelized (cut-and-fill) deposition.

Operations

This operations summary covers the Leg 4 transit from Site NGHP-01-18 (MNGH-REL 5) to Site NGHP-01-19 (MNGH-Gap Site) and drilling/coring operations for Holes NGHP-01-19A and NGHP-01-19B (fig. 5). Schedule details and statistics for this site can be found as Appendixes:

- Appendix 1: NGHP Expedition 01 Operations Schedules
- Appendix 2: NGHP Expedition 01 Operations Statistics

Included in the "Methods" chapter is a list of standard or commonly used operations terms and acronyms.

Hole NGHP-01-19A

Hole NGHP-01-19A was occupied on Leg 4 of NGHP Expedition 01 and was the first of what ultimately became two holes drilled at this site. The 11.5 NMI transit from Site NGHP-01-18 (MNGH-REL 5) was complicated by a large low pressure cell that enveloped a large portion of the Bay of Bengal, producing strong winds (30–40 kt) and heavy seas/swells (15–20 ft) throughout the transit. In addition, a strong current from variable directions first assisted and then impeded progress. The move between sites was originally planned as a DP transit with the current assisting the move from the stern. Because of the heavy seas, the ship would have been unable to transit at more than half-speed in cruise mode. Therefore, the drill collars were racked and secured in the derrick rather than broken down and laid out. This saved ~2.0 hr of operating time that would have been required to layout the collars and then pick them up again a few hours later. It was also deemed safer to do this rather than handling the heavy collars under the vessel motion conditions present at the time. The DP move was also preferred because the resultant heading in transit mode would have led to major vessel rolling. At 0200 hr on 4 August, the ship began moving to the next site in heavy seas and very high swells. Soon into the move, the current shifted directions causing a further reduction in speed. At 0613 hr, the port propulsion shaft had to be taken offline due to an overheating gearbox. With one shaft offline, the vessel barely made steerage way and for a while was actually being pushed back toward the previous site. The shaft was back on line at 1210 hr after the lubrication system was thoroughly flushed and the oil injection nozzles were cleaned of debris. The source of the contamination was not identified at that time. Because of the slow rate of progress during the initial phase of the transit, it was decided that the remaining distance be conducted in cruise mode. Thrusters were pulled and the move resumed in transit mode. Even in this mode, the rate of speed was limited to <4 kt since shaft RPM had to be vastly reduced to keep the propellers from coming out of the water and over speeding. The 12.0 NMI transit was ultimately completed in 12.8 hr at an overall (DP plus cruise mode) average speed of 0.9 kt.

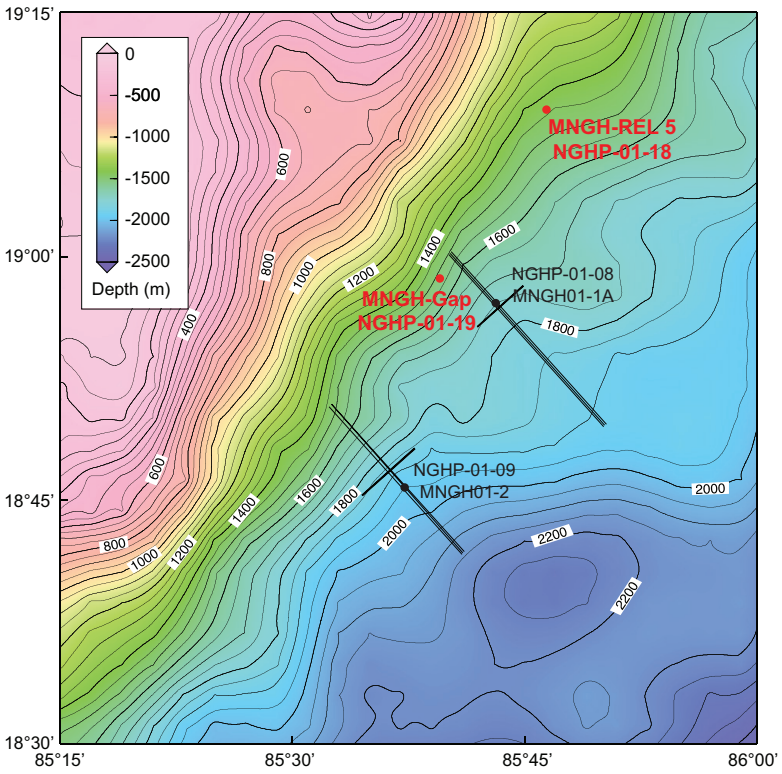


Figure 1. Bathymetric map showing the area of the Mahanadi Basin and Site NGHP-01-19 (Prospectus Site MNGH-Gap). Also shown is Site NGHP-01-08 (Prospectus MNGH01-1A) and Site NGHP-01-09 (Prospectus Site MNGH01-2); both sites were established during LWD (Leg 2) program. [LWD, logging-while-drilling]

The vessel was switched from cruise mode to DP control at 1510 hr on 4 August. A positioning beacon was deployed at 1539 hr with the vessel over the site coordinates. The ice bath was installed in the moon pool and the same BHA as had been used on all previous cored sites was made up and deployed.

Hole NGHP-01-19A was planned as a continuous APC/XCB cored hole to 300.0 mbsf with two packages of pressure cores targeting the gas hydrate stability zone. Temperature measurements were also to be taken using the APCT-3 and DVTP systems to define a thermal gradient from seafloor to total depth. A complete suite of wireline logs (triple combo, FMS-sonic, and VSP) was also scheduled.

The drill string was tripped to the seafloor and the top drive was picked up in preparation for spudding; however, this activity was deferred because the port shaft gear box was once again overheating and was taken off-line. It was not considered prudent to spud the hole with only one propulsion shaft on-line. Therefore, the vessel stood by with the bit above the seafloor until the source of the problem could be identified and a risk mitigation plan could be put in place. After analysis, it was determined that the overheating of the gearbox was caused by aluminum particles coming from a disintegrating bearing sprayer ring which blocked the oil filters and plugged up the bearing spray nozzles. To prevent a reoccurrence of the problem, the ship's engineers instituted a program in which the gearbox lubrication system filters were cleaned every hour. In addition, the oil was periodically drained from the oil sump to remove any remaining particles. Finally, it was decided that a risk mitigation plan was required that would allow drilling operations to continue while at the same time limiting the risk to personnel and equipment to that of normal operations. To do this, the Automated Station Keeping (ASK) limits were redefined to a more conservative operating range for the remainder of the expedition. In essence, this meant limiting operations to those environmental conditions that would allow the ship to still be able to maintain position over the drill site should one of the two propulsion shafts need to be taken off-line. Restricting the positioning limit within this range reduced the potential of losing the location due to a mechanical failure and also reduced the risk of damage to the drilling/coring equipment. A series of DP system tests were conducted through the night to verify the limits of the ASK system within the current environmental conditions. Procedures were established for the drilling crew that allowed the drill string to be pulled above the seafloor in the shortest time possible should the ability to hold location come into question. In addition, protocols were established for the drill crews to work in close coordination with the DP personnel and to advise them of the minimum time required to clear the seafloor should it appear imminent that the maximum positioning limits might be exceeded.

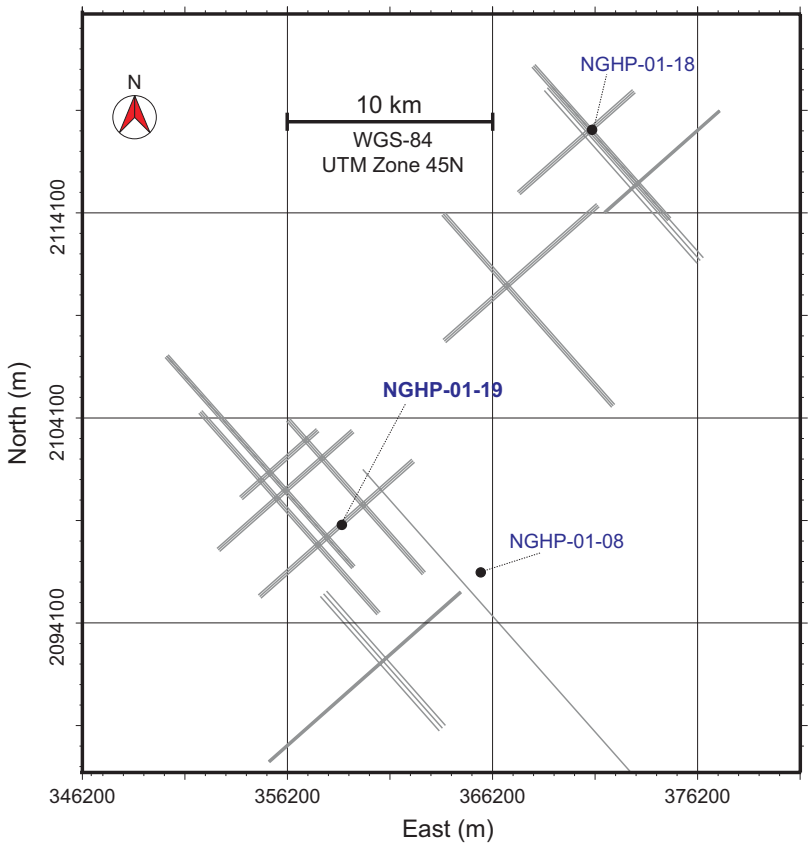


Figure 2. Map of the area in the Mahanadi Basin showing available seismic data and Site NGHP-01-19. All seismic data available were extracted from a 3D seismic volume.

At 0530 hr on 5 August, the drill pipe was spaced out and the APC core barrel was deployed. Hole NGHP-01-19A was spudded at 0700 hr, which established a seafloor depth of 1,434.2 mbrf. The PDR depth for this site, corrected to the rig floor DES, was 1,439.3 mbrf.

APC Core NGHP-01-19A-01H was on-deck at 0715 hr and APC coring continued through Core NGHP-01-19A-11H to a depth of 98.3 mbsf. APC coring was halted at this depth due to an incomplete stroke with 3.5 m of advance. During the APC cored interval, a short 4.0 m drilled advance was made from 62.3 mbsf to 66.3 mbsf. This occurred after Core NGHP-01-19A-07H and prior to Core NGHP-01-19A-08H in order to adjust the drilling kelly.

Successful temperature measurements were taken using the APCT-3 shoe on Cores NGHP-01-19A-03H (at 24.3 mbsf), NGHP-01-19A-05H (at 43.3 mbsf), and NGHP-01-19A-07H (at 62.3 mbsf).

Coring continued with the XCB coring system recovering Cores NGHP-01-19A-12X through NGHP-01-19A-14X to a depth of 126.0 mbsf setting up the first planned series of pressure cores. A single DVTP temperature measurement was attempted after Core NGHP-01-19A-13X at a depth of 117.4 mbsf; however, this was unsuccessful because the formation was still too soft for a good seal.

The first pressure core target zone was located at 131.0 mbsf + 5 m. PCS Core NGHP-01-19A-15P was cut from 126.0 mbsf to 127.0 mbsf. This was followed by FPC Core NGHP-01-19A-16Y from 127.0 mbsf to 128.0 mbsf. The third pressure core of the series was HRC Core NGHP-01-19A-17E from 128.0 mbsf to 129.0 mbsf.

Coring resumed with the XCB coring system recovering Cores NGHP-01-19A-18X through NGHP-01-19A-24X to a depth of 193.3 mbsf—this set up the second planned series of pressure cores. Another DVTP temperature measurement was attempted after Core NGHP-01-19A-20X at a depth of 157.9 mbsf; however, this was also unsuccessful due to soft sediment.

The second pressure coring package began with a PCS Core NGHP-01-19A-25P recovered from 194.3 mbsf followed by an FPC Core NGHP-01-19A-26Y advanced from 194.3 mbsf to 195.3 mbsf. The final pressure core of the series was an HRC Core NGHP-01-19A-27E from 195.3 mbsf to 196.3 mbsf. A third DVTP temperature measurement was taken after HRC Core NGHP-01-19A-27E at a depth of 196.3 mbsf and recovered useable data.

Coring resumed with the XCB coring system recovering Cores NGHP-01-19A-28X through NGHP-01-19A-38X to a depth of 300.0 mbsf. A DVTP temperature measurement was taken after Core NGHP-01-19A-38X at TD; however,

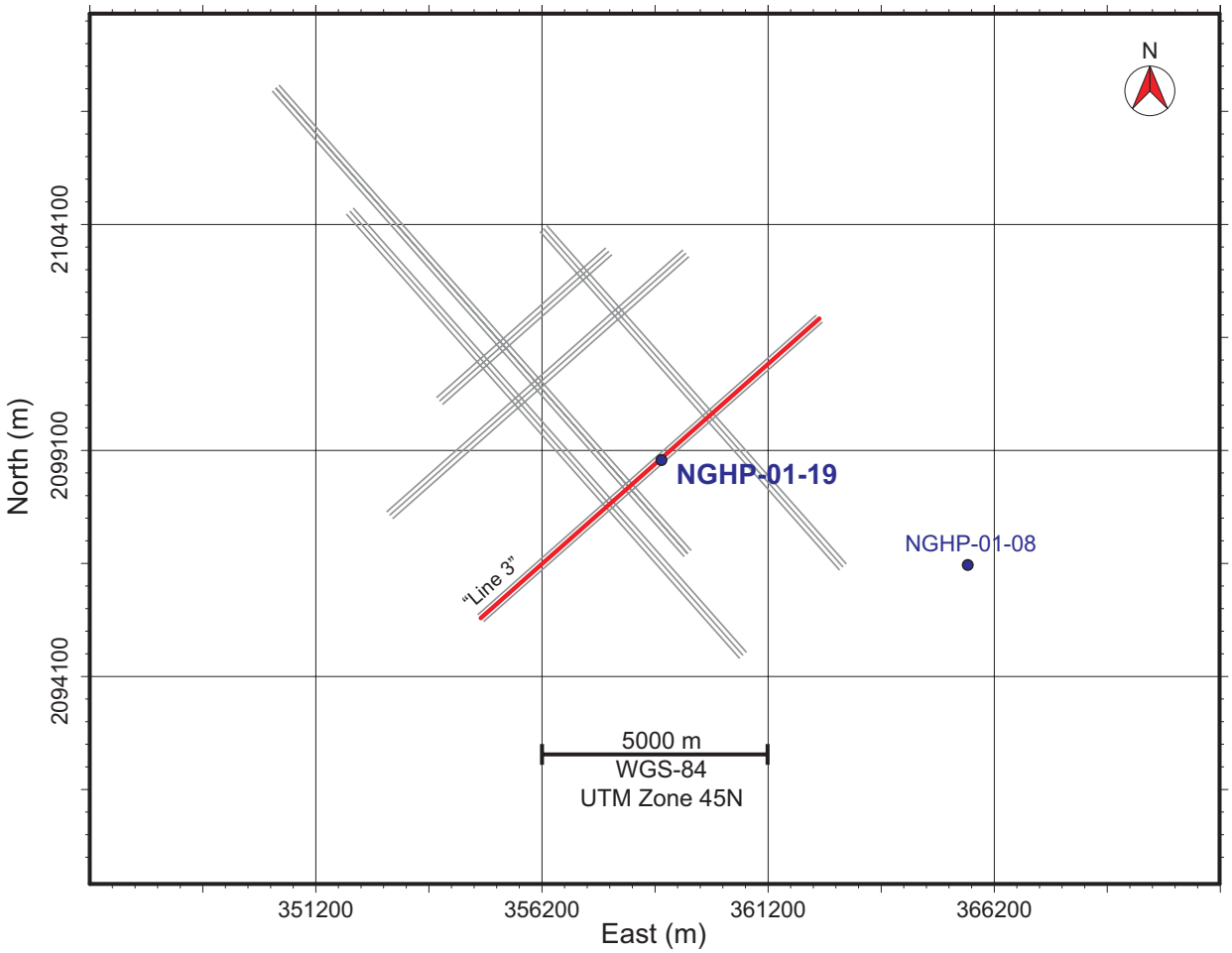


Figure 3. Detailed map of the area of Site NGHP-01-19 in the Mahanadi Basin showing available seismic data as black and red track lines. All seismic data available were extracted from a 3D seismic volume.

the data were considered suspect at the time (later found to be adequate). Therefore, the hole was deepened another 5.0 m and a final DVTP temperature measurement was taken at a TD of 305.0 mbsf and useable data were obtained.

Both PCS deployments included successful recovery of data with the PCS Methane tool. Penetration rates with the XCB ranged from 23.0 m/h to 78.0 m/h while core recovery ranged from 16 percent to 99 percent with an average for the hole of 86.1 percent.

Whirlpaks (microbeads) commonly used for assessing microbiological contamination were not used. Accelerated core barrel handling protocols were used for all APC/XCB core bbl deployed in this hole. All core bbl were laid down immediately upon arrival at the rig floor before making another drill pipe connection or deploying the next core barrel.

For all HYACINTH pressure coring systems (FPC and HRC), and the TAMU PCS system, a 15–20 min wait period was employed at the mudline on the way in the hole and again during retrieval. This was to cool the core bbl down, thus aiding in keeping any entrained gas hydrate within the stability field. At the rig floor, all pressure core bbl (PCS, FPC, and HRC) showing signs of proper actuation were placed in the moon pool ice bath prior to processing.

After reaching TD at 305.0 mbsf, 3 hr were spent sweeping the hole and conducting a wiper trip to logging depth and back. The last 17.0 m of the wiper trip required reaming with the top drive and 5.0 m of fill on-bottom required circulating out of the hole. An expendable go-devil was deployed to lock the LFV in the open position and the hole was displaced with 100 bbls of 10.5 ppg weighted mud. The drill string was then tripped setting the EOP at 61.8 mbsf.

At 0730 hr on 7 August, rig-up for logging began. The first logging run was made with the triple combo tool suite. This suite of tools was unable to pass 145.8 mbsf. This was 134.2 m off the hole TD and ~54 m above the BSR. Considering options to move the tools past the obstruction, it was decided to drill a dedicated logging hole. The triple combo tool suite was used to log the hole above the bridge and the tools were then recovered and rigged down. The Schlumberger logging sheaves were rigged down and the drill string was pulled clear of the seafloor at 1425 hr on 7 August—this ended Hole NGHP-01-19A and began Hole NGHP-01-19B.

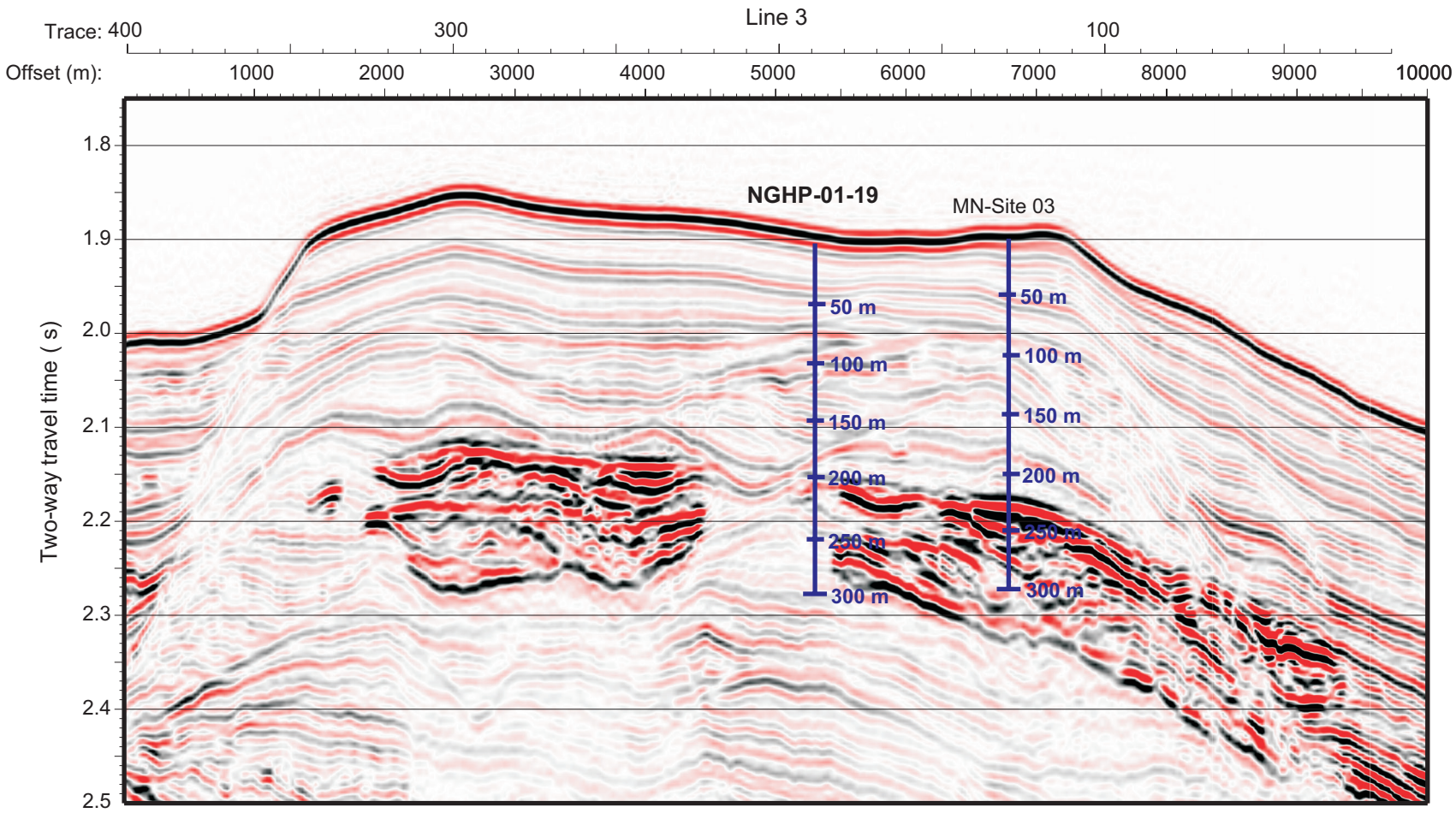


Figure 4. Seismic line (SW-NE oriented) crossing Site NGHP-01-19 ("Line-3"). The site is located at around trace 190 within a gap in the prominent BSR reflection. The depth of the formation tops was estimated using a uniform velocity of 1,600 m/s. [BSR, bottom-simulating reflector; m/s, meters per second]

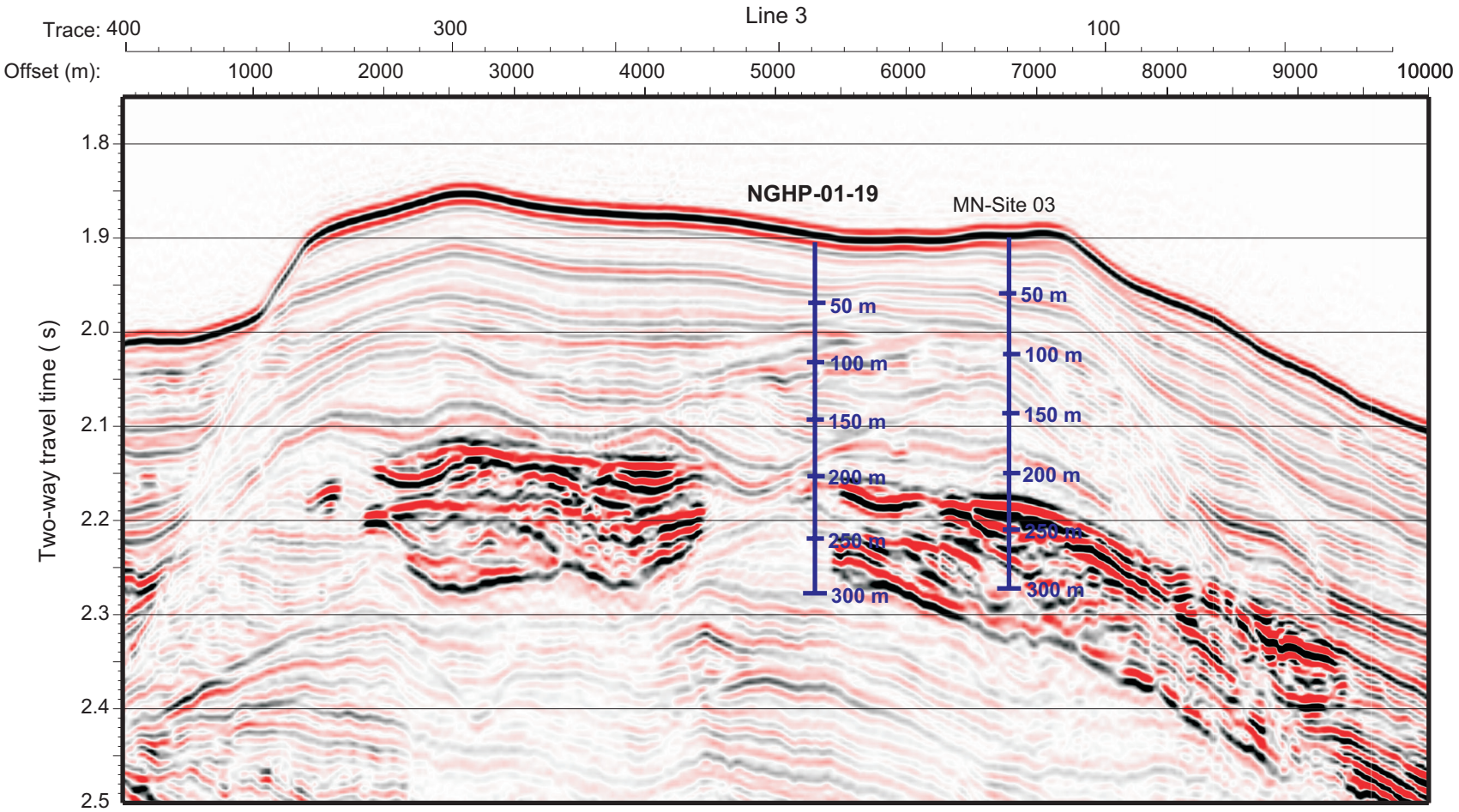


Figure 5. Map showing all holes occupied at Site NGHP-01-19 (MNGH-Gap Site).

Hole NGHP-01-19B

The vessel was offset 10 m SW of Hole NGHP-01-19A on a bearing of 228°. The drill pipe was spaced out and an APC core barrel was deployed. Hole NGHP-01-19B was spudded at 1545 hr on 7 August, establishing a seafloor depth of 1,433.2 mbrf. This new hole provided an opportunity to obtain additional mudline cores for high-resolution sampling. As such, three APC cores were recovered. APC Core NGHP-01-19B-01H was on-deck at 1555 hr and APC coring continued through Core NGHP-01-19B-03H to a depth of 26.3 mbsf. The APC core bbl were laid out, an XCB center bit was deployed, and drilling commenced at 1730 hr. Six and one half hours were spent drilling to a depth of 280.0 mbsf at an average net ROP of 40.1 m/h. This corresponded to an actual drilling rate of 62.4 m/h. The hole was then displaced with 100 bbl of 10.5 ppg Sepiolite mud and the drill pipe was pulled back positioning the EOP at a logging depth of 61.8 mbsf.

Rig-up for wireline logging began at 0200 hr on 8 August. The first logging run was made with the triple combo tool suite. The tools successfully passed several tight spots before reaching TD at 280.0 mbsf. After logging up from that point, the tools were recovered and laid out. The logging line and sheaves were then secured back out of the way and four stands of drill pipe were added to the string lowering the EOP to 177.3 mbsf. Although this left only 103 m of hole for logging, it was deemed important to attempt acoustic log data acquisition from below the BSR. The VSP logging tools were rigged up and deployed at 0930 hr on 8 August. This tool string reached 262.8 mbsf and logs were recovered above that point. Once VSP operations were completed, the tools were recovered and laid out. As on all other sites, all VSP operations were conducted during daylight hours while adhering to the IODP policies and mammal protection guidelines. The logging line and sheaves were then secured back out of the way for the second time and the four-stands of drill pipe previously added to the drill string were removed. This positioned the EOP at the original logging depth of 61.8 mbsf. The third tool suite consisted of the FMS-sonic. This tool string was made up and deployed at 1715 hr reaching 266.8 mbsf. Two passes were made with this tool suite and once logging was completed the tools were recovered and laid out. The wireline logging equipment was rigged down by 2345 hr on 8 August and the drill string was pulled clear of the seafloor at 0005 hr on 9 August.

The positioning beacon was recovered at 0316 hr during the pipe trip back to the surface. Thrusters were raised and the rig was secured for transit. The vessel officially got underway back to Site NGHP-01-18A at 0354 hr on 9 August. The ship returned to the previous site so as to recover the positioning beacon left behind due to the rough sea state and poor weather conditions prevalent at the time of departure.

Lithostratigraphy

Site NGHP-01-19 (See "Operations") was the second of two sites cored and drilled in the Mahanadi Basin. NGHP-01-19A was cored to a depth of 305 mbsf (APC/XCB and pressure cores) and NGHP-01-19B, was drilled and wireline logged to 280 mbsf. Three APC cores were collected at the top of NGHP-01-19B for high-resolution sampling.

The sedimentary sequence recovered at Hole NGHP-01-19A was divided into two lithostratigraphic units (Unit I and Unit II; fig. 6A and Site NGHP-01-19 Visual Core Descriptions) and we recognize four subunits within Unit II (IIa, IIb, IIc, and IId) based on sedimentological criteria (for example, variations in lithogenic, volcanogenic, authigenic, and biogenic components as well as sedimentary structures and grain size) and physical properties (for example, magnetic susceptibility). Sediments recovered in Hole NGHP-01-19B (fig. 6B and Site NGHP-01-19 Visual Core Descriptions) are from the upper part of Unit I. We also integrate the core data with the available seismic data to help define and interpret the stratigraphic sequence cored at Site NGHP-01-19.

Hole NGHP-01-19A exhibits the most varied lithology drilled during NGHP Expedition 01 (fig. 6A and Site NGHP-01-19 Visual Core Descriptions). Unit I is characterized by clays (with varying amounts of volcanic glass, pyrite, authigenic carbonate and aragonite, plant debris, nannofossils, and foraminifera) that alternate with less amounts of oozes. The oozes are rarely pure and commonly contain clay, volcanic glass, and(or) foraminifera. Unit II is a sequence of clays with secondary components. Based on the dominance of one or another secondary component, we distinguish four subunits: Subunit IIa is characterized by the presence of volcanic glass; Subunit IIb is mainly composed of pure clays; Subunit IIc has glauconite as the dominant secondary component; and Subunit IId includes biosiliceous secondary components. The last appearance (LA) of *Discoaster* spp. in Core NGHP-01-19A-09H suggests that sediments recovered at Site NGHP-01-19 below ~80 mbsf are older than Quaternary.

Lithostratigraphic Units

Lithostratigraphic Unit I

Intervals: Hole NGHP-01-19A, Sections NGHP-01-19A -1H-1 to NGHP-01-19A -9H-05; Hole NGHP-01- 19B, Sections NGHP-01-19B -1H-1 to 3H-CC (EOH)

Depth: Hole NGHP-01-19A, 0-83.2 mbsf; Hole NGHP-01-19B, 0-26.3 mbsf

Age: Pleistocene to Recent

Core recovery was good in both Hole NGHP-01-19A and Hole NGHP-01-19B in Unit I (figs. 6A, 6B, and Site NGHP-01-19 Visual Core Descriptions). The unit is composed of clays alternating with a few thin intervals of oozes. Unit I contains

biogenic (nannofossils, foraminifera, biosiliceous, plant debris), authigenic (carbonate, aragonite, pyrite) and volcanogenic (glass) components in suitable amounts (from bearing to rich), allowing for the recognition of fifteen different lithologies (see fig. 6, tables 1 and 2, and Site NGHP-01-19 Visual Core Descriptions). The color of sediments ranges from olive (5Y 4/3), to light to very dark greenish gray (10Y 7/1, 5GY 5/1, 5GY 4/1, 5GY 3/1, 10Y 3/1), and to greenish black (10Y 2.5/1) (fig. 6A and Site NGHP-01-19 Visual Core Descriptions). Unit I corresponds to a sediment sequence displaying subhorizontal layering (see seismic data in "Background and Objectives"). As *Discoaster* spp. is present just at the very bottom of Lithostratigraphic Unit I (Section NGHP-01-19A-09H-4), it is likely that the unit is Quaternary to Recent in age; however, post-cruise biostratigraphic work may help to better constrain the age of the Unit I stratigraphy.

Shell fragments and visible foraminifera tests occur sporadically throughout Unit I and are consistently present in the coarse fractions and smear slides (figs. 6A, 7, and 8, and Site NGHP-01-19 Visual Core Descriptions). Terrestrial organic matter is observed in Core NGHP-01-19A-05H (figs. 6A, 7, and 9, and Site NGHP-01-19 Visual Core Descriptions). A volcanic ash bed, silt to very fine sand grain size and pinkish gray in color (7.5R 5/1 or weak red Munsell) was observed in Cores NGHP-01-19A-02H and NGHP-01-19B-02H (fig. 10). The relatively large thickness of this bed (~8 cm) and its stratigraphic position near the sea floor suggests that it could be the Toba Ash, which was deposited between ~70 to ~75 ka in this region (Ninkovich and others, 1978; Rose and Chesner, 1990; Westgate and others, 1997; Kudrass and others, 2001). Other occurrences of volcanic ash are visible sporadically in Unit I as subcentimeter patches, likely burrows filled with ash (fig. 6A and Site NGHP-01-19 Visual Core Descriptions). Detrital volcanic glass shards were also observed in smear slides taken throughout the Unit from trace to 15 percent amounts and in the coarse fraction as trace to 5 percent (fig. 7 and tables 1, 2, and 3). Bioturbation is rare to abundant throughout Unit I (fig. 6A). Bioturbated zones are also most easily seen in lighter-colored portions of the cores, where these zones are highlighted by dark-grey- to black-colored iron sulfide precipitates. Iron monosulfides and pyrite are present throughout Unit I, but are rarer below Core NGHP-01-19A-06H (fig. 6A, 7B and Site NGHP-01-19 Visual Core Descriptions), Pyrite and other iron sulfides are present in coarse fraction (>63 μm; trace up to 25 percent) throughout the unit (fig. 7B and table 3).

Downcore magnetic susceptibility is relatively low in magnitude throughout the unit compared to typical slope sites fed by terrigenous sediments, but it does show significant variations downhole (fig. 6A). Changes in primary magnetic mineral grains present in the more clay-rich (biogenic poor) zones may explain some of the variability. Magnetic iron sulfides (likely gregite and(or) pyrrhotite) may also be responsible for some of the observed magnetic susceptibility highs. The gamma density data show a generally constant bulk density throughout Unit I (fig. 6A).

The major lithologies of Lithostratigraphic Unit I determined from smear slides consist primarily of clay-sized (70–99 percent) grains with minor amounts of silt-sized grains (up to 20 percent) and rare sand (up to 10 percent) (tables 1 and 2). Minor lithologies described in smear slides include burrow fills and variably colored sediments (tables 1 and 2). The lithogenic components of Lithostratigraphic Unit I are clay minerals, and subordinately quartz, mica, and heavy minerals. Opaque grains, mostly iron sulfides in irregular and framboidal forms, are common in all grain sizes, and typically trace to 10 percent of the total sediment (tables 1, 2, and 3). Authigenic grains other than iron sulfides include calcite and(or) dolomite and aragonite. The total biogenic component of the sediment is dominated by calcareous nannofossils, which comprise trace to 50 percent of the total (biogenic and non-biogenic) sediment grains (tables 1 and 2). Foraminifera occur (trace to 40 percent) in smear slides; however, they are more abundant (trace to 90 percent) in the coarse fractions of the sediments (table 3). Undetermined carbonate shell fragments are an important component of the coarse fraction (up to 85 percent). Terrestrial organic matter is common (trace to 25 percent) in smear slides taken throughout Unit I (tables 1 and 2).

Lithostratigraphic Unit II

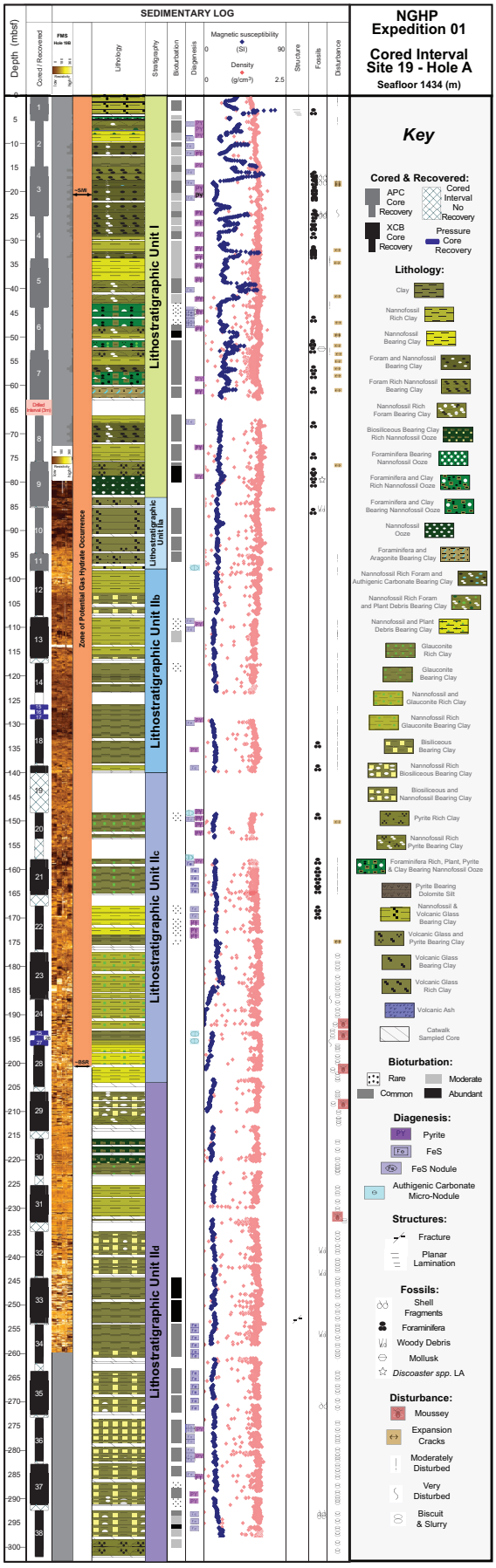
Intervals: Hole NGHP-01-19A, Sections NGHP-01-19A-09H-06 to NGHP-01-19A-38X-CC(EOH)

Depth: Hole NGHP-01-19A, 83.2-300.0 mbsf

Age: Late Miocene to Late Pliocene

Core recovery decreased in Unit II at Hole NGHP-01-19A compared to Unit I, particularly between Core NGHP-01-19A-13H and Core NGHP-01-19A-22X (fig. 6 and Site NGHP-01-19 Visual Core Descriptions). Unit II is composed of the clays and oozes that were typical of Unit I. Similar to Unit I, sediments in Unit II often contain minor components with abundances from component-bearing to -rich, but overall Unit II still exhibits less variability than Unit I. The minor components in Unit II are biogenic (biosiliceous, nannofossils, foraminifera), authigenic (glauconite, pyrite) and volcanogenic (glass) (see fig. 6, table 1 and Site NGHP-01-19 Visual Core Descriptions). The color of the sediments is much less variable

Figure 6 (following page). Lithostratigraphic summary of Hole NGHP-01-19A. Note: Colored intervals exceed symbol size when there is a range in the occurrence. Center point of each symbol represents true depth of occurrence. Therefore, colored bars may slightly exceed core recovery; see Site NGHP-01-19 Visual Core Descriptions for the expanded scale and detailed core descriptions; see Site NGHP-01-19 Oversized Figures for the enlarged version of this summary. [RAB, resistivity-at-bit; SMI, sulfate-methane interface]


SEDIMENTARY LOG
Depth (mbsf)
Core / Recovered
FMS Hole 19B
Lithology
Stratigraphy
Bioturbation
Diagenesis
Magnetic susceptibility
(SI)
Density
(g/cm³)
Structure
Fossils
Disturbance
Lithostratigraphic Unit I
Lithostratigraphic Unit IIa
Lithostratigraphic Unit IIb
Lithostratigraphic Unit IIc
Lithostratigraphic Unit IId
Zone of Potential Gas Hydrate Occurrence
BSR
NGHP Expedition 01
Cored Interval
Site 19 - Hole A
Seafloor 1434 (m)
Key
Cored & Recovered:
APC Core Recovery
Cored Interval No Recovery
XCB Core Recovery
Pressure Core Recovery
Lithology:
Clay
Nannofossil Rich Clay
Nannofossil Bearing Clay
Foram and Nannofossil Bearing Clay
Foram Rich Nannofossil Bearing Clay
Nannofossil Rich Foram Bearing Clay
Biosiliceous Bearing Clay Rich Nannofossil Ooze
Foraminifera Bearing Nannofossil Ooze
Foraminifera and Clay Rich Nannofossil Ooze
Foraminifera and Clay Bearing Nannofossil Ooze
Nannofossil Ooze
Foraminifera and Aragonite Bearing Clay
Nannofossil Rich Foram and Authigenic Carbonate Bearing Clay
Nannofossil Rich Foram and Plant Debris Bearing Clay
Nannofossil and Plant Debris Bearing Clay
Glauconite Rich Clay
Glauconite Bearing Clay
Nannofossil and Glauconite Rich Clay
Nannofossil Rich Glauconite Bearing Clay
Biosiliceous Bearing Clay
Nannofossil Rich Biosiliceous Bearing Clay
Biosiliceous and Nannofossil Bearing Clay
Pyrite Rich Clay
Nannofossil Rich Pyrite Bearing Clay
Foraminifera Rich, Plant, Pyrite & Clay Bearing Nannofossil Ooze
Pyrite Bearing Dolomite Silt
Nannofossil & Volcanic Glass Bearing Clay
Volcanic Glass and Pyrite Bearing Clay
Volcanic Glass Bearing Clay
Volcanic Glass Rich Clay
Volcanic Ash
Catwalk Sampled Core
Bioturbation:
Rare
Moderate
Common
Abundant
Diagenesis:
Pyrite
FeS
FeS Nodule
Authigenic Carbonate Micro-Nodule
Structures:
Fracture
Planar Lamination
Fossils:
Shell Fragments
Foraminifera
Woody Debris
Mollusk
Discoaster spp. LA
Disturbance:
Moussey
Expansion Cracks
Moderately Disturbed
Very Disturbed
Biscuit & Slurry

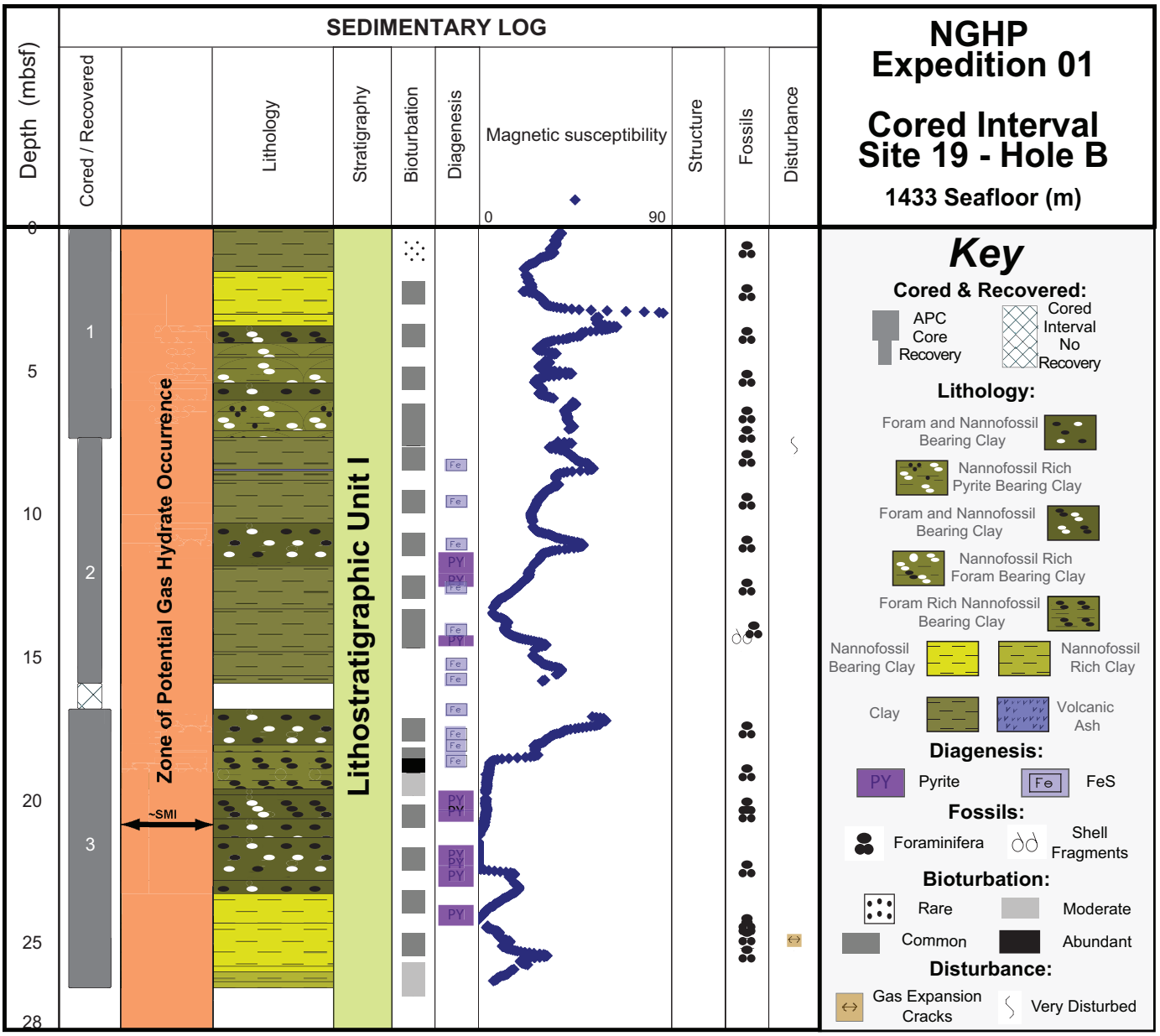


Figure 6. Lithostratigraphic summary of Hole NGHP-01-19A. Note: Colored intervals exceed symbol size when there is a range in the occurrence. Center point of each symbol represents true depth of occurrence. Therefore, colored bars may slightly exceed core recovery; see Site NGHP-01-19 Visual Core Descriptions for the expanded scale and detailed core descriptions; see Site NGHP-01-19 Oversized Figures for the enlarged version of this summary. [RAB, resistivity-at-bit; SMI, sulfate-methane interface]—Continued

than in Unit I with dark greenish gray (10Y 4/1, 5GY 4/1) being dominant, whereas olive (5Y 4/4) or very dark greenish gray (5GY 3/1, 10Y 3/1) occur only occasionally (fig. 6A and Site NGHP-01-19 Visual Core Descriptions). In the seismic data, Unit II corresponds to wavy reflectors underlying the subhorizontal reflectors of Unit I. As the *Discoaster* spp. last appears at the base of Unit I, it is likely that Unit II is older than Quaternary; however, post-cruise biostratgraphic work may help to better constrain the age of the Unit II stratigraphy.

The tentative age of Late Miocene to Late Pliocene note above, is based on an estimated sedimentation rate (described below under "Sedimentary Environment").

Fossil remains, visible at the core surface, are rarer than in Unit I and are dominated by foraminifera; shell fragments and wood pieces occur sporadically (fig. 6 and Site NGHP-01-19 Visual Core Descriptions). In the coarse fraction, fossil remains occur more frequently and are more diverse (that is, foraminifera, shell fragments, plant debris, diatoms, radiolarians, sponge spicules, silicoflagellates, and undetermined biosiliceous shell fragments) (fig. 6A, 7B, 7C, Site NGHP-01-19 Visual Core Descriptions, and table 3). Remarkably, volcanic glass is visible throughout Unit II as mm-sized patches, which are most likely burrows filled with detrital ash (fig. 6 and Site NGHP-01-19 Visual Core Descriptions). Detrital volcanic glass shards were also observed in smear slides taken throughout Unit II as trace to 15 percent amounts, but were rare in the coarse fraction (trace to 1 percent; tables 1 and 2). In Unit II, we were generally able to estimate a broad degree of bioturbation (from rare to abundant) in APC cores (Cores NGHP-01-19A-10H and NGHP-01-19A-11H), which were consistently less disturbed than the XCB cores. Bioturbation was also estimated in XCB cores of semi-lithified sediments where core "biscuits" preserved primary structures and core splitting with a mechanical saw as opposed to a wire resulted in a smooth, undisturbed surface of the biscuits (below Core NGHP-01- 19A-32X). Disturbance of other XCB cores during drilling or splitting precluded any reliable observation of bioturbation. In some cases, recognition of bioturbated zones was aided in the cores by highlighting dark-grey to black-colored iron sulfide precipitates. Iron monosulfides and pyrite are present in the upper and lower part of Unit II, but are absent from Core NGHP-01-19A-06H to Core NGHP-01-33X (fig. 6 and Site NGHP-01-19 Visual Core Descriptions). In contrast, in the coarse fractions, pyrite and other iron sulfides are present (trace up to 25 percent) throughout the unit (fig. 7 and table 3). Notably, Unit II of Site NGHP-01-19 was the only unit observed during NGHP Expedition 01 to contain authigenic dolomite concretions (fig. 11). Not all recovered dolomite concretions were *in situ*; however, some of them were found at the disturbed top of cores, indicating that they may have fallen into the hole during drilling from a shallower dolomitic horizon.

Downcore magnetic susceptibility is low in Unit II and much less variable than in Unit I (fig. 6). This suggests that magnetic iron sulfides are probably in low abundance or non-existent in Unit II (see above). Furthermore, there are no coarse grained sand or silt beds that would carry a strong primary magnetic susceptibility signal through detrital ferrimagnetic mineral grains; this is also confirmed by the generally lower silt content in sediments of Unit II compared to Unit I (table 1). The gamma density data continue to show a generally constant bulk density throughout Unit II (similar to Unit I), suggesting little variation in the bulk sediment composition, texture, and(or) fluid content (fig. 6).

The major lithologies of Lithostratigraphic Unit II determined from smear slides consist primarily of clay-sized grains (60–99 percent) with minor amounts of silt-sized grains (up to 40 percent) and rare sand (up to 10 percent) (table 1). Minor lithologies described in smear slides included burrow fills and variably colored sediments (table 1). The lithogenic smear-slide-estimated components are predominantly clay minerals with lesser amounts of quartz. In the coarse fraction, combined lithogenic grains (quartz, mica, heavy minerals) amount to a few percent (table 3). Opaque grains (mostly iron sulfides in irregular and framboidal forms) are common in all grain sizes of the total sediment (typically trace to 30 percent in smear sides and up to over 80 percent in the coarse fraction) (tables 1 and 3). Glauconite is the other dominant authigenic mineral in the smear slide and coarse fraction analysis that could reach up to 50 percent, but generally occurs as trace to 20 percent (tables 1 and 3). Additional authigenic grains other than iron sulfides include rare calcite and(or) dolomite encountered in smear slides (table 1). The total biogenic component of the sediment is dominated by calcareous nannofossils, which comprise trace to 40 percent of the total (biogenic and non-biogenic) sediment grains (table 1). Foraminifera occur (trace to a few percent) in smear slides; however, they are more abundant (trace to 90 percent) in the coarse fractions of the sediments (tables 1 and 3). The presence of siliceous microfossils increased significantly in Unit II compared to Unit I (from <5 percent to over 50 percent); diatoms and sponge spicules dominate this assemblage in smear slides, whereas radiolarians can reach up to 30 percent in the coarse fraction (tables 1 and 3). Undetermined carbonate and silica shell fragments are also an important component of the coarse fraction. Terrestrial organic matter is rare but was persistently found downcore (0–10 percent; fig. 7C) in smear slides taken throughout Unit II, but is not present in the coarse fraction (table 1).

Table 1. Smear-slide data for Hole NGHP-01-19A.

Sample reference			Texture			Mineral											
Core, section, depth (cm, in section)	MBSF	Lithology	Sand	Silt	Clay	Quartz	Feldspar	Mica	Heavy minerals	Clay minerals	Volcanic glass	Glauconite	Framboidal pyrite	Pyrite	Iron sulfides	Rock framents	Authigenic carbonates
NGHP-01-19A																	
1H-2,80	2.3	D		5	95	1				50	6				1		
1H-4,30	4.8	D		5	95	2				32	7				1		
2H-1,40	5.7	D		10	90	3				67	trace						
2H-1,110	6.4	D		15	85	5				72	3				1		
2H-2,60	7.4	M		5	95	1				49	3						
2H-2,70	7.5	M		99	1					1	99						
2H-2,90	7.7	D		1	99	1				79	3						
2H-3,50	8.8	D		2	98	1				86	2				1		
2H-4,20	10	D		2	98					77	2						
2H-6,70	13.5	D		5	95	5				88	3						
3H-2,10	16.4	D		5	95					69	trace						
3H-2,20	16.5	M	10	85	5	40				trace	trace		20				
3H-2,129	17.59	D		2	98					85	trace						
3H-3,36	18.16	D		2	98					69	trace						5
3H-3,101	18.81	D		10	90	trace				84	trace			2			
3H-6,72	23.02	D		1	99					83	trace		1				
4H-2,113	26.93	D		20	80	trace				42	trace						
4H-4,50	29.3	D			100	trace				56	trace						
4H-6,65	32.45	D	10	20	70					49	trace		1				
5H-2,85	36.15	D		4	96	4	1		1	84	2						1
5H-4,70	39	D		6	94	1			2	45	1		2				2
5H-5,64	40.44	D		5	95	1			1	49	trace		1				1
6H-2,85	45.65	D		15	85	1			1	20	trace		10				1
6H-4,60	48.4	D		1	99	2				70	1		3	4			
6H-5,42	49.72	D		3	97	3	1		1	48	2		1	1			
6H-7,13	52.43	D		7	93	1	trace		1	46	1		1				2
6H-6,135	52.15	D		20	80	2	3			9	1		10				
7H-2,50	54.8	D		4	96	1			1	52	1		1	4			2
7H-2,80	55.1	D		3	97	trace			1	53	trace		2				1
7H-3,90	56.7	D		20	80	3				51	1		2				1
7H-4,74	58.04	D		20	80	trace			1	34	trace		2	2			
7H-6,52	60.82	D		15	85	trace				49	trace		1				7
8H-1,10	66.4	M		75	25	trace								75			
8H-2,70	67.68	D		10	90	2	1	trace		75	1		1				2
8H-3,40	68.2	D		5	95	1	1	trace		61	trace						
8H-6,100	73.3	D		1	99	1	1			76	trace						
9H-2,70	78	D		15	85	2				73	3	2			12		
9H-4,70	80.9	D		2	98	1				43	3			trace			
9H-6,130	84.5	D		10	90	2				80	15			2			
10H-1,2	85.32	M		90	10	1				10	2			5			82
10H-2,70	87.5	D		10	90	3				90	6	trace		1			
10H-6,80	93.6	D		10	90	4				84	5		5				trace
11H-1,90	95.7	D		10	90	4				79	12			1			
11H-3,28	97.69	D		5	95	1				82	10			trace			
12X-2,112	99.95	D		6	94	2				55	3	trace			trace		
12X-5,20	103.14	D		10	90	2				85	3			1			
13X-2,115	109.3	D		5	95	1				54	2			2			
13X-7,41	116.06	D		10	90	2				79	trace			1			
14X-2,93	119.83	D		3	97					92	trace		4				
14X-4,83	122.73	D		2	98					98	1						
15P-1,4	126.04	D		1	99	trace				94	trace	1	2				
18X-2,70	131.2	D		2	98					94			2				
18X-4,105	134.55	M		90	10						trace	78	20				

Table 1. Smear-slide data for Hole NGHP-01-19A.—Continued

Sample reference	Biogenic								Comments
Core, section, depth (cm, in section)	Fora-minifera	Nanno-fossils	Carbonate shell fragments	Diatoms	Radio-larians	Silico-flagellates	Sponge spicules	Plant debris	
NGHP-01-19A—Continued									
1H-2,80	1	40		trace			1	trace	
1H-4,30	7	50					trace	1	
2H-1,40	5	20						5	
2H-1,110	12	5						2	
2H-2,60	7	30						10	from clay above ash bed
2H-2,70				trace					from ash layer, many morphologies of glass, possibly Toba Ash
2H-2,90	2	10					trace	5	
2H-3,50	2	5						3	
2H-4,20	10	8						3	
2H-6,70	trace	2						2	
3H-2,10	20	10						1	
3H-2,20	40								from burrow fill
3H-2,129	5	10						trace	
3H-3,36	10	15						1	authigenic carbonate is dolomite or calcite rhombs
3H-3,101	5	8						1	
3H-6,72	5	10						1	
4H-2,113	15	40						3	
4H-4,50	2	40						2	
4H-6,65	20	30							
5H-2,85		6						1	
5H-4,70	7	40							
5H-5,64	5	40						2	
6H-2,85	15	50						2	
6H-4,60	3	15						2	
6H-5,42	2	40						1	
6H-7,13	4	40	3					1	
6H-6,135	20	45						10	
7H-2,50	2	35						1	
7H-2,80	2	40						1	
7H-3,90	15	25						2	foraminifera mostly broken tests
7H-4,74	20	40						1	
7H-6,52	7	35						1	foraminifera mostly broken tests, aragonite needles
8H-1,10		25							pyrite in cubic and pyritahedron forms
8H-2,70	1	15						2	
8H-3,40	12	25							foraminifera mostly broken tests
8H-6,100	10	12						trace	
9H-2,70	4	3					trace	1	both fine and coarse grained FeS
9H-4,70	3	50						trace	trace discoasters
9H-6,130	trace	trace			trace		trace	1	
10H-1,2				trace			trace	trace	Calcite or dolomite rhombs.
10H-2,70	trace	trace		trace			trace	trace	
10H-6,80	trace	2		trace	trace		trace	trace	Calcite or dolomite rhombs; trace discoasters
11H-1,90	trace	4			trace		trace	trace	trace discoasters
11H-3,28	trace	7					trace		trace discoasters
12X-2,112	trace	40		trace			trace	trace	trace discoasters
12X-5,20	1	3		3	trace	1	1	trace	discoasters 1%
13X-2,115	1	40		trace	trace	trace	trace	trace	trace discoasters
13X-7,41	1	10		5		trace	2	trace	
14X-2,93		1		2	trace			1	
14X-4,83				trace			trace	1	
15P-1,4		2						1	
18X-2,70	trace			2			1	1	
18X-4,105				trace				2	

Table 1. Smear-slide data for Hole NGHP-01-19A.—Continued

Sample reference			Texture			Mineral											
Core, section, depth (cm, in section)	MBSF	Lithology	Sand	Silt	Clay	Quartz	Feldspar	Mica	Heavy minerals	Clay minerals	Volcanic glass	Glauconite	Framboidal pyrite	Pyrite	Iron sulfides	Rock framents	Authigenic carbonates
NGHP-01-19A—Continued																	
18X-6,80	137.28	D		2	98	trace				94			3				trace
19X-1,33	138.93	D		5	95					86	1		1				
20X-2,83	150.63	D		10	90					75	1	20	2				
20X-4,25	153.05	D		5	95					90		5	3				
21X-1,72	168.22	D		5	95	2				75	1	10	1				
21X-4,130	163.69	D		5	95	5				78		10					trace
24X-2,75	189.05	D		3	97					77	1	7		1			
24X-5,30	193.1	D		7	93	trace			1	73		15		2			2
22X-2,70	169.7	D		5	95	8				82	2						
22X-5,60	174.1	D		2	98	5				90	trace		1				
23X-2,80	179.4	D		5	95	1				64	trace	15			1		1
23X-6,60	184.91	D		2	98			trace	2	75	1				2		3
25P-1,40	193.7	D		2	98					97	trace						
27E-1,42	195.72	D		5	95	trace				54		15					
28X-2,86	197.59	D		2	98	trace				75	2	10					
28X-5,64	201.57	D		1	99	trace	trace			86	2	3			trace		
29X-2,93	207.35	D		10	90	2				45	2	3		1			
29X-5,75	211.67	D		10	90	1				47	2	3		1			
30X-2,100	216.75	D		10	90	3				37	1	3		trace			
31X-6,20	232.41	D		5	95	2				82	1	10		trace			
31X-1,70	225.9	D		5	95	2				61	1	4		trace			
31X-6,50	232.71	D		5	95	2				80	1	9		trace			
32X-2,90	236.54	D		2	98					68		4					
32X-5,90	241.04	D		1	99					91			1				
33X-2,127	246.24	D		1	99	trace				86	1		2				
33X-5,129	250.66	D		2	98	1				96			1				
34X-2,91	255.48	D		1	99					97	trace		1				
34X-5,94	269.97	D		2	98	1				93	trace		1				
35X-2,94	265.47	D		2	98	trace				89	trace						
35X-5,98	270.01	D	1	1	98					82			1				
36X-2,75	275.85	D		3	97	3				65	2			trace			tracc
36X-6,63	281.22	D		2	98	3				75	trace	trace		trace			
37X-1,50	283.3	D		2	98	2				81	trace	trace		trace			2
37X-6,60	290.08	D		2	98	trace				73		trace		2			
38X-1,102	293.42	D		5	95	trace				83		2					
38X-4,33	297.23	D		10	90					64		1	35				
38X-5,130	299.7	M	10	30	60	trace				19	trace	50	20				

Table 1. Smear-slide data for Hole NGHP-01-19A.—Continued

Sample reference	Biogenic								Comments
Core, section, depth (cm, in section)	Fora-minifera	Nanno-fossils	Carbonate shell fragments	Diatoms	Radio-larians	Silico-flagellates	Sponge spicules	Plant debris	
NGHP-01-19A—Continued									
18X-6,80	1							2	
19X-1,33	trace	12							trace discoasters
20X-2,83	trace	trace						2	
20X-4,25								2	
21X-1,72	3	2		3		2	trace	1	
21X-4,130		3		1		trace	1	2	
24X-2,75	trace	12				trace		2	trace discoasters
24X-5,30		5		trace	trace		trace	2	
22X-2,70		5		1		trace	1	1	
22X-5,60	trace	3		trace			trace	1	trace discoasters
23X-2,80	1	15		trace		trace	trace	2	trace discoasters
23X-6,60	trace	15		trace				2	trace discoasters
25P-1,40	1	1					trace	1	trace discoasters
27E-1,42	trace	30			trace			1	trace discoasters
28X-2,86	1	10		trace		trace	1	1	trace discoasters
28X-5,64		7		1			1		discoasters 1%
29X-2,93	2	40		2		trace	3	trace	trace discoasters
29X-5,75	7	36		2			1	trace	trace discoasters
30X-2,100		50		2		trace	4	trace	trace discoasters
31X-6,20	trace	1		1			3	trace	
31X-1,70	trace	30		1			1	trace	discoasters 1%
31X-6,50	trace	5		1			2	trace	
32X-2,90		5		3	trace		20		
32X-5,90		2		1			5		1 discoaster
33X-2,127	2	3		3			3		
33X-5,129		1						1	trace discoasters
34X-2,91		1		1	trace		trace		
34X-5,94	trace			2		trace	3		discoasters present
35X-2,94		3		3			5	trace	trace discoasters
35X-5,98	trace	5		5	trace		7		
36X-2,75	trace			5		trace	25		
36X-6,63	trace	7		5		trace	10		trace discoasters
37X-1,50	trace	trace		3		2	10		discoasters 2%
37X-6,60		15		2		3	5		trace discoasters
38X-1,102	3	5		5	trace	trace	2		discoasters present
38X-4,33	trace	trace				trace	trace		trace discoasters
38X-5,130	5	5						1	

Note: M = minor lithology, D = dominant lithology

Table 2. Smear-slide data for Hole NGHP-01-19B.

Sample reference			Texture			Mineral											
Core, section, depth (cm, in section)	MBSF	Lithology	Sand	Silt	Clay	Quartz	Feldspar	Mica	Heavy minerals	Clay minerals	Volcanic glass	Glauconite	Framboidal pyrite	Pyrite	Iron sulfides	Rock framents	Authigenic carbonates
NGHP-01-19B																	
1H-1,10	0.1	D		3	97	1			2	88	1	2			1		
1H-2,40	1.9	D		2	98	3			2	73	3	2			2		1
1H-3,40	3.4	D		5	95	3			2	53	3						2
1H-3,100	4	D		7	93	2			1	59	3	1	1		2		
1H-4,10	4.6	D		10	90	2			2	60	2		3				2
1H-4,50	5	D		3	97	4				67	2	trace					2
1H-4,90	5.4	D		5	95	1				71	3				2		4
1H-5,50	6.5	D		4	96	trace				66	2			10			2
2H-1,100	8.3	D		1	99					92	3						
2H-1,130	8.6	D		3	97					92	trace						
2H-3,40	10.7	D		3	97					87	1		1				
2H-4,50	12.3	D		2	98					92	1		1				
2H-5,60	13.9	D		3	97	trace				94	trace						
2H-6,60	15.4	D		2	98	1				94	2						
3H-1,35	17.15	D	5	10	85	5				70	1						trace
3H-1,93.5	17.735	M	80	10	10						trace						
3H-1,125	18.05	D		3	97					75	trace						
3H-2,20	18.5	D	1	5	94					73	2	trace					
3H-2,130	19.6	D		3	97					72	trace		1				
3H-3,84	20.64	D		5	95	1				81	1						
3H-5,45	23.25	D		2	98	trace				90	trace						
3H-6,114	25.44	D		2	98	1				85	2						1
3H-7,20	26	D		1	99	3				78	3						

Sample reference	Biogenic								Comments
Core, section, depth (cm, in section)	Foraminifera	Nanno_fossils	Carbonate shell fragments	Diatoms	Radiolarians	Silicoflagellates	Sponge spicules	Plant debris	
NGHP-01-19B—Continued									
1H-1,10	trace	3		1			trace	1	trace tourmaline
1H-2,40	1	10		1	trace			2	
1H-3,40	20	15						2	foraminifera mostly broken tests
1H-3,100	7	20						4	
1H-4,10	10	15						4	
1H-4,50	7	15						3	
1H-4,90	9	10							foraminifera mostly broken tests
1H-5,50	3	15						2	
2H-1,100	3	2					trace		volcanic glass prevalent
2H-1,130	2	3				trace		3	
2H-3,40	5	5						1	
2H-4,50	2	3						1	
2H-5,60	3	3						trace	
2H-6,60	trace	2						1	
3H-1,35	15	8						1	
3H-1,93.5	90	10							foraminifera whole tests and fragments
3H-1,125	20	5							
3H-2,20	15	10						trace	
3H-2,130	12	12						3	
3H-3,84	5	10						2	foraminifera mostly broken tests
3H-5,45	3	5						2	
3H-6,114	1	10							
3H-7,20		15						1	

Note: M = minor lithology, D = dominant lithology

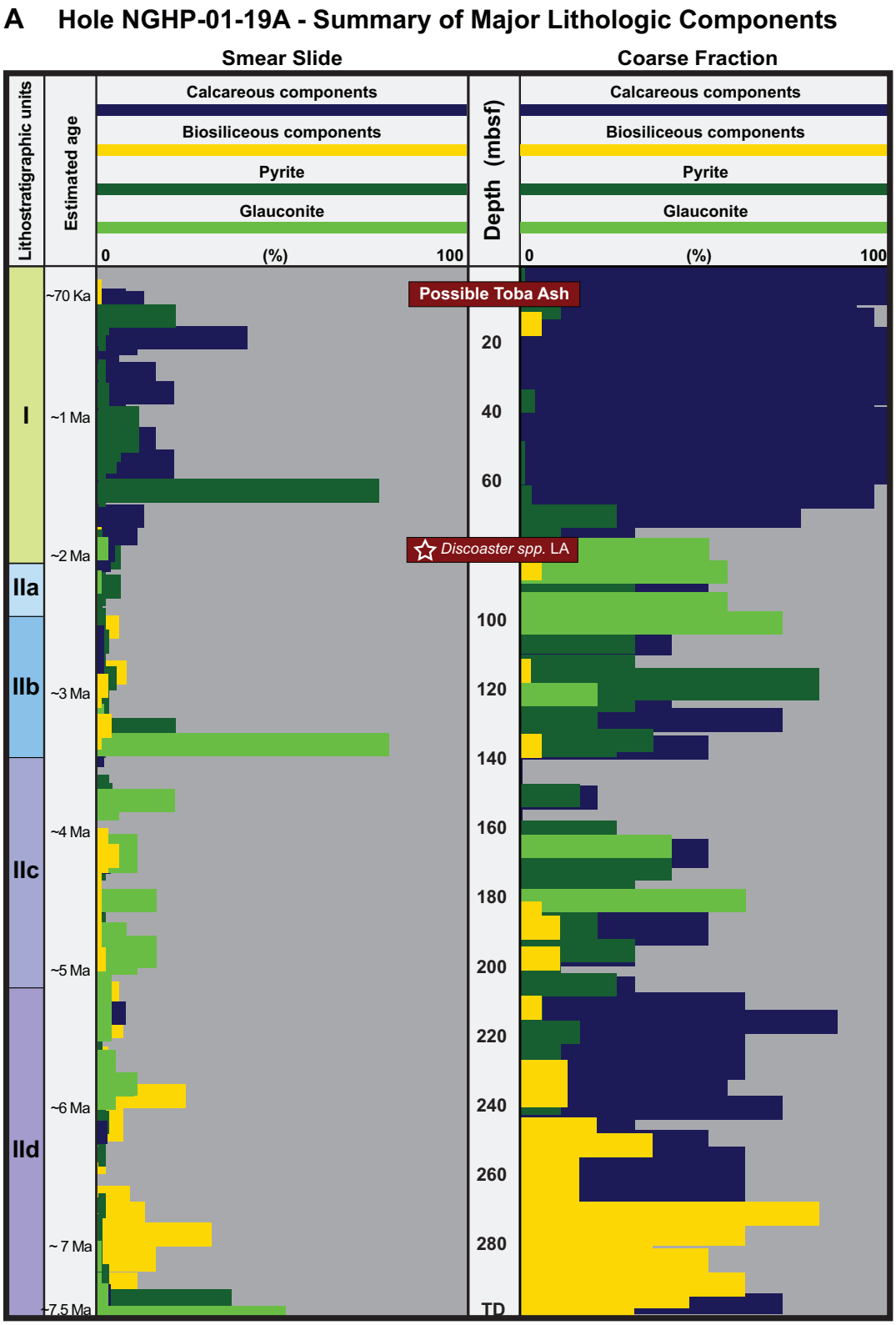


Figure 7. A, Major lithologic components in smear slide (see table 1) and coarse fraction (see table 3) plotted from percent visual estimation. Major lithologic components shown, for clarity, as individual abundance plots in coarse fraction and smear slides. A, Age estimates based on the last appearance of *Discoaster* spp. at 80.9 mbsf. Given this datum, a sedimentation rate of 4 cm/1,000 yr can be calculated and extrapolated to the bottom of the hole to yield a first-order age model. B, Calcareous components, pyrite, other iron sulfides, and glauconite observed in smear slides and coarse fractions; C, Biosiliceous components observed in smear slides and coarse fractions. [mbsf, meters below sea floor]

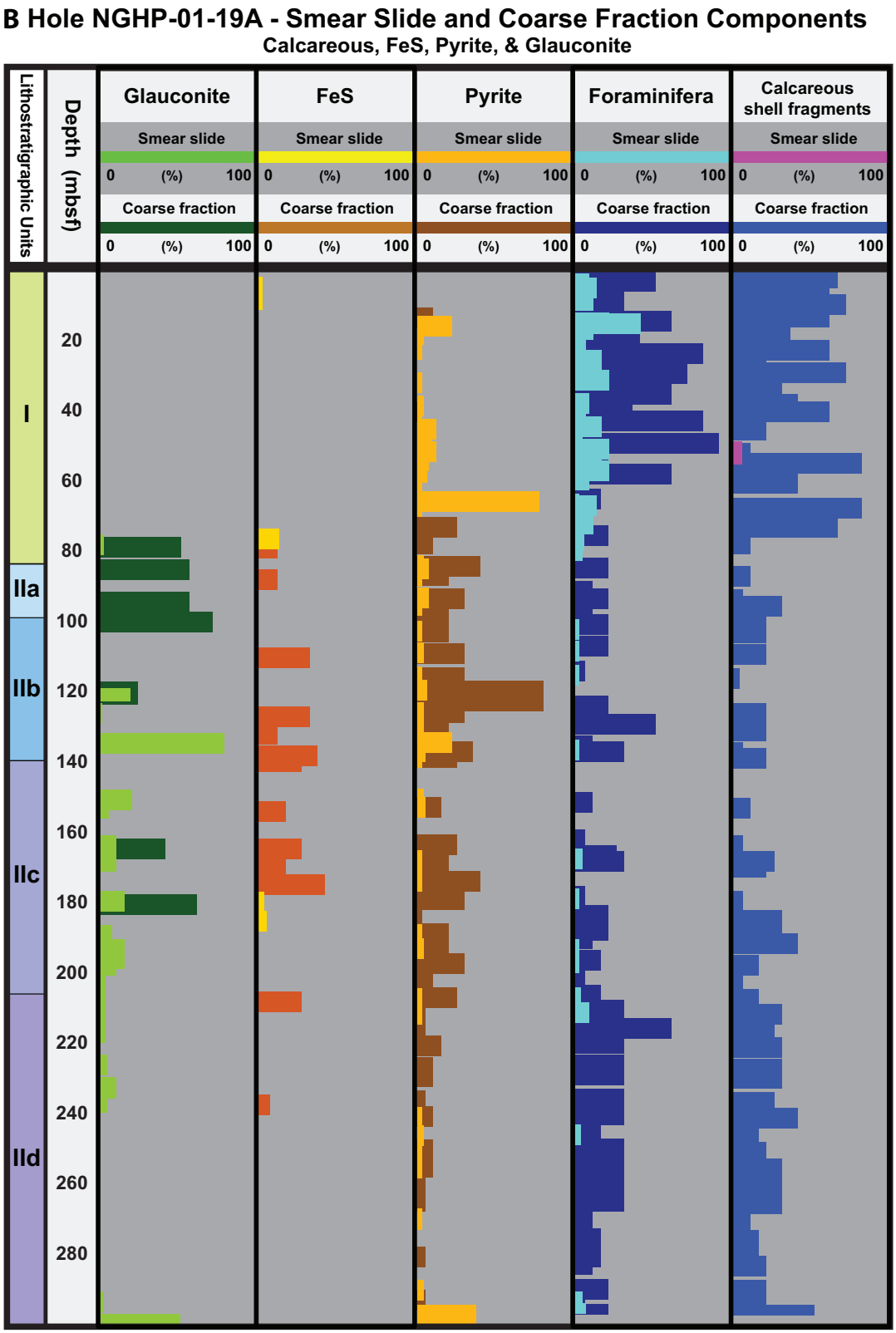


Figure 7. A, Major lithologic components in smear slide (see table 1) and coarse fraction (see table 3) plotted from percent visual estimation. Major lithologic components shown, for clarity, as individual abundance plots in coarse fraction and smear slides. A, Age estimates based on the last appearance of *Discoaster* spp. at 80.9 mbsf. Given this datum, a sedimentation rate of 4 cm/1,000 yr can be calculated and extrapolated to the bottom of the hole to yield a first-order age model. B, Calcareous components, pyrite, other iron sulfides, and glauconite observed in smear slides and coarse fractions; C, Biosiliceous components observed in smear slides and coarse fractions. [mbsf, meters below sea floor]—Continued

C Hole NGHP-01-19A - Smear Slide and Coarse Fraction Components

Biosiliceous

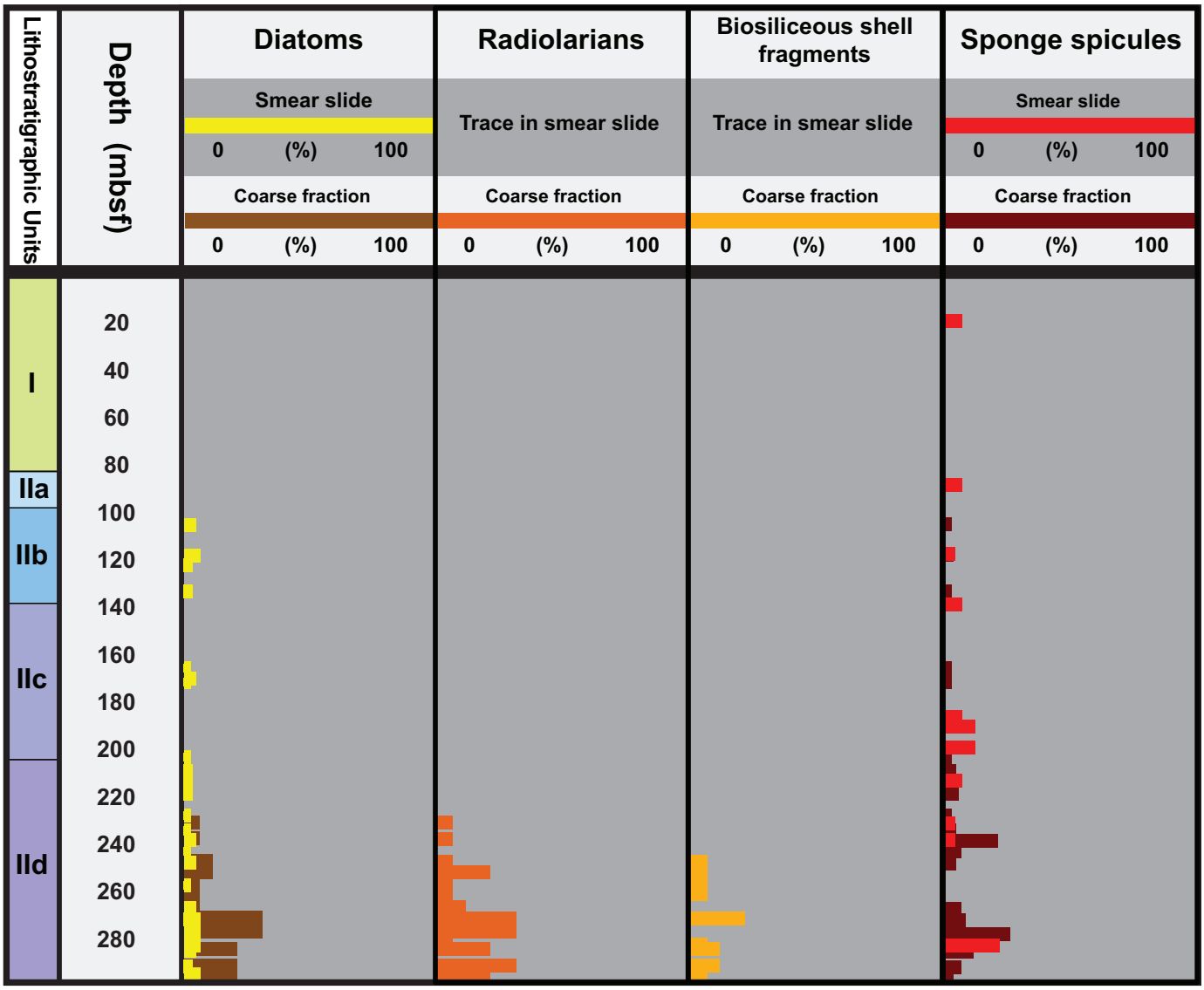


Figure 7. A, Major lithologic components in smear slide (see table 1) and coarse fraction (see table 3) plotted from percent visual estimation. Major lithologic components shown, for clarity, as individual abundance plots in coarse fraction and smear slides. A, Age estimates based on the last appearance of *Discoaster* spp. at 80.9 mbsf. Given this datum, a sedimentation rate of 4 cm/1,000 yr can be calculated and extrapolated to the bottom of the hole to yield a first-order age model. B, Calcareous components, pyrite, other iron sulfides, and glauconite observed in smear slides and coarse fractions; C, Biosiliceous components observed in smear slides and coarse fractions. [mbsf, meters below sea floor]—Continued

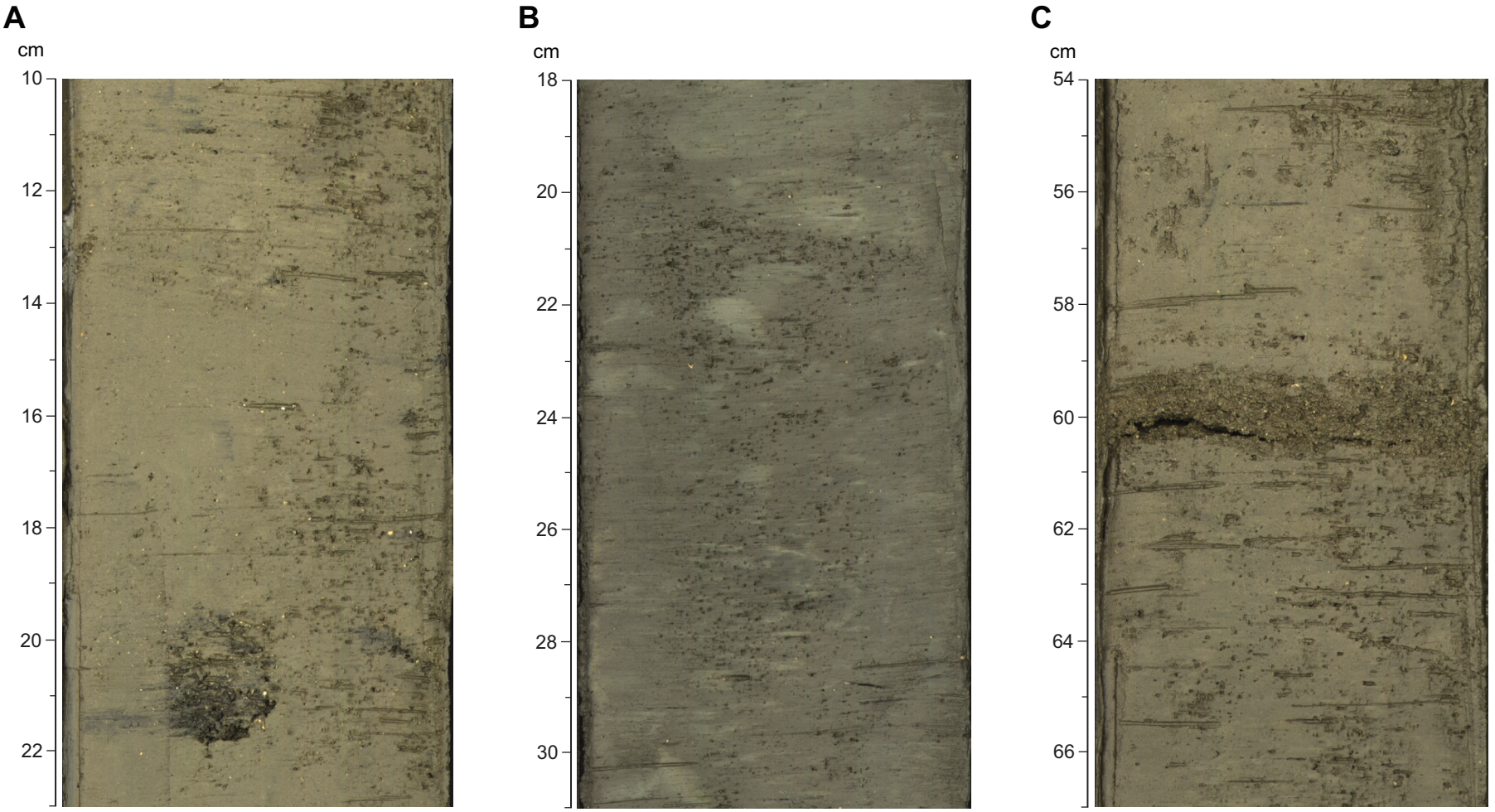


Figure 8. Visible foraminifera and shell fragments observed throughout Unit I. A, Section NGHP-01-19A-01H-3; B, Section NGHP-01-19A-03H-2; *C*, Section NGHP-01-19A-04H-2.

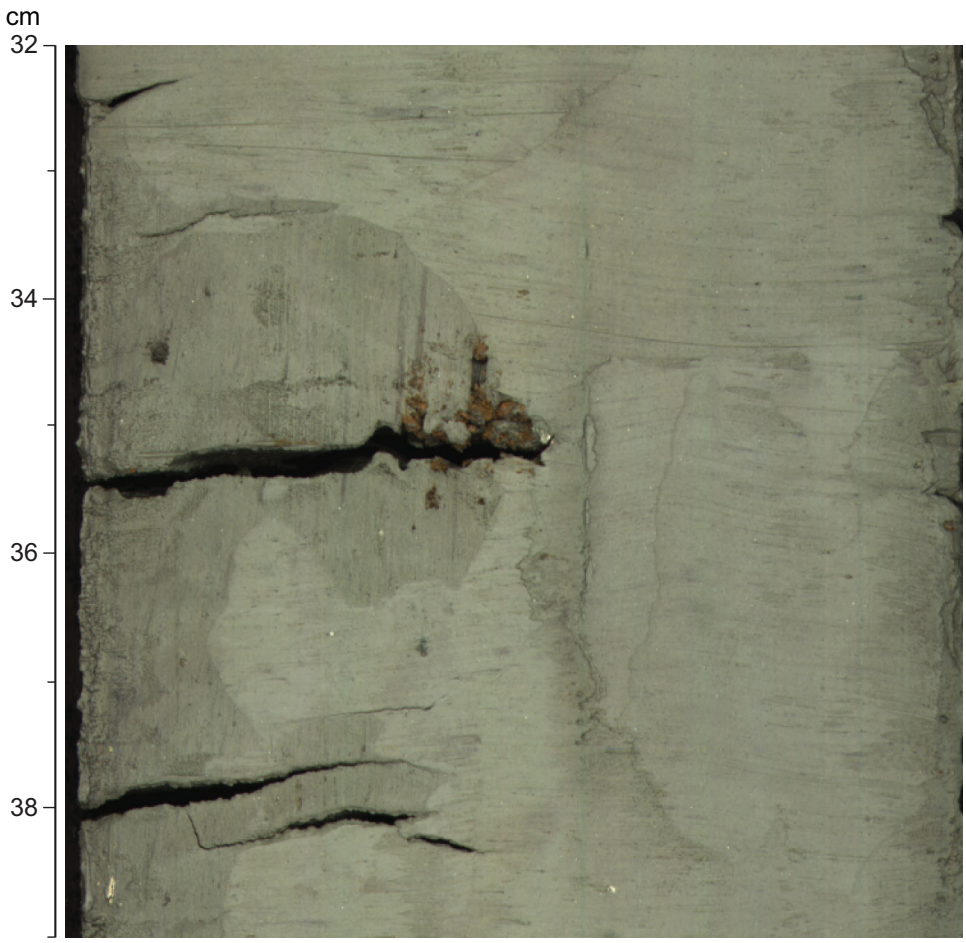


Figure 9. Terrestrial organic debris recovered in Section NGHP-01-19A-05H-2.

Subunit IIa

Intervals: Hole NGHP-01-19A,
Sections NGHP-01-19A-09H-06
to NGHP-01-19A-11H-CC

Depth: Hole NGHP-01-19A, 83.2-98.3 mbsf

Sediments in this subunit are clays enriched in volcanic glass that help to distinguished this subunit from the subunits below (figs. 6, 7, Site NGHP-01-19 Visual Core Descriptions, and tables 2 and 3). Glauconite as well as pyrite and other iron sulfides are abundant in this subunit (figs. 7A and 7B).

Subunit IIb

Intervals: Hole NGHP-01-19A,
Sections NGHP-01-19A-12H-01
to NGHP-01-19A-19X-CC

Depth: Hole NGHP-01-19A, 98.3-140.1 mbsf

Subunit IIb is composed primarily of clays (fig. 6 and Site NGHP-01-19 Visual Core Descriptions); nannofossil-bearing to -rich clays, at a level justifying lithologic recognition, are rare and thin. Pyrite and other iron sulfides are also common in this Subunit (fig. 7).

Subunit IIc

Intervals: Hole NGHP-01-19A,
Sections NGHP-01-19A-20X-01
to NGHP-01-19A-28X-CC

Depth: Hole NGHP-01-19A, 140.1-205.9 mbsf

Glauconite enrichments are the principal characteristic for the clays of Subunit IIc and are recognized as individualized lithologies (figs. 6, 7, Site NGHP-01-19 Visual Core Descriptions, and tables 2 and 3). Pyrite and other iron sulfides continue to be common in this subunit (fig. 7B).

Subunit IId

Intervals: Hole NGHP-01-19A,
Sections NGHP-01-19A-29X-01
to NGHP-01-19A-38X-CC(EOH)

Depth: Hole NGHP-01-19A, 205.9-300.0 mbsf

In this subunit, both biosiliceous and biogenic carbonate increase in abundance, reaching levels which justify lithologic recognition (that is, bearing- or rich-) in the dominant clays (figs. 7A and 7C). Pyrite and glauconite contents generally decrease, although glauconite is locally enriched and visually observable at the bottom of the hole (fig. 12).

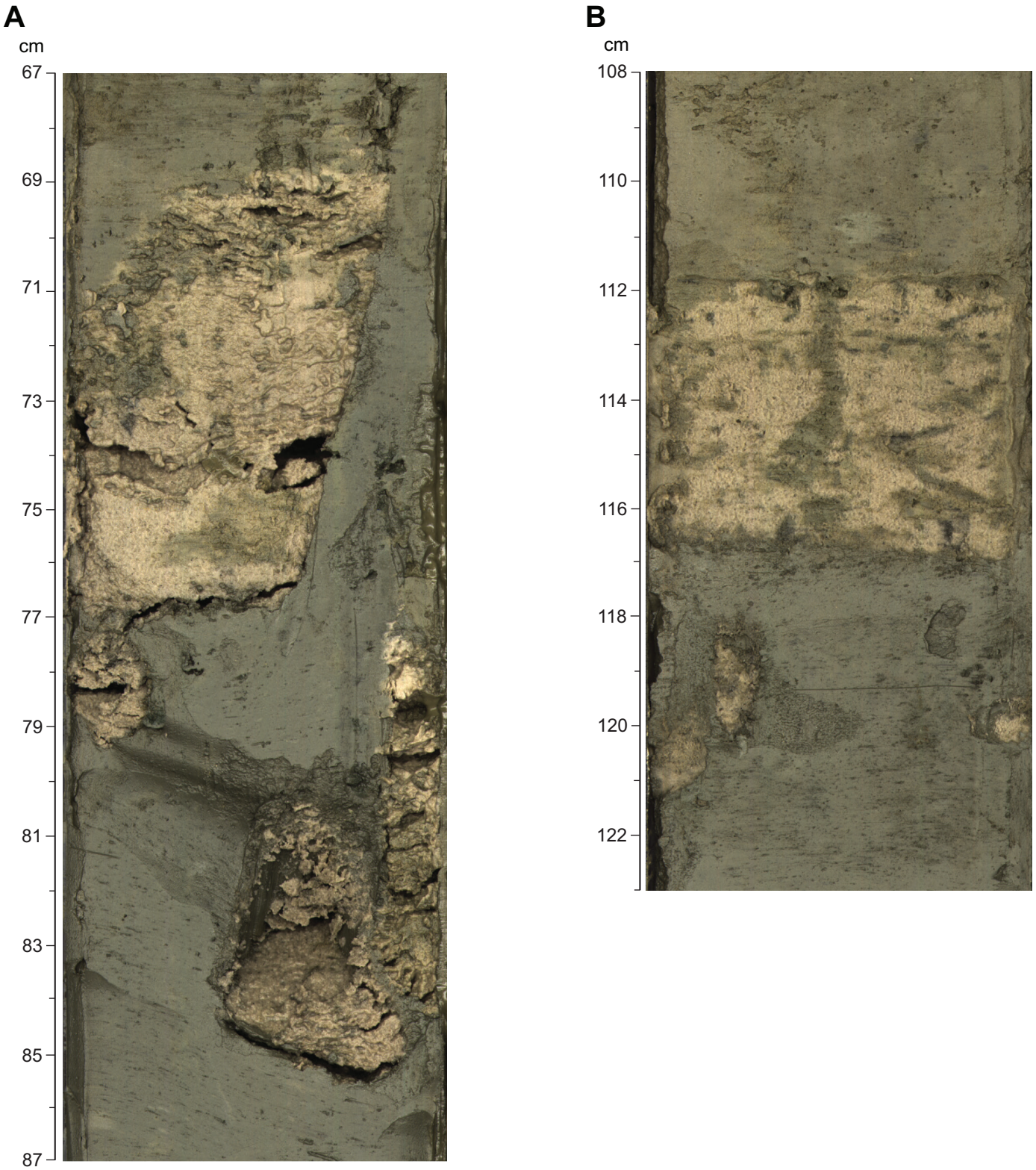


Figure 10. Thick ash bed, possibly the Toba ash (~70–75 ka) in Section NGHP-01-19A-02H-2 and NGHP-01-19B-02H-1. Note the ash in *A* is disturbed and has expanded due to coring. [ka, thousand years ago]

Sedimentary Environment

The presence of a thick, near-surface ash bed in Core 2H in both Holes NGHP-01-19A and NGHP-01-19B is consistent with the Toba Ash occurrence (75 ka) in this region (Kudrass and others, 2001). Assuming this unit is the Toba Ash, a sedimentation rate of 10–11 cm/ky is estimated for the upper parts of Hole NGHP-01-19A (~7.5 m) and Hole NGHP-01-19B (–8.5 m). The sedimentation rate calculated for the last ~2 Ma in Hole NGHP-01-19A based on the occurrence of *Discoaster* spp. is much less (~4 cm/ky) than the one estimated in the upper part of the holes based on the possible Toba Ash position. The large water content and less-consolidated character of the upper ~20 m at Holes NGHP-01-19A and NGHP-01-19B (see "Physical Properties") can influence estimation of sedimentation rates. Until sediments lose the large amount of water typical of the upper 20 m, calculated apparent accumulation rates vary as a function of water content; thus, the sedimentation rate of 4 cm/kyr (based on the LA of *Discoaster* . spp.) should be closer to a long term sedimentation rate for Site NGHP-01-19. Using this rate of sedimentation (4 cm/ky), the extrapolated age at the bottom of Hole NGHP-01-19A is ~7.5 Ma (fig. 7A). Based on this preliminary age model, biosiliceous sedimentation stopped to be a persistent feature at Site NGHP-01-19 between 5 and 4 Ma similar to Site NGHP- 01-17 near the Andaman Islands, suggesting that Site NGHP-01-19A may have recorded Bengal Bay-wide ecosystem changes probably related to the tapering out of the "biogenic bloom" observed throughout the tropical Indo-Pacific (for example, Dickens and Owen, 1999; see "Lithostratigraphy" in "Site NGHP-01-17"). Also similar to the Andaman site, pyrite and glauconite contents are high in the ~2 to 6 Ma interval (fig. 7A). Elevated levels of pyrite could be related to an elevated organic matter input which lead to a more intense redox diagenesis during the Miocene-Pliocene biogenic bloom. Typically, glauconite forms in low sedimentation rates on the shelf and slope (Hesselbo and Huggett, 2001 and references therein). Regardless of the location where this glauconite has formed (that is, on the shelf and then transported on the slope versus *in situ* on the slope), its presence suggests that sediments deposited between 2–6 Ma were weakly reducing and the organic matter content in the sediment was relatively high; consistent with idea of a Miocene-Pliocene biogenic bloom. As at Site NGHP-01-17, environmental conditions appeared to have changed significantly in the Quaternary, becoming more favorable for foraminifera development as suggested by the increase in both foraminifera and calcareous test fragments contents to more than double their abundances prior to the Quaternary (fig. 7B). This faunal change could be related to the global cooling during this period and(or) to the parallel intensification of the monsoon (Clift, 2006 and references therein).

Correlation between Sites NGHP-01-18 and NGHP-01-19

Based on the last occurrence of *Discoaster* spp. at 80.9 mbsf at Site NGHP-01-19 (fig. 6A), and the lack of *Discoaster* spp. at Site NGHOP-01-18, we suspect that the stratigraphy at Site NGHP-01-18 is expanded relative to Site NGHP-01-19. This is consistent with the observation that the variable lithologies observed at Site NGHP-01-19 in Subunits IIa-d are not encountered at Site NGHP-01-18. Although, the upper stratigraphy at both sites may be correlative, the shallow ash bed recovered at Site NGHP-01-19 (Core NGHP-01-19A-02H) was not observed at Site NGHP-01-18. A lack of deposition, slope failure, or bottom current reworking may explain the absence of the ash at this site. Post-cruise biostratigraphic analyses may help to correlate the stratigraphy between both Sites NGHP-01-18 and NGHP-01-19.

Gas-Hydrate Occurrence

At Site NGHP-01-19, a general decrease in core temperature was observed in the IR data from the cores (See "Physical Properties" NGHP-01-19) above the BSR (~170 mbsf to ~210 mbsf) and from ~125 mbsf to ~130 mbsf (see "Physical Properties"). This type of IR response is generally indicative of diffuse gas hydrate presence. Samples of Interstitial Water (IW) taken from these IR anomalies also showed porewater freshening in Cores NGHP-01-19A-15P, -17E, -28X and -27E (see "Inorganic Geochemistry"). Pressure core NGHP-01-27P contained an estimated 2.4 percent gas hydrate (averaged over the 1-m core), while an IW sample taken from a zone within the pressure core indicated ~10 percent gas hydrate in that particular IW interval (see "Physical Properties" and "Inorganic Geochemistry"). Pressure Core NGHP-01-19A-17E also contained abundant methane in excess of saturation (indicative of gas hydrate) and an IW sample taken from this core also showed pore water freshening (see "Inorganic Geochemistry"). At Site NGHP-01-19, there were no significant changes in lithology associated with these gas hydrate zones, suggesting that the gas hydrate, where present, existed in a disseminated state within the fine-grained clay as fracture fill and(or) as micro-pore filing; this is consistent with the broad IR anomalies described above. Mousse-like texture was observed in the split cores at several locations throughout the hole including several occurrences observed below the BSR (fig. 6). Similar to Site NGHP-01-18, there were no gas hydrate related porewater chemistry anomalies proximal to these moussey intervals. Therefore, these textures were likely the result of extreme drilling disturbance caused by rough seas at the time of XCB coring and(or) degassing of the core upon recovery.

Table 3. Coarse-fraction sieve data for Hole NGHP-01-19A.

Sample reference		Mineral											
Core, section, depth (cm, in section)	MBSF	Quartz	Feld-spar	Mica	Heavy minerals	Volcanic glass	Pyrite	Iron sulfides	Framboidal pyrite	Rock fragments	Pumice	Other minerals	Authigenic carbonates
						NGHP-01-19A							
1H-2,80	2.3			trace			trace	trace					
1H-4,30	4.8				trace								
2H-1,110	6.4				trace		trace						
2H-3,50	8.8												
2H-4,20	10						trace						
2H-6,70	13.5						10						
3H-2,129	17.59			trace		trace	trace						
3H-6,72	23.02			trace	trace	trace							
4H-2,85	26.65			60	5	5	trace						
4H-2,113	26.93			trace	trace		trace						
4H-4,50	29.3				trace		trace						
4H-6,65	32.45				trace		trace						
5H-4,7	38.37	trace											
5H-5,64	40.44			trace			3		2				
6H-2,85	45.65	trace											
6H-6,135	52.15												
7H-2,80	55.1	trace					trace						
7H-6,52	60.82	trace					trace						
8H-2,70	67.68	trace		1			2	2					
8H-6,100	73.3						25						
9H-2,70	78						10	10				50	
9H-6,130	84.5			trace	5		40					55	
10H-2,20	87				5		20	10				30	
10H-6,80	93.6						30					55	
11H-1,88	95.68						20					30	
11H-3,26	97.67						20					50	
12X-2,42	99.25					trace	20					70	
12X-5,20	103.14						20					40	
13X-2,113	109.28						30	30					
13X-7,57	116.22						30					60	
14X-2,93	119.83						80					20	
14X-4,83	122.73						80					20	
15P-1,5	126.05						30	30					
18X-2,70	131.2						20	10					
18X-6,80	137.28						35	35				10	
19X-1,33	138.93						25	25					
20X-4,25	153.05						15	15				50	
21X-1,72	168.22						15	15				20	
21X-4,130	163.69						25	25				40	
22X-2,70	169.7			trace			20					30	
22X-5,60	174.1						40	40				20	
23X-2,80	179.4						30					60	
23X-6,60	184.91						3	2				40	
24X-2,70	189						20					20	
24X-4,30	191.6						20					30	
28X-2,80	197.53						30					30	
28X-5,61	201.54						10					80	
29X-2,93	207.35						25	25				20	
29X-5,74	211.66						5					30	
30X-2,100	216.75						5					10	
30X-6,30	220.95	20			5		15						
31X-2,70	227.11						10					30	
31X-4,50	229.91	3			5		10					10	
32X-2,90	236.54	3					5	5				20	
32X-5,90	241.04	5		5			10					10	
33X-2,127	246.24											50	
33X-5,129	250.66						10					5	
34X-5,96	260.03						5					20	
34X-2,91	255.48						10					15	
35X-5,98	270.01						trace					trace	
35X-2,94	265.47						5					20	
36X-2,75	275.85											10	
36X-6,63	281.22						5					30	
37X-1,50	283.3											20	
37X-6,60	290.08												
38X-1,102	293.42	1	1	1	1	1	5					20	
38X-4,33	297.23												

Table 3. Coarse-fraction sieve data for Hole NGHP-01-19A.—Continued

Sample reference		Biogenic										Comments
Core, section, depth (cm, in section)	MBSF	Foraminifera	Carbonate shell fragments	Diatoms	Radiolarians	Silicoflagellates	Siliceous shell fragments	Sponge spicules	Fish remains	Other biogenic	Plant debris	
NGHP-01-19A—Continued												
1H-2,80	2.3	30	65						5			possible lepidolite
1H-4,30	4.8	40	60					trace				
2H-1,110	6.4	50	50					trace				
2H-3,50	8.8											
2H-4,20	10	30	70									
2H-6,70	13.5	30	60									
3H-2,129	17.59	60	35					5				
3H-6,72	23.02	40	60						trace			
4H-2,85	26.65	10	20						trace			
4H-2,113	26.93	80	20									
4H-4,50	29.3	30	70									many broken fragments
4H-6,65	32.45	70	30									
5H-4,7	38.37	60	40									
5H-5,64	40.44	35	60					trace				
6H-2,85	45.65	80	20	trace	trace			trace				
6H-6,135	52.15	90	10									
7H-2,80	55.1	20	80					trace			trace	
7H-6,52	60.82	60	40					trace				
8H-2,70	67.68	15	80									
8H-6,100	73.3	10	65									
9H-2,70	78	20	10									other mineral is glauconite
9H-6,130	84.5	trace	trace									other mineral is glauconite
10H-2,20	87	20	10					5				
10H-6,80	93.6	10	5									other mineral is glauconite
11H-1,88	95.68	20	30									other mineral is glauconite
11H-3,26	97.67	10	20									
12X-2,42	99.25	5	5					trace				other mineral is glauconite
12X-5,20	103.14	20	20									
13X-2,113	109.28	20	20									
13X-7,57	116.22	5	3					2				
14X-2,93	119.83											other mineral is glauconite
14X-4,83	122.73											
15P-1,5	126.05	20	20									
18X-2,70	131.2	50	20									
18X-6,80	137.28	10	5					5				
19X-1,33	138.93	30	20									
20X-4,25	153.05	10	10					trace				
21X-1,72	168.22	25	25									pyritahedrons
21X-4,130	163.69	5	5									other mineral is glauconite
22X-2,70	169.7	30	20									
22X-5,60	174.1	trace	trace									
23X-2,80	179.4	5	5									other mineral is glauconite; trace bentonite
23X-6,60	184.91	20	30					5				
24X-2,70	189	20	30					10				
24X-4,30	191.6	10	40									
28X-2,80	197.53	15	15					10				
28X-5,61	201.54	5	5									
29X-2,93	207.35	15	15				trace	trace				
29X-5,74	211.66	30	30					5				
30X-2,100	216.75	60	25					trace				
30X-6,30	220.95	30	30									
31X-2,70	227.11	30	30									
31X-4,50	229.91	30	30	5	5			2				
32X-2,90	236.54	30	25	5	5			2				
32X-5,90	241.04	30	40									
33X-2,127	246.24	15	15	10	5		5					
33X-5,129	250.66	30	20	10	20		5					
34X-5,96	260.03	30	30	5	5		5					
34X-2,91	255.48	30	30	5	5		5	trace				
35X-5,98	270.01	10	10	30	30		20					
35X-2,94	265.47	30	30	5	10							
36X-2,75	275.85	15	15	30	30							
36X-6,63	281.22	15	15	5	5		5	20				
37X-1,50	283.3	10	20	20	20		10					
37X-6,60	290.08	20	20	20	30		10					
38X-1,102	293.42	5	20	20	20		5					
38X-4,33	297.23	20	50	10	20							

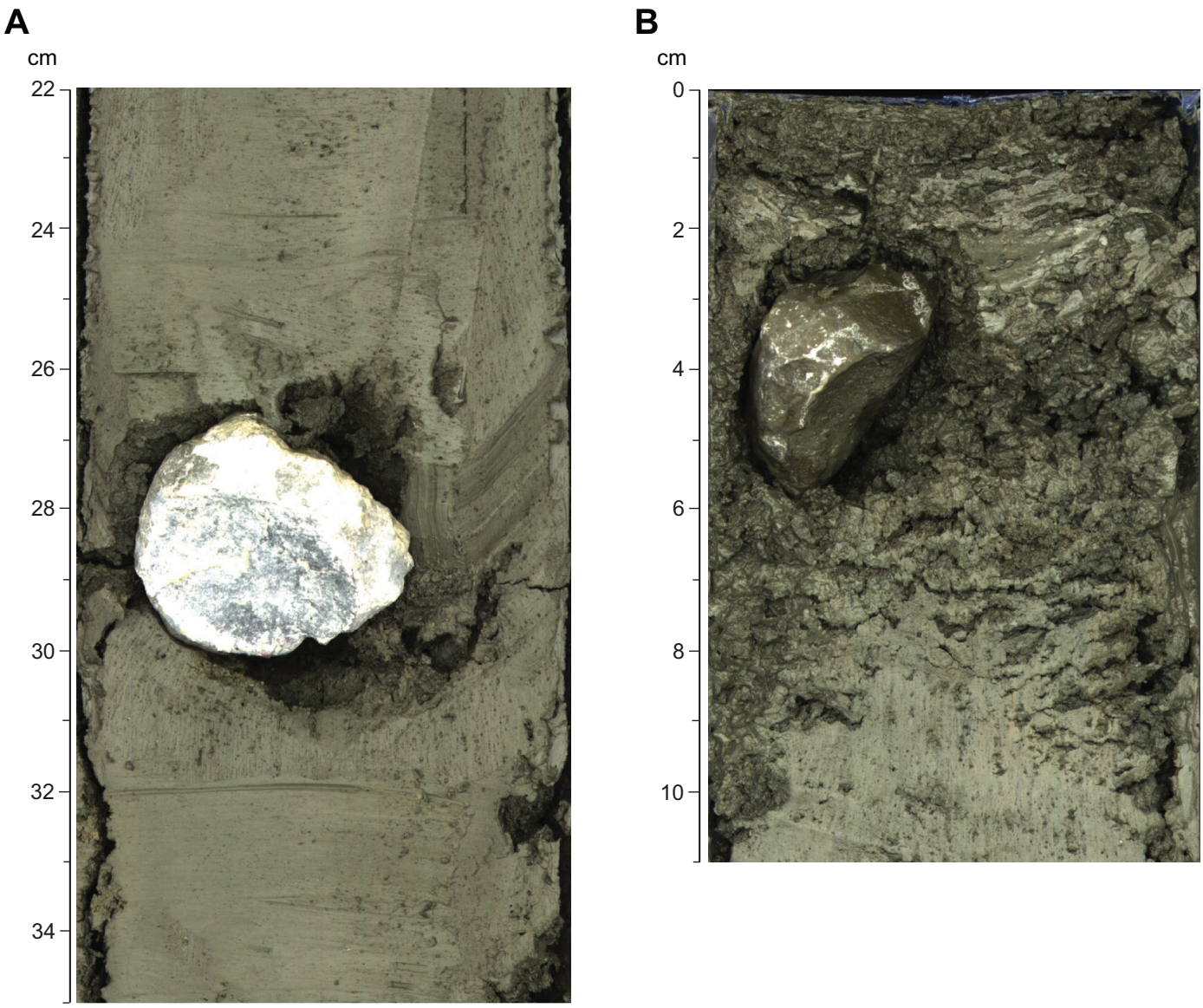


Figure 11. Dolomite concretions in A, Sections NGHP-01-19A-11H-3 and B, NGHP-01-19A-20X-1.

Inorganic Geochemistry

Site NGHP-01-19 is the second of two sites drilled in the Mahanadi Basin to evaluate the gas hydrate distribution and abundance in this region. The main goals of the inorganic geochemistry program in this region were to constrain the biogeochemical and hydrological characteristics of this basin at a site where there is no seismic evidence for faulting and there are no underlying reflectors beneath the GHSZ as observed at Site NGHP-01-18, an adjacent channel-fill site. Thus, it is safe to drill through the seismic BSR. A geochemical comparison between the two sites should provide inferences on the role of structural controls on gas-hydrate distribution and concentration in the Mahanadi Basin and possibly at other passive margins. The absence of apparent significant accumulation of free gas beneath the base of the GHSZ, beneath the local BSR at this site provided the opportunity to drill deeper in the sediment section. The IW chemical data are tabulated in tables 4 and 5, and illustrated in figures 13, 14, and 15.

A total of 57 samples were collected and processed for IW analyses at Site NGHP-01-19, in coordination with both the organic geochemistry and microbiology sampling programs. These included all of the conventional cores plus four pressure cores (Cores NGHP-01-19A-15P, -17E, -26Y, -27E). Pressure cores NGHP-01-19A-15P, -17E, and -27E were recovered under pressure and upon depressurization contained ~1, <3, and ~8 L of gas, respectively, suggesting no gas hydrate in Core NGHP-01-19A-15P, ~0.3 percent gas hydrate in Core NGHP-01-19A-17E, and ~3 percent in Core NGHP-01-19A-27E (see "Pressure Coring"). Core NGHP-01-19A-26Y was not recovered under pressure; it was subsampled because its proximity to the base of the GHSZ might provide another valuable datum point on "background"-disseminated gas hydrate in this critical depth interval. Sampling of the pressure cores for IW analyses was guided by X-ray images of these cores (see "e"). Core NGHP-01-19A-15P suggested homogeneous sediment; therefore, just one subsample was processed for geochemistry. Core NGHP-01-19A-17E, on the other hand, showed slight differences in the sediment texture, and thus two samples were taken to evaluate potential down-core differences in the abundance of gas hydrate. Cores NGHP-01-19A-26Y and NGHP-01-19A-27E were recovered from depth intervals situated close to the base of the GHSZ, therefore, despite their rather homogeneous X-ray images, two samples per core were processed to further constrain the depth distribution of gas hydrate above the GHSZ. It is important to note that the P-and-E-type pressure cores (PCS and HRC respectively), that operate on a similar coring principle, contained up to 1.2 mM drill-water sulfate (~ 4.2 percent seawater value), whereas the Y pressure core (FPC) that operates on a different coring principle, recovered pristine cores that were not contaminated by drilling fluid, as indicated in table 4.

Whole-round lengths for the conventional core samples ranged from 10 to 45 cm, with longer sections sub-sampled from cores recovered deeper within the hole. In the upper 25 mbsf, 12 whole-round samples were collected to constrain the SMI and provide supporting data and samples for studies on the microbial dynamics of the SMI. Three whole round samples were taken in Core NGHP-01-19A-04H, followed by one sample per core to TD (298 mbsf), except for the depth section straddling the base of the GHSZ (Cores NGHP-01-19A-22X to NGHP-01-19A-31X; 170 to 230 mbsf), from which two samples were collected from each core.

All cores were scanned by IR imaging on the catwalk, in an effort to identify gas hydrate presence for sampling of specifically targeted gas-hydrate-bearing intervals. No discrete IR anomalies were observed at this site. However, there is an observable distinct decrease in the background temperature imaged by the IR camera from Core NGHP-01-19A-20X (152 mbsf), and most pronounced at the base of the GHSZ, in Core NGHP-01-19A-28X (~200 mbsf). The overall trend of cooling corresponded with freshening of the IW due to gas-hydrate dissociation, particularly in Cores NGHP-01-19A-24X, -26Y, -27E, and -28X, between ~190 and 202 mbsf, at and just above the base of the GHSZ. In a few cases, however, similar to observations at Site NGHP-01-18, minor variations in the IR intensity within a core (Core NGHP-01-19A-22X, for example) corresponded with a higher quality sediment sample recovered, containing more intact 'biscuits' than the 'warmer' sample.

Interstitial Water Chloride and Salinity

Chloride concentrations were measured by titration with $AgNO_3$ and with the precision of chloride values averaging 0.2 percent, and salinity was determined by refractometry. The chloride concentration and salinity data are presented in table 5 and illustrated in figure 13.

The salinity-depth profile is overall similar to that obtained at Site NGHP-01-18. It shows a steady decrease with depth from 34.8 to a minimum salinity of 30 to 31 at the bottom of the section drilled (fig. 13B). In the uppermost ~30 mbsf, the salinity is influenced by the diagenetic loss of sulfate (and very likely some of the major seawater cations, primarily Ca^{2+} and Mg^{2+}) by biogeochemical reactions that induce authigenic carbonate formation. Deeper in the section, salinity mostly mimics the chlorinity profile. Of particular significance is the presence of distinct excursions in the salinity to lower values in two horizons, at ~125 mbsf and at and(or) close to the depth of the base of the GHSZ, at ~200 mbsf. The most intense salinity minima are observed in the Pressure Core NGHP-01-19A-27E-1 and in Core NGHP-01-19A-28X-2, between 195 and 202 mbsf. Core NGHP-01-19A-28X also had the coldest catwalk temperature recorded by IR imaging (see "IR Imaging" in "Physical Properties"). At a water depth of 1,434 m, with a bottom-water temperature of 4.8 °C and 5.23 °C/100m geothermal gradient, the base of the methane-hydrate stability zone is calculated to be at ~205 mbsf; this depth is close to being coincident with the bottom of Core NGHP-01-19A-28X. The minimum salinity obtained at this

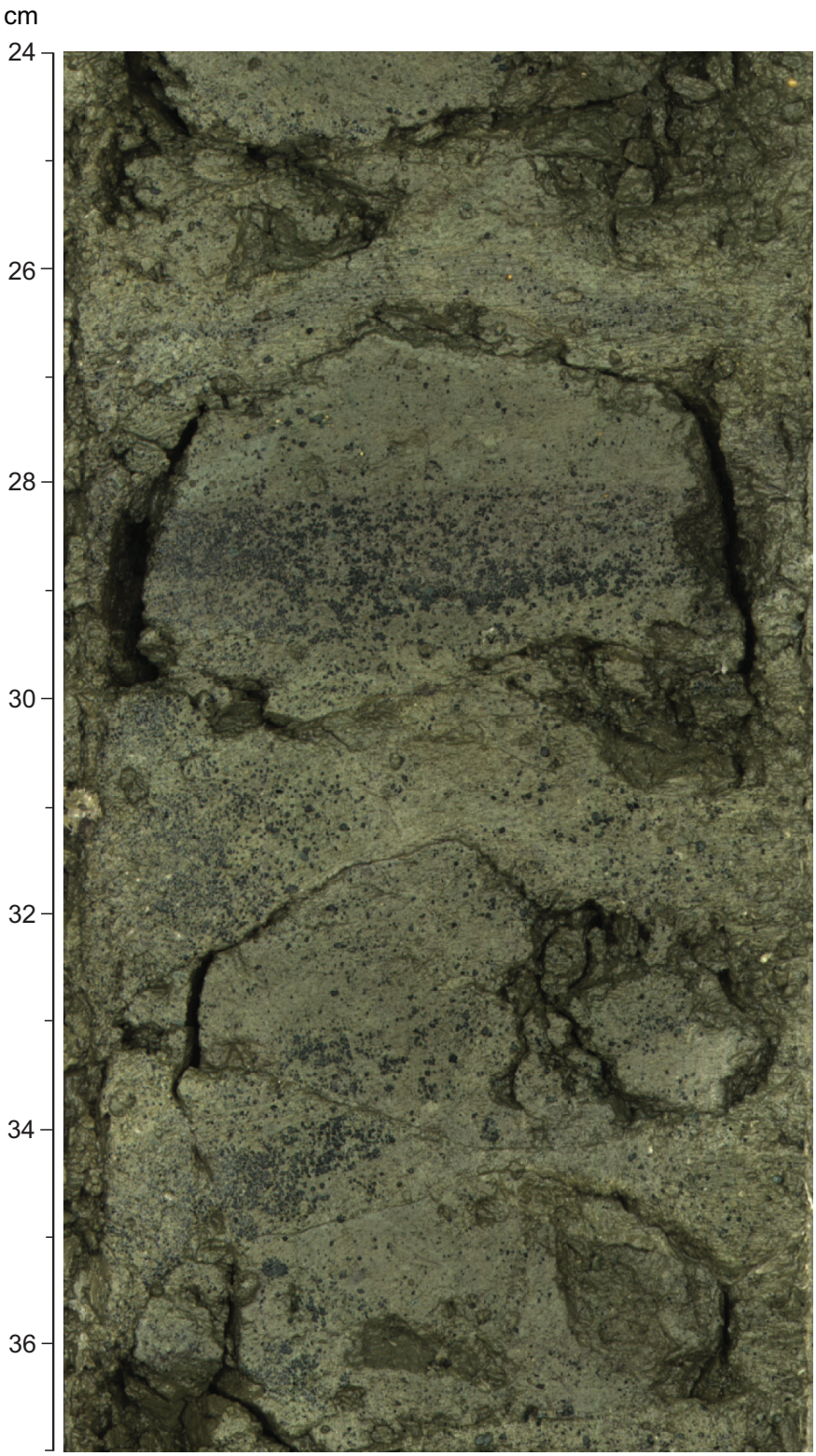


Figure 12. Visible glauconite grains in Section NGHP-01-19A-38X-6.

depth is 28.0 against a background salinity of 31.5 (table 5). The discrete low-salinity values at this depth interval coincide with low chlorinity values (table 5 and fig. 13) and indicate the presence of gas hydrate in these sediments, as discussed below. The minimum salinity values of ~29.3 and 29.8 in the two Pressure Cores NGHP-01-19A-15P and NGHP-01-19A-17Y, at ~125 mbsf, must as well be caused by gas hydrate dissociation. The cause of the increase in gas-hydrate concentration, manifested by the salinity minima at ~125 mbsf depicted in figure 13B is as yet unexplained, because no abrupt lithological variations were observed at this depth. It may represent the depth where the dissolved gas content reached gas-hydrate solubility. It is important to note that the salinity/chlorinity minima at ~125 mbsf are only observed in the two pressure cores, but not in the adjacent XCB cores.

The chloride concentration depth profile (fig. 13A) shows a continuous increase from ~557 to ~563 mM in the upper 60 mbsf that may reflect the relic oceanic salinity increase during the last glacial maximum. From 60 mbsf to TD, Cl^- remains close to constant at ~550 mM. Superimposed are small, distinct excursions to low chloride values at ~125 and 195–200 mbsf, that coincide with the salinity minima, as discussed above. Similar to salinity, the chloride anomalies at ~125 mbsf, corresponding to 94–96 percent seawater chlorinity values (table 5) were detected in the two Pressure Cores NGHP-01-19A-15P and NGHP-01-19A-17E. However, only in one of them (Core NGHP-01-19A-17E), the depressurization experiment indicated gas saturation with respect to gas hydrate stability; 3.5 L of methane were recovered that are equivalent to ~0.6 percent void space occupancy with gas hydrate. In Core NGHP-01-19A-15P, only 1.6 L methane were recovered (see "Pressure Coring"). The more distinctive Cl^- concentration minima occured near the base of the gas hydrate stability zone, at ~200 mbsf. Five IW samples (three from XCB Cores NGHP-01-19A-24X and 28X and two from Pressure Core NGHP-01-19A-27E) that were obtained from this depth interval show significant Cl^- concentration anomalies. The lowest Cl^- values analyzed were 498 and 509 mM, in Cores NGHP-01-19A-27E and NGHP-01-19A-28X, respectively, equal to ~89 and 91 percent seawater Cl^- value. At this depth interval, the IR imaging records indicate that the gas hydrate occurs in a disseminated mode. Upon depressurization of Core NGHP-01-19A-27E, ~8 litres of gas were obtained, suggesting an average gas hydrate void occupancy of ~3 percent (see "Pressure Coring"). The Cl^- concentrations measured in this core were 498 mM at 33–43 cm and 541 mM at 76–88 cm, corresponding to 10 percent and ~1 percent pore space occupancy, assuming 50 percent porosity. The minimum Cl^- concentration of 509 mM in Core NGHP-01-19A-28X-2 at 90–120 cm, at 197.6 mbsf, represents 8 percent pore space occupancy. However, in the same core about 3 m deeper, in Section 4 at 200.5 mbsf, gas hydrate occupancy is just under 0.5 percent, indicating the uneven distribution of gas hydrate even at the base of the GHSZ, as also observed in Pressure Core NGHP-01-19A-27E. Shore-based grain-size analyses may reveal some subtle lithological controls on the depth distribution of gas hydrate. The adjacent unsuccessful Pressure Core NGHP-01-19A-26Y does not have salinity or chlorinity minima. The small minima at ~232 mbsf (Sample 31X-5, 100–130 cm) of 536 mM Cl^- (~96 percent seawater value) and 30.0 salinity (fig. 13 and table 5) may correspond to the depth of a second possible BSR observed in seismic records from the nearby channel-fill sites.

Sulfate and Alkalinity Concentrations: Characterization of the SMI

The primary objectives of the higher resolution sampling in the upper 25 m of the sediment section were to delineate and characterize the SMI for future geochemical modeling of methane fluxes and to provide supporting data and samples for studies on the microbial dynamics of the SMI. At Site NGHP-01-19, the SMI is located at 21 mbsf, as illustrated in figure 14B, coincident with the sulfate gradient observed at Site NGHP-01-18. This suggests that the methane flux at these two sites is very similar. Also, in agreement with the results of Site NGHP-01-18, the methane maximum from 20 to 80 mbsf probably represents the zone of most intense methanogenesis that follows sulfate depletion. Alkalinity shows a broad maximum from 20 to 40 mbsf, where it reaches 24.8 mM (fig. 14A), and reflects the combined effects of organic-matter decomposition and anaerobic-methane oxidation. However, the alkalinity concentration is significantly lower than the predicted production value by bacterial sulfate reduction or anaerobic methane oxidation, suggesting a significant loss of alkalinity by authigenic carbonate formation. At this site alkalinity decreases with depth below ~35 mbsf. This may be due to carbonate precipitation at depth or carbonate dissolution driven by methanogenesis in the region of the alkalinity maximum. However, in contrast with the observations at Site NGHP-01-18, there is no increase in alkalinity values with depth beneath 120 mbsf, suggesting a balance between alkalinity production and utilization by carbonate and methane formation. The Ca^{2+} and Mg^{2+} concentration profiles will be used to calculate total alkalinity loss by authigenic carbonate formation throughout the section.

The sulfate profile will be used to compute the vertical component of the methane flux at this site. Below the SMI, sulfate concentrations remain zero throughout the drilled section; the few slightly higher than 0.10 mM sulfate values, reported in table 4, most likely indicate contamination by drill-water. The most difficult samples to clean from drill-water contamination were the XCB cores, which were highly disturbed due to high swell conditions during drilling. The sulfate concentrations in these samples were used to calculate the amount of drill-water contamination, and the salinity, alkalinity, Cl^-, and Br^- concentrations were corrected for the contamination. The corrected concentration values are listed in table 5.

Table 4. Interstitial-water data for Hole NGHP-01-19A. The samples that were corrected for drill-water contamination are marked by bold data in the sulfate concentration column.

["-", value not determined]

Sample name	Depth (mbsf)	Vol. (mL)	pH	Alk (mM)	Salinity	Titr Cl (mM)	Br (mM)	SO_4 (mM)	Comments
1H-1 140-150	1.4	40.0	7.4	4.77	34.8	556	0.88	25.61	Green silty clay with sand and forams
1H-2 140-150	2.9	40.0	7.3	5.86	34.8	558	0.88	23.88	Green silty clay with sand and forams
1H-3 113-123	4.4	40.0	7.4	7.62	34.8	555	0.88	21.84	Green silty clay with sand and forams
1H-4 48-58	5.0	40.0	7.4	8.21	34.8	557	0.89	21.01	Green silty clay with sand and less forams
2H-1 140-150	6.7	40.0	7.4	10.41	34.5	556	0.88	18.35	Green silty clay with sand. No coarser particles. Some forams. Sulfide mottling
2H-3 140-150	9.7	40.0	7.6	12.72	34.0	557	0.89	15.14	Green silty clay with sand. No coarser particles. Some forams. Sulfide mottling
2H-5 140-150	12.7	40.0	7.6	16.73	33.5	558	0.88	10.18	Green silty clay with sand. No coarser particles. Some forams. Sulfide mottling
2H-7 56-67	14.9	40.0	7.6	18.87	33.0	560	0.88	6.73	Green silty, fine clay
3H-1 140-150	16.2	40.0	7.7	22.21	33.0	558	0.79	1.53	Silty clay with lots of forams
3H-3 140-150	19.2	40.0	7.7	23.56	33.2	558	0.90	0.15	Silty clay with lots of forams
3H-5 140-150	22.2	40.0	7.8	24.56	33.0	563	0.88	0.00	Silty clay with lots of forams and pyritized burrows
3H-7 52-62	24.3	40.0	7.8	24.71	33.0	562	0.87	0.00	Silty clay with lots of forams and pyritized burrows
4H-2 140-150	27.2	40.0	7.8	24.72	33.0	563	0.85	0.07	Silty clay with lots of forams
4H-4 140-150	30.2	37.0	7.8	24.74	32.5	559	0.88	0.10	Very fine, dark grey-green clay with some forams
4H-6 90-100	32.7	40.0	7.6	26.93	32.2	562	0.90	0.00	Very fine, dark grey-green clay with some forams
5H-5 135-150	41.2	40.0	7.6	25.14	32.2	563	0.90	0.00	Very fine, dark grey-green clay with some forams
6H-5 135-150	50.7	40.0	7.7	-	32.0	562	0.92	0.00	Very fine, green-dark grey clay with some forams and large carbonate filled burrows
7H-5 135-150	60.2	37.0	7.7	18.16	32.0	562	0.91	0.00	Fine, dark grey-green clay with forams
8H-5 130-150	72.1	37.0	7.8	15.55	31.2	557	0.88	0.00	Fine, dark grey-green clay with forams
9H-5 130-150	83.0	35.0	7.7	12.56	31.5	556	0.88	0.00	Less clayey and more silty grey-green sediment with forams
10H-4 130-150	91.1	34.0	7.9	13.13	31.0	556	0.88	0.00	Less clayey and more silty grey-green sediment with forams
11H-2 110-130	97.2	39.0	7.9	11.77	30.8	557	0.89	0.47	Highly disturbed with hard rock pieces
12X-6 130-150	105.6	19.0	-	-	31.0	559	0.91	0.08	A few small biscuits. Fine grained green-grey clay-silt
13X-5 120-150	113.9	11.0	-	-	30.8	556	0.89	0.17	In top ~12cm contained large to small rocks (carbonate) pieces, plus light-colored ash, also cemented. The rest was broken-up biscuits. It may be contaminated
14X-3 120-150	121.6	27.0	7.4	14.35	31.0	554	0.90	0.12	A highly disturbed sample with very few small, broken-up biscuits
15P-1 25-35	126.3	10.0	-	-	30.5	544	0.88	0.95	Green clay. This pressure core was pressurized, but contained only ~1 liter of gas upon depressurisation
17E-1 32-47	128.3	10.0	-	-	31.0	551	0.92	1.00	Background sediment in X-ray scan
17E-1 64-74	128.6	10.0	-	-	31.5	552	0.87	0.50	Suggestion of gas hydrate in X-ray scans. No lithologic control apparent. ~0.3% hydrate

Table 4. Interstitial-water data for Hole NGHP-01-19A. The samples that were corrected for drill-water contamination are marked by bold data in the sulfate concentration column.—Continued

["-", value not determined]

Sample name	Depth (mbsf)	Vol. (mL)	pH	Alk (mM)	Salinity	Titr Cl (mM)	Br (mM)	SO_4 (mM)	Comments
18X-3 120-150	133.2	40.0	7.6	15.03	31.0	557	0.91	0.13	Disturbed sample. Few biscuits. (IR: 420-450)
19X-1 96-126	139.6	-	-	-	-	-			Small core. Sample discarded, nothing but drilling mud. (IR: 100–130)
20X-3 120-150	152.5	29.0	7.7	14.55	31.0	553	0.91	0.00	Colder section of the core based on IR scan
21X-1 120-150	159.1	40.0	7.8	15.76	31.0	552	0.93	0.48	No IR anomaly
22X-3 120-150	171.7	40.0	7.7	15.08	32.0	553	0.95	0.05	"Normal" section. Sticky clay. Hard to clean. Highly fractured (IR: 415-445)
22X-5 72-102	174.2	40.0	7.4	15.54	31.0	553	0.90	0.14	Colder section of the core. No lithologic control, but perhaps more fractures. Pictures taken. (IR: 720–750)
23X-3 120-150	181.3	40.0	7.6	14.91	31.5	553	0.94	0.11	"Normal" section
23X-6 101-131	185.3	40.0	7.8	13.36	31.5	556	0.86	0.07	Colder section of the core. Fractured clay
24X-3 120-150	191.0	40.0	7.5	14.20	32.0	538	0.94	0.27	Fractured clay
24X-5 120-150	194.0	40.0	7.6	14.85	31.5	550	0.91	0.55	Fractured clay (IR: 720–750)
26Y-1 34-44	194.6	14.0	-	-	30.5	558	0.95	0.06	This pressure core was not pressurized. Used for possible background Cl^- value
26Y-1 50-65	194.8	16.0	-	-	30.8	561	0.93	0.05	This pressure core was not pressurized. Used for possible background Cl^- value
27E-1 33-43	195.6	25.0	7.8	-	29.5	525	0.90	1.20	This pressure core was pressurized. Depressurisation experiment resulted in 8.0 liters of gas. 2–3% hydrate
27E-1 76-88	196.1	19.0	7.7	-	30.2	548	0.95	0.35	This pressure core was pressurized. Depressurisation experiment resulted in 8.0 liters of gas
28X-2 90-120	197.6	35.0	7.5	14.18	30.0	509	0.91	0.07	Approximately the BSR depth. Colder section of the two samples from this core, as indicated by the stronger IR image. Good, but small biscuits.
28X-4 120-150	200.6	25.0	7.5	14.88	31.5	552	0.92	0.05	Background sample. Fewer biscuits
29X-3 120-150	209.1	29.0	7.2	14.67	31.5	554	0.97	0.06	No difference in IR anomaly in the two 29X samples. Very good biscuits
29X-6 81-111	213.1	36.0	7.4	14.27	31.5	554	0.95	0.08	No difference in IR anomaly in the two 29X samples
30X-2 120-150	217.0	42.0	7.4	14.55	30.8	558	0.95	0.09	Less intense IR image
30X-4 10-40	218.9	33.0	7.5	14.79	31.0	554	0.96	0.13	More intense IR image, but only slightly
31X-2 120-150	227.6	39.0	7.3	14.38	31.0	554	0.95	0.22	No IR anomaly
31X-5 100-130	231.9	32.0	7.2	13.91	30.5	544	0.91	0.39	No IR anomaly
32X-4 120-150	239.8	38.0	7.4	14.17	30.5	553	0.93	0.13	No IR anomaly
33X-4 120-150	249.1	30.0	7.3	13.43	30.8	558	0.96	0.05	This sample was mistakeably cut in half with a wire
34X-6 90-120	261.2	28.5	7.6	11.32	30.2	560	0.96	0.09	No IR anomaly
35X-4 120-150	268.7	40.0	7.3	12.69	31.0	559	0.99	0.15	Organic smell (Petroleum smell)
36X-4 95-140	278.8	41.0	7.3	11.97	30.5	551	0.95	0.31	Organic smell (Petroleum smell)
37X-3 120-150	286.3	28.0	7.2	12.39	30.8	551	0.94	0.25	Organic smell (Petroleum smell)
38X-4 120-150	298.1	32.0	7.1	12.60	30.8	552	0.97	0.05	Organic smell (Petroleum smell)

Table 5. Interstitial-water data corrected for drill-water contamination based on sulfate concentration, for Hole NGHP-01-19A. The samples that were corrected for drill-water contamination are marked by bold data in the sulfate concentration column.

["-", value not determined]

Sample name	Depth (mbsf)	V Samp (mL)	pH	Alk (mM)	Salinity	Titr Cl^- (mM)	Br^- (mM)	Br^-/Cl^-	SO_4^{2-} (mM)
1H-1 140-150	1.4	40.0	7.4	4.77	34.8	556	0.88	0.0016	25.61
1H-2 140-150	2.9	40.0	7.3	5.86	34.8	558	0.88	0.0016	23.88
1H-3 113-123	4.4	40.0	7.4	7.62	34.8	555	0.88	0.0016	21.84
1H-4 48-58	5.0	40.0	7.4	8.21	34.8	557	0.89	0.0016	21.01
2H-1 140-150	6.7	40.0	7.4	10.41	34.5	556	0.88	0.0016	18.35
2H-3 140-150	9.7	40.0	7.6	12.72	34.0	557	0.89	0.0016	15.14
2H-5 140-150	12.7	40.0	7.6	16.73	33.5	558	0.88	0.0016	10.18
2H-7 56-67	14.9	40.0	7.6	18.87	33.0	560	0.88	0.0016	6.73
3H-1 140-150	16.2	40.0	7.7	22.21	33.0	558	0.77	0.0014	1.53
3H-3 140-150	19.2	40.0	7.7	23.56	33.2	558	0.90	0.0016	0.15
3H-5 140-150	22.2	40.0	7.8	24.56	33.0	563	0.88	0.0016	0.00
3H-7 52-62	24.3	40.0	7.8	24.71	33.0	562	0.87	0.0016	0.00
4H-2 140-150	27.2	40.0	7.8	24.72	33.0	563	0.85	0.0015	0.07
4H-4 140-150	30.2	37.0	7.8	24.74	32.5	559	0.88	0.0016	0.10
4H-6 90-100	32.7	40.0	7.6	26.93	32.2	562	0.90	0.0016	0.00
5H-5 135-150	41.2	40.0	7.6	25.14	32.2	563	0.90	0.0016	0.00
6H-5 135-150	50.7	40.0	7.7	-	32.0	562	0.92	0.0016	0.00
7H-5 135-150	60.2	37.0	7.7	18.16	32.0	562	0.91	0.0016	0.00
8H-5 130-150	72.1	37.0	7.8	15.55	31.2	557	0.88	0.0016	0.00
9H-5 130-150	83.0	35.0	7.7	12.56	31.5	556	0.88	0.0016	0.00
10H-4 130-150	91.1	34.0	7.9	13.13	31.0	556	0.88	0.0016	0.00
11H-2 110-130	97.2	39.0	7.9	11.73	30.2	548	0.87	0.0016	0.00
12X-6 130-150	105.6	19.0	-	-	31.0	559	0.91	0.0016	0.08
13X-5 120-150	113.9	11.0	-	-	30.6	553	0.89	0.0016	0.00
14X-3 120-150	121.6	27.0	7.4	14.34	30.9	552	0.90	0.0016	0.00
15P-1 25-35	126.3	10.0	-	-	29.3	526	0.85	0.0016	0.00
17E-1 32-47	128.3	10.0	-	-	29.8	532	0.89	0.0017	0.00
17E-1 64-74	128.6	10.0	-		30.9	542	0.86	0.0016	0.00
18X-3 120-150	133.2	40.0	7.6	15.02	30.8	554	0.91	0.0016	0.00
19X-1 96-126	139.6	-	-	-	-	-	-	-	-
20X-3 120-150	152.5	29.0	7.7	14.55	31.0	553	0.91	0.0017	0.00
21X-1 120-150	159.1	40.0	7.8	15.72	30.4	543	0.92	0.0017	0.00
22X-3 120-150	171.7	40.0	7.7	15.08	32.0	553	0.95	0.0017	0.05
22X-5 72-102	174.2	40.0	7.4	15.53	30.8	550	0.90	0.0016	0.00
23X-3 120-150	181.3	40.0	7.6	14.90	31.4	551	0.94	0.0017	0.00
23X-6 101-131	185.3	40.0	7.8	13.36	31.5	556	0.86	0.0015	0.07
24X-3 120-150	191.0	40.0	7.5	14.18	31.7	533	0.93	0.0017	0.00
24X-5 120-150	194.0	40.0	7.6	14.81	30.8	539	0.89	0.0016	0.00
26Y-1 34-44	194.6	14.0	-	-	30.5	558	0.95	0.0017	0.06
26Y-1 50-65	194.8	16.0	-	-	30.8	561	0.93	0.0017	0.05
27E-1 33-43	195.6	25.0	7.8	-	28.0	502	0.86	0.0017	0.00
27E-1 76-88	196.1	19.0	7.7	-	29.8	541	0.94	0.0017	0.00
28X-2 90-120	197.6	35.0	7.5	14.18	30.0	509	0.91	0.0018	0.07
28X-4 120-150	200.6	25.0	7.5	14.88	31.5	552	0.92	0.0017	0.05
29X-3 120-150	209.1	29.0	7.2	14.67	31.5	554	0.97	0.0017	0.06
29X-6 81-111	213.1	36.0	7.4	14.27	31.5	554	0.95	0.0017	0.08
30X-2 120-150	217.0	42.0	7.4	14.55	30.8	558	0.95	0.0017	0.09
30X-4 10-40	218.9	33.0	7.5	14.78	30.8	551	0.95	0.0017	0.00
31X-2 120-150	227.6	39.0	7.3	14.36	30.7	550	0.95	0.0017	0.00
31X-5 100-130	231.9	32.0	7.2	13.88	30.0	537	0.89	0.0017	0.00
32X-4 120-150	239.8	38.0	7.4	14.16	30.3	551	0.92	0.0017	0.00
33X-4 120-150	249.1	30.0	7.3	13.43	30.8	558	0.96	0.0017	0.05
34X-6 90-120	261.2	28.5	7.6	11.32	30.2	560	0.96	0.0017	0.09
35X-4 120-150	268.7	40.0	7.3	12.68	30.8	556	0.99	0.0018	0.00
36X-4 95-140	278.8	41.0	7.3	11.95	30.1	545	0.94	0.0017	0.00
37X-3 120-150	286.3	28.0	7.2	12.37	30.5	546	0.94	0.0017	0.00
38X-4 120-150	298.1	32.0	7.1	12.60	30.8	552	0.97	0.0018	0.05

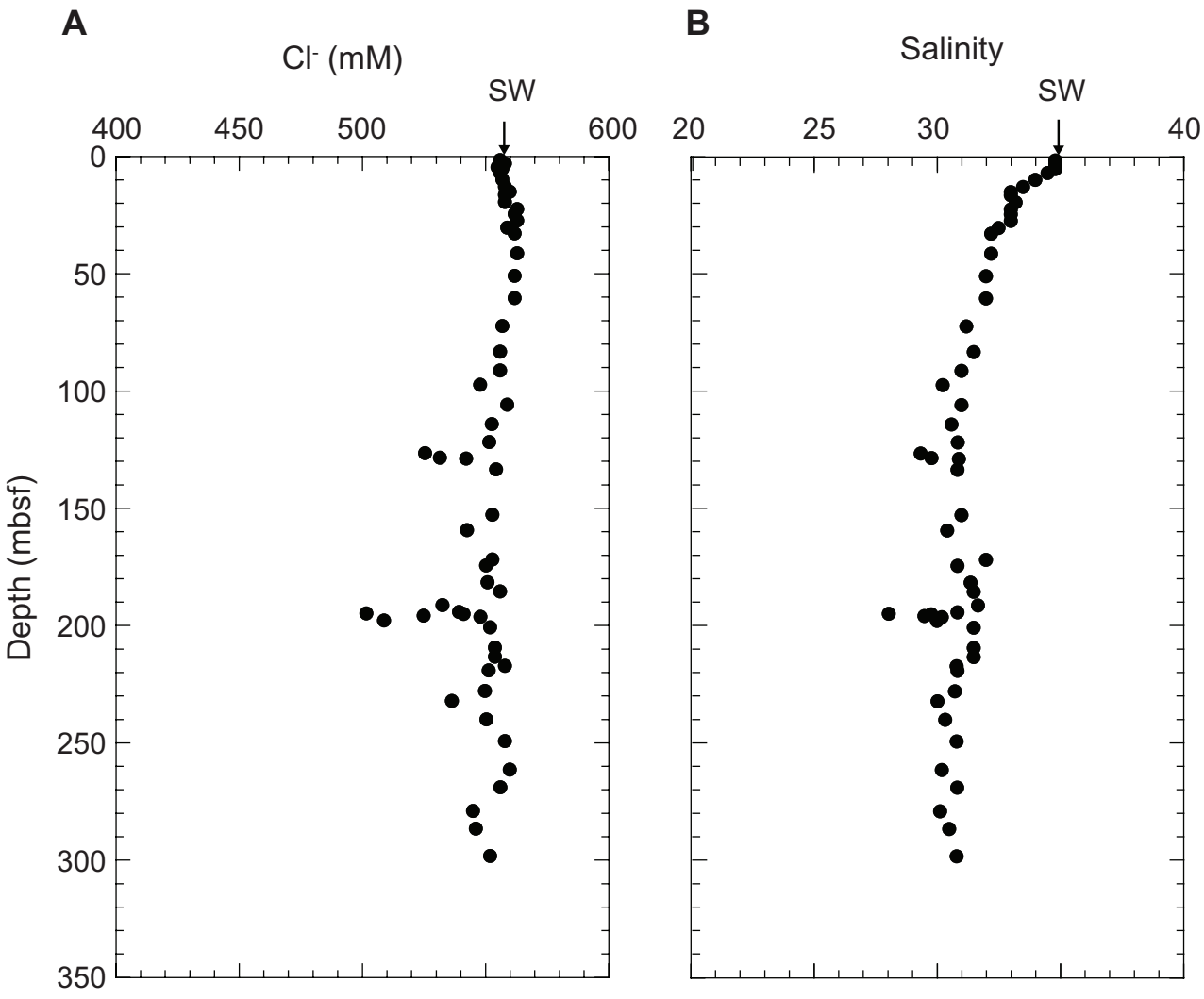


Figure 13. Concentration-depth profiles of A, chloride and B, salinity at NGHP-01-19A. Seawater value is designated as "sw" in A and B.

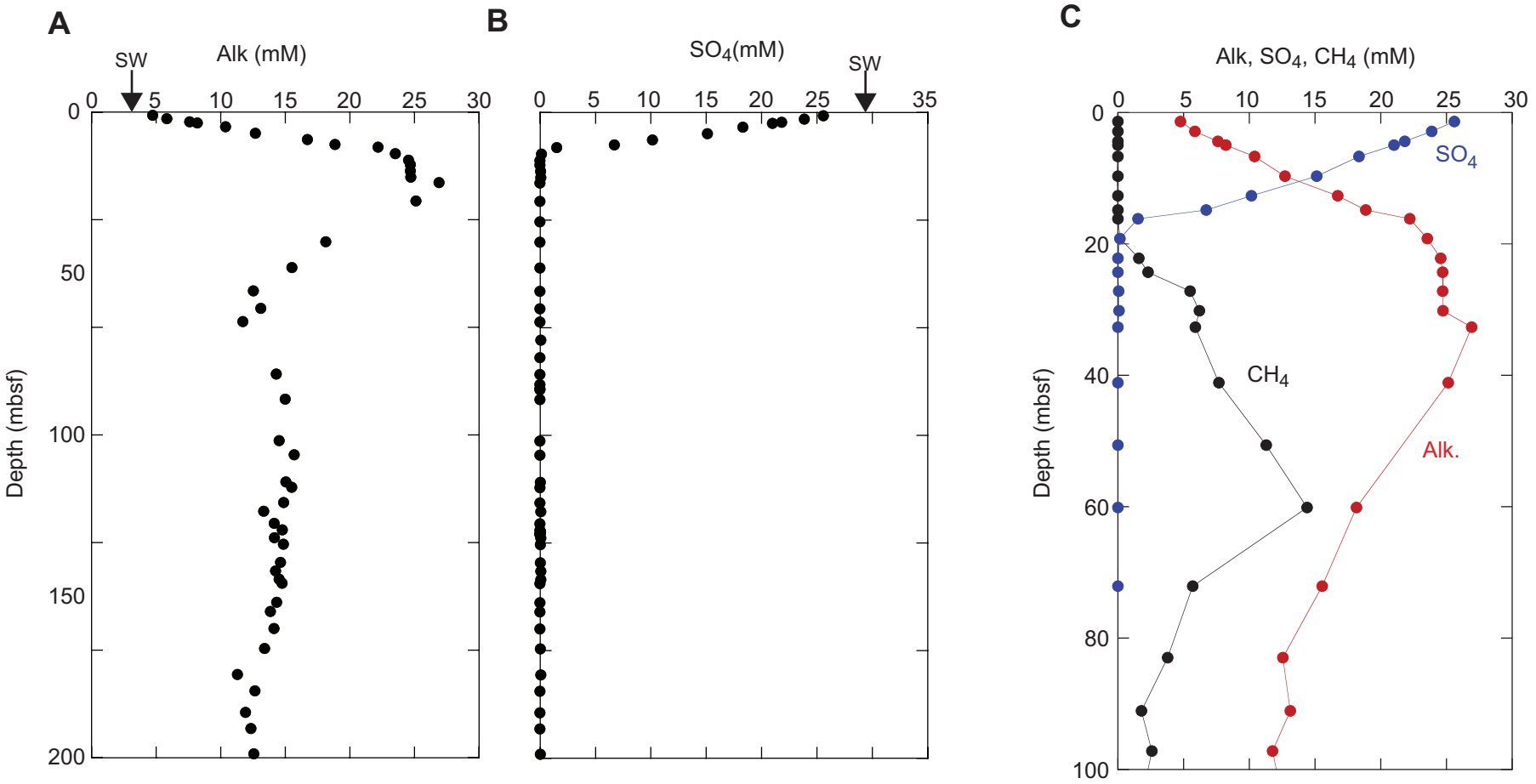


Figure 14. Concentration-depth profiles of A, alkalinity; B, sulfate; and C, sulfate, methane, and alkalinity at Hole NGHP-01-19A. Note the alkalinity maximum at the SMI depth (21 mbsf) and the steep increase in methane concentration below the SMI. Seawater value is designated as "sw" in *A* and *B*. [SMI, sulfate-methane interface]

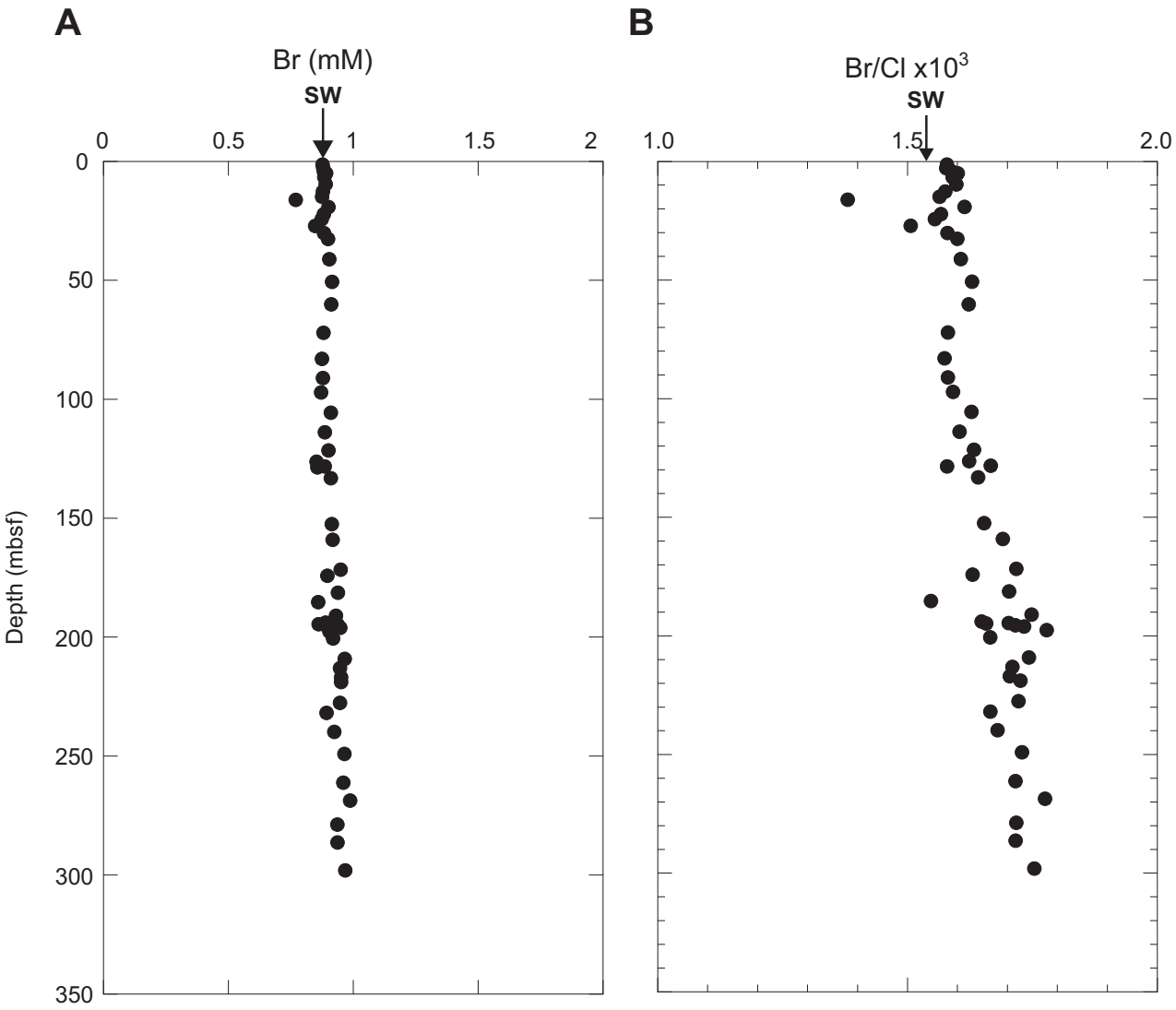


Figure 15. Concentration-depth profile of dissolved bromide at Hole NGHP-01-19A. Seawater value is designated as “sw.”

Bromide Concentrations

At Site NGHP-01-19A, both the dissolved Br^- concentration and Br^-/Cl^- ratio depth profiles show a small, steady increase, as shown in figure 15, suggesting that the majority of the organic carbon fueling sulfate reduction and methanogenesis at this site is of terrestrial origin. This is consistent with sediment input to this basin via the Mahanadi River system.

Organic Geochemistry

The shipboard organic geochemistry program at Site NGHP-01-19 included analysis of the composition of volatile hydrocarbons including methane, ethane, and propane (C_1–C_3) and fixed natural gases (that is, O_2, CO_2, and N_2+Ar) from headspace, void gas, and PCS degassing experiments. In general, these analyses indicate that methane is the predominant hydrocarbon gas found in the cores at Site NGHP-01-19. However, ethane was present at low levels (<100 ppmv) in headspace below 21.8 mbsf and in moderate concentrations in void gas samples collected below 54 mbsf. Propane was also detected at low levels (<120 ppmv) in void gas samples. The headspace samples above the SMI were dominated by air and slightly depleted in carbon dioxide. Methane was enriched below the SMI and above the seismically-inferred BSR extrapolated from Site NGHP-01-18.

Headspace gas analyses were performed on 57 samples from NGHP-01-19A ranging in depth from 1.35 to 297.7 mbsf. The concentrations given here represent minimum proxy measurements of the actual concentrations due to limitations of the gas headspace method (Kvenvolden and Lorenson, 2000). The sediment pore water contained methane at concentrations ranging from non-detectable near the surface to 14.4 mM at ~50 mbsf (table 6). Theoretical methane saturation in pore water under site-specific physical conditions, calculated using the Duan and others (1992) and Xu (2002, 2004) methodologies, increases from 51.8 mM at the seafloor to 146 mM at 230 mbsf, then decreases to 139.1 mM near the borehole completion depth of 300 mbsf. Ethane (C_2) ranged from non-detectable just below the SMI to a maximum of 100 ppmv (0.02 mM) at 190.6 mbsf (table 6). No C_{3+} hydrocarbon gases were detected in headspace samples, which may suggest a microbial source of methane; however, post expedition isotopic analyses will further constrain the source of gas.

Methane concentrations increase step-wise from non-detectable at 16.2 mbsf to 1.6 mM at ~21.8 mbsf, concomitant with a depletion in pore water sulfate (fig. 16; see "Inorganic Geochemistry") consistent with the depth of the SMI. Methane concentrations peak below both the SMI and 50 mbsf where the alkalinity concentrations are at 14.4 mM. Methane concentration is relatively uniform (~2-3 mM) from ~75 mbsf to the BSR, with one peak at ~175 mbsf, and may be associated with the presence of gas hydrate. Other proxy measurements (that is, IR anomalies and downhole logging) point to the presence of gas hydrate in this interval (see "IR Imaging" in "Physical Properties"). Methane concentration decreases slightly and varies to a greater extent near the BSR inferred from Site NGHP-01-18. The methane concentrations were generally an order of magnitude below theoretical *in-situ* saturation throughout the length of the borehole (fig. 6); however, this may be due to preferential losses of methane during sampling and coring.

Carbon dioxide (CO_2) concentrations ranged from 0.2 to 9 mM in pore water contained within the sediment (table 6). Concentrations of CO_2 show a general increase with depth, though this trend is not consistent (fig. 17). Concentrations of CO_2 increase at ~0.01 mM per meter (mM/m) to the SMI and then at a higher rate below the SMI (~0.1 mM/m). Below 120 mbsf, concentrations were highly variable, ranging in concentration from ~0.4 to 7.5 mM. Some portion of the variability observed for samples obtained at depths greater than 120 mbsf is likely due to XCB coring agitation and can be seen by the data scatter below 120 mbsf in figure 17. The methane to CO_2 ratio indicated that methane may be preferentially concentrated from just below the SMI to ~75 mbsf and again below ~120 mbsf to the BSR (fig. 18). The air gases (N_2+Ar), and O_2 were the balance gases, however the (N_2+Ar)/O_2 ratios were typically greater than air, possibly reflecting the ratio within porewaters or indicating that some air was trapped in the headspace samples and some oxygen was likely dissolved preferentially compared to N_2. Air gases were present in all samples as the core plugs were degassed in an air headspace.

Void gas samples were collected from 26 different void spaces ranging in depth from 54 to 298.5 mbsf. Methane concentrations within voids averaged nearly 906,300 (±180,700) parts per million by volume (ppmv) (or 90.6 percent ± 18.1 percent). The void gases contained methane above 87 percent at all intervals except two, located near 70 mbsf and 240–250 mbsf (table 7). These low concentrations are believed to be due to contamination during sampling and(or) core handling because the ratio of (N_2+Ar)/O_2 corresponds to the atmospheric value (~3.73). Ethane was detected at levels ranging from ~90 to 1,490 ppmv. Propane was also detected at low levels with a maximum concentration of 190 ppmv (average of 70 ppmv ± 40 ppmv); however, higher molecular weight gases (C_{4+}) were not detected (table 7).

Carbon dioxide concentrations in void gas ranged from ~2,820 to 24,200 ppmv and are tabulated with other gas data in table 7. The methane to CO_2 ratios were fairly uniform at ~100 with increasing depth between the SMI and the BSR, indicating that any existing gas hydrate may have consistently concentrated the C_1 relative to CO_2 with depth (fig. 18). This appears consistent with the headspace C_1/CO_2 trend, but deviations are likely due to preferential loss of methane in headspace sampling and(or) XCB coring agitation. Void gas C_1/CO_2 is regularly two orders of magnitude greater than

headspace due to the preferential loss of volatile methane by the headspace sample method. Ratio values for C_1 to C_2 gases averaged ~1,050 and showed the typical decreasing trend with depth (fig. 19). The concentrations are focused along the border of the 'anomalous' and 'normal' division as depicted in the graph. These high-methane concentrations versus moderate concentrations of ethane and propane (table 7) suggest a mixed microbial-thermogenic hydrocarbon gas source with a predominance of microbially sourced methane. Shore-based isotope analysis of methane and ethane gases will assist in the determination of sources. The air gases (N_2+Ar), and O_2 composed the balance gases.

Gas was collected from three PCS cores in Hole NGHP-01-19A. The gas concentration results showed trends similar to the void gas results (tables 7 and 8). However, CO_2 concentrations were ~1 order of magnitude lower. The decrease in concentration may be attributed to the sampling method, whereby pressure cores are degassed through water-filled chambers prior to analysis. PCS core gas analysis also confirmed the presence of C_2 and C_3 in Hole NGHP-01-19A, with concentrations ranging from 610 to 1,690 and trace to 130 ppmv, respectively. Ratio values for C_1 to C_2 gases ranged from ~830 to ~13,000. Ethane levels increase through ~80 mbsf (temperature of ~9 °C), and then appear to level-off through the BSR depth (fig. 19). The lower C_1/C_2 ratios suggest microbial and possibly minor thermogenic hydrocarbon gas sources are present. Heavier (C_{4+}) hydrocarbons were not detected, thus the gas is likely to be dominated by microbial methanogenesis; however, post-cruise isotopic evaluations of hydrocarbon gases will assist in source discrimination. The increased concentration of ethane in the gas hydrate bearing zone could be due to ethane enrichment by gas hydrate formation; however, ethane and propane concentrations increase with depth which suggests that thermogenic gas diffusing up from below is the likely cause of the increased ethane concentrations (see also "Physical Properties" and "Inorganic Geochemistry"). The C_1/C_2 ratios are "anomalous" with depth (fig. 19), which also suggest that a thermogenic hydrocarbon source is present.

Microbiology

Hole NGHP-01-19A

Analysis of all microbiological samples will be shore-based. Eleven samples were collected for cell enumeration (CEL), thirty-one for hydrogenase activity analysis (SPH), six samples for detailed microbiological studies (MAF, MAG, MAR) and nine samples for background section (MBF, MBG, MBR) (table 9). Additional microbiological samples were taken, Lab code JUD (thirty-one samples) and Lab code JAN (thirty-one samples).

Physical Properties

Whole-round cores at NGHP Expedition 01, Site 19 were imaged using an IR camera on the catwalk to determine the location of temperature anomalies on the surface of core liners and to enable sections containing potential gas hydrate to be quickly removed, preserved, and studied. After IR imaging was finished, non-destructive measurements were conducted on temperature-equilibrated whole-round core sections with the MSCL. Thermal conductivity measurements were also conducted on whole-round cores. Various tests were performed on split cores including: electrical resistivity by use of a Wenner array, *P*-wave velocity by inserted spades, and shear strength by mini-vane and Pocket Penetrometer. Core subsamples were placed in 10-mL beakers and dried at 105 °C for at least 24 hr to determine water content. Subsequently, the dried samples were analyzed for grain density using gas pycnometers and other sediment parameters were then calculated. See the "Physical Properties" section of the "Methods" chapter for more details.

The physical properties program at Site NGHP-01-19 focused primarily on Hole NGHP-01-19A located within the Mahanadi Basin off the east coast of India in ~1,422 m of water. Hole NGHP-01-19A, the second core hole drilled in this basin during this project, was continuously cored to 305 mbsf and had an overall core recovery of 91.6 percent. Two LWD holes were also drilled at this site. IR images indicated that gas hydrate may have been present in disseminated form from ~170 mbsf to the base of gas hydrate stability at ~205 mbsf.

Infrared Imaging

Environmental Conditions

The catwalk environment was monitored during the entire drilling operation at Site NGHP-01-19 (Hole NGHP-01-19A). Temperature on the catwalk averaged ~28 °C, ranging from 25 to 30.5 °C during the drilling operation, with significant relatively rapid temperature changes (fig. 20). Relative humidity ranged from 75 to 96 percent (fig. 20), which is consistent with a marine environmental setting of the northwestern Bay of Bengal, but again varied notably during the last third of the drilling activities. Other than transients in temperature and relative humidity, adverse environmental conditions were not present during drilling operations at this site. Occasional rainstorms occurred typically associated with rapid thermal changes.

Near-surface seawater temperature was measured at this site using a temperature logger deployed over the port side mid-ship. Seawater temperature was relatively constant at 28 to 29 °C.

Table 6. Headspace gas composition for Site NGHP-01-19.

Sample	Site	Hole	Core	Section	Interval (cm)	Sed wt. (g)	Sample depth (mbsf)	CO_2	C_1	C_2
									(ppmv)	
19A-1H1-135-140	19	A	1	1	135–140	8.2	1.35	1,500	nd	nd
19A-1H2-135-140	19	A	1	2	135–140	7.9	2.85	2,100	nd	nd
19A-1H3-95-100	19	A	1	3	95–100	7.5	3.95	2,700	nd	nd
19A-1H4-43-48	19	A	1	4	43–48	9.5	4.93	2,600	nd	nd
19A-2H1-135-140	19	A	2	1	135–140	8.0	6.65	2,800	nd	nd
19A-2H3-125-130	19	A	2	3	125–130	8.3	9.55	4,900	nd	nd
19A-2H5-95-100	19	A	2	5	95–100	7.7	12.25	6,600	nd	nd
19A-2H7-52-57	19	A	2	7	52–57	8.9	14.82	2,300	nd	nd
19A-3H1-135-140	19	A	3	1	135–140	9.4	16.15	11,600	nd	nd
19A-3H3-95-100	19	A	3	3	125–130	9.4	19.05	10,500	1,600	nd
19A-3H5-95-100	19	A	3	5	95–100	8.5	21.75	10,900	9,200	10
19A-3H7-47-52	19	A	3	7	47–52	10.0	24.27	11,100	16,400	10
19A-4H2-125-130	19	A	4	2	125–130	8.2	27.05	15,500	29,200	20
19A-4H4-95-100	19	A	4	4	95–100	8.5	29.75	13,100	34,600	30
19A-4H6-85-90	19	A	4	6	85–90	9.3	32.65	14,800	36,800	30
19A-5H4-145-150	19	A	5	4	145–150	8.9	39.75	13,700	43,900	50
19A-5H5-90-95	19	A	5	5	90–95	9.2	40.70	13,600	67,500	70
19A-6H5-90-95	19	A	6	5	90–95	8.6	50.20	15,300	76,700	70
19A-7H5-90-96	19	A	7	5	90–95	9.7	59.70	20,300	35,400	40
19A-8H5-85-90	19	A	8	5	85–90	11.6	71.65	35,300	29,800	40
19A-9H5-85-90	19	A	9	5	85–90	11.8	82.55	28,200	14,700	30
19A-10H4-80-85	19	A	10	4	80–85	9.3	90.65	29,200	14,500	40
19A-11H2-65-70	19	A	11	2	65–70	7.3	96.76	32,500	6,700	20
19A-12X6-85-90	19	A	12	6	85–90	9.0	105.17	39,200	9,400	30
19A-13X5-75-80	19	A	13	5	75–80	7.2	113.40	29,800	10,300	20
19A-14X3-75-80	19	A	14	3	75–80	8.8	121.15	28,200	24,800	40
19A-15P-20-25	19	A	15	P	20–25	9.9	126.20	8,600	8,500	20
19A-17E-27-32	19	A	17	E	27–32	8.3	128.27	4,500	2,100	10
19A-17E-59-64	19	A	17	E	59–64	8.6	128.59	7,000	3,500	20
19A-18X3-75-80	19	A	18	3	75–80	11.2	132.75	16,300	18,600	40
19A-19X1-91-96	19	A	19	1	91–96	9.3	139.51	27,900	15,200	30
19A-20X3-75-80	19	A	20	3	75–80	9.7	152.05	19,900	16,200	30
19A-21X1-75-80	19	A	21	1	75–80	10.1	158.65	9,500	18,000	60
19A-22X3-75-80	19	A	22	3	75–80	6.7	171.25	11,100	9,000	20
19A-22X5-67-72	19	A	22	5	67–72	7.9	174.17	8,700	26,400	90
19A-22X6-100-105	19	A	22	6	100–105	7.9	175.52	8,600	16,500	30
19A-23X3-75-80	19	A	23	3	75–80	9.6	180.85	17,200	14,900	50
19A-23X6-96-101	19	A	23	6	96–101	9.8	185.27	14,200	14,800	40
19A-24X3-75-80	19	A	23.5	3	75–80	8.9	190.55	23,000	14,500	100
19A-24X5-115-120	19	A	23.9	5	115–120	8.0	193.95	15,900	14,500	40
19A-26Y-45-50	19	A	26	Y	45–50	7.2	194.75	8,400	5,400	20
19A-27E-28-33	19	A	27	E	28–33	10.8	195.58	8,600	9,500	20
19A-28X2-85-90	19	A	28	2	85–90	10.0	197.58	3,100	5,600	10
19A-28X4-75-80	19	A	28	4	75–80	11.7	200.18	6,500	8,900	nd
19A-29X3-105-110	19	A	29	3	105–110	12.0	208.97	7,000	7,600	nd
19A-29X6-36-41	19	A	29	6	36–41	8.0	212.62	34,100	14,000	30
19A-30X2-105-110	19	A	30	2	105–110	10.5	216.80	55,300	19,500	60
19A-30X4-5-10	19	A	30	4	5–10	8.4	218.80	38,900	12,800	30
19A-31X2-105-110	19	A	31	2	105–110	13.1	227.46	34,000	15,000	50
19A-31X5-55-60	19	A	31	5	55–60	8.9	231.46	3,800	5,000	nd
19A-32X4-75-80	19	A	32	4	75–80	9.7	239.39	58,500	15,900	70
19A-33X4-75-80	19	A	33	4	75–80	9.9	248.62	30,500	12,100	20
19A-34X6-45-50	19	A	34	6	45–50	9.2	260.76	16,400	9,700	20
19A-35X4-75-80	19	A	35	4	75–80	6.7	268.28	20,400	15,200	30
19A-36X4-50-55	19	A	36	4	50–55	11.2	278.05	18,500	17,800	60
19A-37X3-75-80	19	A	37	3	75–80	10.6	285.83	2,800	7,600	nd
19A-38X4-75-80	19	A	38	4	75–80	10.6	297.65	13,900	12,700	40

Table 6. Headspace gas composition for Site NGHP-01-19.—Continued

Sample	C_3	O_2	N_2+Ar	H_2S	C_1 (mL/L WS)	C_1 (mM PW)	CO_2 (mL/L WS)	CO_2 (mM PW)	C_1/CO_2
		(ppmv)							
19A-1H1-135-140	nd	193,100	754,500	nd	nd	nd	4,200	0.2	-
19A-1H2-135-140	nd	193,100	754,400	nd	nd	nd	6,200	0.3	-
19A-1H3-95-100	nd	190,200	752,100	nd	nd	nd	8,600	0.5	-
19A-1H4-43-48	nd	197,500	770,500	nd	nd	nd	6,100	0.3	-
19A-2H1-135-140	nd	193,100	747,900	nd	nd	nd	8,300	0.5	-
19A-2H3-125-130	nd	195,600	763,700	nd	nd	nd	13,600	0.8	-
19A-2H5-95-100	nd	190,500	748,600	nd	nd	nd	20,400	1.2	-
19A-2H7-52-57	nd	195,400	751,400	nd	nd	nd	5,900	0.4	-
19A-3H1-135-140	nd	189,400	743,700	nd	nd	nd	27,200	1.7	-
19A-3H3-95-100	nd	190,100	749,400	nd	3,600	0.2	24,700	1.6	0.2
19A-3H5-95-100	nd	187,700	746,400	nd	24,800	1.6	29,500	1.9	0.8
19A-3H7-47-52	nd	188,400	743,800	nd	35,200	2.3	23,800	1.6	1.5
19A-4H2-125-130	nd	183,100	734,400	nd	82,900	5.5	44,000	2.9	1.9
19A-4H4-95-100	nd	181,700	734,100	nd	93,600	6.2	35,400	2.4	2.6
19A-4H6-85-90	nd	172,500	724,100	nd	87,800	5.9	35,300	2.4	2.5
19A-5H4-145-150	nd	179,400	727,700	nd	111,600	7.7	34,800	2.4	3.2
19A-5H5-90-95	nd	169,700	714,400	nd	163,600	11.3	32,900	2.3	5.0
19A-6H5-90-95	nd	159,900	713,300	nd	204,100	14.4	40,600	2.9	5.0
19A-7H5-90-96	nd	164,300	741,000	nd	79,600	5.7	45,500	3.3	1.7
19A-8H5-85-90	nd	161,900	723,000	nd	51,200	3.8	60,600	4.5	0.8
19A-9H5-85-90	nd	170,000	731,800	nd	24,500	1.8	47,100	3.6	0.5
19A-10H4-80-85	nd	165,700	735,900	nd	34,500	2.6	69,700	5.2	0.5
19A-11H2-65-70	nd	165,800	747,400	nd	22,200	1.7	107,800	8.1	0.2
19A-12X6-85-90	nd	151,000	761,200	nd	23,400	1.6	98,000	6.8	0.2
19A-13X5-75-80	nd	173,400	754,600	nd	34,700	2.0	100,500	5.8	0.3
19A-14X3-75-80	nd	157,400	743,000	nd	63,900	3.7	72,700	4.2	0.9
19A-15P-20-25	nd	153,600	782,600	nd	18,500	1.2	18,800	1.2	1.0
19A-17E-27-32	nd	161,600	775,600	nd	5,900	0.4	12,600	0.8	0.5
19A-17E-59-64	nd	151,600	760,500	nd	9,300	0.6	18,700	1.1	0.5
19A-18X3-75-80	nd	162,700	757,500	nd	33,700	2.1	29,500	1.8	1.1
19A-19X1-91-96	nd	159,700	737,900	nd	36,300	2.2	66,600	4.1	0.5
19A-20X3-75-80	nd	163,300	745,900	nd	36,400	2.2	44,700	2.7	0.8
19A-21X1-75-80	nd	143,800	772,700	nd	38,100	2.5	20,100	1.3	1.9
19A-22X3-75-80	nd	179,400	733,400	nd	33,400	2.8	41,200	3.4	0.8
19A-22X5-67-72	nd	168,500	743,900	nd	78,800	5.8	26,000	1.9	3.0
19A-22X6-100-105	nd	165,400	748,200	nd	49,300	3.5	25,600	1.8	1.9
19A-23X3-75-80	nd	134,900	790,700	nd	34,000	2.5	39,300	2.9	0.9
19A-23X6-96-101	nd	123,400	807,300	nd	32,800	2.7	31,500	2.5	1.0
19A-24X3-75-80	nd	100,300	815,200	nd	36,800	2.7	58,400	4.3	0.6
19A-24X5-115-120	nd	115,900	819,800	nd	42,500	3.1	46,600	3.4	0.9
19A-26Y-45-50	nd	164,200	794,400	nd	18,300	1.4	28,500	2.2	0.6
19A-27E-28-33	nd	129,500	786,800	nd	18,200	1.4	16,500	1.3	1.1
19A-28X2-85-90	nd	178,800	753,300	nd	12,000	0.8	6,600	0.5	1.8
19A-28X4-75-80	nd	158,200	756,600	nd	15,000	1.2	10,900	0.9	1.4
19A-29X3-105-110	nd	154,300	760,300	nd	12,400	1.0	11,300	0.9	1.1
19A-29X6-36-41	nd	136,300	779,400	nd	41,000	2.8	100,100	6.8	0.4
19A-30X2-105-110	nd	71,900	828,700	nd	38,900	2.6	110,700	7.5	0.4
19A-30X4-5-10	nd	120,600	806,500	nd	35,100	2.3	107,000	7.1	0.3
19A-31X2-105-110	nd	87,000	830,200	nd	21,000	1.5	47,700	3.5	0.4
19A-31X5-55-60	nd	159,100	762,500	nd	12,600	0.9	9,500	0.6	1.3
19A-32X4-75-80	nd	42,800	849,700	nd	35,800	2.4	131,500	9.0	0.3
19A-33X4-75-80	nd	72,100	830,700	nd	26,400	2.0	66,600	5.1	0.4
19A-34X6-45-50	nd	171,300	744,400	nd	23,500	1.7	39,800	2.8	0.6
19A-35X4-75-80	nd	165,400	751,100	nd	56,200	2.6	75,400	3.5	0.7
19A-36X4-50-55	nd	161,700	742,600	nd	32,200	2.3	33,500	2.4	1.0
19A-37X3-75-80	nd	176,500	739,200	nd	14,900	1.1	5,600	0.4	2.7
19A-38X4-75-80	nd	155,500	764,300	nd	25,000	2.0	27,500	2.1	0.9

Notes: nd = not detected. WS = Wet sediment. PW = porewater. Approximate detection limits are about 15 ppmv for methane, 30 ppmv for ethane, 50 ppmv for propane, and 20 ppmv for hydrogen sulfide.

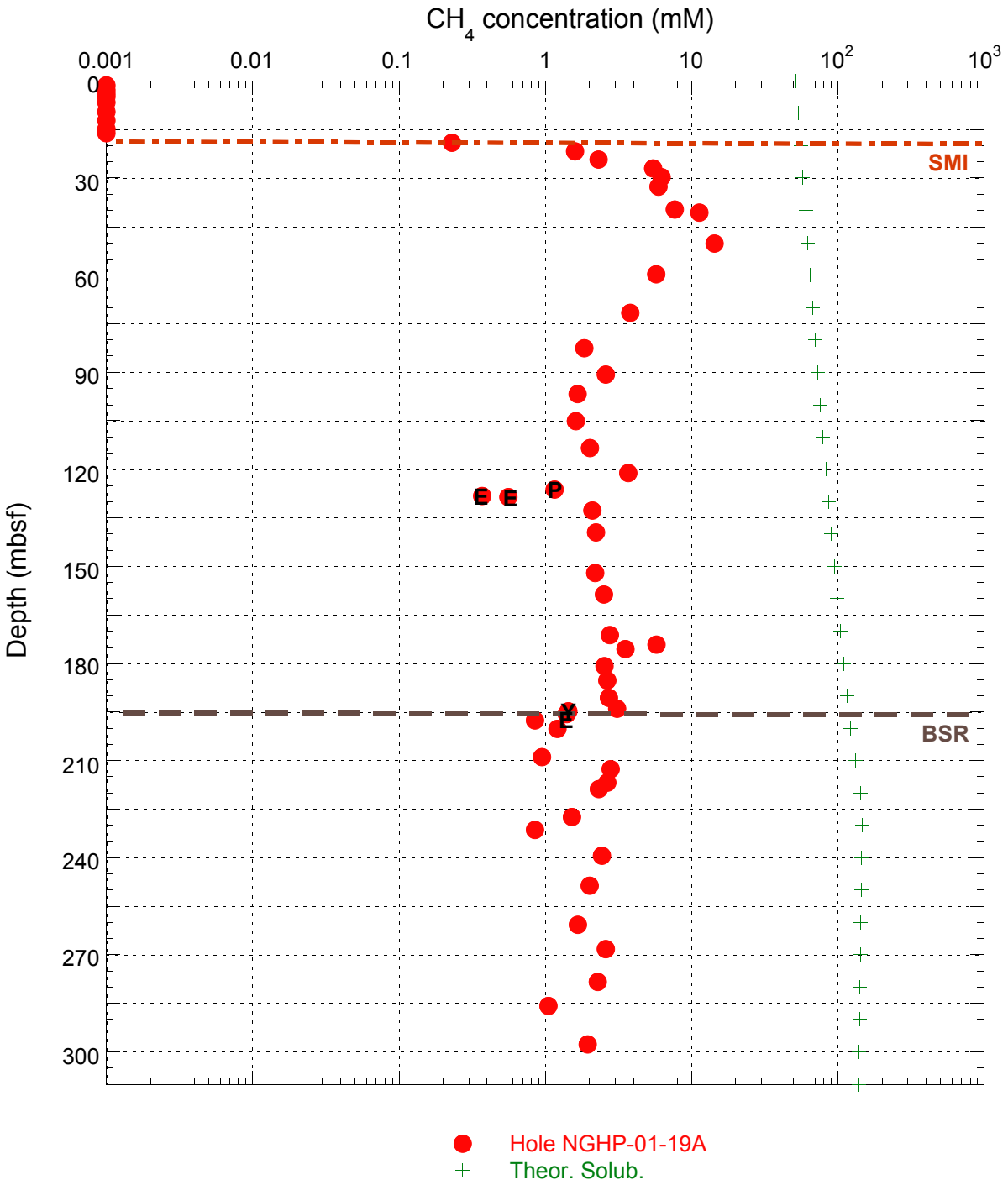


Figure 16. Plot of headspace methane gas concentration (mM) with depth for Hole NGHP-01-19A. Note the methane gradient just below 19 mbsf, indicating that the SMI occurs in this interval. Values less than 0.003 mM are below instrument detection limits, but plotted for reference. Text inside a symbol denotes special coring tool (E, HRC; P, PCS; Y, FPC). Theoretical solubility of methane calculated using the Duan and others (1992) and Xu (2002, 2004) methodologies. [SMI, sulfate-methane interface]

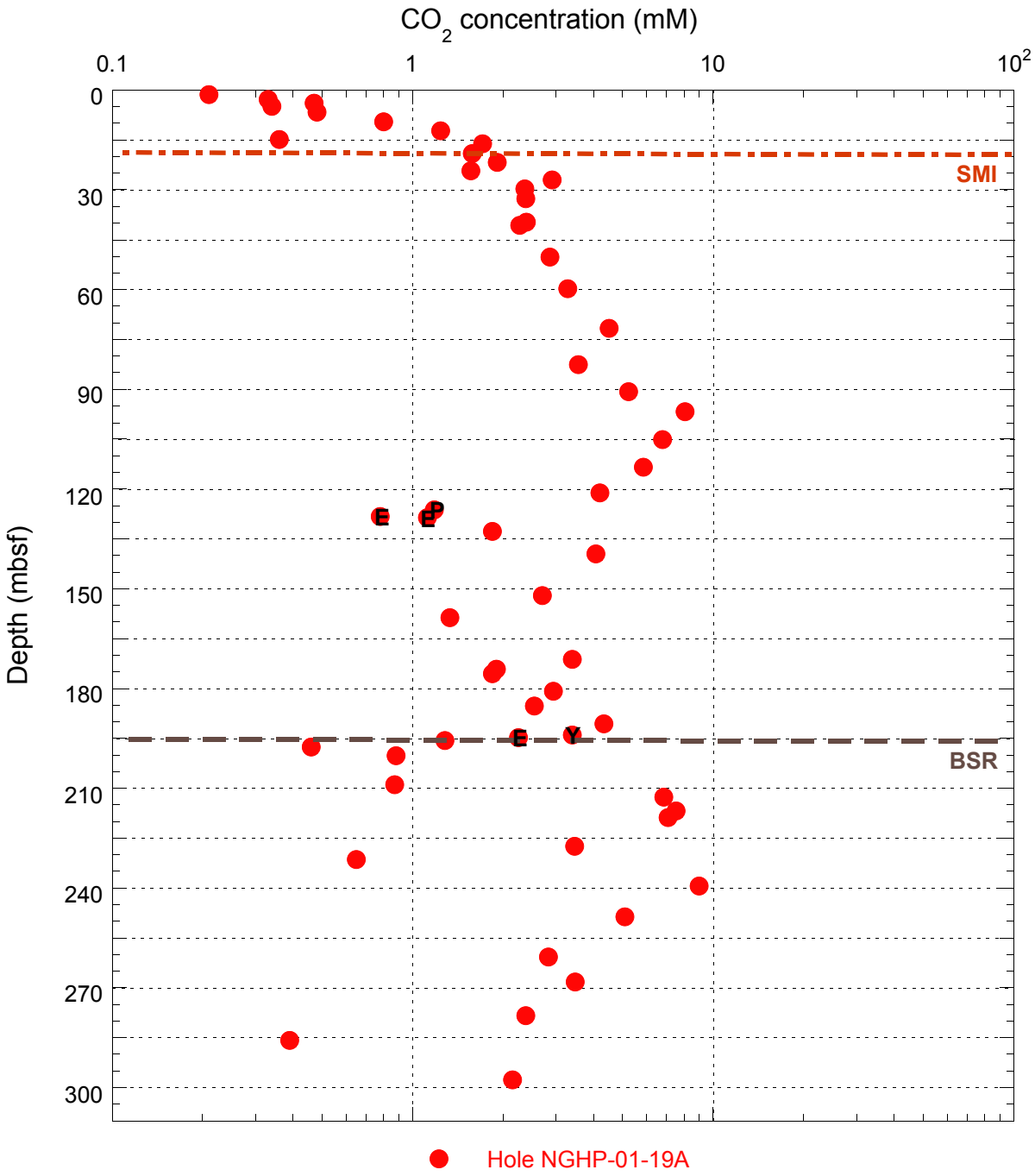


Figure 17. Plot of headspace carbon dioxide gas concentration (mM) with depth for Hole NGHP-01-19A. Text inside a symbol denotes special coring tool (E, HRC; P, PCS; Y, FPC).

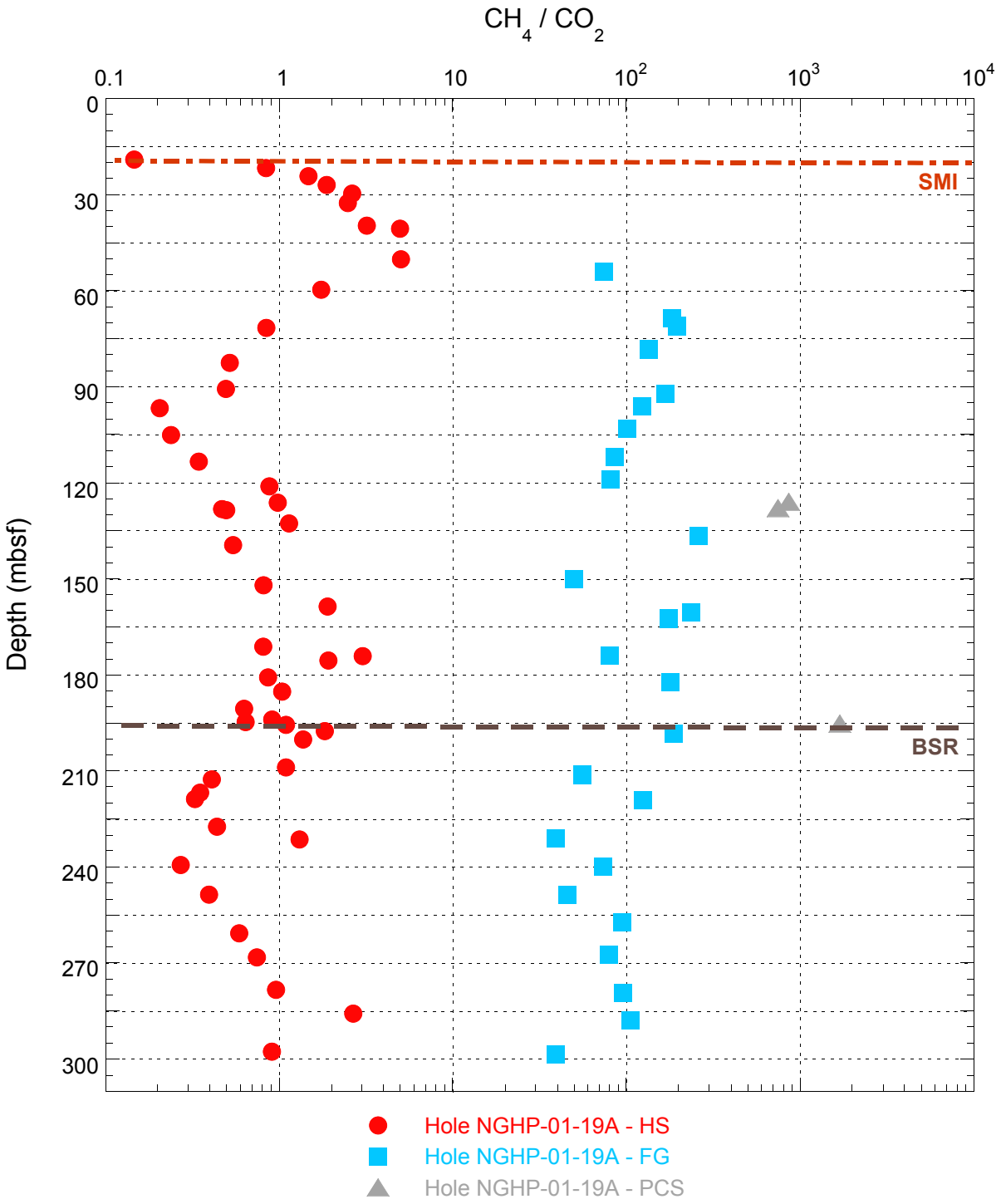


Figure 18. Plot of methane to carbon dioxide gas ratio with depth for headspace, free/void gas, and PCS gas for Hole NGHP-01-19A. Note the minor peaks in methane concentration, perhaps indicating the presence of free gas or gas hydrate. Preferential losses of methane during core handling and by sample procedures results in the order of magnitude difference in ratio magnitude. [PCS, pressure core sampler]

Table 7. Void gas composition for Site NGHP-01-19.

Section	Interval (cm)	Sample depth (mbsf)	CO_2	C_1	C_2	C_3	O_2	N_2+Ar	H_2S	C_1/CO_2	C_1/C_2
			(ppmv) normalized to nitrogen+argon								
1	24	54.04	13,000	961,700	720	nd	2,500	22,100	nd	70	1,300
3	77	68.57	5,300	964,500	730	60	3,200	26,300	nd	180	1,300
5	24	71.04	2,800	550,600	490	20	96,700	349,300	nd	200	1,100
2	98	78.28	7,200	973,900	770	50	2,100	16,000	nd	140	1,300
5	96	92.26	5,200	878,400	760	70	24,500	91,000	nd	170	1,200
1	123	96.03	8,000	977,000	810	80	1,800	12,300	nd	120	1,200
5	20	103.14	9,700	978,900	900	100	1,400	9,000	nd	100	1,100
4	91	112.06	11,300	962,800	870	60	6,200	18,800	nd	90	1,100
2	3	118.93	12,100	976,300	830	80	1,800	8,900	nd	80	1,200
6	1	136.49	3,800	986,400	740	20	1,000	8,100	nd	260	1,300
2	40	150.2	19,400	969,100	1,160	90	2,200	8,100	nd	50	800
2	116	160.56	4,200	987,100	830	50	1,000	6,900	nd	240	1,200
4	1	162.4	5,500	968,000	840	30	6,600	19,100	nd	180	1,200
5	43	173.93	12,200	978,700	1,410	70	1,500	6,100	nd	80	700
4	57	182.17	5,500	986,600	830	40	1,000	6,000	nd	180	1,200
3	53	198.46	5,200	972,200	790	50	5,700	16,100	nd	190	1,200
5	25	211.17	17,300	962,600	710	70	5,000	14,400	nd	60	1,400
5	8	219.23	7,800	975,500	770	90	3,600	12,300	nd	130	1,300
5	6	230.97	23,800	933,200	1,070	70	11,600	30,300	nd	40	900
4	119	239.83	2,900	211,800	90	10	158,600	626,600	nd	70	2,400
4	87	248.74	12,500	570,900	760	140	92,700	323,100	nd	50	800
3	113	257.2	10,300	978,500	980	90	1,700	8,400	nd	100	1,000
3	126	267.29	12,300	976,500	1,080	50	1,900	8,100	nd	80	900
5	17	279.12	10,000	958,900	1,030	120	8,000	22,000	nd	100	900
5	1	287.99	9,300	979,000	1,140	90	1,800	8,700	nd	110	900
5	7	298.47	24,200	945,900	1,490	190	7,900	20,300	nd	40	600

Infrared Images

All APC and XCB cores from Site NGHP-01-19, Hole A were systematically scanned upon arrival on the catwalk using the track-mounted IR camera described in the "Physical Properties" section of the "Methods" chapter. IR anomalies, commonly referred to as "cold spots," indicate gas hydrate dissociation during core recovery, which subsequently provides guidance to catwalk sampling. Summary digital maps of the scans of all cores are available on the data DVD that accompanies this report and listings of the image files are presented in tables 10 and 11. Temperature arrays in text-formatted files were exported from the IR camera software and then concatenated for each core. The arrays were then further concatenated for all cores available in a given borehole. Downcore temperatures were averaged for each pixel row in the array, excluding pixels ~1 cm from the edge of the image and 2 cm along the midline of the image. Exclusion of these pixels minimized the effects caused by major thermal artifacts in the images. This processing enabled us to measure the average amplitude of the cold anomalies and identify warm anomalies due to voids from the background temperature field.

IR track imaging at Site NGHP-01-19A consisted of 32 scans for a total scanned core length of ~270 m. The complete set of IR images collected for Hole NGHP-01-19A is presented in figure 21 along with the corresponding downcore temperatures. The core liner surface temperature extracted from the IR images for Hole NGHP-01-19A ranged from a high of ~27 °C on void sections of the core liner throughout the hole to a low of ~17 to ~18 °C near the top of the borehole and near the BSR (~205 mbsf). High-temperature spikes at the end of cores were as high as 30 °C. Core liners near the top of the borehole were cooler due to relatively cold seafloor sediments, in this case decreasing to ~60 mbsf. The first IR anomaly attributable to gas hydrate occurred in Core NGHP-01-19A-20X (~151 mbsf). Below ~170 mbsf, cores gradually decreased in temperature to Core NGHP-01-19A-28X (~208 mbsf). Remarkably, the IR anomalies involve entire cores or large parts of cores instead of single narrow zones of cooler temperatures common at other sites. This mode of occurrence, combined with the overall small ΔT (1 to ~4 °C), suggests that gas hydrate is disseminated in these fine-grained sediments. The correlation of the observed IR anomalies near the BSR is also marked by a decrease in chlorinity (see "Inorganic Geochemistry") and by a single pressure core (NGHP-01-19A-27E) which is estimated to contain 2.4 percent of pore space occupied by methane hydrate (see "Pressure Coring"). Samples from the bottom of Core NGHP-01-19A-28X do not show a decrease in chlorinity but are relatively cold, perhaps as a result of free gas entering the hole and cooling the cores. A rapid ambient temperature drop occurred during the time Cores NGHP-01-19A-24X and NGHP-01-19A-28X were scanned (fig. 20), which required additional analysis to ensure that the observed core liner temperature shift near the BSR is real, not an artifact of the temperature drop. The ambient temperature change is expected to decrease the observed liner temperature shown in figure 21 for Core NGHP-01-19A-24X by only 0.2 °C and by about half of that amount for Core NGHP-01-19A-28X, causing no effect on the cooling trend near the BSR.

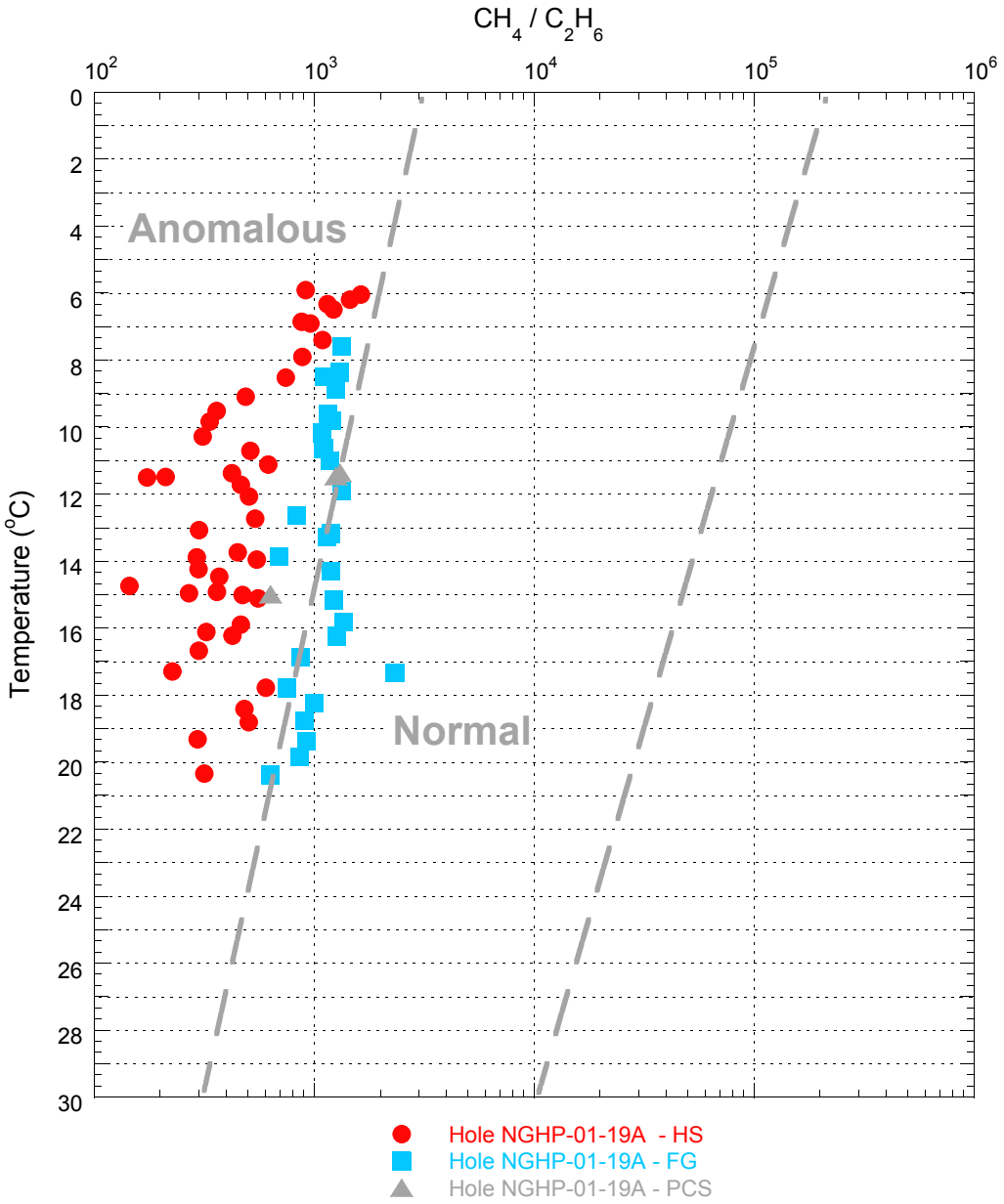


Figure 19. Plot of free/void gas and PCS methane to ethane gas ratio with depth for Hole NGHP-01-19A. Ethane levels were slightly above detection limits for all headspace samples (table 6). Note that the hydrocarbon gas occurrences trend toward the typical range with depth. [PCS, pressure core sampler]

Table 8. Pressure Core Sampler gas composition for Site NGHP-01-19.

Sample	Site	Hole	Core	Section	Sample depth (mbsf)	Time	Gas vol. (ml)	CO_2	C_1	C_2	C_3	O_2	N_2+Ar	H_2S	C_1/CO_2	C_1/C_2
								(ppmv) normalized to nitrogen+argon								
19A-15P-t1	19	A	15	P	126	1	-	700	961,000	720	10	5,400	32,200	nd	1,400	1,300
19A-15P-t2	19	A	15	P	126	2	-	2,500	963,200	740	50	3,600	29,800	nd	400	1,300
19A-17E-t1	19	A	17	E	128	1	-	1,100	938,000	700	130	12,600	47,600	nd	900	1,300
19A-17E-t2	19	A	17	E	128	2	-	1,100	721,400	610	20	38,100	238,700	nd	700	1,200
19A-27E-t1	19	A	27	E	195.3	1	-	300	980,200	1,630	60	4,200	13,700	nd	3,300	600
19A-27E-t2	19	A	27	E	195.3	2	-	800	984,700	1,370	40	2,800	10,300	nd	1,200	700
19A-27E-t3	19	A	27	E	195.3	3	-	3,000	980,800	1,690	20	3,600	10,900	nd	300	600

Notes: nd = not detected. Approximate detection limits are about 15 ppmv for methane, 30 ppmv for ethane, 50 ppmv for propane, and 20 ppmv for hydrogen sulfide.

Table 9. List of microbiological samples taken for Site NGHP-01-19.—Continued

Sample reference						Comments
Core, section	Sample code	Top (cm)	Bottom (cm)	Depth (mbsf)	Volume (cc)	
NGHP-01-19A						
1H-3	CEL	95	100	3.95	5	
2H-5	CEL	95	100	12.25	5	
3H-5	CEL	95	100	21.75	5	
4H-4	CEL	95	100	29.75	5	
5H-5	CEL	90	95	40.7	5	
6H-5	CEL	90	95	50.2	5	
7H-5	CEL	90	95	59.7	5	
8H-5	CEL	85	90	71.65	5	
9H-5	CEL	85	90	82.55	5	
10H-4	CEL	85	90	90.65	5	
11H-2	CEL	65	70	96.76	5	
1H-3	JAN	105	110	4.05	187	
2H-5	JAN	105	110	12.35	187	
3H-5	JAN	105	110	21.85	187	
4H-4	JAN	105	110	29.85	187	
5H-5	JAN	100	105	40.8	187	
6H-5	JAN	100	105	50.3	187	
7H-5	JAN	100	105	59.8	187	
8H-5	JAN	95	100	71.75	187	
9H-5	JAN	95	100	82.65	187	
10H-4	JAN	95	100	90.75	187	
11H-2	JAN	75	80	96.86	187	
12X-6	JAN	95	100	105.27	187	
13X-5	JAN	85	90	113.5	187	
14X-3	JAN	85	90	121.25	187	
18X-3	JAN	85	90	132.85	187	
20X-3	JAN	85	90	152.15	187	
21X-1	JAN	85	90	158.75	187	
22X-3	JAN	85	90	171.35	187	
23X-3	JAN	85	90	180.95	187	
24X-3	JAN	85	90	190.65	187	
28X-4	JAN	85	90	200.28	187	
29X-6	JAN	46	51	212.72	187	
30X-3	JAN	115	120	218.4	187	
31X-5	JAN	65	70	231.56	187	
32X-4	JAN	85	90	239.49	187	
33X-4	JAN	85	90	248.72	187	
34X-6	JAN	55	60	260.86	187	
35X-4	JAN	85	90	268.38	187	
36X-4	JAN	60	65	278.15	187	
37X-3	JAN	85	90	285.93	187	
38X-4	JAN	85	90	297.75	187	
1H-3	JUD	120	130	4.2	374	
2H-5	JUD	120	130	12.5	374	
3H-5	JUD	120	130	22	374	
4H-4	JUD	120	130	30	374	
5H-5	JUD	115	125	40.95	374	
6H-5	JUD	115	125	50.45	374	
7H-5	JUD	115	125	59.95	374	
8H-5	JUD	110	120	71.9	374	
9H-5	JUD	110	120	82.8	374	
10H-4	JUD	110	120	90.9	374	
11H-2	JUD	90	100	97.01	374	
12X-6	JUD	110	120	105.42	374	
13X-5	JUD	100	110	113.65	374	
14X-3	JUD	100	110	121.4	374	
18X-3	JUD	100	110	133	374	
20X-3	JUD	100	110	152.3	374	
21X-1	JUD	100	110	158.9	374	

Table 9. List of microbiological samples taken for Site NGHP-01-19.—Continued

Sample reference						Comments
Core, section	Sample code	Top (cm)	Bottom (cm)	Depth (mbsf)	Volume (cc)	
NGHP-01-19A—Continued						
22X-3	JUD	100	110	171.5	374	
23X-3	JUD	100	110	181.1	374	
24X-3	JUD	100	110	190.8	374	
28X-4	JUD	100	110	200.43	374	
29X-6	JUD	61	71	212.87	374	
30X-3	JUD	130	140	218.55	374	
31X-5	JUD	80	90	231.71	374	
32X-4	JUD	100	110	239.64	374	
33X-4	JUD	100	110	248.87	374	
34X-6	JUD	70	80	261.01	374	
35X-4	JUD	100	110	268.53	374	
36X-4	JUD	75	85	278.3	374	
37X-3	JUD	100	110	286.08	374	
38X-4	JUD	100	110	297.9	374	
22X-6	MAF	115	125	175.67	374	
28X-6	MAF	79	84	202.72	187	MBIO ANOM FREEZER
22X-6	MAG	125	135	175.77	374	
28X-6	MAG	84	89	202.77	187	MBIO ANOM GRAINSIZE
22X-6	MAR	105	115	175.57	374	
28X-6	MAR	74	79	202.67	187	MBIO ANOM REEFER
22X-2	MBF	125	130	170.25	187	
22X-2	MBF	140	145	170.4	187	
29X-2	MBF	120	125	207.62	187	MBIO BKG-FREEZER
22X-2	MBG	130	135	170.3	187	
22X-2	MBG	145	150	170.45	187	
29X-2	MBG	125	130	207.67	187	MBIO BKG-GRAINSIZE
22X-2	MBR	120	125	170.2	187	
22X-2	MBR	135	140	170.35	187	
29X-2	MBR	115	120	207.57	187	MBIO BKG-REEFER
1H-3	SPH	100	105	4	187	
2H-5	SPH	100	105	12.3	187	
3H-5	SPH	100	105	21.8	187	
4H-4	SPH	100	105	29.8	187	
5H-5	SPH	95	100	40.75	187	
6H-5	SPH	95	100	50.25	187	
7H-5	SPH	95	100	59.75	187	
8H-5	SPH	90	95	71.7	187	
9H-5	SPH	90	95	82.6	187	
10H-4	SPH	90	95	90.7	187	
11H-2	SPH	70	75	96.81	187	
12X-6	SPH	90	95	105.22	187	
13X-5	SPH	80	85	113.45	187	
14X-3	SPH	80	85	121.2	187	
18X-3	SPH	80	85	132.8	187	
20X-3	SPH	80	85	152.1	187	
21X-1	SPH	80	85	158.7	187	
22X-3	SPH	80	85	171.3	187	
23X-3	SPH	80	85	180.9	187	
24X-3	SPH	80	85	190.6	187	
28X-4	SPH	80	85	200.23	187	
29X-6	SPH	41	46	212.67	187	
30X-3	SPH	110	115	218.35	187	
31X-5	SPH	60	65	231.51	187	
32X-4	SPH	80	85	239.44	187	
33X-4	SPH	80	85	248.67	187	
34X-6	SPH	50	55	260.81	187	
35X-4	SPH	80	85	268.33	187	
36X-4	SPH	55	60	278.1	187	
37X-3	SPH	80	85	285.88	187	
38X-4	SPH	80	85	297.7	187	

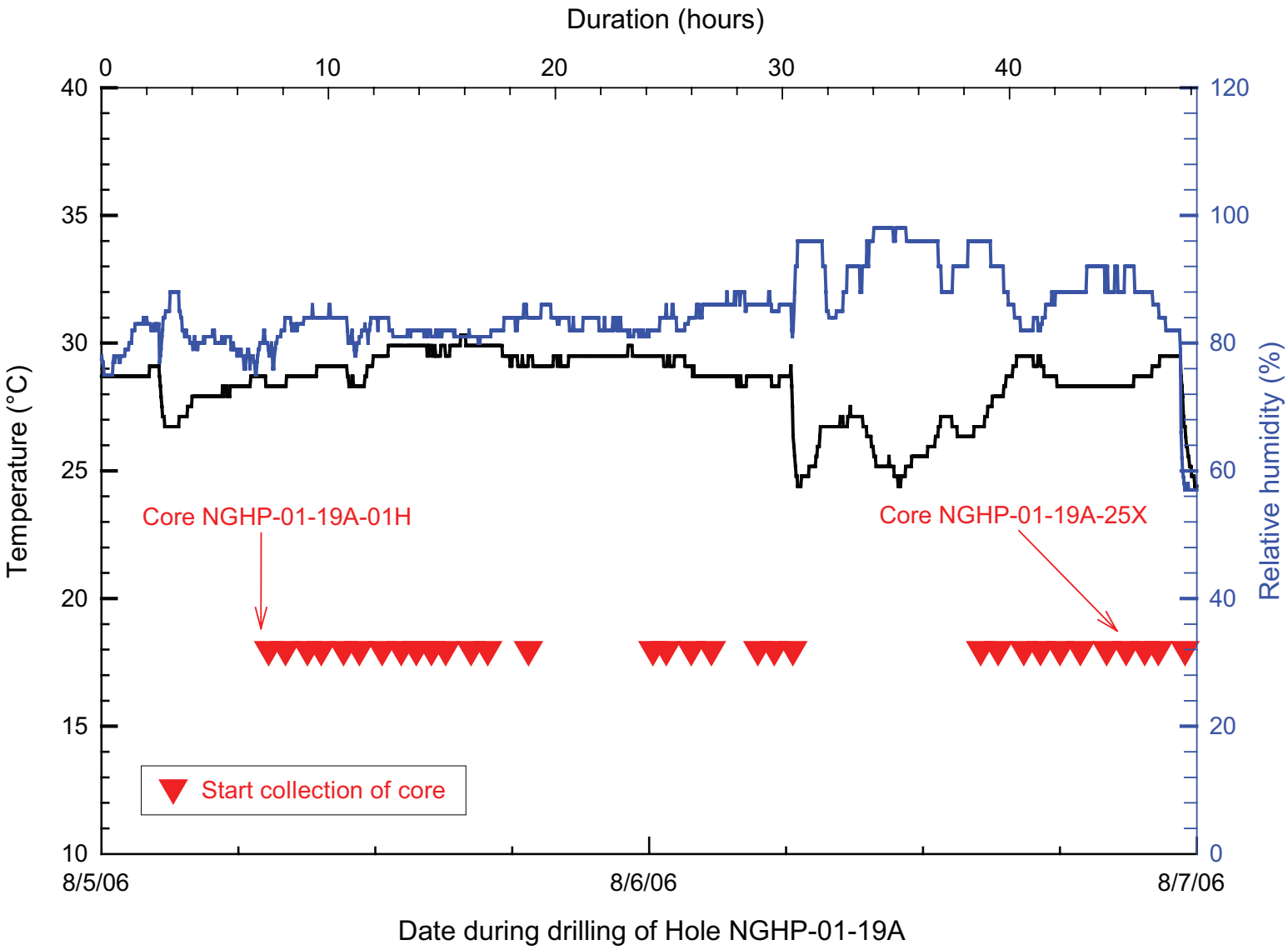


Figure 20. Catwalk temperature and humidity measurements as a function of time during drilling operations at Site NGHP-01-19.

Table 10. List of infrared images collected from Hole NGHP-01-19A.

Core	Imaging length (cm)	First run	Date	Start time	Temperature (start/end) (°C)	Comments
1H	510	x	8/5	7:20	28.7/28.7	Wind from stern, significant odor of exhaust gas.
2H	970	x	8/5	8:04	28.3/28.3	
3H	970	x	8/5	9:02	28.7/28.7	
4H	930	x	8/5	9:38	28.7/28.7	
5H	970	x	8/5	10:37	29.1/29.1	
6H	970	x	8/5	11:18	28.7/28.7	
7H	970	x	8/5	12:18	29.1/29.1	End extruded. Possible that down-core cooling is caused by cool lab stack air hitting core, but is also seen in core ends (see below).
8H	970	x	8/5	13:08	29.5/29.9	Act. 980 cm of core liner. T rising, warm core, lab stack door shut. False anaomaly at top of core caused by cracked liner, exposed sediment.
9H	930	x	8/5	13:48	29.9/29.9	Door open. No effect on core liner T. Second warm core in a row.
10H	910	x	8/5	14:28	29.9/29.9	Core hard to pull from barrel.
11H	360	x	8/5	15:05	29.5/29.5	Short core, water at top
12X	950	x	8/5	16:12	29.9/29.9	
13X	950	x	8/5	16:56	29.9/29.9	
14X	630	x	8/5	18:43	29.5/29.1	
15P						Pressure core, no IR
16Y						Pressure core, no IR
17E						Pressure core, no IR
18X	950	x	8/6	0:45	29.5/29.5	
19X	150	x	8/6	1:51	29.5/29.5	
20X	540	x	8/6	2:44	28.7/28.7	
21X	950	x	8/6	4:46	28.3/28.3	
22X	950	x	8/6	5:29	28.7/28.7	
23X	950	x	8/6	6:18	28.7/28.7	IR anomaly (unusual, flat, broad)
24X	810	x	8/6	0:10	24.8/24.8	IR anomaly (unusual, flat, broad)
25p			8/6			Pressure core, no IR
26Y			8/6			Pressure core, no IR
27E			8/6			Pressure core, no IR
28X	950	x	8/6	14:32	26.3/26.3	Generally cool, possible IR anomaly @ 90 to 120 cm
29X	870	x	8/6	15:18	27.1/27.1	Slightly cooler downcore, large void at bottom except 851 to 870
30X	950	x	8/6	16:25	28.7/28.7	
31X	950	x	8/6	17:09	29.5/29.5	Water in lower part, not full core
32X	950	x	8/6	18:00	28.7/28.7	
33X	950	x	8/6	18:54	28.3/28.3	
34X	950	x	8/6	20:03	28.3/28.3	Down cooling, subtle cooler zones, some gas bubbling and wet zones (drill water?)
35X	950	x	8/6	20:54	28.3/28.3	Warm core, no cool spots
36X	950	x	8/6	21:43	28.3/28.3	
37X	940	x	8/6	22:19	29.1/29.1	20 cm cut off bottom (dented liner)
38X	825	x	8/6	23:29	29.5/29.5	Warm core, good recovery

Table 11. List of infrared image files collected on section ends from Hole NGHP-01-19A.

Core	Section	Top	Bottom	Date	Time	Image #	Comments
1H	3	x		8/5	7:30	G0805-01, 02,	IMG file odd numbers, BMP even #'s
2H	3	x		8/5	8:15	G0805-03, 04	
3H	4	x		8/5	9:15	G0805-05, 06	
4H	2	x		8/5	9:50	G0805-07, 08	
5H	3	x		8/5	10:51	G0805-09, 10	
6H	3	x		8/5	11:31	G0805-11, 12	
7H	3		x	8/5	12:28	G0805-13, 14	False cold spot is hole, fresh cut
7H	7		x	8/5	12:35	G0805-15, 16	Fresh cut at probe location, use for emmissivity calc
8H	last		x	8/5	13:10	G0805-17, 18	Fresh break at bottom of core
8H	4		x	8/5	13:21	G0805-19, 20	Fresh cut
9H	3		x	8/5	13:58	G0805-21, 22	Fresh cut
10H	2		x	8/5	14:35	G0805-23, 24	Fresh cut
11H				8/5			No images, short core
12X	3	x		8/5	16:30	G0805-25, 26	
13X	4		x	8/5	17:09	G0805-27, 28	Gashes in cut, fresh
14X	2	x		8/5	18:56	G0805-29, 30	Fresh cut, rough
18X	4	x		8/6	1:00	G0806-01, 02	
19X	1	x		8/6	1:54	G0806-03, 04	
20X	3	x		8/6	2:51	G0806-05, 06	
21X	2		x	8/6	5:00	G0806-07, 08	
22X	5		x	8/6	5:47	G0806-09, 10	
23X	4		x	8/6	6:31	G0806-11, 12	Top of IW anomaly
23X	6		x	8/6	6:33	G0806-13, 14	Top of IW anomaly
24X	5	x		8/6	7:17	G0806-15, 16	
28X	4		x	8/6	14:48	G0806-17, 18	At head space sample location
29X	4	x		8/6	15:30	G0806-19, 20	Fresh cut below IW
30X	3		x	8/6	16:41	G0806-21, 22	
31X	2		x	8/6	17:18	G0806-23, 24	Above IW and other samples
32X	4		x	8/6	18:16	G0806-25, 26	Above IW and other samples
33X	3		x	8/6	19:00	G0806-27, 28	Very fresh, good image but out of focus
34X	3		x	8/6	20:12	G0806-29, 30	Good image, possibly at former gas void, but out of focus
35X	3		x	8/6	21:10	G0806-31, 32	Out of focus
36X	3		x	8/6	21:50	G0806-33, 34	In focus again from here on
37X	3		x	8/6	22:52	G0806-35, 36	
38X	3		x	8/6	23:37	G0806-37, 38	

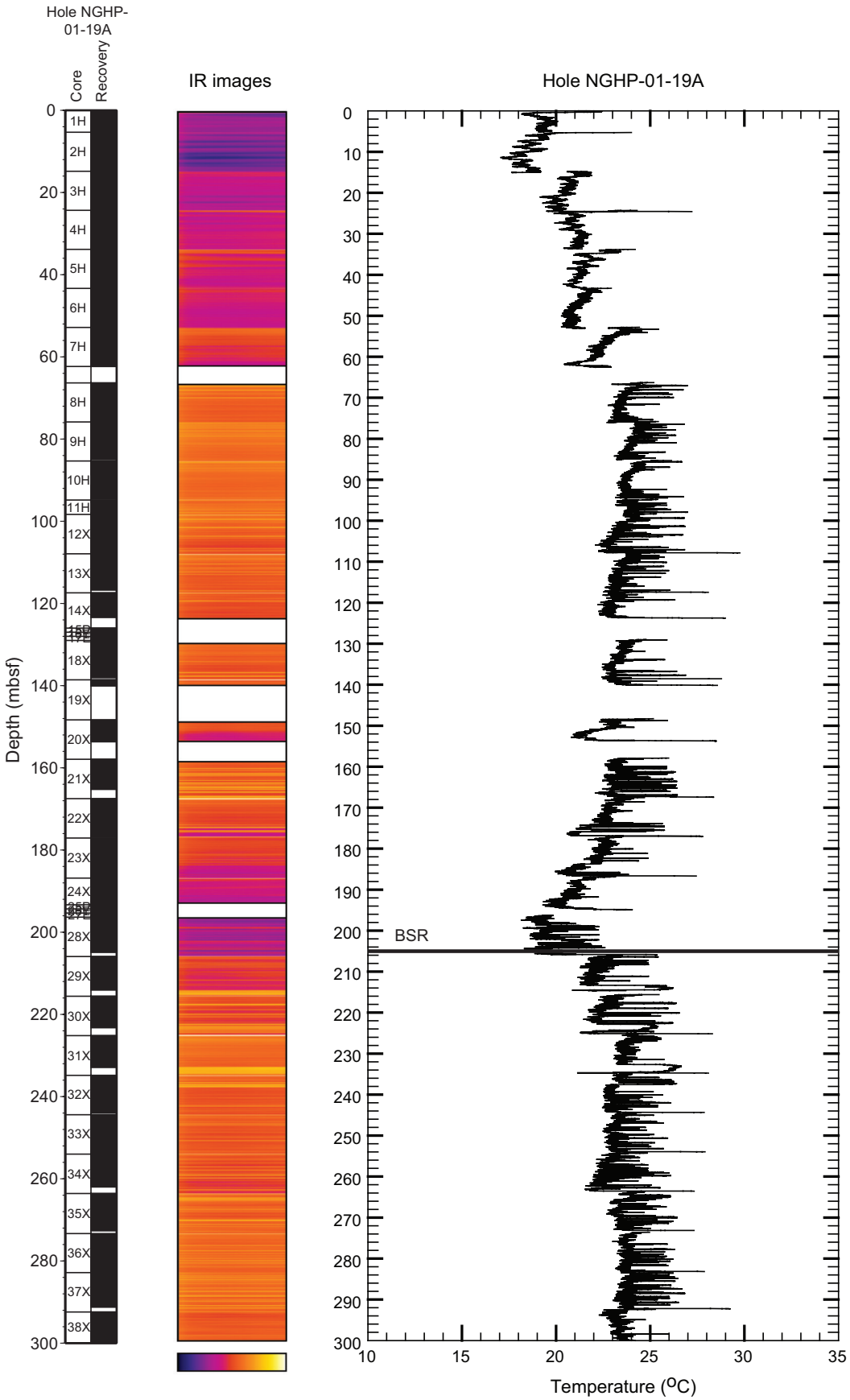


Figure 21. Infrared imaging and the derived downhole temperature profile for Hole NGHP-01-19A.

Section-end IR images can also be used to verify that core sediment temperatures are consistent with the observed IR imaging of core liners. Figure 22 shows core section end images and their thermal profiles corrected for appropriate ambient temperature conditions. Results show that cooling does progress downhole in sediments, particularly in Cores NGHP-01-19A-23X, -24X, -28X and -29X. Section end NGHP-01-19A-29X-4 (top) is cooler than expected (dark blue profile line), but lower section ends return warmer conditions as shown by section end NGHP-01-19A-32X-4 (bot) (black profile line). Section-end IR temperature measurements at the center of each core (averaged over a ~1 cm diameter circle) are plotted for the interval from 175 to 240 mbsf in figure 23 (red inverted triangles). These results generally are consistent with a cooling trend downhole toward the BSR, but show less downhole warming below the BSR than expected. This result could be caused by differences in the spatial relationship to the cut which would expose the core to slurry and biscuits created by XCB coring.

Core-End Temperature Readings

Core-end-temperature readings were taken on most cores immediately following the IR track imaging (table 12). Typically, four temperature probes were inserted ~8 cm into the end of each core and allowed to remain there until the core was completely processed and removed from the catwalk. Temperatures from the center position probes are typically 5 to 10 °C less than the IR temperatures (as expected) since the IR images measure the liner temperature which has warmed closer to ambient temperatures than the center of the core (except where significant gas hydrate is present). Figure 23 shows measured center probe temperatures for Hole NGHP-01-19A over the interval 165 to 245 mbsf. These results do not show the expected down-core temperature shift across the BSR, likely because of variability in sediment hardness affecting initial thermal conditions when the probe is inserted, variability in the thermal history near the drill bit, and the effect of the amount of drill slurry associated with XCB coring.

Estimate of Gas Hydrate Concentration Based on IR Temperature Change

The occurrence of disseminated gas hydrate in Hole NGHP-01-19A makes it possible to perform a bounding estimate of gas hydrate concentration, based on the endothermic nature of gas hydrate dissociation. The estimate is made by calculating the amount of gas hydrate (in volume percent of pore space) required to produce an observed drop in ΔT based on the negative heat of dissociation of methane hydrate. This approach differs from the empirical approach used by Trehu and others (2004) and is enabled by the disseminated nature of gas hydrate at this site. Input data of porosity (64.5 ± 3.6 percent) and bulk density (1.62 ± 0.06 percent?) are taken from MAD data over the interval of 60 to 300 m in Hole NGHP-01-19A (see table 13). The heat capacity of sediment was estimated by calculating the relative contribution of solids and pore water to the heat capacity, by using the heat capacity of quartz as representative of the solid phase. Results of the calculation are shown in figure 24, showing a maximum estimate of ~10 percent of pore space occupied by gas hydrate near the BSR and ranging from 0 (at a depth of 150 mbsf) to ~7 percent (at about 194 mbsf), with most values below 5 percent. These estimates are virtually identical to results from chlorinity measurements (10 percent, see "Inorganic Geochemistry") and broadly consistent with data from a single pressure core (2.4 percent from NGHP-01-19A-27E). Considering the detailed variation in gas hydrate apparent from density scans on pressure cores (see "Pressure Coring"), the estimates from all three methods are remarkably consistent. The method used to estimate gas hydrate from ΔT assumes that all heat energy from gas hydrate instantly produces a temperature drop and thus does not consider kinetic effects delaying gas hydrate dissociation and assumes that the observed ΔT is the maximum ΔT. The estimated gas-hydrate concentration is therefore likely to be biased toward lower values. The calculation also does not consider the thermal effects of the liner. However, a key assumption of the method is that background and gas-hydrate-containing cores experience similar temperature-pressure histories and thus ΔT's are directly comparable to the heat-energy calculation given the assumption that the maximum ΔT has been observed during IR scanning. As noted above, the effect of this assumption not being true is to underestimate the amount of hydrate regardless of whether the ΔT is captured prior to its maximum or after.

Index Properties

Water content, porosity, bulk density, and magnetic susceptibility vary downhole such that three physical-property units can be defined with boundaries at about 70 and 188 mbsf (figs. 25 and 26). The first PP unit is characterized by a decrease in water content and porosity, an increase in bulk density, and a strongly erratic magnetic susceptibility signal. The second PP unit has undulating water content, porosity, and bulk density, whereas the magnetic susceptibility is significantly lower and more uniform. The deepest physical-property unit has linear mass-related properties with depth and a slightly lower magnetic susceptibility. The change in some physical behavior at 70 mbsf roughly agrees with the Lithostratigraphic description at this site that shows the common presence of oozes above 83 mbsf but rarely below that depth (see "Lithostratigraphy"). Except for two spikes at about 111 to 115 mbsf, the porosity and density wireline logs agree remarkably well with the measured PP below 65 m. Valid downhole log readings do not extend above that depth.

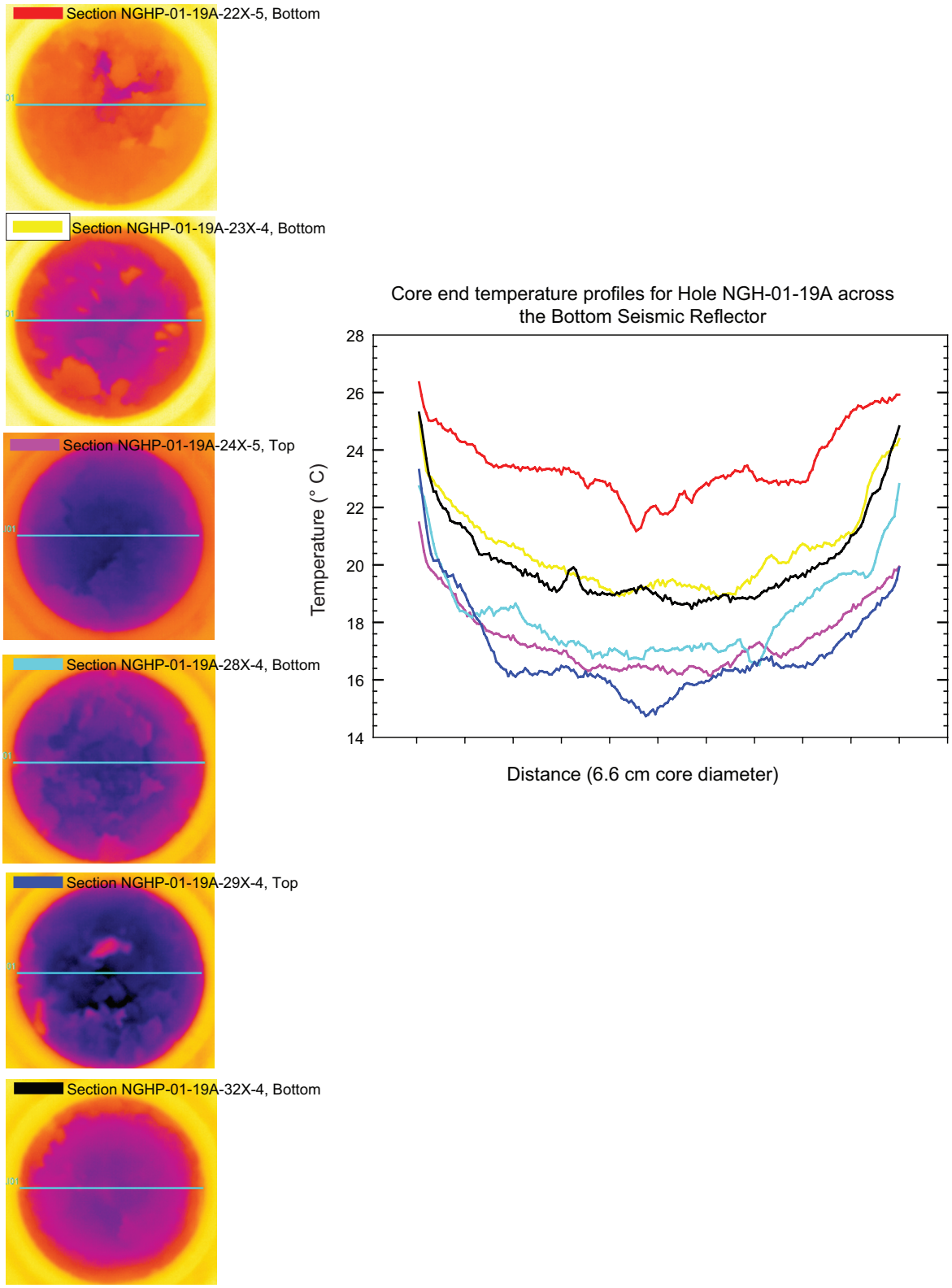


Figure 22. Comparison of core end infrared images and cross-core temperature profiles from two different parts of Hole NGHP-01-19A.

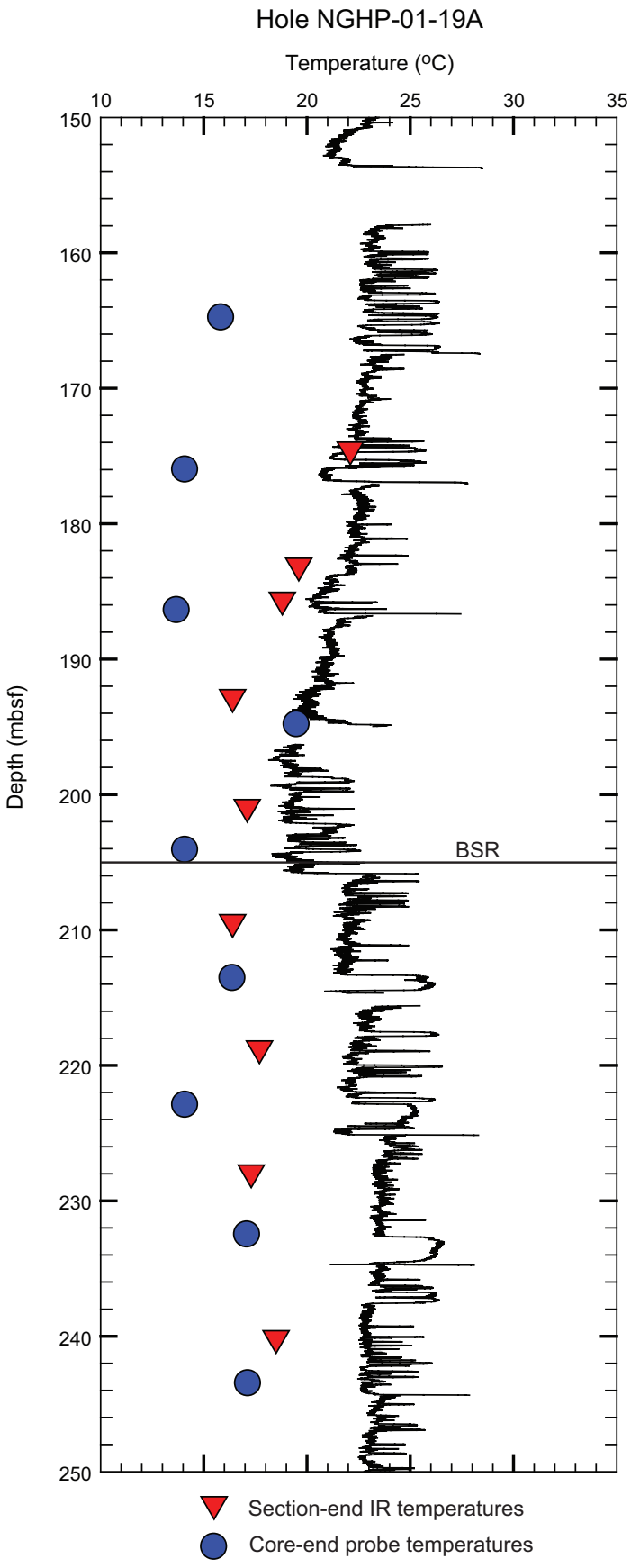


Figure 23. Down-core temperature profile for Hole NGHP-01-19A.

Table 12. List of temperature-probe data collected at bottom of cores from Hole NGHP-01-19A.

Core	Section	Bottom	Date	In time	Out time	Temperature probe #	Comments
1H	last	X	8/5	7:21	7:27	F-1, F-2, F-3, F-4	Alternate pattern to core 18X, probe 2 center, 1 up, 3 down 4 side, until 7H.
2H	last	X	8/5	8:05	8:15	F-1, F-2, F-3, F-4	
3H	last	X	8/5	22:47	9:14	F-1, F-2, F-3, F-4	
4H	last	X	8/5	9:45	9:50	F-1, F-2, F-3, F-4	
5H	last	X	8/5	10:38	10:50	F-1, F-2, F-3, F-4	
6H	last	X	8/5	11:19	11:30	F-1, F-2, F-3, F-4	
7H	last	X	8/5	12:21	12:34	F-1, F-2, F-3, F-4	Used standard pattern(1, 4 on edge 90 deg apart, 3 center, 2 between 1 and 3 (now adopted for remainder of cruise)
8H	last	X	8/5	13:11	13:20	F-1, F-2, F-3, F-4	
9H	last	X	8/5	13:51	14:03	F-1, F-2, F-3, F-4	Good insertion
10H	last		8/5	14:30	14:39	F-1, F-2, F-3, F-4	Good insertion
11H	last	X	8/5	15:07	15:12	F-1, F-2, F-3, F-4	Good insertion, except F-1 (short)
12X	last	X	8/5	16:15	16:25	F-1, F-2, F-3, F-4	Poor insertion, broken and disturbed sediments
13X	last	X	8/5	17:00	17:08	F-1, F-2, F-3, F-4	Good insertion, core end was wet
14X	last	X	8/5	18:45	NA	F-1, F-2, F-3, F-4	F-2 and F-3 in same spot
18X	last	X	8/6	0:46	1:00	F-1, F-2, F-3, F-4	Std pattern now adopted on Midnight to Noon shift
19X	last	X	8/6	1:50	1:55	F-1, F-2, F-3, F-4	
20X	last	X	8/6	2:44	2:52	F-1, F-2, F-3, F-4	
21X	last	X	8/6	4:48	5:01	F-1, F-2, F-3, F-4	
22X	last	X	8/6	5:30	5:40	F-1, F-2, F-3, F-4	
23X	last	X	8/6	6:20	6:31	F-1, F-2, F-3, F-4	
24X	last	X	8/6	7:10	7:17	F-1, F-2, F-3, F-4	
28X	last	X	8/6	14:34	14:50	F-1, F-2, F-3, F-4	Good insertion
29X	last	X	8/6	15:22	15:30	F-1, F-2, F-3, F-4	Good insertion in section at bottom. Out time is approximate.
30X	last	X	8/6	16:28	16:28	F-1, F-2, F-3, F-4	Good insertion
31X	last	X	8/6	17:12	17:21	F-1, F-2, F-3, F-4	Poor insertion, crack at ~8cm in.
32X	last	X	8/6	18:03	18:17	F-1, F-2, F-3, F-4	Excellent insertion
33X	last	X	8/6	18:56	19:06	F-1, F-2, F-3, F-4	Good insertion except F-3 which entered slurry
34X	last	X	8/6	20:07	20:20	F-1, F-2, F-3, F-4	Excellent insertion, F-1 pulled out temporarily toward end.
35X	last	X	8/6	20:57	21:10	F-1, F-2, F-3, F-4	Good insert, cracked but hard push.
36X	last	X	8/6	21:45	21:57	F-1, F-2, F-3, F-4	Insert OK, but cracked through middle of core
37X	last	X	8/6	22:43	22:54	F-1, F-2, F-3, F-4	OK insert, F-2 and F-3 at ~ the same location near center of core
38X	last	X	8/6	23:37	23:40	F-1, F-2, F-3, F-4	Insert into crumbly material but seemingly tight and OK

The water content (100 percent) (related to solids) in the uppermost part of the core (table 13) is somewhat lower than at most previous sites and decreases to 60 percent at the bottom of the hole. Porosity varies from about 73 percent at the top to 61 percent at the bottom of the hole. An ash layer at 7.51 mbsf has a water content of 53 percent and a porosity of 55 percent (table 13). Water content and porosity increase at about 72 mbsf and more abruptly at 100 mbsf, whereas both parameters are more uniform in the disseminated gas-hydrate zone from about 170 to 200 mbsf. Porosity changes little in PP unit 3, below 188 mbsf. Except for an ash layer at 7.51 mbsf (grain density equals 2.40 g/cm^3), grain density varies from 2.62 to 2.76 g/cm^3 in Hole NGHP-01-19A (average value of 2.69 g/cm^3) and roughly decreases with depth.

Strength

Shear strength increases uniformly and linearly to 20 mbsf and then increases somewhat erratically to the bottom of the hole (tables 14, 15, and fig. 25). The boundary between APC and XCB coring is 97 mbsf. Below that depth, slightly more variation in strength measurements exists, illustrating the effect of disturbance caused by rotary coring on sediment. Although testing was to be restricted to intact biscuits, it was occasionally difficult to differentiate between biscuits and adjacent disturbed sediment. Strength measurements performed in the sediment below 242 m were invalid because cracks formed in the sediment biscuits during insertion of the Pocket Penetrometer.

The measured shear strengths were normalized to the effective vertical stress (σ'_v) (fig. 27) to provide qualitative information on the stress history of the sediment. The strength/effective vertical stress ranges from ~0.4 at the top of the hole to an average of about 0.1 deeper in the hole. These values are in overall agreement with a number of other normally consolidated clays (Holtz and Kovacs, 1981). Hunt (1984) states that the strength/effective vertical stress ratio typically is between 0.4 and 0.16. The wide scatter in the results at the top of the hole reflects the dependency of this ratio on the stress path as well as on the test method (Bjerrum, 1972; Ladd, and others, 1977). Because the values are below 0.4, the implication is that these sediments have not experienced a vertical effective stress greater than what is now being applied *in situ*. They have not been overconsolidated by erosional or other geologic processes.

Table 13. Moisture and density (MAD) physical properties for Hole NGHP-01-19A.

Core, section	Sample code	Depth, int, from (cm)	Depth, int, to (cm)	Depth (mbsf)	WCt (%)	WCs (%)	Grain density (g/cm³)	Bulk density (g/cm³)	Dry bulk density (g/cm³)	Porosity (%)	Void ratio	Unit weight (kN/m³)
NGHP-01-19A												
1H-3	MAD	81	83	3.81	50.41	101.66	2.69	1.48	0.73	72.69	2.66	14.52
1H-3	MAD	81	83	3.81	49.79	99.18	2.69	1.49	0.75	72.19	2.60	14.60
1H-4	MAD	34	36	4.84	51.57	106.49	2.66	1.46	0.71	73.42	2.76	14.33
2H-1	MAD	76	78	6.06	46.63	87.37	2.70	1.53	0.82	69.70	2.30	15.05
2H-2	MAD	62	64	7.42	48.94	95.85	2.64	1.49	0.76	71.14	2.47	14.64
2H-2	MAD	71	73	7.51	34.70	53.14	2.40	1.64	1.07	55.36	1.24	16.06
2H-3	MAD	62	64	8.92	53.05	113.00	2.71	1.45	0.68	74.90	2.98	14.22
2H-4	MAD	48	50	10.28	48.89	95.67	2.71	1.50	0.77	71.62	2.52	14.75
2H-5	MAD	39	41	11.69	49.25	97.03	2.64	1.49	0.76	71.40	2.50	14.60
2H-7	MAD	45	47	14.75	42.40	73.60	2.70	1.60	0.92	65.94	1.94	15.66
3H-1	MAD	37	39	15.17	49.00	96.08	2.70	1.50	0.77	71.63	2.52	14.72
3H-2	MAD	37	39	16.67	45.59	83.79	2.71	1.55	0.84	68.84	2.21	15.20
3H-4	MAD	37	39	19.67	46.13	85.64	2.71	1.54	0.83	69.34	2.26	15.13
3H-5	MAD	37	39	21.17	45.67	84.07	2.69	1.55	0.84	68.81	2.21	15.17
3H-6	MAD	37	39	22.67	43.43	76.79	2.70	1.58	0.89	66.85	2.02	15.50
3H-7	MAD	37	39	24.17	45.55	83.66	2.71	1.55	0.84	68.79	2.20	15.21
4H-1	MAD	42	44	24.72	36.60	57.72	2.73	1.70	1.08	60.55	1.53	16.66
4H-2	MAD	42	44	26.22	44.82	81.23	2.68	1.56	0.86	67.97	2.12	15.27
4H-3	MAD	42	44	27.72	41.42	70.71	2.71	1.61	0.95	65.08	1.86	15.82
4H-4	MAD	42	44	29.22	42.79	74.78	2.69	1.59	0.91	66.22	1.96	15.58
4H-5	MAD	42	44	30.72	42.59	74.18	2.65	1.58	0.91	65.70	1.92	15.53
4H-6	MAD	42	44	32.22	42.88	75.07	2.70	1.59	0.91	66.36	1.97	15.58
4H-7	MAD	42	44	33.22	42.69	74.48	2.71	1.59	0.91	66.29	1.97	15.64
5H-2	MAD	48	50	35.78	43.58	77.26	2.72	1.58	0.89	67.15	2.04	15.51
5H-3	MAD	48	50	37.28	42.16	72.88	2.76	1.61	0.93	66.21	1.96	15.81
5H-4	MAD	48	50	38.78	41.03	69.57	2.67	1.61	0.95	64.41	1.81	15.81
5H-5	MAD	48	50	40.28	39.91	66.41	2.70	1.64	0.98	63.55	1.74	16.03
5H-6	MAD	48	50	41.78	38.32	62.13	2.71	1.67	1.03	62.15	1.64	16.33
5H-7	MAD	48	50	43.28	40.05	66.81	2.71	1.63	0.98	63.78	1.76	16.03
6H-1	MAD	42	44	43.72	41.26	70.24	2.73	1.62	0.95	65.10	1.87	15.89
6H-2	MAD	42	44	45.22	44.01	78.59	2.71	1.57	0.88	67.44	2.07	15.43
6H-3	MAD	42	44	46.72	42.17	72.93	2.71	1.60	0.93	65.78	1.92	15.70
6H-4	MAD	42	44	48.22	39.88	66.33	2.72	1.64	0.99	63.69	1.75	16.08
6H-5	MAD	42	44	49.72	37.94	61.14	2.70	1.67	1.04	61.68	1.61	16.37
6H-6	MAD	42	44	51.22	39.40	65.02	2.73	1.65	1.00	63.36	1.73	16.19
6H-7	MAD	42	44	52.72	39.22	64.54	2.69	1.64	1.00	62.84	1.69	16.13
7H-2	MAD	83	85	55.13	40.39	67.75	2.70	1.63	0.97	64.01	1.78	15.96
7H-4	MAD	57	59	57.87	41.36	70.52	2.70	1.61	0.95	64.98	1.86	15.82
7H-5	MAD	56	58	59.36	38.43	62.41	2.71	1.66	1.02	62.22	1.65	16.30
7H-6	MAD	56	58	60.86	38.13	61.64	2.72	1.67	1.03	62.05	1.64	16.38
7H-7	MAD	58	60	62.38	40.20	67.23	2.73	1.64	0.98	64.12	1.79	16.06
8H-1	MAD	25	27	66.55	41.25	70.20	2.74	1.62	0.95	65.18	1.87	15.91
8H-2	MAD	35	37	67.33	39.00	63.95	2.72	1.65	1.01	62.86	1.69	16.23
8H-3	MAD	66	68	68.46	37.60	60.27	2.72	1.68	1.05	61.50	1.60	16.47
8H-4	MAD	65	67	69.95	38.84	63.50	2.72	1.66	1.01	62.75	1.68	16.27
8H-6	MAD	38	40	72.68	34.70	53.15	2.72	1.73	1.13	58.47	1.41	16.96
8H-7	MAD	38	40	74.18	35.34	54.67	2.76	1.73	1.12	59.48	1.47	16.95
8H-8	MAD	38	40	75.18	40.50	68.06	2.72	1.63	0.97	64.36	1.81	16.00
9H-1	MAD	67	69	76.47	35.64	55.38	2.74	1.72	1.11	59.67	1.48	16.86
9H-2	MAD	67	69	77.97	36.94	58.58	2.71	1.69	1.06	60.74	1.55	16.56
9H-3	MAD	76	78	79.46	37.13	59.05	2.71	1.69	1.06	60.95	1.56	16.53
9H-4	MAD	66	68	80.86	40.30	67.50	2.68	1.62	0.97	63.75	1.76	15.93
9H-5	MAD	65	67	82.35	40.54	68.18	2.66	1.62	0.96	63.88	1.77	15.86
9H-6	MAD	38	40	83.58	44.27	79.42	2.67	1.56	0.87	67.38	2.07	15.33
10H-1	MAD	66	68	85.96	42.59	74.20	2.69	1.59	0.91	66.04	1.94	15.61
10H-2	MAD	66	68	87.46	39.88	66.34	2.71	1.64	0.99	63.65	1.75	16.07
10H-3	MAD	66	68	88.96	39.54	65.40	2.69	1.64	0.99	63.17	1.72	16.09
10H-4	MAD	66	68	90.46	40.35	67.63	2.68	1.62	0.97	63.85	1.77	15.93
10H-5	MAD	66	68	91.96	37.21	59.25	2.69	1.68	1.05	60.86	1.56	16.47
10H-6	MAD	65	67	93.45	38.65	62.99	2.70	1.66	1.02	62.33	1.65	16.24

Table 13. Moisture and density (MAD) physical properties for Hole NGHP-01-19A.—Continued

Core, section	Sample code	Depth, int, from (cm)	Depth, int, to (cm)	Depth (mbsf)	WCt (%)	WCs (%)	Grain density (g/cm³)	Bulk density (g/cm³)	Dry bulk density (g/cm³)	Porosity (%)	Void ratio	Unit weight (kN/m³)
NGHP-01-19A—Continued												
11H-1	MAD	78	80	95.58	36.83	58.30	2.72	1.69	1.07	60.69	1.54	16.59
11H-2	MAD	26	28	96.37	36.34	57.08	2.73	1.70	1.08	60.27	1.52	16.70
11H-3	MAD	37	39	97.78	36.36	57.14	2.71	1.70	1.08	60.14	1.51	16.65
12X-1	MAD	28	30	98.58	39.70	65.83	2.70	1.64	0.99	63.37	1.73	16.07
12X-2	MAD	76	78	99.59	39.49	65.26	2.72	1.65	1.00	63.34	1.73	16.15
12X-3	MAD	67	69	101.00	41.49	70.91	2.73	1.62	0.95	65.32	1.88	15.85
12X-4	MAD	67	69	102.11	38.15	61.68	2.74	1.67	1.04	62.18	1.64	16.41
12X-5	MAD	67	69	103.61	44.37	79.77	2.70	1.57	0.87	67.74	2.10	15.37
12X-6	MAD	68	70	105.00	41.72	71.57	2.70	1.61	0.94	65.31	1.88	15.76
12X-7	MAD	68	70	106.50	44.96	81.67	2.67	1.55	0.85	67.97	2.12	15.22
13X-2	MAD	70	72	108.85	45.23	82.59	2.71	1.56	0.85	68.52	2.18	15.25
13X-3	MAD	70	72	110.35	46.46	86.76	2.68	1.53	0.82	69.34	2.26	15.03
13X-4	MAD	70	72	111.85	49.57	98.28	2.65	1.49	0.75	71.70	2.53	14.56
13X-5	MAD	42	44	113.07	48.89	95.64	2.67	1.50	0.77	71.30	2.48	14.68
13X-6	MAD	70	72	114.85	47.46	90.33	2.67	1.52	0.80	70.13	2.35	14.88
13X-7	MAD	52	54	116.17	47.31	89.79	2.66	1.52	0.80	69.90	2.32	14.88
14X-1	MAD	85	87	118.25	47.38	90.02	2.70	1.52	0.80	70.27	2.36	14.93
14X-2	MAD	92	94	119.82	45.46	83.35	2.72	1.55	0.85	68.79	2.20	15.24
14X-3	MAD	51	53	120.91	48.74	95.09	2.66	1.50	0.77	71.09	2.46	14.69
14X-4	MAD	61	63	122.51	44.72	80.90	2.69	1.56	0.86	67.91	2.12	15.29
15P-1	MAD	56	58	126.56	45.59	83.80	2.72	1.55	0.84	68.96	2.22	15.23
16Y-1	MAD	30	32	127.30	44.50	80.19	2.70	1.56	0.87	67.81	2.11	15.34
17E-1	MAD	85	87	128.85	47.31	89.79	2.67	1.52	0.80	70.02	2.34	14.90
18X-1	MAD	91	93	129.91	48.02	92.37	2.67	1.51	0.79	70.63	2.41	14.81
18X-2	MAD	82	84	131.32	46.72	87.70	2.67	1.53	0.81	69.49	2.28	14.97
18X-3	MAD	70	72	132.70	45.79	84.47	2.68	1.54	0.84	68.83	2.21	15.14
18X-4	MAD	80	82	134.30	45.19	82.46	2.68	1.55	0.85	68.30	2.15	15.22
18X-5	MAD	52	54	135.52	43.04	75.55	2.68	1.58	0.90	66.38	1.97	15.53
18X-6	MAD	60	62	137.08	43.90	78.27	2.72	1.58	0.89	67.50	2.08	15.48
19X-1	MAD	69	71	139.29	46.62	87.32	2.74	1.54	0.82	69.98	2.33	15.12
20X-1	MAD	34	36	148.64	44.09	78.87	2.69	1.57	0.88	67.40	2.07	15.39
20X-3	MAD	57	59	151.87	46.83	88.07	2.64	1.52	0.81	69.41	2.27	14.92
20X-4	MAD	33	35	153.13	45.80	84.51	2.70	1.55	0.84	68.98	2.22	15.16
21X-1	MAD	34	36	158.24	43.61	77.35	2.72	1.58	0.89	67.20	2.05	15.51
21X-2	MAD	34	36	159.74	44.47	80.09	2.72	1.57	0.87	67.96	2.12	15.39
21X-3	MAD	89	91	161.79	43.41	76.70	2.71	1.58	0.90	66.95	2.03	15.53
21X-5	MAD	64	66	164.53	44.87	81.40	2.64	1.55	0.85	67.68	2.09	15.19
22X-1	MAD	72	74	168.22	41.22	70.14	2.67	1.61	0.95	64.59	1.82	15.78
22X-2	MAD	72	74	169.72	41.90	72.11	2.73	1.61	0.94	65.73	1.92	15.80
22X-3	MAD	66	68	171.16	35.26	54.46	2.73	1.72	1.11	59.12	1.45	16.88
22X-4	MAD	66	68	172.66	40.30	67.50	2.70	1.63	0.97	63.96	1.77	15.98
22X-5	MAD	64	66	174.14	39.62	65.62	2.72	1.65	0.99	63.52	1.74	16.14
22X-6	MAD	65	67	175.17	40.30	67.51	2.71	1.63	0.97	64.03	1.78	16.00
23X-1	MAD	40	42	177.50	37.38	59.69	2.74	1.69	1.06	61.40	1.59	16.54
23X-3	MAD	40	42	180.50	39.29	64.71	2.75	1.66	1.01	63.39	1.73	16.25
23X-4	MAD	40	42	182.00	37.18	59.19	2.74	1.69	1.06	61.19	1.58	16.57
23X-5	MAD	40	42	183.50	37.46	59.90	2.72	1.68	1.05	61.35	1.59	16.49
23X-6	MAD	40	42	184.71	36.40	57.24	2.73	1.70	1.08	60.39	1.52	16.70
23X-7	MAD	40	42	186.02	37.06	58.88	2.73	1.69	1.06	61.06	1.57	16.59
24X-1	MAD	28	30	187.08	39.72	65.90	2.74	1.65	0.99	63.79	1.76	16.17
24X-2	MAD	93	95	189.23	41.19	70.04	2.72	1.62	0.95	64.98	1.86	15.88
24X-3	MAD	47	49	190.27	39.31	64.76	2.71	1.65	1.00	63.11	1.71	16.17
24X-5	MAD	96	98	193.76	41.26	70.23	2.71	1.62	0.95	64.96	1.85	15.85
25P-1	MAD	51	53	193.81	38.24	61.92	2.70	1.66	1.03	61.97	1.63	16.32
26Y-1	MAD	72	74	195.02	35.59	55.25	2.72	1.71	1.10	59.43	1.46	16.81
27E-1	MAD	27	29	195.57	38.24	61.91	2.69	1.66	1.03	61.87	1.62	16.29

Table 13. Moisture and density (MAD) physical properties for Hole NGHP-01-19A.—Continued

Core, section	Sample code	Depth, int, from (cm)	Depth, int, to (cm)	Depth (mbsf)	WCt (%)	WCs (%)	Grain density (g/cm³)	Bulk density (g/cm³)	Dry bulk density (g/cm³)	Porosity (%)	Void ratio	Unit weight (kN/m³)
NGHP-01-19A—Continued												
28X-3	MAD	87	89	198.80	37.52	60.05	2.74	1.69	1.05	61.59	1.60	16.53
28X-4	MAD	37	39	199.80	36.78	58.18	2.74	1.70	1.07	60.85	1.55	16.66
28X-5	MAD	45	47	201.38	37.76	60.66	2.72	1.68	1.04	61.66	1.61	16.44
28X-6	MAD	37	39	202.30	36.05	56.37	2.72	1.71	1.09	59.87	1.49	16.72
28X-7	MAD	19	21	203.01	37.44	59.85	2.74	1.69	1.06	61.50	1.60	16.54
29X-1	MAD	19	21	206.09	39.14	64.31	2.70	1.65	1.00	62.85	1.69	16.17
29X-2	MAD	96	98	207.38	38.52	62.65	2.69	1.66	1.02	62.12	1.64	16.24
29X-3	MAD	90	92	208.82	38.78	63.33	2.74	1.66	1.02	62.83	1.69	16.32
29X-4	MAD	91	93	210.33	39.52	65.33	2.71	1.65	1.00	63.33	1.73	16.14
29X-5	MAD	73	75	211.65	38.91	63.70	2.67	1.65	1.01	62.37	1.66	16.14
29X-6	MAD	31	33	212.57	42.08	72.65	2.67	1.60	0.92	65.42	1.89	15.65
30X-3	MAD	28	30	217.53	42.53	74.00	2.65	1.59	0.91	65.67	1.91	15.55
30X-5	MAD	124	126	220.39	44.09	78.85	2.65	1.56	0.87	67.03	2.03	15.31
30X-6	MAD	61	63	221.26	41.57	71.14	2.69	1.61	0.94	65.11	1.87	15.77
30X-7	MAD	24	26	221.91	39.51	65.31	2.70	1.64	0.99	63.17	1.72	16.10
30X-8	MAD	22	24	222.36	39.54	65.41	2.69	1.64	0.99	63.14	1.71	16.08
31X-2	MAD	55	57	226.96	40.15	67.09	2.65	1.62	0.97	63.36	1.73	15.89
31X-3	MAD	81	83	228.72	41.49	70.91	2.70	1.61	0.94	65.06	1.86	15.79
31X-4	MAD	42	44	229.83	44.28	79.47	2.67	1.56	0.87	67.37	2.06	15.32
31X-5	MAD	32	34	231.23	42.42	73.67	2.65	1.59	0.91	65.57	1.90	15.56
32X-1	MAD	14	16	234.94	43.50	76.98	2.64	1.57	0.89	66.43	1.98	15.38
32X-5	MAD	29	31	240.43	42.26	73.20	2.64	1.59	0.92	65.28	1.88	15.55
32X-6	MAD	47	49	241.91	40.82	68.96	2.66	1.61	0.95	64.09	1.78	15.81
32X-7	MAD	12	14	242.33	38.74	63.24	2.70	1.65	1.01	62.43	1.66	16.23
33X-2	MAD	33	35	245.30	39.19	64.44	2.68	1.64	1.00	62.72	1.68	16.12
33X-3	MAD	109	111	247.46	42.64	74.33	2.62	1.58	0.90	65.44	1.89	15.45
33X-4	MAD	55	57	248.42	38.49	62.58	2.69	1.66	1.02	62.13	1.64	16.25
33X-5	MAD	40	42	249.77	37.80	60.76	2.70	1.67	1.04	61.53	1.60	16.39
33X-6	MAD	71	73	251.58	38.61	62.91	2.70	1.66	1.02	62.30	1.65	16.25
33X-7	MAD	42	44	252.57	38.22	61.86	2.67	1.66	1.02	61.71	1.61	16.26
34X-1	MAD	26	28	254.26	39.30	64.74	2.67	1.64	0.99	62.72	1.68	16.07
34X-2	MAD	66	68	255.23	39.63	65.64	2.65	1.63	0.98	62.90	1.70	15.98
34X-3	MAD	34	36	256.41	31.77	46.56	2.68	1.77	1.21	54.88	1.22	17.39
34X-4	MAD	28	30	257.85	39.87	66.32	2.69	1.63	0.98	63.47	1.74	16.03
34X-6	MAD	20	22	260.51	40.71	68.67	2.67	1.62	0.96	64.12	1.79	15.86
35X-1	MAD	47	49	264.07	40.44	67.91	2.67	1.62	0.96	63.81	1.76	15.89
35X-2	MAD	30	32	264.83	39.88	66.34	2.64	1.62	0.98	63.07	1.71	15.92
35X-3	MAD	57	59	266.60	42.60	74.22	2.66	1.59	0.91	65.83	1.93	15.56
35X-6	MAD	56	58	271.02	41.48	70.89	2.64	1.60	0.94	64.61	1.83	15.68
36X-1	MAD	23	25	273.53	42.01	72.44	2.64	1.59	0.92	65.07	1.86	15.60
36X-3	MAD	39	41	276.69	39.08	64.15	2.67	1.64	1.00	62.51	1.67	16.11
36X-4	MAD	11	13	277.66	39.58	65.52	2.70	1.64	0.99	63.30	1.73	16.10
36X-5	MAD	18	20	279.13	42.93	75.22	2.65	1.58	0.90	65.96	1.94	15.47
36X-6	MAD	22	24	280.51	40.83	69.02	2.66	1.61	0.95	64.11	1.79	15.81
37X-1	MAD	36	38	283.16	40.66	68.51	2.63	1.61	0.95	63.72	1.76	15.78
37X-2	MAD	42	44	284.00	40.70	68.63	2.64	1.61	0.96	63.86	1.77	15.80
37X-3	MAD	19	21	285.27	41.23	70.15	2.67	1.61	0.94	64.56	1.82	15.77
37X-4	MAD	85	87	287.43	39.15	64.34	2.65	1.64	1.00	62.41	1.66	16.05
37X-5	MAD	22	24	288.20	38.48	62.54	2.66	1.65	1.01	61.81	1.62	16.18
37X-6	MAD	27	29	289.75	39.47	65.20	2.66	1.64	0.99	62.85	1.69	16.04
38X-1	MAD	57	59	292.97	39.95	66.53	2.70	1.64	0.98	63.63	1.75	16.04
38X-2	MAD	45	47	294.35	41.25	70.22	2.69	1.61	0.95	64.76	1.84	15.81
38X-3	MAD	47	49	295.87	38.82	63.45	2.64	1.64	1.00	62.02	1.63	16.09
38X-4	MAD	51	53	297.41	37.91	61.06	2.70	1.67	1.04	61.59	1.60	16.36
38X-5	MAD	65	67	299.05	35.84	55.86	2.71	1.71	1.09	59.57	1.47	16.74
38X-6	MAD	60	62	300.50	37.51	60.03	2.68	1.67	1.04	61.02	1.57	16.38

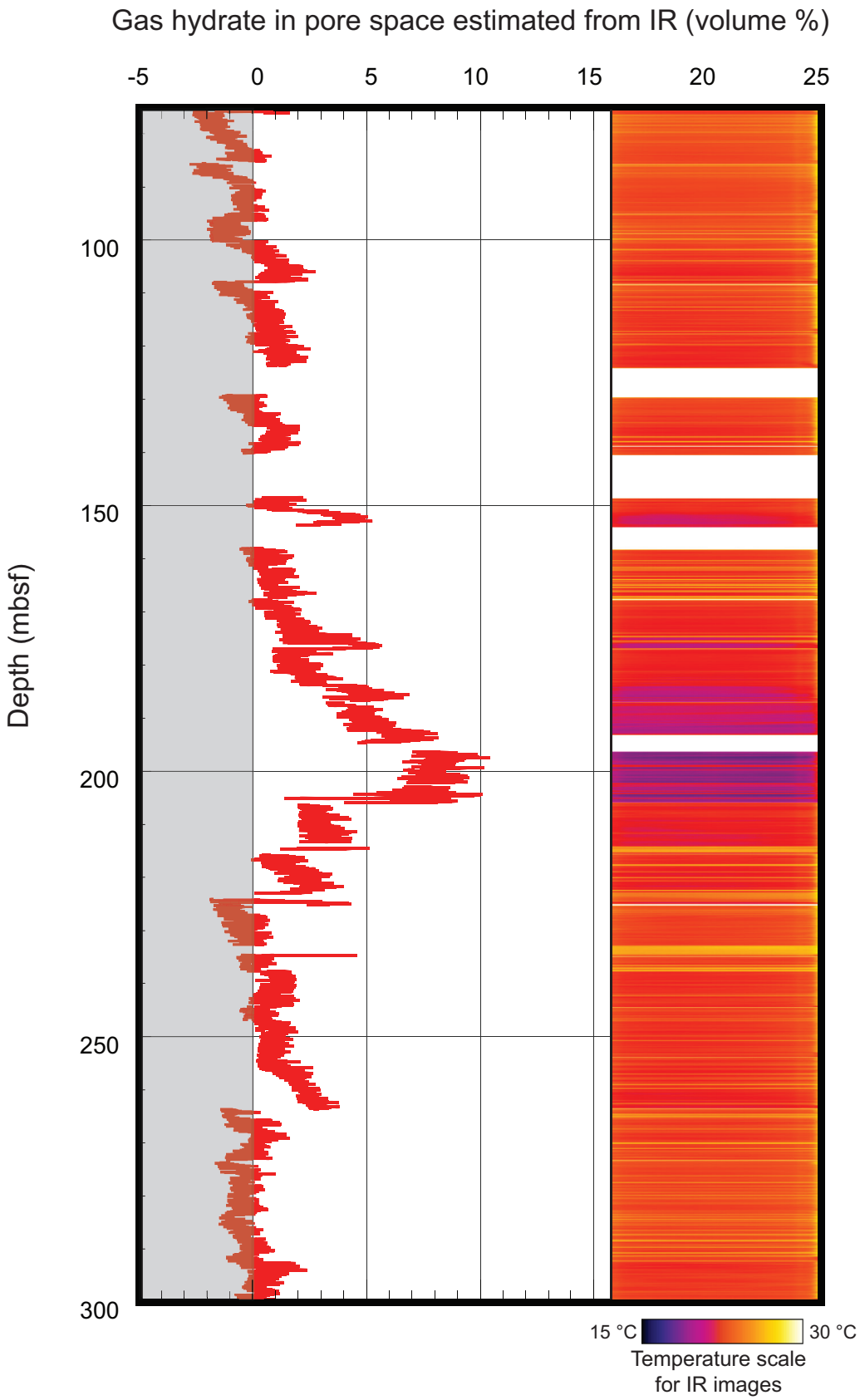


Figure 24. Estimate of gas-hydrate abundance based on downcore temperature anomalies for Hole NGHP-01-19A.

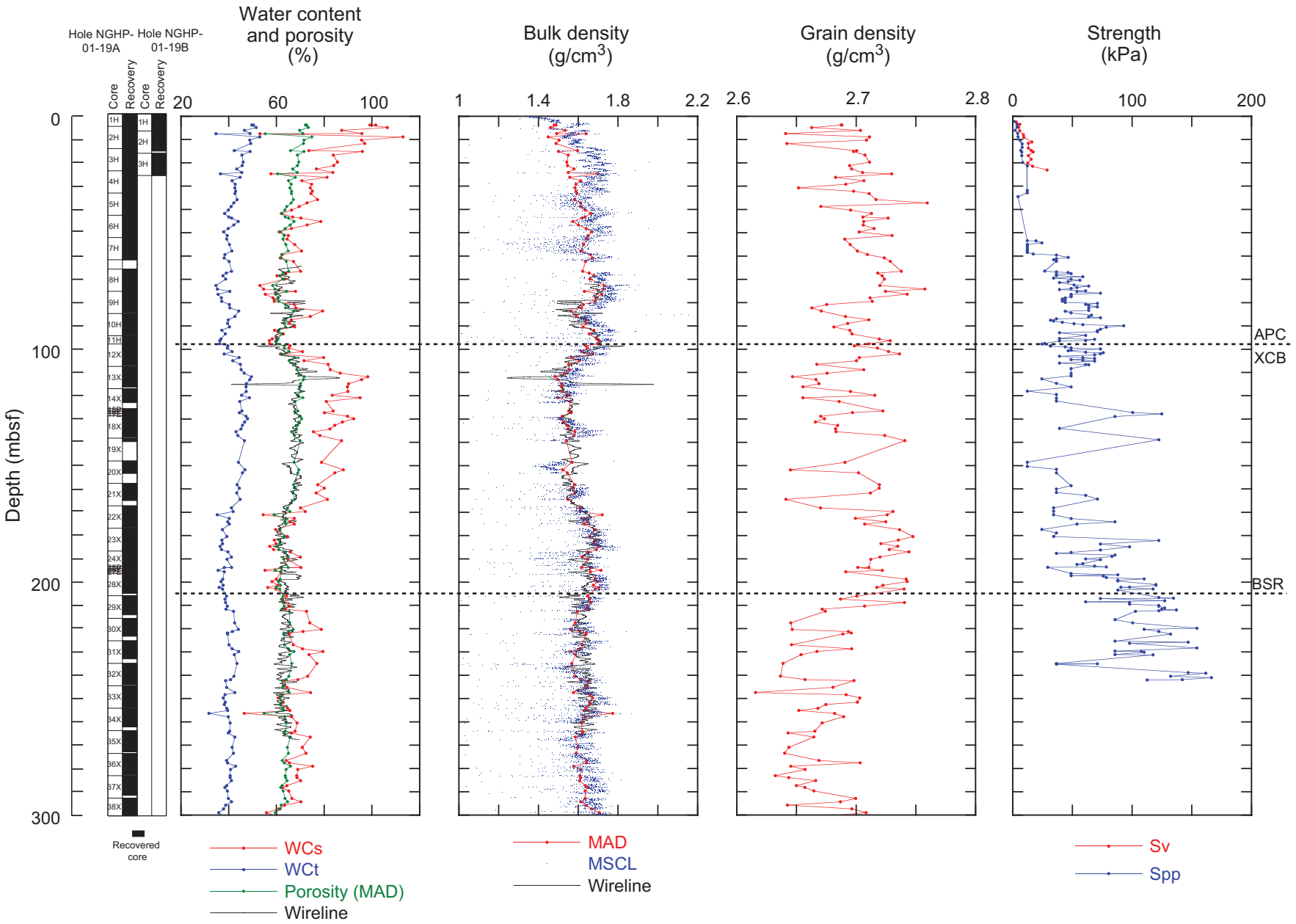


Figure 25. Profiles of core recovery, index, and strength properties for Site NGHP-01-19.

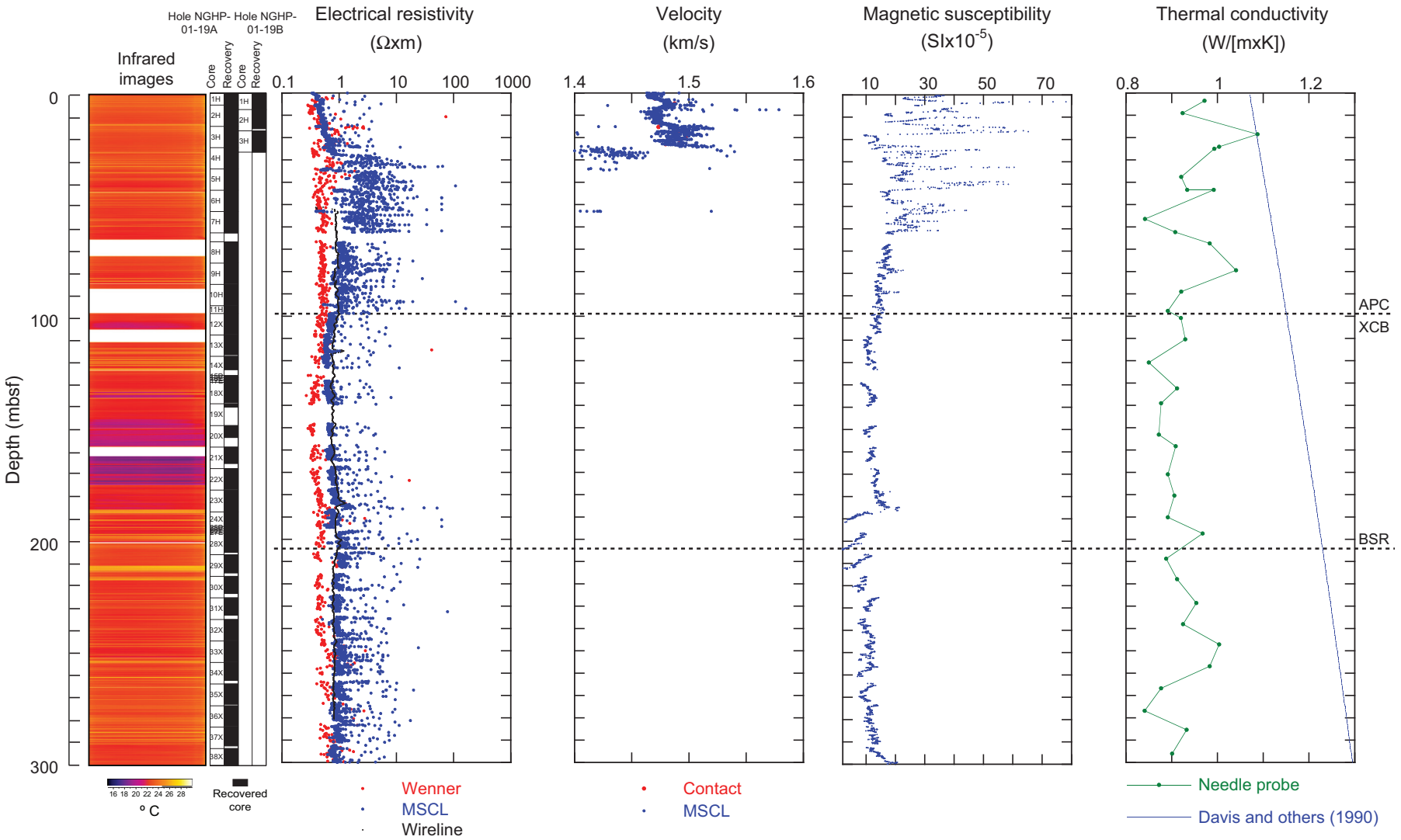


Figure 26. Profiles of infrared images, core recovery, electrical resistivity, acoustic *P*-wave velocity, magnetic susceptibility, and thermal conductivity for Site NGHP-01-19.

Table 14. Vane shear strength results for Hole NGHP-01-19A.

Core, section	Sample	Top (cm)	Depth (mbsf)	Sv (kPa)	Sres (kPa)	Srem (kPa)	St
NGHP-01-19A							
1H-2	VS	105	2.55	3.1	1.7	1.3	2.4
1H-3	VS	44	3.44	6.0	3.1	1.6	3.7
1H-4	VS	20	4.70	5.0	3.2	1.9	2.6
2H-1	VS	92	6.22	5.8	3.3	1.1	5.5
2H-2	VS	118	7.98	9.1	2.5	1.6	5.8
2H-3	VS	75	9.05	9.4	3.5	2.1	4.6
2H-4	VS	126	11.06	16.0	4.9	4.1	3.9
2H-5	VS	37	11.67	13.2	6.6	4.9	2.7
2H-6	VS	89	13.69	13.2	6.6	3.8	3.5
2H-7	VS	36	14.66	15.6	6.6	4.9	3.2
3H-1	VS	53	15.33	17.2	8.2	4.9	3.5
3H-2	VS	60	16.90	13.2	6.6	3.9	3.4
3H-3	VS	63	18.43	15.6	9.2	5.3	3.0
3H-4	VS	82	20.12	12.6	4.9	3.0	4.3
3H-5	VS	71	21.51	16.7	8.6	6.6	2.5
3H-6	VS	84	23.14	28.8	11.4	7.2	4.0

The peak (Sv) and remolded (Srem) vane shear strengths clearly increase with subbottom depth (fig. 28) and the sensitivity (St), which equals Sv/Srem, typically varies between 2.5 and 6. Sensitivity values represent the amount of strength loss after remolding and in extreme examples can reach values of 500 (Lambe and Whitman, 1969). This sediment has low to medium sensitivity (Holtz and Kovacs, 1981). High values of sensitivity are indicative of good quality core recovery because the sediment has not been highly disturbed.

Electrical Resistivity

Strong agreement exists between electrical resistivity values produced by wireline logging and the MSCL. The resistivity values determined using the Wenner array on split cores are on the low side of the MSCL data (fig. 26), in part because the Wenner measurements are conducted on intact core material, rather than on a wider portion of core that may contain voids, small expansion cracks, or slurry. Lower MSCL values are more representative of undisturbed sediment as they are less impacted by the presence of such micro voids caused by gas expansion.

Unlike other holes (for example, NGHP-01-10B), the low wireline resistivity values do not reflect zones of exceptionally high gas hydrate concentrations in Hole NGHP-01-19A. Resistivity determined using both the MSCL and the Wenner array on split cores (table 16) increased between 20 and 21.7 (1 data point) mbsf, respectively, which is at or near the depth of the SMI (20 mbsf). A possible explanation for this agreement is that methane is produced below the SMI and this gas expands upon core recovery and disrupts the sediment structure.

The apparent formation factor is the ratio of the resistivity of a saturated sediment to the resistivity of the pore fluid; this ratio provides an indication of the relationships between sediment structure, void space, tortuosity, and other factors, and the ability of fluid to flow through the formation. Because pore water salinity typically varies a small amount in the recovered sediment and is similar to that of seawater (see "Inorganic Geochemistry"), we have normalized the measured Wenner resistivity values by that of seawater ~0.2 ohm-m) (Ω-m; table 15). Values range from about 1.5 at the top of the hole to <6.0 at the bottom (fig. 29). Other equations and methods exist for calculating formation factor; however, they require the use of empirical constants that have not yet been determined for the sediments at this location.

P-Wave Velocity

P-wave velocity (V_p), measured with the MSCL, increased slightly from 1.46 km/s in the top of the hole (fig. 26) to 1.54 km/s at a subbottom depth of 24 m, which represents the depth where gas and voids present in the sediment prevented further valid measurements from being logged. The contact V_p values of 1.46 to 1.50 km/s (table 17) are in overall agreement with the MSCL values. Valid contact V_p measurements could not be determined below 23.0 mbsf. Both techniques are adversely affected by the SMI located at about 20 mbsf (see "Organic Geochemistry" and "Inorganic Geochemistry"). Methane, which is typically produced below the SMI, may come out of solution if present in a high enough concentration and may attenuate acoustic signals.

Magnetic Susceptibility

Magnetic susceptibility values are variable down to 62 mbsf (fig. 26), but they are still lower than at sites located in the Krishna-Godavari (KG) Basin drilled earlier during Expedition 01. Below 62 mbsf, magnetic susceptibility is uniform and low. These measurements most likely reflect a lack of terrigenous magnetic minerals in the sediment (see "Lithostratigraphy").

Table 15. Pocket Penetrometer strength results for Hole NGHP-01-19A.

Core, section	Sample	Top (cm)	Depth (mbsf)	Spp (kPa)	Core, section	Sample	Top (cm)	Depth (mbsf)	Spp (kPa)
NGHP-01-19A									
1H-2	PP	74	2.24	1.2	9H-1	PP	18	75.98	73.5
1H-3	PP	46	3.46	3.7	9H-1	PP	72	76.52	49.0
1H-4	PP	21	4.71	3.7	9H-1	PP	131	77.11	49.0
2H-1	PP	81	6.11	2.1	9H-2	PP	18	77.48	49.0
2H-2	PP	55	7.35	4.3	9H-2	PP	73	78.03	44.1
2H-3	PP	55	8.85	4.6	9H-2	PP	118	78.48	41.7
2H-4	PP	61	10.41	6.1	9H-3	PP	18	78.88	44.1
2H-5	PP	55	11.85	8.0	9H-3	PP	73	79.43	41.7
2H-6	PP	55	13.35	8.0	9H-3	PP	125	79.95	44.1
2H-7	PP	40	14.70	6.7	9H-4	PP	18	80.38	71.1
3H-1	PP	59	15.39	7.7	9H-4	PP	57	80.77	61.3
3H-2	PP	59	16.89	7.7	9H-4	PP	94	81.14	63.7
3H-4	PP	59	19.89	8.4	9H-5	PP	18	81.88	71.1
3H-5	PP	59	21.39	12.3	9H-5	PP	56	82.26	63.7
4H-6	PP	8	31.88	12.3	9H-6	PP	18	83.38	63.7
4H-7	PP	7	32.87	12.3	9H-6	PP	56	83.76	44.1
5H-1	PP	79	34.59	4.6	9H-6	PP	125	84.45	49.0
7H-1	PP	64	53.44	12.3	10H-1	PP	18	85.48	66.2
7H-1	PP	71	53.51	19.6	10H-1	PP	80	86.10	63.7
7H-2	PP	6	54.36	24.5	10H-1	PP	118	86.48	73.5
7H-2	PP	74	55.04	12.3	10H-2	PP	18	86.98	36.8
7H-2	PP	120	55.50	12.3	10H-2	PP	79	87.59	31.9
7H-3	PP	11	55.91	12.3	10H-2	PP	120	88.00	34.3
7H-3	PP	74	56.54	12.3	10H-3	PP	18	88.48	41.7
7H-3	PP	142	57.22	12.3	10H-3	PP	78	89.08	51.5
7H-4	PP	17	57.47	12.3	10H-3	PP	117	89.47	58.8
7H-4	PP	55	57.85	12.3	10H-4	PP	18	89.98	93.1
7H-4	PP	117	58.47	12.3	10H-4	PP	77	90.57	78.4
7H-5	PP	39	59.19	17.2	10H-5	PP	18	91.48	73.5
7H-5	PP	81	59.61	36.8	10H-5	PP	76	92.06	71.1
7H-6	PP	32	60.62	46.6	10H-5	PP	125	92.55	71.1
7H-6	PP	86	61.16	36.8	10H-6	PP	18	92.98	39.2
7H-6	PP	130	61.60	34.3	10H-6	PP	125	94.05	61.3
7H-7	PP	41	62.21	36.8	11H-1	PP	66	95.46	39.2
8H-1	PP	18	66.48	27.0	11H-1	PP	106	95.86	68.6
8H-1	PP	59	66.89	36.8	11H-2	PP	18	96.29	61.3
8H-2	PP	14	67.12	46.6	11H-2	PP	35	96.46	39.2
8H-2	PP	61	67.59	49.0	11H-3	PP	18	97.59	27.0
8H-3	PP	14	67.94	36.8	11H-3	PP	44	97.85	24.5
8H-3	PP	58	68.38	36.8	12X-1	PP	24	98.54	31.9
8H-3	PP	113	68.93	58.8	12X-1	PP	43	98.73	31.9
8H-4	PP	18	69.48	34.3	12X-2	PP	18	99.01	44.1
8H-4	PP	68	69.98	49.0	12X-2	PP	70	99.53	49.0
8H-4	PP	110	70.40	56.4	12X-2	PP	113	99.96	73.5
8H-5	PP	18	70.98	46.6	12X-3	PP	18	100.51	49.0
8H-5	PP	62	71.42	39.2	12X-3	PP	40	100.73	46.6
8H-6	PP	18	72.48	51.5	12X-3	PP	102	101.35	61.3
8H-6	PP	60	72.90	63.7	12X-4	PP	16	101.60	76.0
8H-6	PP	124	73.54	53.9	12X-4	PP	62	102.06	73.5
8H-7	PP	18	73.98	49.0	12X-4	PP	108	102.52	68.6
8H-7	PP	66	74.46	39.2	12X-5	PP	18	103.12	39.2
8H-8	PP	18	74.98	61.3	12X-5	PP	70	103.64	58.8
8H-8	PP	53	75.33	53.9	12X-5	PP	109	104.03	68.6

Table 15. Pocket Penetrometer strength results for Hole NGHP-01-19A.—Continued

Core, section	Sample	Top (cm)	Depth (mbsf)	Spp (kPa)	Core, section	Sample	Top (cm)	Depth (mbsf)	Spp (kPa)
NGHP-01-19A—Continued									
12X-6	PP	18	104.50	49.0	25P-1	PP	36	193.66	29.4
12X-6	PP	50	104.82	58.8	28X-1	PP	10	196.40	49.0
12X-6	PP	80	105.12	68.6	28X-2	PP	17	196.90	88.2
12X-7	PP	18	106.00	39.2	28X-2	PP	56	197.29	49.0
12X-7	PP	80	106.62	61.3	28X-2	PP	73	197.46	76.0
12X-7	PP	95	106.77	63.7	28X-3	PP	11	198.04	78.4
13X-2	PP	25	108.40	49.0	28X-3	PP	75	198.68	110.3
13X-3	PP	83	110.48	49.0	28X-3	PP	126	199.19	88.2
13X-4	PP	35	111.50	49.0	28X-4	PP	16	199.59	88.2
13X-5	PP	18	112.83	24.5	28X-5	PP	20	201.13	120.1
13X-6	PP	56	114.71	36.8	28X-5	PP	51	201.44	120.1
13X-7	PP	62	116.27	49.0	28X-6	PP	24	202.17	98.0
14X-1	PP	66	118.06	12.3	28X-6	PP	35	202.28	90.7
14X-2	PP	62	119.52	36.8	28X-7	PP	20	203.02	117.6
14X-3	PP	75	121.15	36.8	28X-7	PP	64	203.46	88.2
14X-4	PP	48	122.38	36.8	29X-2	PP	15	206.57	122.5
16Y-1	PP	24	127.24	100.5	29X-2	PP	48	206.90	134.8
16Y-1	PP	83	127.83	125.0	29X-2	PP	67	207.09	73.5
17E-1	PP	89	128.89	85.8	29X-3	PP	16	208.08	127.4
18X-4	PP	55	134.05	39.2	29X-3	PP	63	208.55	61.3
19X-1	PP	34	138.94	122.5	29X-3	PP	92	208.84	98.0
20X-1	PP	24	148.54	12.3	29X-4	PP	8	209.50	98.0
20X-2	PP	60	150.40	12.3	29X-4	PP	60	210.02	122.5
20X-3	PP	27	151.57	36.8	29X-4	PP	93	210.35	122.5
20X-4	PP	43	153.23	36.8	29X-5	PP	26	211.18	127.4
21X-1	PP	72	158.62	49.0	29X-5	PP	74	211.66	125.0
21X-2	PP	67	160.07	36.8	29X-5	PP	102	211.94	137.2
21X-3	PP	66	161.56	36.8	29X-6	PP	9	212.35	122.5
21X-4	PP	37	162.76	61.3	29X-6	PP	32	212.58	102.9
21X-5	PP	45	164.34	71.1	30X-2	PP	40	216.15	85.8
22X-1	PP	66	168.16	34.3	30X-3	PP	29	217.54	100.5
22X-2	PP	66	169.66	34.3	30X-5	PP	66	219.81	154.4
22X-3	PP	64	171.14	34.3	30X-5	PP	116	220.31	110.3
22X-4	PP	73	172.73	49.0	30X-6	PP	62	221.27	122.5
22X-5	PP	62	174.12	85.8	30X-8	PP	23	222.37	132.3
22X-6	PP	62	175.14	53.9	31X-1	PP	19	225.39	85.8
23X-1	PP	36	177.46	24.5	31X-1	PP	65	225.85	147.0
23X-2	PP	36	178.96	36.8	31X-1	PP	109	226.29	98.0
23X-3	PP	36	180.46	34.3	31X-3	PP	40	228.31	154.4
23X-4	PP	56	182.16	122.5	31X-4	PP	24	229.65	85.8
23X-5	PP	60	183.70	73.5	31X-4	PP	43	229.84	107.8
23X-6	PP	64	184.95	98.0	31X-4	PP	71	230.12	110.3
23X-7	PP	64	186.26	73.5	31X-5	PP	25	231.16	85.8
24X-1	PP	51	187.31	49.0	31X-5	PP	34	231.25	117.6
24X-1	PP	87	187.67	36.8	32X-1	PP	16	234.96	36.8
24X-2	PP	16	188.46	85.8	32X-1	PP	30	235.10	71.1
24X-2	PP	73	189.03	83.3	32X-1	PP	51	235.31	36.8
24X-3	PP	33	190.13	61.3	32X-4	PP	30	238.94	147.0
24X-3	PP	61	190.41	73.5	32X-4	PP	54	239.18	161.7
24X-4	PP	77	192.07	58.8	32X-5	PP	30	240.44	132.3
24X-4	PP	118	192.48	53.9	32X-5	PP	92	241.06	166.6
24X-5	PP	38	193.18	68.6	32X-6	PP	48	241.92	142.1
24X-5	PP	75	193.55	78.4	32X-6	PP	60	242.04	112.7

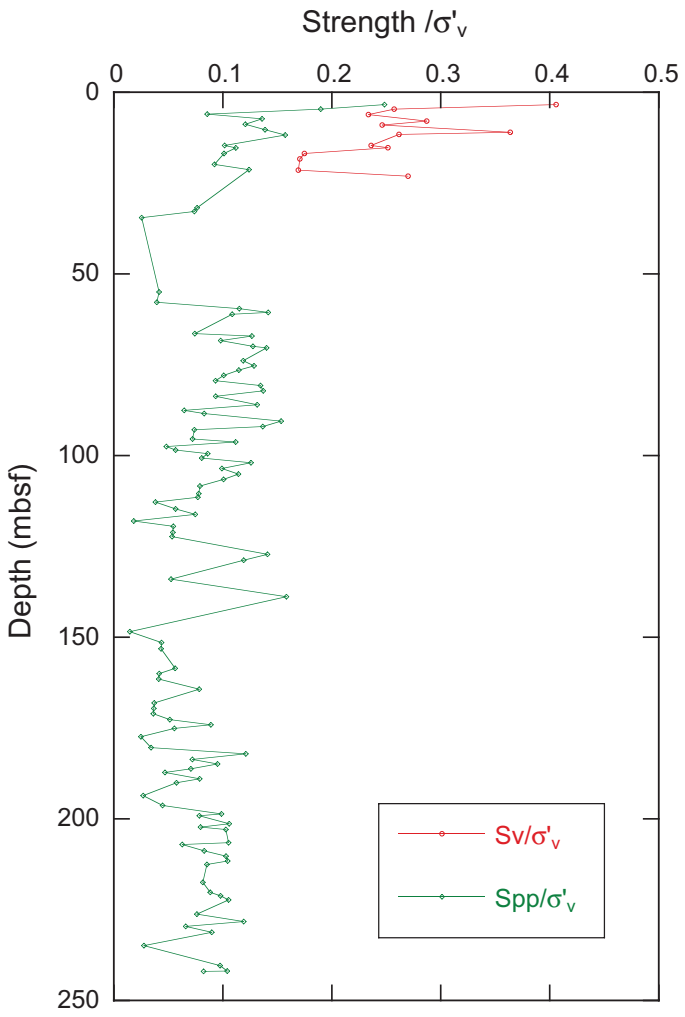


Figure 27. Shear strengths normalized by the effective vertical stress versus sub-bottom depth for Hole NGHP-01-19A.

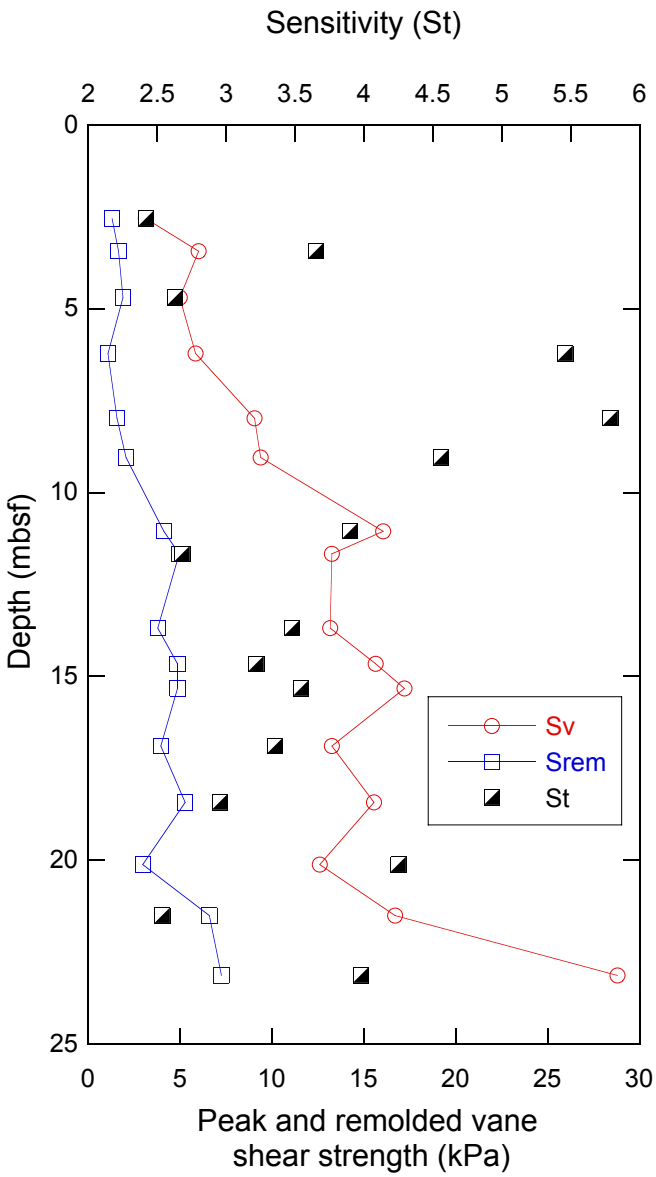


Figure 28. Peak and remolded vane shear strengths and sensitivity for Hole NGHP-01-19A. [Sv, peak vane shear strength; Srem, remolded vane shear strength; St, shear strength sensitivity]

Table 16. Wenner array electrical resistivity and formation factor results for Hole NGHP-01-19A. (To view complete table, please refer to the **ASCII** files.)

Core, section	Sample	Top (cm)	Depth (mbsf)	Electrical resistivity (W×m)	Apparent formation factor	Core, section	Sample	Top (cm)	Depth (mbsf)	Electrical resistivity (W×m)	Apparent formation factor
NGHP-01-19A											
1H-2	ER	61	2.11	0.59	2.97	3H-1	ER	78	15.58	0.62	3.11
1H-2	ER	83	2.33	0.77	3.83	3H-1	ER	94	15.74	0.30	1.52
1H-2	ER	103	2.53	0.50	2.52	3H-1	ER	114	15.94	0.40	2.01
1H-2	ER	120	2.70	0.62	3.11	3H-1	ER	134	16.14	0.68	3.40
1H-3	ER	20	3.20	0.34	1.69	3H-2	ER	18	16.48	0.83	4.13
1H-3	ER	40	3.40	0.42	2.08	3H-2	ER	45	16.75	0.92	4.62
1H-3	ER	62	3.62	0.38	1.89	3H-2	ER	65	16.95	0.58	2.89
1H-3	ER	62	3.62	0.39	1.96	3H-2	ER	85	17.15	0.88	4.39
1H-3	ER	79	3.79	0.37	1.87	3H-2	ER	105	17.35	0.87	4.35
1H-4	ER	20	4.70	0.39	1.94	3H-2	ER	125	17.55	0.96	4.81
1H-4	ER	40	4.90	0.39	1.94	3H-3	ER	20	18.00	0.56	2.79
2H-1	ER	20	5.50	0.29	1.43	3H-3	ER	45	18.25	0.84	4.22
2H-1	ER	40	5.70	0.29	1.45	3H-3	ER	65	18.45	0.53	2.64
2H-1	ER	60	5.90	0.31	1.55	3H-3	ER	90	18.70	1.00	5.02
2H-1	ER	80	6.10	0.33	1.67	3H-3	ER	93	18.73	0.56	2.78
2H-1	ER	100	6.30	0.35	1.73	3H-3	ER	113	18.93	0.75	3.74
2H-1	ER	120	6.50	0.32	1.60	3H-5	ER	18	20.98	0.59	2.94
2H-2	ER	10	6.90	0.36	1.82	3H-5	ER	28	21.08	0.81	4.04
2H-2	ER	20	7.00	0.36	1.78	3H-5	ER	46	21.26	0.44	2.18
2H-2	ER	30	7.10	0.35	1.75	3H-5	ER	57	21.37	0.46	2.30
2H-2	ER	40	7.20	0.37	1.86	3H-5	ER	80	21.60	0.48	2.38
2H-2	ER	50	7.30	0.34	1.71	3H-5	ER	86	21.66	1.02	5.11
2H-2	ER	60	7.40	0.35	1.76	3H-6	ER	20	22.50	0.37	1.83
2H-2	ER	72	7.52	0.47	2.33	3H-6	ER	44	22.74	1.40	6.98
2H-2	ER	88	7.68	0.31	1.56	3H-6	ER	45	22.75	0.43	2.14
2H-2	ER	100	7.80	0.33	1.66	3H-6	ER	65	22.95	0.83	4.16
2H-2	ER	110	7.90	0.33	1.67	3H-6	ER	81	23.11	0.71	3.55
2H-2	ER	120	8.00	0.32	1.58	3H-6	ER	111	23.41	0.63	3.13
2H-2	ER	130	8.10	0.32	1.61	3H-6	ER	131	23.61	0.57	2.83
2H-2	ER	140	8.20	0.34	1.68	3H-7	ER	20	24.00	0.44	2.21
2H-3	ER	20	8.50	0.31	1.54	3H-7	ER	40	24.20	0.58	2.90
2H-3	ER	40	8.70	0.30	1.51	4H-1	ER	20	24.50	0.54	2.68
2H-3	ER	60	8.90	0.30	1.50	4H-1	ER	40	24.70	0.57	2.85
2H-3	ER	80	9.10	0.35	1.73	4H-1	ER	60	24.90	0.68	3.42
2H-3	ER	100	9.30	0.31	1.56	4H-1	ER	80	25.10	0.34	1.70
2H-4	ER	25	10.05	0.47	2.34	4H-1	ER	100	25.30	0.47	2.33
2H-4	ER	45	10.25	0.44	2.19	4H-1	ER	120	25.50	0.55	2.76
2H-4	ER	65	10.45	0.44	2.19	4H-1	ER	140	25.70	0.37	1.83
2H-4	ER	85	10.65	0.48	2.39	4H-2	ER	20	26.00	0.34	1.72
2H-4	ER	105	10.85	0.45	2.25	4H-2	ER	40	26.20	0.37	1.87
2H-4	ER	125	11.05	0.54	2.70	4H-2	ER	60	26.40	0.41	2.03
2H-5	ER	20	11.50	0.37	1.83	4H-2	ER	80	26.60	0.40	1.98
2H-5	ER	37	11.67	0.45	2.26	4H-2	ER	100	26.80	0.40	2.02
2H-5	ER	45	11.75	1.07	5.36	4H-2	ER	119	26.99	0.35	1.74
2H-5	ER	57	11.87	0.49	2.46	4H-2	ER	120	27.00	0.35	1.75
2H-5	ER	77	12.07	0.41	2.07	4H-3	ER	20	27.50	0.38	1.89
2H-6	ER	20	13.00	0.42	2.09	4H-3	ER	40	27.70	0.42	2.11
2H-6	ER	40	13.20	0.46	2.31	4H-3	ER	60	27.90	0.36	1.80
2H-6	ER	80	13.60	0.68	3.40	4H-3	ER	80	28.10	0.44	2.22
2H-6	ER	100	13.80	0.44	2.19	4H-3	ER	100	28.30	0.37	1.84
2H-6	ER	120	14.00	0.45	2.25	4H-3	ER	120	28.50	0.36	1.78
2H-7	ER	15	14.45	0.47	2.34	4H-4	ER	24	29.04	0.62	3.11
2H-7	ER	35	14.65	0.44	2.19	4H-4	ER	42	29.22	0.78	3.89
3H-1	ER	58	15.38	0.51	2.57	4H-4	ER	62	29.42	0.69	3.46
3H-1	ER	74	15.54	0.44	2.18	4H-4	ER	80	29.60	0.69	3.44

Table 16. Wenner array electrical resistivity and formation factor results for Hole NGHP-01-19A. (To view complete table, please refer to the **ASCII** files.)—Continued

Core, section	Sample	Top (cm)	Depth (mbsf)	Electrical resistivity (W×m)	Apparent formation factor	Core, section	Sample	Top (cm)	Depth (mbsf)	Electrical resistivity (W×m)	Apparent formation factor
NGHP-01-19A—Continued											
4H-5	ER	20	30.50	0.58	2.89	5H-7	ER	20	43.00	0.47	2.37
4H-5	ER	20	30.50	0.61	3.04	5H-7	ER	41	43.21	0.47	2.36
4H-5	ER	40	30.70	0.68	3.39	5H-7	ER	60	43.40	1.12	5.60
4H-5	ER	60	30.90	0.67	3.36	5H-7	ER	78	43.58	0.45	2.24
4H-5	ER	80	31.10	0.78	3.88	6H-1	ER	31	43.61	0.42	2.10
4H-5	ER	100	31.30	0.93	4.65	6H-1	ER	51	43.81	0.47	2.33
4H-5	ER	100	31.30	1.06	5.28	6H-1	ER	71	44.01	0.50	2.50
4H-5	ER	120	31.50	0.78	3.89	6H-1	ER	91	44.21	0.42	2.12
4H-5	ER	140	31.70	1.11	5.55	6H-1	ER	111	44.41	0.39	1.94
4H-6	ER	20	32.00	0.80	3.99	6H-1	ER	131	44.61	0.43	2.15
4H-6	ER	40	32.20	0.70	3.48	6H-2	ER	20	45.00	0.74	3.70
4H-6	ER	60	32.40	0.80	3.98	6H-2	ER	44	45.24	0.38	1.89
4H-6	ER	80	32.60	0.77	3.83	6H-2	ER	61	45.41	0.52	2.59
4H-7	ER	15	32.95	0.62	3.10	6H-2	ER	81	45.61	0.37	1.84
4H-7	ER	35	33.15	0.61	3.04	6H-3	ER	20	46.50	0.42	2.08
4H-7	ER	55	33.35	0.76	3.79	6H-3	ER	44	46.74	0.35	1.77
4H-7	ER	75	33.55	0.68	3.39	6H-3	ER	64	46.94	0.55	2.76
5H-1	ER	26	34.06	0.38	1.92	6H-3	ER	84	47.14	0.45	2.24
5H-1	ER	55	34.35	0.42	2.11	6H-3	ER	104	47.34	0.45	2.27
5H-1	ER	84	34.64	0.62	3.10	6H-3	ER	124	47.54	0.64	3.19
5H-1	ER	104	34.84	0.48	2.42	6H-3	ER	141	47.71	0.43	2.16
5H-1	ER	124	35.04	1.88	9.41	6H-4	ER	20	48.00	0.58	2.89
5H-1	ER	124	35.04	0.97	4.83	6H-4	ER	44	48.24	0.42	2.08
5H-2	ER	20	35.50	0.48	2.41	6H-4	ER	60	48.40	0.47	2.33
5H-2	ER	40	35.70	0.87	4.37	6H-4	ER	80	48.60	0.43	2.17
5H-2	ER	60	35.90	0.57	2.87	6H-4	ER	100	48.80	0.47	2.36
5H-2	ER	80	36.10	0.54	2.71	6H-4	ER	120	49.00	0.45	2.27
5H-2	ER	100	36.30	0.40	2.00	6H-4	ER	139	49.19	0.59	2.96
5H-2	ER	120	36.50	1.28	6.39	6H-5	ER	16	49.46	0.43	2.17
5H-3	ER	20	37.00	1.54	7.68	6H-5	ER	36	49.66	0.57	2.87
5H-3	ER	20	37.00	0.68	3.41	6H-5	ER	55	49.85	0.61	3.07
5H-3	ER	42	37.22	0.82	4.10	6H-5	ER	75	50.05	0.41	2.06
5H-3	ER	60	37.40	0.65	3.26	6H-5	ER	90	50.20	0.45	2.25
5H-3	ER	80	37.60	1.12	5.59	6H-6	ER	20	51.00	0.44	2.18
5H-3	ER	100	37.80	0.46	2.30	6H-6	ER	39	51.19	0.47	2.34
5H-3	ER	120	38.00	0.82	4.08	6H-6	ER	59	51.39	0.59	2.94
5H-3	ER	140	38.20	0.50	2.48	6H-6	ER	79	51.59	0.45	2.27
5H-4	ER	20	38.50	0.45	2.26	6H-6	ER	99	51.79	0.48	2.40
5H-4	ER	42	38.72	0.36	1.81	6H-6	ER	119	51.99	0.41	2.05
5H-4	ER	62	38.92	0.61	3.05	6H-6	ER	139	52.19	0.42	2.11
5H-4	ER	80	39.10	0.60	3.00	6H-7	ER	20	52.50	0.44	2.19
5H-4	ER	101	39.31	0.47	2.35	6H-7	ER	38	52.68	0.47	2.33
5H-4	ER	121	39.51	0.70	3.52	6H-7	ER	58	52.88	0.48	2.38
5H-4	ER	140	39.70	0.87	4.36	7H-1	ER	63	53.43	0.47	2.35
5H-5	ER	20	40.00	0.63	3.15	7H-1	ER	73	53.53	0.46	2.28
5H-5	ER	43	40.23	0.45	2.26	7H-1	ER	88	53.68	0.54	2.69
5H-5	ER	61	40.41	0.48	2.38	7H-1	ER	120	54.00	0.50	2.52
5H-5	ER	81	40.61	0.57	2.87	7H-1	ER	138	54.18	0.55	2.74
5H-6	ER	20	41.50	0.54	2.72	7H-2	ER	9	54.39	0.55	2.74
5H-6	ER	42	41.72	0.39	1.97	7H-2	ER	75	55.05	0.53	2.65
5H-6	ER	60	41.90	0.51	2.55	7H-2	ER	84	55.14	0.60	3.00
5H-6	ER	80	42.10	0.52	2.58	7H-2	ER	121	55.51	0.52	2.58
5H-6	ER	100	42.30	0.75	3.75	7H-2	ER	137	55.67	0.63	3.13
5H-6	ER	120	42.50	0.82	4.09	7H-3	ER	8	55.88	0.55	2.75
5H-6	ER	140	42.70	0.68	3.41	7H-3	ER	51	56.31	0.68	3.40

Table 16. Wenner array electrical resistivity and formation factor results for Hole NGHP-01-19A. (To view complete table, please refer to the **ASCII** files.)—Continued

Core, section	Sample	Top (cm)	Depth (mbsf)	Electrical resistivity (W×m)	Apparent formation factor	Core, section	Sample	Top (cm)	Depth (mbsf)	Electrical resistivity (W×m)	Apparent formation factor
NGHP-01-19A—Continued											
7H-3	ER	76	56.56	0.50	2.50	8H-6	ER	137	73.67	0.54	2.71
7H-3	ER	139	57.19	0.52	2.62	8H-7	ER	15	73.95	0.50	2.50
7H-4	ER	19	57.49	0.55	2.75	8H-7	ER	35	74.15	0.54	2.69
7H-4	ER	36	57.66	0.58	2.89	8H-7	ER	54	74.34	0.56	2.79
7H-4	ER	53	57.83	0.53	2.65	8H-7	ER	73	74.53	0.49	2.44
7H-4	ER	87	58.17	0.63	3.14	8H-7	ER	89	74.69	0.57	2.85
7H-4	ER	109	58.39	0.53	2.66	8H-8	ER	15	74.95	0.54	2.71
7H-4	ER	129	58.59	0.74	3.72	8H-8	ER	31	75.11	0.51	2.55
7H-5	ER	9	58.89	0.61	3.03	8H-8	ER	53	75.33	0.51	2.56
7H-5	ER	29	59.09	0.52	2.61	9H-1	ER	15	75.95	0.48	2.41
7H-5	ER	50	59.30	0.51	2.56	9H-1	ER	35	76.15	0.50	2.52
7H-5	ER	70	59.50	0.60	2.98	9H-1	ER	55	76.35	0.48	2.40
7H-5	ER	85	59.65	0.49	2.45	9H-1	ER	75	76.55	0.52	2.60
7H-6	ER	15	60.45	0.43	2.14	9H-1	ER	96	76.76	0.51	2.55
7H-6	ER	35	60.65	0.40	2.02	9H-1	ER	118	76.98	0.58	2.92
7H-6	ER	56	60.86	0.47	2.33	9H-1	ER	138	77.18	0.57	2.85
7H-6	ER	76	61.06	0.49	2.46	9H-2	ER	14	77.44	0.57	2.87
7H-6	ER	96	61.26	0.45	2.24	9H-2	ER	35	77.65	0.53	2.63
7H-6	ER	120	61.50	0.54	2.69	9H-2	ER	55	77.85	0.55	2.76
7H-6	ER	143	61.73	0.51	2.56	9H-2	ER	75	78.05	0.54	2.72
7H-7	ER	7	61.87	0.43	2.17	9H-2	ER	95	78.25	0.56	2.80
7H-7	ER	34	62.14	0.54	2.70	9H-2	ER	117	78.47	0.45	2.24
7H-7	ER	47	62.27	0.52	2.61	9H-2	ER	134	78.64	0.54	2.70
7H-7	ER	58	62.38	0.57	2.87	9H-3	ER	15	78.85	0.49	2.44
8H-1	ER	20	66.50	0.47	2.34	9H-3	ER	40	79.10	0.52	2.62
8H-1	ER	40	66.70	0.40	1.99	9H-3	ER	42	79.12	0.55	2.74
8H-1	ER	60	66.90	0.48	2.40	9H-3	ER	65	79.35	0.55	2.73
8H-2	ER	20	67.18	0.49	2.46	9H-3	ER	87	79.57	0.53	2.67
8H-2	ER	40	67.38	0.50	2.48	9H-3	ER	107	79.77	0.52	2.59
8H-2	ER	60	67.58	0.49	2.46	9H-3	ER	131	80.01	0.57	2.84
8H-3	ER	15	67.95	0.57	2.84	9H-3	ER	143	80.13	0.48	2.39
8H-3	ER	35	68.15	0.52	2.58	9H-4	ER	15	80.35	0.54	2.68
8H-3	ER	55	68.35	0.51	2.56	9H-4	ER	35	80.55	0.65	3.23
8H-3	ER	75	68.55	0.55	2.76	9H-4	ER	55	80.75	0.53	2.63
8H-3	ER	98	68.78	0.50	2.51	9H-4	ER	75	80.95	0.51	2.56
8H-3	ER	115	68.95	0.71	3.54	9H-4	ER	96	81.16	0.54	2.69
8H-3	ER	134	69.14	0.47	2.36	9H-4	ER	117	81.37	0.47	2.33
8H-4	ER	13	69.43	0.61	3.04	9H-5	ER	15	81.85	0.53	2.67
8H-4	ER	37	69.67	0.50	2.52	9H-5	ER	35	82.05	0.45	2.24
8H-4	ER	58	69.88	0.48	2.38	9H-5	ER	55	82.25	0.55	2.74
8H-4	ER	78	70.08	0.48	2.42	9H-5	ER	74	82.44	0.49	2.45
8H-4	ER	98	70.28	0.50	2.48	9H-6	ER	15	83.35	0.46	2.29
8H-4	ER	118	70.48	0.54	2.72	9H-6	ER	35	83.55	0.46	2.32
8H-4	ER	138	70.68	0.50	2.50	9H-6	ER	55	83.75	0.52	2.58
8H-5	ER	10	70.90	0.53	2.66	9H-6	ER	89	84.09	0.55	2.73
8H-5	ER	30	71.10	0.48	2.40	9H-6	ER	113	84.33	0.47	2.36
8H-5	ER	50	71.30	0.47	2.34	9H-6	ER	129	84.49	0.54	2.68
8H-5	ER	70	71.50	0.49	2.44	10H-1	ER	15	85.45	0.41	2.04
8H-5	ER	80	71.60	0.44	2.22	10H-1	ER	35	85.65	0.40	1.99
8H-6	ER	15	72.45	0.51	2.54	10H-1	ER	55	85.85	0.61	3.05
8H-6	ER	38	72.68	0.49	2.46	10H-1	ER	75	86.05	0.49	2.45
8H-6	ER	58	72.88	0.54	2.69	10H-1	ER	95	86.25	0.52	2.59
8H-6	ER	79	73.09	0.54	2.72	10H-1	ER	115	86.45	0.45	2.25
8H-6	ER	98	73.28	0.50	2.50	10H-1	ER	135	86.65	0.50	2.48
8H-6	ER	118	73.48	0.47	2.36	10H-2	ER	15	86.95	0.53	2.63

Table 16. Wenner array electrical resistivity and formation factor results for Hole NGHP-01-19A. (To view complete table, please refer to the **ASCII** files.)—Continued

Core, section	Sample	Top (cm)	Depth (mbsf)	Electrical resistivity (W×m)	Apparent formation factor	Core, section	Sample	Top (cm)	Depth (mbsf)	Electrical resistivity (W×m)	Apparent formation factor
NGHP-01-19A—Continued											
10H-2	ER	35	87.15	0.60	2.98	12X-4	ER	15	101.59	0.47	2.34
10H-2	ER	55	87.35	0.56	2.82	12X-4	ER	35	101.79	0.72	3.61
10H-2	ER	75	87.55	0.69	3.44	12X-4	ER	56	102.00	0.65	3.25
10H-2	ER	95	87.75	0.56	2.78	12X-4	ER	75	102.19	0.51	2.53
10H-2	ER	115	87.95	0.51	2.57	12X-4	ER	95	102.39	0.42	2.11
10H-2	ER	135	88.15	0.59	2.93	12X-4	ER	115	102.59	0.59	2.93
10H-3	ER	15	88.45	0.58	2.91	12X-4	ER	135	102.79	0.51	2.56
10H-3	ER	35	88.65	0.65	3.27	12X-5	ER	15	103.09	0.53	2.67
10H-3	ER	55	88.85	0.55	2.76	12X-5	ER	42	103.36	0.45	2.25
10H-3	ER	80	89.10	0.51	2.54	12X-5	ER	68	103.62	0.46	2.32
10H-3	ER	100	89.30	0.57	2.85	12X-5	ER	88	103.82	0.41	2.04
10H-3	ER	120	89.50	0.53	2.65	12X-5	ER	108	104.02	0.53	2.64
10H-3	ER	140	89.70	0.48	2.40	12X-5	ER	127	104.21	0.43	2.14
10H-4	ER	15	89.95	0.51	2.55	12X-6	ER	15	104.47	0.44	2.20
10H-4	ER	35	90.15	0.53	2.63	12X-6	ER	47	104.79	0.48	2.38
10H-4	ER	55	90.35	0.45	2.26	12X-6	ER	67	104.99	0.47	2.33
10H-4	ER	75	90.55	0.61	3.04	12X-6	ER	83	105.15	0.78	3.90
10H-5	ER	15	91.45	0.51	2.54	12X-7	ER	14	105.96	0.50	2.48
10H-5	ER	35	91.65	0.52	2.59	12X-7	ER	36	106.18	0.50	2.51
10H-5	ER	55	91.85	0.46	2.29	12X-7	ER	56	106.38	0.52	2.62
10H-5	ER	75	92.05	0.55	2.77	12X-7	ER	76	106.58	0.52	2.59
10H-5	ER	95	92.25	0.60	3.01	12X-7	ER	97	106.79	0.39	1.93
10H-5	ER	115	92.45	0.53	2.63	13X-1	ER	20	108.10	0.39	1.96
10H-5	ER	135	92.65	0.50	2.51	13X-1	ER	40	108.30	0.37	1.87
10H-6	ER	10	92.90	0.50	2.50	13X-1	ER	60	108.50	0.38	1.92
10H-6	ER	35	93.15	0.54	2.71	13X-1	ER	80	108.70	0.55	2.76
10H-6	ER	55	93.35	0.63	3.17	13X-1	ER	100	108.90	0.38	1.88
10H-6	ER	84	93.64	0.62	3.10	13X-1	ER	120	109.10	0.61	3.07
10H-6	ER	112	93.92	0.49	2.46	13X-1	ER	140	109.30	0.52	2.61
10H-6	ER	132	94.12	0.56	2.81	13X-2	ER	20	108.35	0.48	2.38
11H-1	ER	64	95.44	0.50	2.48	13X-2	ER	40	108.55	0.54	2.72
11H-1	ER	84	95.64	0.49	2.45	13X-2	ER	60	108.75	0.47	2.35
11H-1	ER	104	95.84	0.49	2.44	13X-2	ER	80	108.95	0.39	1.95
11H-1	ER	125	96.05	0.47	2.36	13X-2	ER	100	109.15	0.50	2.50
11H-2	ER	15	96.26	0.61	3.05	13X-2	ER	120	109.35	0.48	2.42
11H-2	ER	33	96.44	0.53	2.66	13X-4	ER	20	111.35	0.61	3.06
11H-3	ER	15	97.56	0.50	2.52	13X-4	ER	40	111.55	0.73	3.65
11H-3	ER	43	97.84	0.60	3.01	13X-4	ER	60	111.75	0.64	3.20
12X-1	ER	20	98.50	0.51	2.54	13X-4	ER	80	111.95	0.49	2.43
12X-1	ER	33	98.63	0.70	3.51	13X-4	ER	100	112.15	0.68	3.40
12X-1	ER	48	98.78	0.58	2.92	13X-4	ER	120	112.35	0.56	2.81
12X-2	ER	15	98.98	0.51	2.56	13X-4	ER	140	112.55	0.56	2.79
12X-2	ER	35	99.18	0.51	2.53	13X-5	ER	20	112.85	0.44	2.20
12X-2	ER	54	99.37	0.49	2.44	13X-5	ER	40	113.05	0.51	2.55
12X-2	ER	75	99.58	0.56	2.79	13X-5	ER	60	113.25	0.53	2.63
12X-2	ER	95	99.78	0.62	3.09	13X-6	ER	20	114.35	0.48	2.38
12X-2	ER	115	99.98	0.46	2.28	13X-6	ER	40	114.55	0.48	2.39
12X-2	ER	135	100.18	0.46	2.28	13X-6	ER	60	114.75	0.47	2.35
12X-3	ER	20	100.53	0.43	2.16	13X-6	ER	80	114.95	0.65	3.23
12X-3	ER	39	100.72	0.42	2.08	13X-6	ER	81	114.96	0.51	2.57
12X-3	ER	66	100.99	0.47	2.33	13X-6	ER	100	115.15	0.45	2.24
12X-3	ER	87	101.20	0.50	2.48	13X-6	ER	120	115.35	0.54	2.68
12X-3	ER	102	101.35	0.58	2.92	13X-7	ER	20	115.85	0.46	2.31

Table 16. Wenner array electrical resistivity and formation factor results for Hole NGHP-01-19A. (To view complete table, please refer to the **ASCII** files.)—Continued

Core, section	Sample	Top (cm)	Depth (mbsf)	Electrical resistivity (W×m)	Apparent formation factor	Core, section	Sample	Top (cm)	Depth (mbsf)	Electrical resistivity (W×m)	Apparent formation factor
NGHP-01-19A—Continued											
13X-7	ER	38	116.03	0.51	2.55	18X-6	ER	120	137.68	0.36	1.82
13X-7	ER	60	116.25	0.54	2.71	18X-6	ER	133	137.81	0.33	1.65
14X-1	ER	79	118.19	0.33	1.67	19X-1	ER	20	138.80	0.36	1.80
14X-1	ER	100	118.40	0.39	1.94	19X-1	ER	40	139.00	0.33	1.63
14X-1	ER	120	118.60	0.39	1.94	19X-1	ER	60	139.20	0.31	1.53
14X-1	ER	140	118.80	0.47	2.33	19X-1	ER	80	139.40	0.33	1.66
14X-2	ER	65	119.55	0.38	1.89	20X-1	ER	20	148.50	0.37	1.84
14X-2	ER	93	119.83	0.44	2.21	20X-1	ER	40	148.70	0.35	1.74
14X-2	ER	120	120.10	0.41	2.07	20X-1	ER	60	148.90	0.36	1.82
14X-3	ER	52	120.92	0.39	1.93	20X-1	ER	80	149.10	0.32	1.58
14X-3	ER	85	121.25	0.44	2.21	20X-1	ER	100	149.30	0.31	1.55
14X-4	ER	96	122.86	0.44	2.18	20X-2	ER	20	150.00	0.32	1.61
15P-1	ER	58	126.58	0.32	1.59	20X-2	ER	60	150.40	0.29	1.44
15P-1	ER	66	126.66	0.29	1.45	20X-2	ER	80	150.60	0.31	1.56
15P-1	ER	93	126.93	0.41	2.04	20X-2	ER	100	150.80	0.35	1.76
16P-1	ER	12	127.12	0.53	2.67	20X-2	ER	120	151.00	0.32	1.60
16P-1	ER	34	127.34	0.43	2.13	20X-3	ER	20	151.50	0.36	1.82
16P-1	ER	53	127.53	0.48	2.39	20X-3	ER	40	151.70	0.32	1.62
16P-1	ER	82	127.82	0.49	2.44	20X-3	ER	60	151.90	0.34	1.72
17P-1	ER	90	128.90	0.43	2.16	20X-4	ER	20	153.00	0.34	1.69
18X-1	ER	68	129.68	0.40	2.01	20X-4	ER	20	153.00	0.34	1.71
18X-1	ER	80	129.80	0.37	1.83	20X-4	ER	40	153.20	0.35	1.73
18X-1	ER	100	130.00	0.37	1.86	20X-4	ER	56	153.36	0.35	1.73
18X-1	ER	120	130.20	0.39	1.97	21X-1	ER	18	158.08	0.44	2.21
18X-1	ER	140	130.40	0.41	2.03	21X-1	ER	38	158.28	0.38	1.92
18X-2	ER	20	130.70	0.43	2.14	21X-1	ER	60	158.50	0.37	1.86
18X-2	ER	40	130.90	0.45	2.23	21X-2	ER	25	159.65	0.35	1.77
18X-2	ER	60	131.10	0.51	2.53	21X-2	ER	41	159.81	0.39	1.97
18X-2	ER	80	131.30	0.39	1.96	21X-2	ER	60	160.00	0.36	1.79
18X-2	ER	80	131.30	0.39	1.93	21X-2	ER	80	160.20	0.42	2.10
18X-2	ER	100	131.50	0.39	1.95	21X-2	ER	100	160.40	0.52	2.62
18X-2	ER	120	131.70	0.37	1.84	21X-2	ER	120	160.60	0.34	1.70
18X-2	ER	140	131.90	0.37	1.87	21X-3	ER	40	161.30	0.43	2.15
18X-3	ER	20	132.20	0.38	1.90	21X-3	ER	40	161.30	0.43	2.15
18X-3	ER	40	132.40	0.33	1.64	21X-3	ER	66	161.56	0.37	1.83
18X-3	ER	64	132.64	0.34	1.72	21X-3	ER	91	161.81	0.35	1.75
18X-4	ER	20	133.70	0.43	2.13	21X-3	ER	115	162.05	0.48	2.38
18X-4	ER	60	134.10	0.34	1.71	21X-3	ER	136	162.26	0.33	1.64
18X-4	ER	80	134.30	0.36	1.79	21X-4	ER	20	162.59	0.33	1.67
18X-4	ER	100	134.50	0.34	1.68	21X-4	ER	20	162.59	0.33	1.67
18X-4	ER	120	134.70	0.35	1.77	21X-4	ER	40	162.79	0.36	1.78
18X-4	ER	140	134.90	0.37	1.87	21X-4	ER	75	163.14	0.32	1.62
18X-5	ER	20	135.20	0.41	2.05	21X-4	ER	95	163.34	0.42	2.08
18X-5	ER	40	135.40	0.43	2.15	21X-4	ER	117	163.56	0.47	2.34
18X-5	ER	60	135.60	0.27	1.34	21X-4	ER	138	163.77	0.32	1.61
18X-5	ER	80	135.80	0.38	1.91	21X-5	ER	34	164.23	0.38	1.89
18X-5	ER	100	136.00	0.35	1.77	21X-5	ER	56	164.45	0.58	2.91
18X-5	ER	120	136.20	0.43	2.15	21X-5	ER	77	164.66	0.35	1.74
18X-5	ER	143	136.43	0.42	2.09	22X-1	ER	45	167.95	0.46	2.29
18X-6	ER	20	136.68	0.36	1.82	22X-1	ER	78	168.28	0.47	2.37
18X-6	ER	40	136.88	0.36	1.79	22X-1	ER	121	168.71	0.35	1.74
18X-6	ER	84	137.32	0.33	1.67	22X-2	ER	61	169.61	0.43	2.14
18X-6	ER	100	137.48	0.45	2.24	22X-2	ER	63	169.63	0.41	2.06

Table 16. Wenner array electrical resistivity and formation factor results for Hole NGHP-01-19A. (To view complete table, please refer to the **ASCII** files.)—Continued

Core, section	Sample	Top (cm)	Depth (mbsf)	Electrical resistivity (W×m)	Apparent formation factor	Core, section	Sample	Top (cm)	Depth (mbsf)	Electrical resistivity (W×m)	Apparent formation factor
NGHP-01-19A—Continued											
22X-2	ER	85	169.85	0.32	1.61	23X-6	ER	86	185.17	0.57	2.85
22X-2	ER	101	170.01	0.41	2.04	23X-7	ER	20	185.82	0.47	2.34
22X-2	ER	115	170.15	0.37	1.84	23X-7	ER	38	186.00	0.68	3.40
22X-3	ER	24	170.74	0.34	1.71	23X-7	ER	63	186.25	0.62	3.11
22X-3	ER	24	170.74	0.36	1.80	24X-1	ER	47	187.27	0.45	2.25
22X-3	ER	26	170.76	0.41	2.06	24X-1	ER	82	187.62	0.64	3.22
22X-3	ER	54	171.04	0.35	1.76	24X-1	ER	113	187.93	0.36	1.80
22X-3	ER	70	171.20	0.36	1.82	24X-1	ER	127	188.07	0.50	2.52
22X-4	ER	20	172.20	0.42	2.09	24X-2	ER	8	188.38	0.74	3.70
22X-4	ER	40	172.40	0.45	2.23	24X-2	ER	61	188.91	0.42	2.11
22X-4	ER	55	172.55	0.35	1.75	24X-2	ER	82	189.12	0.65	3.25
22X-4	ER	83	172.83	0.39	1.96	24X-2	ER	103	189.33	0.43	2.14
22X-4	ER	100	173.00	0.39	1.95	24X-2	ER	123	189.53	0.58	2.91
22X-4	ER	120	173.20	0.39	1.94	24X-3	ER	8	189.88	0.75	3.77
22X-4	ER	135	173.35	0.39	1.94	24X-3	ER	22	190.02	0.52	2.59
22X-5	ER	20	173.70	0.38	1.90	24X-3	ER	37	190.17	0.58	2.92
22X-5	ER	44	173.94	0.38	1.89	24X-3	ER	51	190.31	0.56	2.82
22X-5	ER	56	174.06	0.38	1.90	24X-3	ER	59	190.39	0.63	3.14
22X-6	ER	20	174.72	0.44	2.20	24X-3	ER	73	190.53	0.61	3.03
22X-6	ER	73	175.25	0.42	2.08	24X-4	ER	78	192.08	0.45	2.26
22X-6	ER	91	175.43	0.40	1.99	24X-4	ER	100	192.30	0.52	2.60
23X-1	ER	20	177.30	0.43	2.16	24X-4	ER	127	192.57	0.43	2.15
23X-1	ER	47	177.57	0.44	2.18	24X-5	ER	29	193.09	0.46	2.32
23X-1	ER	69	177.79	0.42	2.12	24X-5	ER	40	193.20	0.65	3.23
23X-1	ER	90	178.00	0.45	2.23	24X-5	ER	76	193.56	0.42	2.08
23X-1	ER	110	178.20	0.46	2.32	24X-5	ER	110	193.90	0.42	2.08
23X-1	ER	130	178.40	0.46	2.29	25P-1	ER	17	193.47	0.41	2.07
23X-2	ER	18	178.78	0.40	2.01	25P-1	ER	40	193.70	0.45	2.26
23X-2	ER	45	179.05	0.44	2.19	25P-1	ER	61	193.91	0.47	2.37
23X-2	ER	60	179.20	0.46	2.30	26P-1	ER	17	194.47	0.47	2.33
23X-2	ER	80	179.40	0.46	2.32	26P-1	ER	74	195.04	0.47	2.35
23X-2	ER	100	179.60	0.38	1.90	28X-1	ER	24	196.54	0.55	2.74
23X-2	ER	120	179.80	0.46	2.28	28X-2	ER	17	196.90	0.52	2.58
23X-2	ER	140	180.00	0.51	2.53	28X-2	ER	38	197.11	0.48	2.42
23X-3	ER	18	180.28	0.44	2.18	28X-2	ER	57	197.30	0.52	2.60
23X-3	ER	38	180.48	0.43	2.16	28X-2	ER	79	197.52	0.50	2.51
23X-3	ER	56	180.66	0.46	2.28	28X-3	ER	11	198.04	0.50	2.49
23X-3	ER	73	180.83	0.50	2.50	28X-3	ER	42	198.35	0.48	2.41
23X-4	ER	20	181.80	0.48	2.38	28X-3	ER	93	198.86	0.49	2.45
23X-4	ER	49	182.09	0.42	2.10	28X-3	ER	139	199.32	0.43	2.15
23X-4	ER	69	182.29	0.48	2.41	28X-4	ER	17	199.60	0.54	2.71
23X-4	ER	89	182.49	0.47	2.33	28X-4	ER	65	200.08	0.49	2.44
23X-4	ER	109	182.69	0.49	2.43	28X-5	ER	38	201.31	0.52	2.59
23X-4	ER	130	182.90	0.43	2.13	28X-5	ER	63	201.56	0.40	2.01
23X-5	ER	20	183.30	0.45	2.26	28X-6	ER	5	201.98	0.44	2.22
23X-5	ER	45	183.55	0.44	2.22	28X-6	ER	32	202.25	0.40	2.00
23X-5	ER	65	183.75	0.48	2.41	28X-7	ER	16	202.98	0.47	2.35
23X-5	ER	85	183.95	0.48	2.41	28X-7	ER	40	203.22	0.45	2.23
23X-5	ER	105	184.15	0.50	2.52	28X-7	ER	61	203.43	0.55	2.75
23X-6	ER	20	184.51	0.44	2.22	29X-1	ER	20	206.10	0.43	2.13
23X-6	ER	46	184.77	0.57	2.86	29X-2	ER	16	206.58	0.36	1.80
23X-6	ER	66	184.97	0.51	2.57	29X-2	ER	49	206.91	0.41	2.04

Table 16. Wenner array electrical resistivity and formation factor results for Hole NGHP-01-19A. (To view complete table, please refer to the **ASCII** files.)—Continued

Core, section	Sample	Top (cm)	Depth (mbsf)	Electrical resistivity (W×m)	Apparent formation factor	Core, section	Sample	Top (cm)	Depth (mbsf)	Electrical resistivity (W×m)	Apparent formation factor
NGHP-01-19A—Continued											
29X-2	ER	67	207.09	0.41	2.04	31X-5	ER	10	231.01	0.46	2.29
29X-2	ER	97	207.39	0.43	2.16	31X-5	ER	31	231.22	0.42	2.08
29X-3	ER	18	208.10	0.38	1.89	31X-5	ER	55	231.46	0.46	2.32
29X-3	ER	34	208.26	0.41	2.06	32X-1	ER	22	235.02	0.48	2.40
29X-3	ER	67	208.59	0.43	2.17	32X-2	ER	25	235.89	0.42	2.09
29X-3	ER	92	208.84	0.45	2.25	32X-2	ER	60	236.24	0.40	2.02
29X-4	ER	28	209.70	0.48	2.39	32X-2	ER	72	236.36	0.39	1.94
29X-4	ER	57	209.99	0.97	4.84	32X-2	ER	130	236.94	0.39	1.96
29X-4	ER	99	210.41	0.78	3.90	32X-3	ER	32	237.46	0.44	2.21
29X-4	ER	135	210.77	1.11	5.56	32X-3	ER	74	237.88	0.52	2.62
29X-5	ER	26	211.18	1.10	5.51	32X-3	ER	100	238.14	0.47	2.36
29X-5	ER	58	211.50	0.90	4.48	32X-3	ER	135	238.49	0.48	2.42
29X-5	ER	75	211.67	1.27	6.34	32X-4	ER	19	238.83	0.55	2.73
29X-5	ER	103	211.95	0.93	4.66	32X-4	ER	55	239.19	0.43	2.14
29X-6	ER	10	212.36	0.90	4.51	32X-4	ER	70	239.34	0.67	3.33
29X-6	ER	30	212.56	1.15	5.74	32X-5	ER	20	240.34	0.49	2.47
30X-2	ER	18	215.93	0.47	2.36	32X-5	ER	45	240.59	0.40	2.00
30X-2	ER	41	216.16	0.49	2.43	32X-5	ER	63	240.77	0.42	2.09
30X-2	ER	72	216.47	0.49	2.46	32X-5	ER	88	241.02	0.40	2.01
30X-2	ER	91	216.66	0.44	2.19	32X-5	ER	112	241.26	0.42	2.08
30X-3	ER	11	217.36	0.49	2.44	32X-6	ER	20	241.64	0.55	2.73
30X-3	ER	56	217.81	0.43	2.16	32X-6	ER	40	241.84	0.41	2.06
30X-3	ER	79	218.04	0.43	2.13	32X-6	ER	58	242.02	0.43	2.17
30X-3	ER	102	218.27	0.42	2.12	32X-7	ER	16	242.37	0.47	2.37
30X-5	ER	22	219.37	0.41	2.04	32X-7	ER	44	242.65	0.44	2.19
30X-5	ER	54	219.69	0.41	2.03	32X-7	ER	61	242.82	0.48	2.39
30X-5	ER	66	219.81	0.45	2.24	32X-7	ER	89	243.10	0.49	2.44
30X-5	ER	99	220.14	0.41	2.05	32X-7	ER	120	243.41	0.81	4.07
30X-5	ER	128	220.43	0.46	2.28	33X-2	ER	14	245.11	0.50	2.52
30X-6	ER	19	220.84	0.38	1.91	33X-2	ER	34	245.31	0.55	2.75
30X-6	ER	49	221.14	0.44	2.21	33X-2	ER	63	245.60	0.53	2.64
30X-6	ER	80	221.45	0.51	2.56	33X-2	ER	84	245.81	0.52	2.59
30X-7	ER	26	221.93	0.42	2.09	33X-2	ER	102	245.99	0.54	2.68
30X-8	ER	25	222.39	0.64	3.19	33X-2	ER	127	246.24	0.55	2.76
30X-8	ER	69	222.83	0.62	3.12	33X-3	ER	32	246.69	0.50	2.48
31X-1	ER	20	225.40	0.46	2.29	33X-3	ER	55	246.92	0.55	2.73
31X-1	ER	53	225.73	0.46	2.32	33X-3	ER	75	247.12	0.57	2.86
31X-1	ER	82	226.02	0.43	2.15	33X-3	ER	94	247.31	0.49	2.45
31X-1	ER	113	226.33	0.51	2.54	33X-3	ER	117	247.54	0.55	2.74
31X-2	ER	22	226.63	0.45	2.23	33X-3	ER	148	247.85	0.94	4.68
31X-2	ER	55	226.96	0.42	2.12	33X-4	ER	2	247.89	1.21	6.06
31X-2	ER	91	227.32	0.50	2.51	33X-4	ER	31	248.18	1.01	5.03
31X-3	ER	15	228.06	0.51	2.54	33X-4	ER	57	248.44	1.19	5.94
31X-3	ER	45	228.36	0.57	2.85	33X-4	ER	73	248.60	1.29	6.45
31X-3	ER	82	228.73	0.43	2.16	33X-5	ER	20	249.57	0.63	3.13
31X-3	ER	112	229.03	0.47	2.35	33X-5	ER	40	249.77	1.09	5.43
31X-3	ER	139	229.30	0.44	2.21	33X-5	ER	80	250.17	0.59	2.94
31X-4	ER	22	229.63	0.44	2.18	33X-5	ER	130	250.67	0.80	4.02
31X-4	ER	55	229.96	0.54	2.69	33X-6	ER	47	251.34	0.73	3.65
31X-4	ER	92	230.33	0.42	2.12	33X-6	ER	77	251.64	0.65	3.24
31X-4	ER	116	230.57	0.44	2.22	33X-6	ER	97	251.84	0.68	3.41
31X-4	ER	140	230.81	0.45	2.26	33X-6	ER	113	252.00	0.95	4.73

Table 16. Wenner array electrical resistivity and formation factor results for Hole NGHP-01-19A. (To view complete table, please refer to the **ASCII** files.)—Continued

Core, section	Sample	Top (cm)	Depth (mbsf)	Electrical resistivity (W×m)	Apparent formation factor	Core, section	Sample	Top (cm)	Depth (mbsf)	Electrical resistivity (W×m)	Apparent formation factor
NGHP-01-19A—Continued											
33X-7	ER	20	252.35	0.80	3.99	37X-3	ER	59	285.67	0.52	2.59
33X-7	ER	40	252.55	0.85	4.23	37X-4	ER	18	286.76	0.93	4.67
33X-7	ER	60	252.75	0.80	4.00	37X-4	ER	48	287.06	0.60	2.99
33X-7	ER	80	252.95	0.66	3.31	37X-4	ER	64	287.22	0.58	2.88
33X-7	ER	100	253.15	0.63	3.14	37X-4	ER	82	287.40	0.56	2.82
33X-7	ER	120	253.35	0.88	4.40	37X-4	ER	101	287.59	0.75	3.75
34X-1	ER	27	254.27	0.69	3.47	37X-4	ER	114	287.72	0.66	3.29
34X-2	ER	48	255.05	0.86	4.28	37X-5	ER	38	288.36	0.58	2.92
34X-2	ER	68	255.25	0.86	4.32	37X-5	ER	56	288.54	0.53	2.67
34X-3	ER	91	256.98	0.76	3.78	37X-5	ER	73	288.71	0.60	3.01
34X-3	ER	117	257.24	0.61	3.07	37X-5	ER	101	288.99	0.62	3.09
34X-4	ER	20	257.77	0.47	2.37	37X-5	ER	121	289.19	0.46	2.32
34X-4	ER	62	258.19	0.41	2.07	37X-6	ER	16	289.64	0.81	4.03
34X-5	ER	68	259.75	0.50	2.51	37X-6	ER	54	290.02	0.69	3.47
34X-5	ER	99	260.06	0.47	2.33	37X-7	ER	21	290.41	1.02	5.09
34X-6	ER	14	260.45	0.50	2.52	37X-7	ER	28	290.48	0.70	3.52
35X-1	ER	37	263.97	0.48	2.42	37X-7	ER	39	290.59	0.76	3.79
35X-1	ER	50	264.10	0.54	2.69	37X-7	ER	60	290.80	0.84	4.19
35X-1	ER	86	264.46	0.63	3.16	37X-7	ER	73	290.93	0.80	4.00
35X-2	ER	28	264.81	0.41	2.03	38X-1	ER	28	292.68	0.64	3.18
35X-2	ER	64	265.17	0.61	3.06	38X-1	ER	62	293.02	0.87	4.35
35X-2	ER	89	265.42	0.51	2.54	38X-1	ER	93	293.33	1.06	5.30
35X-2	ER	110	265.63	0.49	2.45	38X-1	ER	112	293.52	0.95	4.73
35X-3	ER	22	266.25	0.84	4.19	38X-1	ER	130	293.70	0.91	4.54
35X-3	ER	22	266.25	0.69	3.44	38X-2	ER	24	294.14	0.72	3.58
35X-3	ER	55	266.58	0.55	2.73	38X-2	ER	41	294.31	0.71	3.53
35X-3	ER	91	266.94	0.57	2.87	38X-2	ER	67	294.57	1.53	7.67
35X-3	ER	136	267.39	0.77	3.85	38X-2	ER	90	294.80	1.12	5.62
35X-4	ER	39	267.92	0.62	3.11	38X-2	ER	115	295.05	0.76	3.82
35X-5	ER	19	269.22	0.73	3.67	38X-2	ER	129	295.19	0.78	3.89
35X-5	ER	45	269.48	0.59	2.94	38X-3	ER	24	295.64	0.66	3.32
35X-5	ER	98	270.01	0.65	3.24	38X-3	ER	44	295.84	0.69	3.44
35X-5	ER	118	270.21	1.03	5.14	38X-3	ER	70	296.10	0.61	3.06
35X-5	ER	118	270.21	0.93	4.64	38X-3	ER	96	296.36	0.48	2.41
35X-6	ER	29	270.75	0.63	3.14	38X-3	ER	113	296.53	0.55	2.74
35X-6	ER	88	271.34	0.84	4.20	38X-3	ER	136	296.76	0.71	3.53
35X-6	ER	142	271.88	0.66	3.29	38X-4	ER	25	297.15	0.63	3.13
36X-1	ER	33	273.63	0.53	2.65	38X-4	ER	71	297.61	0.62	3.08
36X-1	ER	62	273.92	1.18	5.88	38X-5	ER	20	298.60	0.84	4.19
36X-3	ER	27	276.57	0.92	4.60	38X-5	ER	44	298.84	0.79	3.95
36X-3	ER	118	277.48	0.99	4.94	38X-5	ER	76	299.16	0.88	4.42
36X-7	ER	9	281.38	1.10	5.49	38X-5	ER	87	299.27	0.82	4.08
37X-1	ER	25	283.05	0.48	2.39	38X-5	ER	109	299.49	0.63	3.16
37X-2	ER	23	283.81	0.56	2.80	38X-5	ER	134	299.74	1.22	6.08
37X-2	ER	69	284.27	0.58	2.92	38X-6	ER	23	300.13	1.14	5.69
37X-2	ER	99	284.57	0.65	3.25	38X-6	ER	38	300.28	0.79	3.95
37X-2	ER	123	284.81	0.60	3.00	38X-6	ER	55	300.45	0.81	4.07
37X-3	ER	16	285.24	0.47	2.37						

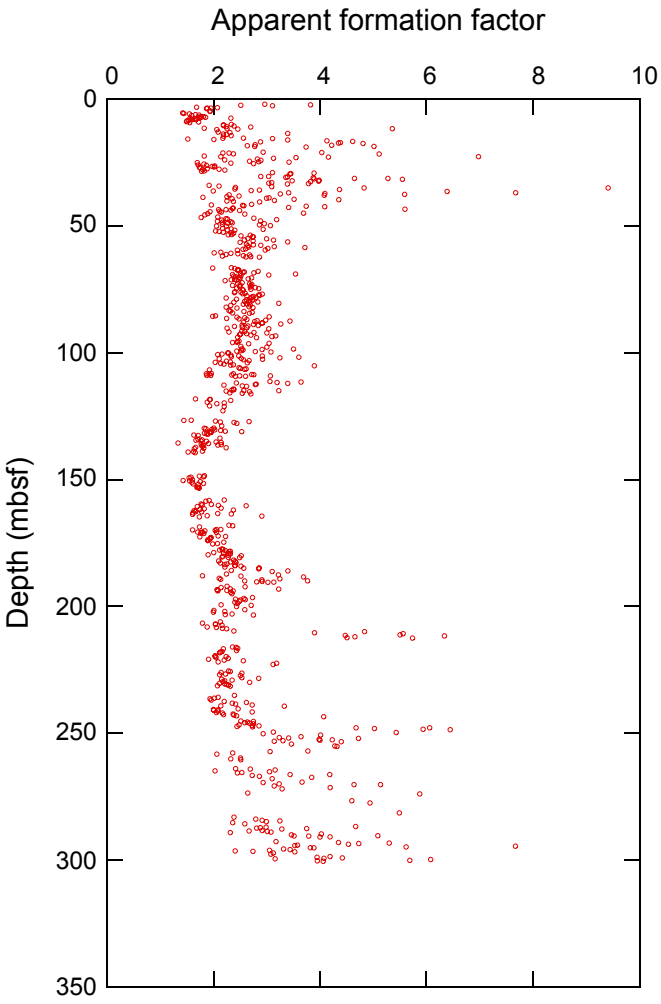


Figure 29. Apparent formation factor versus sub-bottom depth for Hole NGHP-01-19A.

Thermal Conductivity

Thermal conductivities vary between 0.841 and 1.088 and decrease slightly with subbottom depth (table 18 and fig. 26). Such values are well within the range of marine sediments , although they are all lower than values determined by Davis and others (1990) for sediment from Cascadia and the Nankai Trough.

Downhole Temperature Measurements

A number of different tools are available for determining downhole sediment temperature (see "Physical Properties" section of "Methods" chapter). At Site NGHP-01-19, seven attempts were made to measure *in situ* temperature, and six provided usable *in situ* temperature data, although two measurements showed several secondary frictional pulses. Thermal conductivity measurements at this site were less scattered than at most of the other sites, and a measured thermal conductivity of 0.90 W/(m×K) was used to extrapolate data to *in situ* temperature. The seafloor temperature intercept was determined to be 4.8±0.2 °C and the geothermal gradient was determined to be 53±2 °C/km (fig. 30 and table 19). The base of gas hydrate stability is predicted at ~220 mbsf assuming pure methane and porewater salinity of 35 ppt (Sloan, 1998), similar to the BSR depth of 205 mbsf (shipboard calculated seafloor temperature 4.8 °C, geothermal gradient 52 °C/km).

Pressure Coring

The main objectives of pressure coring during NGHP Expedition 01 were to quantify natural gas composition and concentration in sediments and to determine the nature and distribution of gas hydrate and free gas within the sediment matrix. Secondary objectives were to obtain measurements of physical properties on gas-hydrate-bearing sediments under *in situ* conditions, which can be used to help interpret regional seismic data, and to obtain samples under full pressure for shorebased studies. To achieve these objectives, we conducted depressurization experiments and captured resultant gas to calculate gas hydrate quantity, made nondestructive measurements (X-ray imaging, *P*-wave velocity, gamma density) at *in situ* pressures and during depressurization to examine gas hydrate habit within sediments, and archived gas-hydrate-bearing sediments on shore (at *in situ* pressures) for more comprehensive investigations.

Table 17. Contact *P*-wave velocity results determined on split cores sections from Hole NGHP-01-19A.

Core, section	Sample	Top (cm)	Depth (mbsf)	VP (m/s)	VP (km/s)
NGHP-01-19A					
1H-2	VP	104	2.54	1470.21	1.470
1H-3	VP	82	3.82	1481.24	1.481
1H-4	VP	20	4.70	1487.62	1.488
2H-1	VP	92	6.22	1481.24	1.481
2H-2	VP	125	8.05	1470.21	1.470
2H-3	VP	93	9.23	1463.98	1.464
2H-4	VP	126	11.06	1470.21	1.470
2H-5	VP	31	11.61	1473.35	1.473
2H-6	VP	89	13.69	1474.92	1.475
2H-7	VP	36	14.66	1484.43	1.484
3H-1	VP	53	15.33	1473.35	1.473
3H-2	VP	60	16.90	1490.83	1.491
3H-3	VP	63	18.43	1487.62	1.488
3H-4	VP	51	19.81	1497.29	1.497
3H-5	VP	70	21.50	1492.44	1.492
3H-6	VP	73	23.03	1479.66	1.480

Table 18. Thermal conductivity results for Hole NGHP-01-19A.

Core, section	Sample	Top (cm)	Depth (mbsf)	Thermal conductivity (W/[m×K])
NGHP-01-19A				
1H-3	TC	50	3.50	0.972
2H-3	TC	75	9.05	0.924
3H-3	TC	75	18.55	1.088
3H-7	TC	33	24.13	1.004
4H-1	TC	75	25.05	0.993
5H-3	TC	81	37.61	0.921
5H-7	TC	61	43.41	0.992
6H-1	TC	10	43.40	0.934
7H-3	TC	71	56.51	0.842
7H-7	TC	54	62.34	0.908
8H-2	TC	43	67.41	0.983
9H-3	TC	75	79.45	1.041
10H-3	TC	72	89.02	0.921
11H-3	TC	25	97.66	0.892
12X-3	TC	56	100.89	0.920
13X-3	TC	75	110.40	0.930
14X-3	TC	40	120.80	0.850
18X-3	TC	40	132.40	0.912
19X-1	TC	48	139.08	0.877
20X-4	TC	33	153.13	0.872
21X-1	TC	40	158.30	0.909
22X-3	TC	40	170.90	0.892
23X-3	TC	40	180.50	0.906
24X-3	TC	40	190.20	0.892
28X-2	TC	69	197.42	0.968
29X-3	TC	82	208.74	0.888
30X-3	TC	70	217.95	0.912
31X-3	TC	70	228.61	0.954
32X-3	TC	95	238.09	0.926
33X-3	TC	83	247.20	1.004
34X-3	TC	90	256.97	0.983
35X-3	TC	75	266.78	0.877
36X-3	TC	59	276.89	0.841
37X-3	TC	40	285.48	0.933
38X-3	TC	75	296.15	0.901

Site NGHP-01-19, located in the Mahanadi Basin, was located in a gap between a series of very bright reflectors that may indicate gas. The BSR at Site NGHP-01-19 was a weak reflector with an estimated depth of 205 mbsf. The top of these reflectors fall near the expected base of the GHSZ. There were no LWD data for this site. A specific objective at Site NGHP-01-19 was to determine whether there was gas hydrate or free gas near the depths of the nearby reflectors (200–300 mbsf).

Pressure Core Operations and Measurements

Pressure coring tools were deployed six times at Site NGHP-01-19 (table 20); two PCS cores, two FPC cores, and two HRC cores. Weather had been poor at the previous site (Site NGHP-01-18) producing heave in excess of 3 m, which was considered unsafe for pressure coring. At Site NGHP-01-19, the ship's heave had subsided to levels between 1 and 3 m, which was considered workable but not ideal. Both HRC deployments used the new "Viking" auger bit (see "Pressure Coring" in "Site NGHP-01-17"), which successfully recovered 0.87- and 1.07-m-long cores of high quality in "sticky clay" formations at nearly full pressures. Previously, the HRC had not been able to retrieve full cores in these types of formations. Figures 31 and 32 show the pressure and temperature history of the cores during deployment, coring, recovery, and chilling (in the ice shuck) of the pressure coring tools. Figures 33 and 34 show the measurements made on the three successful cores at full pressure and during depressurization. Figures 35 and 36 show the levels of gas and fluid released from the successful cores and the character of the pressure decrease during depressurization.

Core NGHP-01-19A-15P (126.0 mbsf) retrieved a full core (1.00 m) at pressure (table 20). The autoclave was placed in the MSCL-P for X-ray and gamma density measurements, which showed a core containing dense structures in the X-ray of the top half and uniform sediment in the lower half (fig. 34A). The core was depressurized, releasing 1.64 L of methane, which was below methane saturation at *in situ* temperature and pressure (table 21). The core showed slight pressure rebounds versus time but no pressure plateaus versus volume (figs. 35 and 36), consistent with a tight core with little to no methane hydrate. After depressurization, the autoclave was again measured in the MSCL-P, showing gas expansion in both the top (X-ray) and bottom half (gamma density) of the core, and a final X-ray image was collected when the outer barrel was removed (fig. 34A). One chlorinity measurement was made on this core (530 mM, 25–35 cm). Measured chlorinity was somewhat lower than the background chlorinity in cores taken above and below this depth (550–555 mM, see "Inorganic Geochemistry").

Core NGHP-01-19A-17E (128.0 mbsf) retrieved a core (0.87 m) at pressure (table 20). This was the first core taken in soft sediments ("sticky clays") using the new "Viking" auger bit. Core NGHP-01-19A-17E was transferred to the MSCL-P and X-ray images, gamma density data, and *P*-wave velocity measurements were collected (fig. 33A). The core appeared very uniform and was of high quality, as indicated by the details visible in the X-ray image (fine scale iron sulfide structures). There was no evidence for gas-hydrate structures within the core. When depressurized in the MSCL-P, Core NGHP-01-19A-17E released 3.16 L of methane, corresponding to 5.3 mL of gas hydrate or 0.5 percent methane hydrate as a percent of pore volume (table 21). The core showed slight pressure rebounds versus time and no pressure plateaus versus volume (figs. 35 and 36), consistent with a tight core but little to no methane hydrate. A final MSCL-P scan was collected at atmospheric pressure which showed an intact core with one large gas expansion void near the middle (fig. 34B). Two chlorinity measurements were made on this core (532 mM, 32–47 cm; 542 mM, 64–74 cm), which were somewhat lower than the background chlorinity in cores taken above and below this depth (550–555 mM).

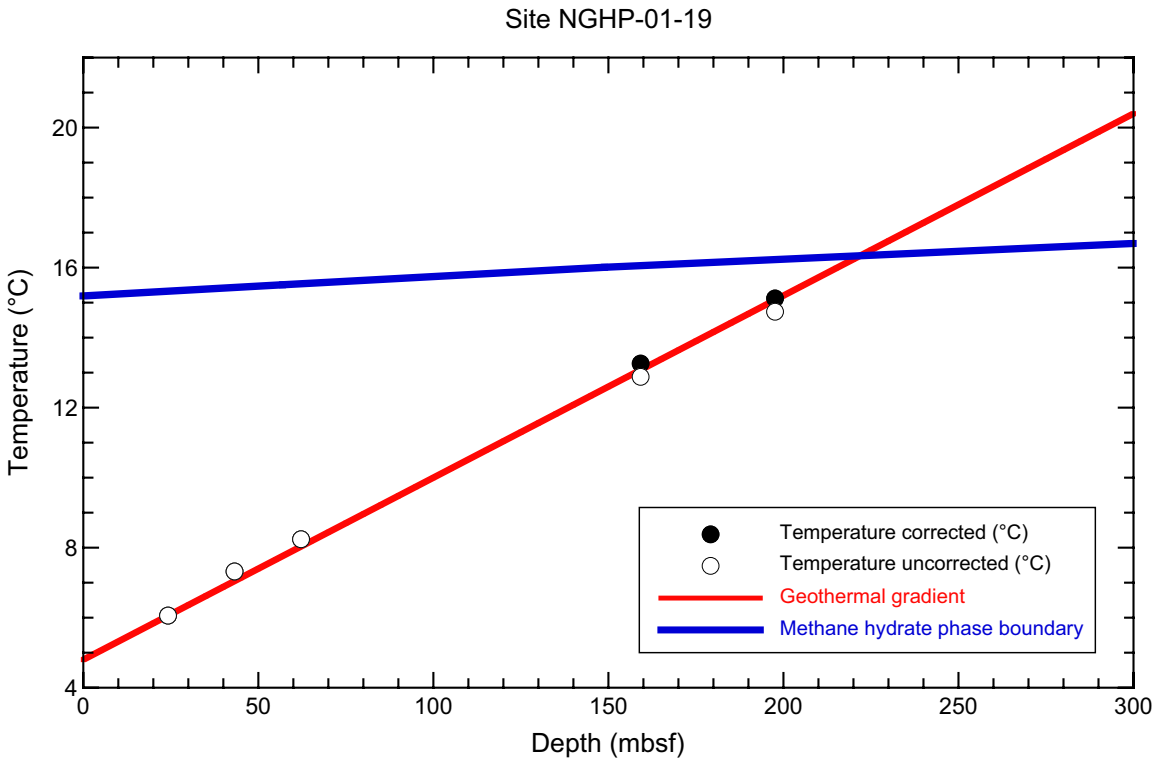


Figure 30. Geothermal gradient and estimated depth to the BSR from *in situ* temperature measurements for Hole NGHP-01-19A. [BSR, bottom-simulating reflector]

Table 19. *In situ* temperature estimates for Hole NGHP-01-19A.

Depth (mbsf)	Core	Assumed thermal conductivity (W/m×K)	Tool	Temperature (°C)	Ad-hoc calibration correction	Corrected temperature (°C)	Estimated uncertainty	Data quality
24.3	A03H	0.9	APCT-3	6.07	0	6.07	0.2	fair
43.3	A05H	0.9	APCT-3	7.33	0	7.33	0.1	good
62.3	A07H	0.9	APCT-3	8.24	0	8.24	0.1	good
118.8	A13X	0.9	DVTP	NA	0.50	NA	NA	run failed
159.3	A20X	0.9	DVTP	12.88	0.50	13.38	0.2	fair
197.7	A27X	0.9	DVTP	14.74	0.50	15.24	0.1	very good
301.4	A38X	0.9	DVTP	20.07	0.50	20.57	0.1	very good

Table 20. Summary of pressure-coring operations at Site NGHP-01-19.

Core ID	Top of core (mbsf)	Length recovered (cm)*	Length curated (cm)*	Pressure at core depth (bar)	Pressure recovered (bar)			Comments
					logged**		gauge***	
NGHP-01-19A								
15P	126.0	100	98	157	90		95	normal operation
16Y	127.0	--	96	157	0		--	overretracted; o-ring on flapper valve displaced
17E	128.0	87	96	157	118	@5 °C	130	used auger bit
25P	193.3	--	85	163	0		--	o-ring failed
26Y	194.3	--	87	163	0		--	overretracted
27E	195.3	107	110	164	126		130	used auger bit

Notes:

Water depth at Site NGHP-01-19 is 1434 m. P=PCS, Y=FPC, E=HRC.

*Length measured from X-ray and gamma density analysis, which may not match curated core length.

**Last pressure recorded before data logger disconnected from corer autoclave. Temperature 2–4 °C unless otherwise noted.

***Pressure measured when autoclave pressure transducer connected to external gauge. Pressure measured at 7 °C unless otherwise noted.

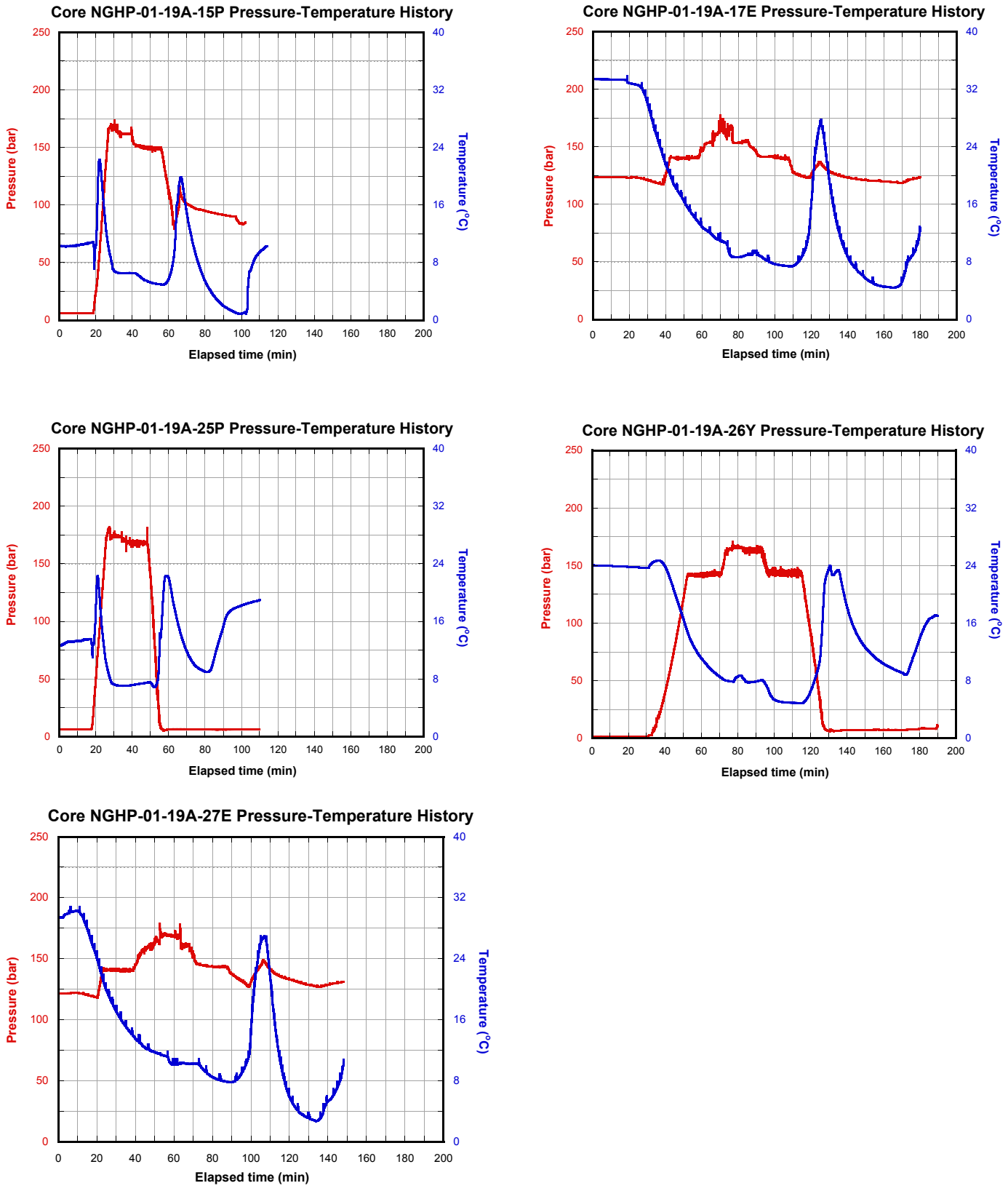


Figure 31. Temperature and pressure versus elapsed time for each pressure corer deployment as recorded by the corer's internal data logger. There are no data for Core NGHP-01-19A-16Y.

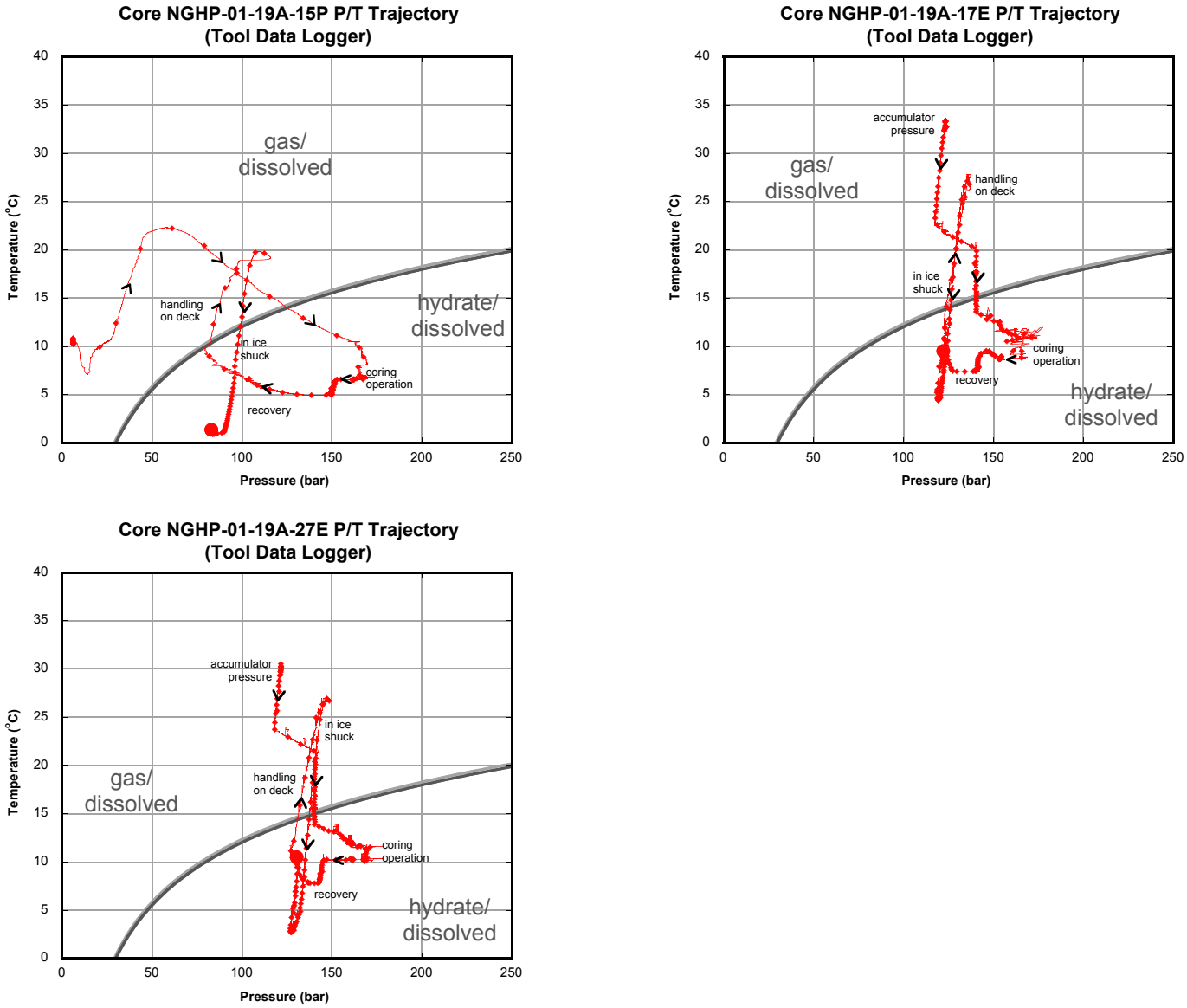


Figure 32. Temperature versus pressure for each successful pressure-corer deployment, showing trajectories relative to gas hydrate stability at 30 ppt and 35 ppt salinity, calculated from Xu (2002, 2004). Small dots are approximately every minute. Large dot is final temperature and pressure of autoclave prior to data logger removal. [ppt, parts per thousand]

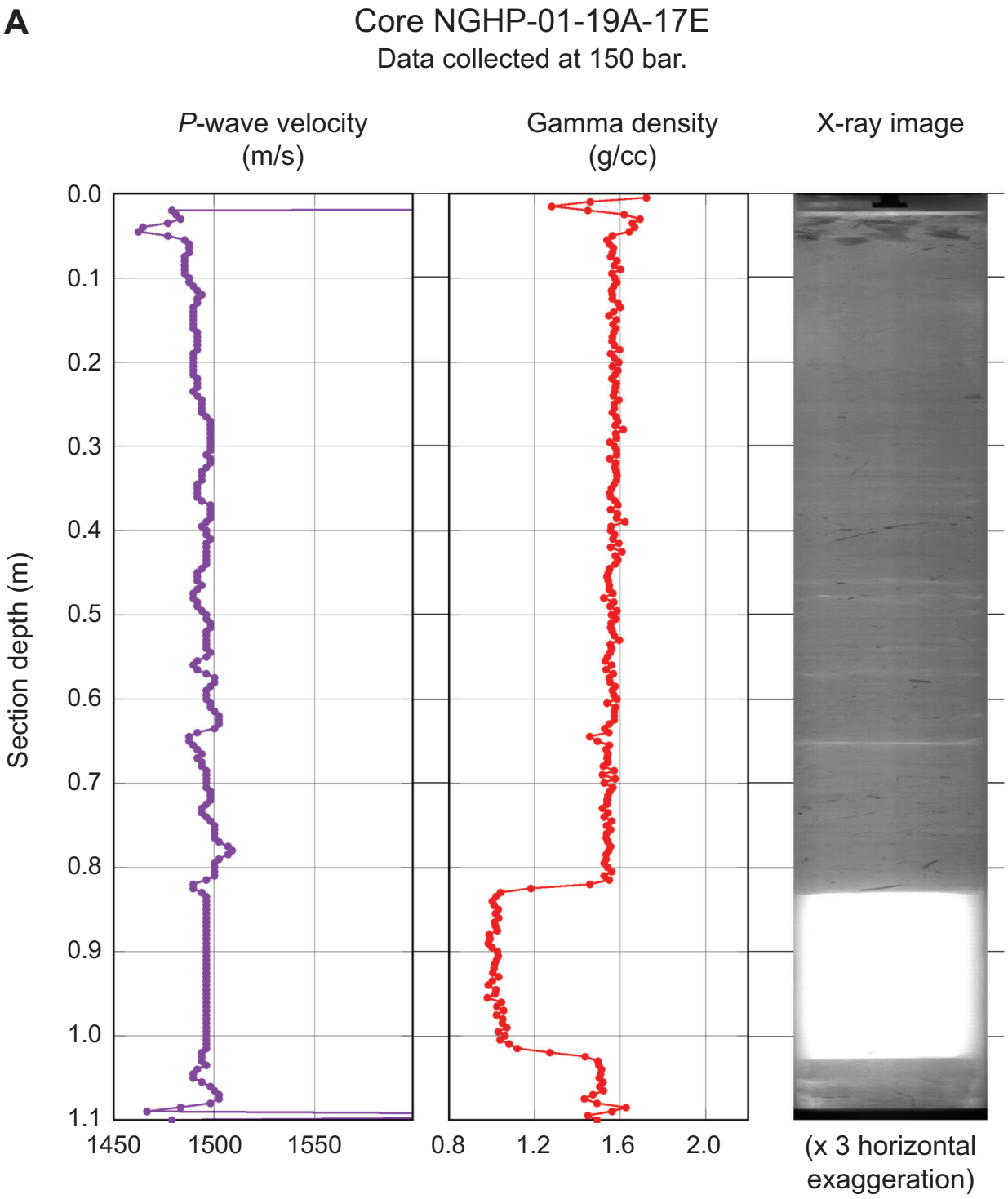


Figure 33. Data collected at near *in situ* pressure and at 7 °C for Cores NGHP-1-19A-17E and -27E, including X-ray images, gamma density, and *P*-wave velocity. X-ray images have been stretched 300 percent in the cross-core direction to show detail.

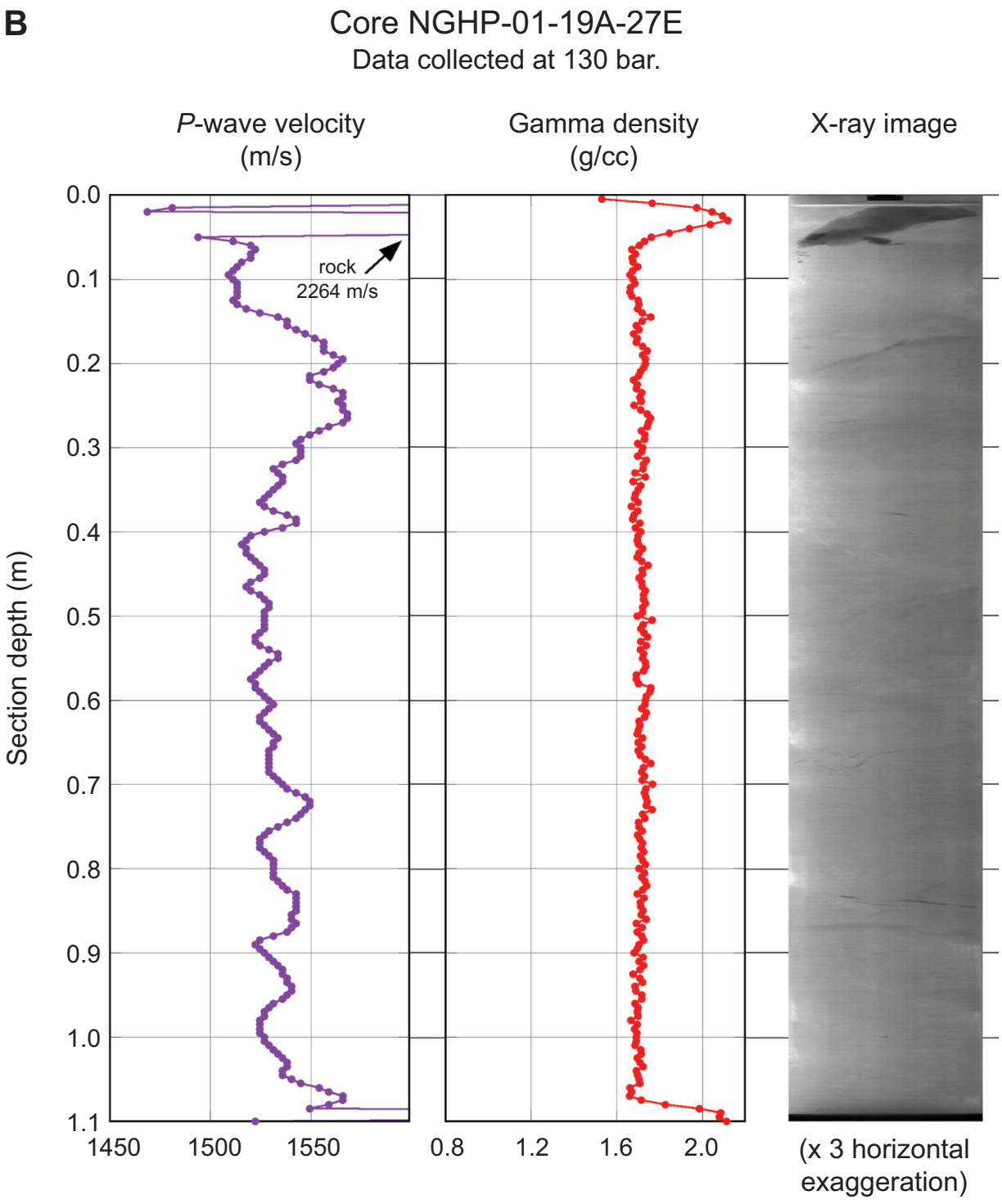


Figure 33. Data collected at near *in situ* pressure and at 7 °C for Cores NGHP-1-19A-17E and -27E, including X-ray images, gamma density, and *P*-wave velocity. X-ray images have been stretched 300 percent in the cross-core direction to show detail.—Continued

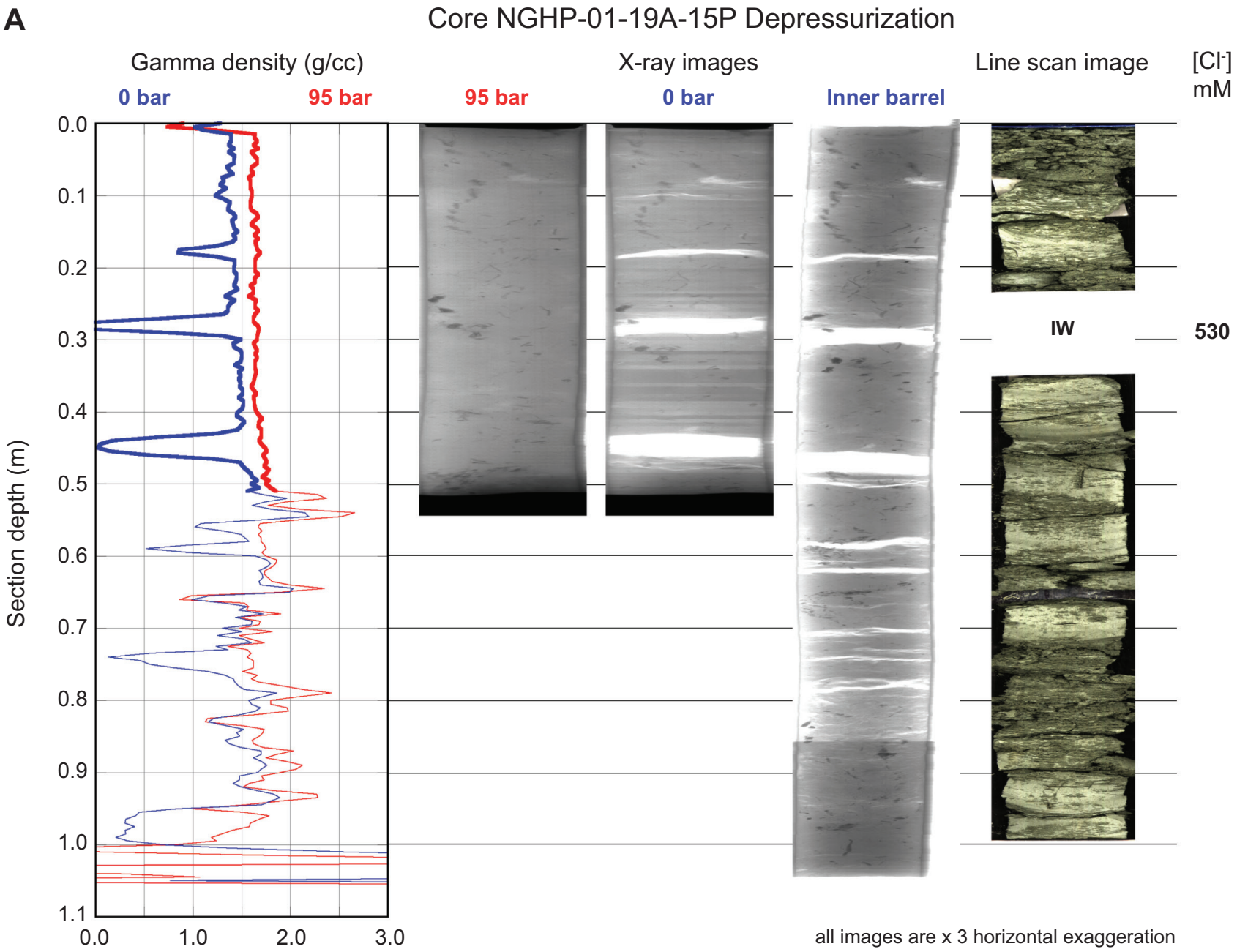


Figure 34. Summary of data taken from successful pressure cores before, during, and after depressurization, including gamma-density profiles collected before and after depressurization, X-ray images collected before and after depressurization, and line-scan images collected after depressurization.

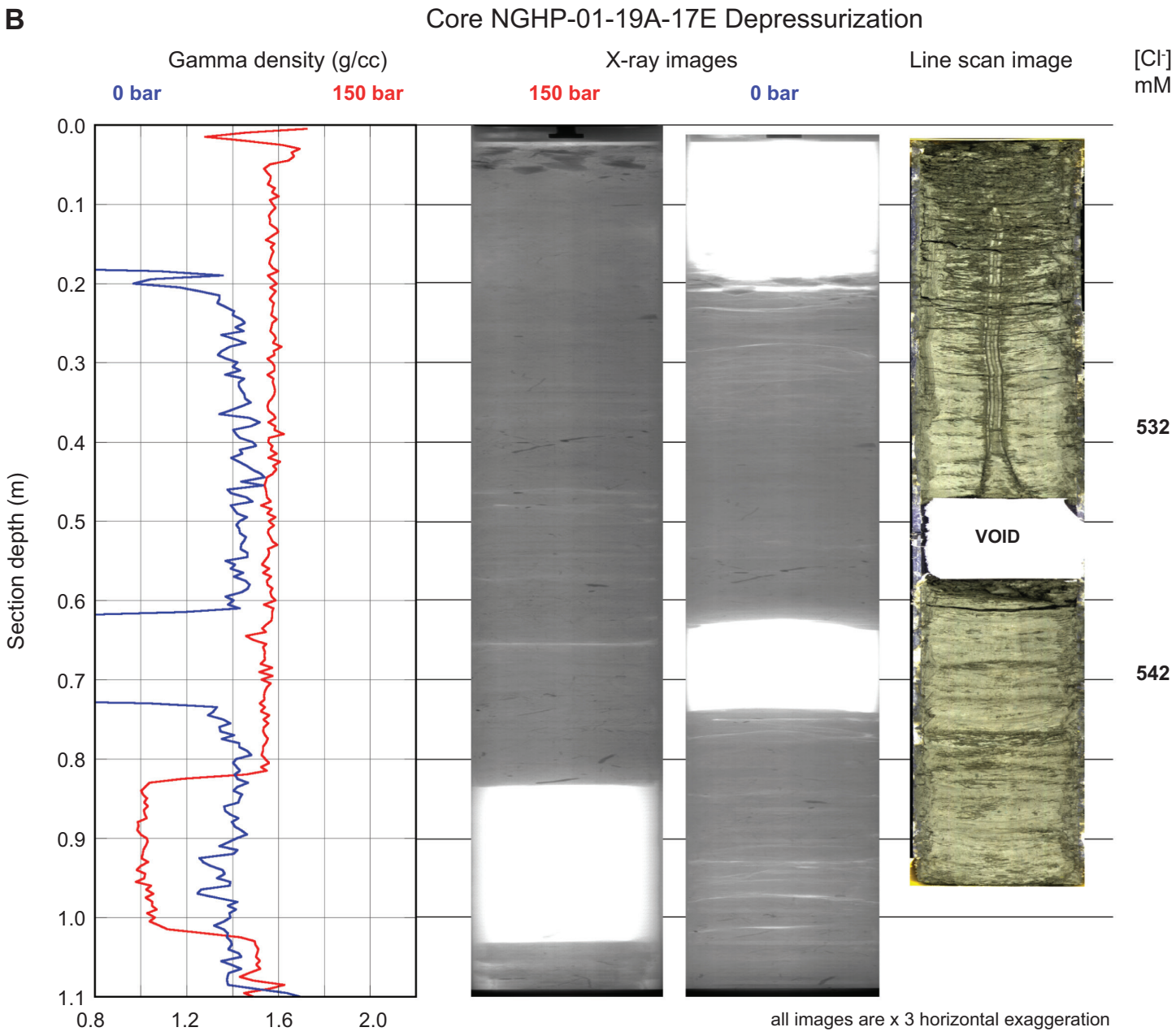


Figure 34. Summary of data taken from successful pressure cores before, during, and after depressurization, including gamma-density profiles collected before and after depressurization, X-ray images collected before and after depressurization, and line-scan images collected after depressurization.—Continued

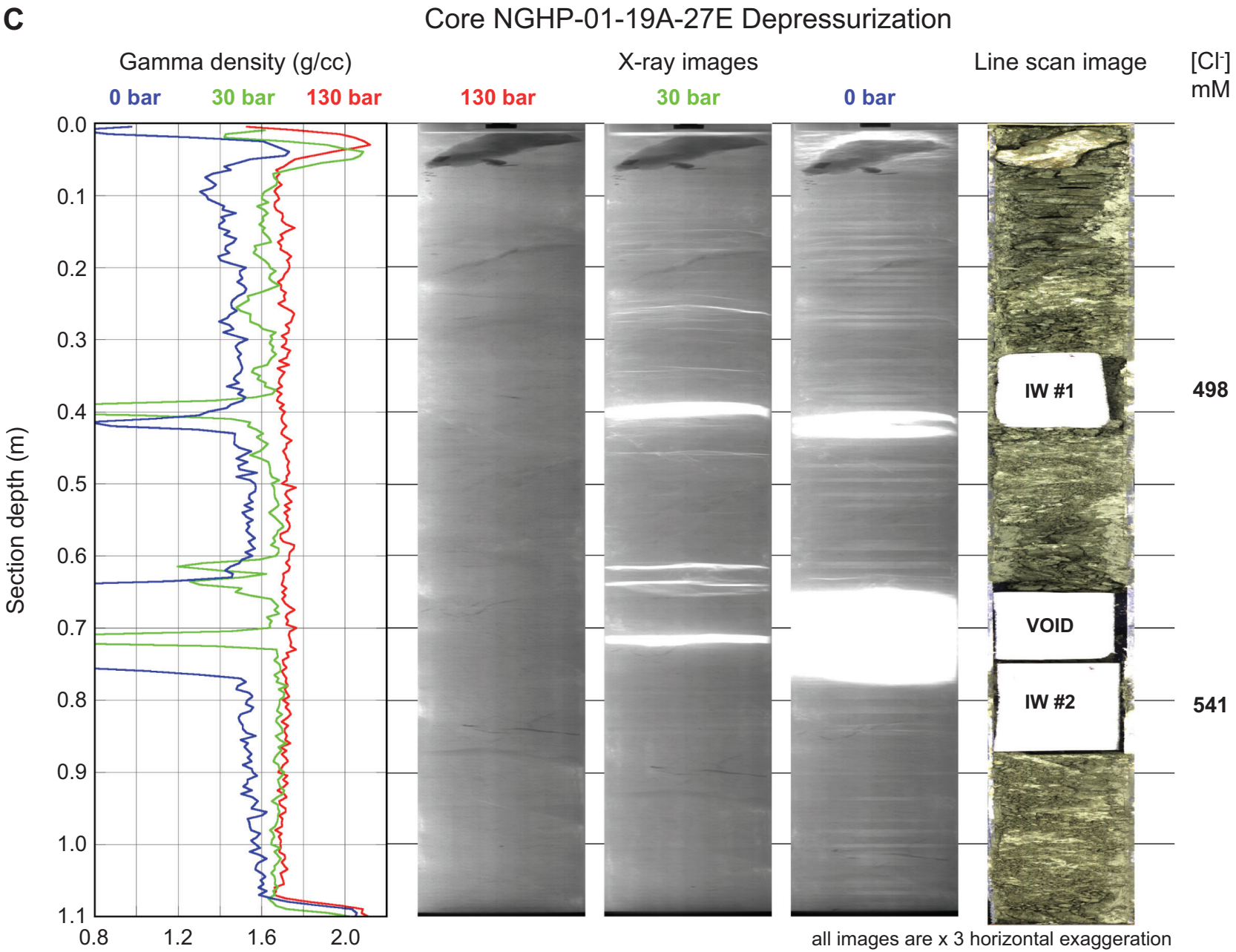


Figure 34. Summary of data taken from successful pressure cores before, during, and after depressurization, including gamma-density profiles collected before and after depressurization, X-ray images collected before and after depressurization, and line-scan images collected after depressurization.—Continued

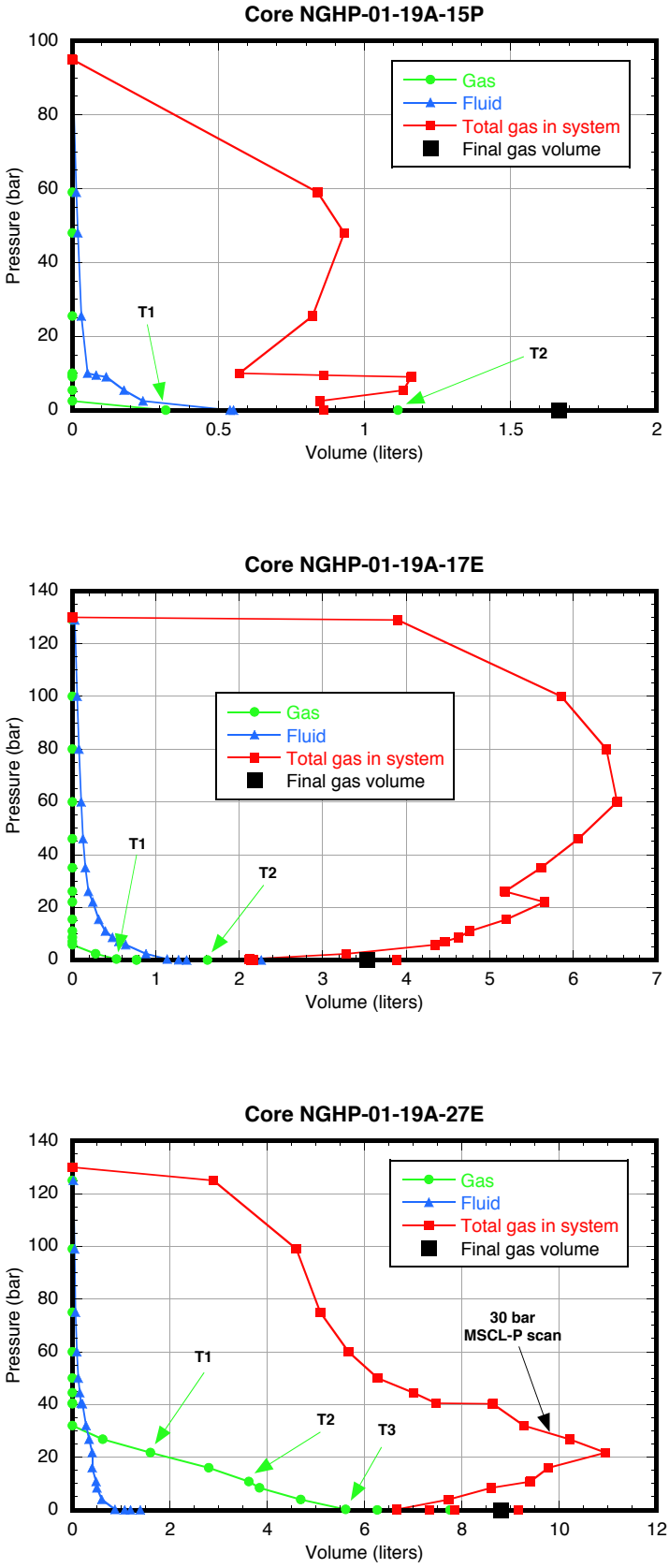


Figure 35. Pressure versus volume for successful pressure cores, also showing placement of gas samples (see "Organic Geochemistry"). [Green circles, gas volume; blue triangles, fluid volume; red squares, total gas volume in system (calculated as described in the "Methods" chapter); large black square, final calculated gas volume from cores; T (number), gas samples]

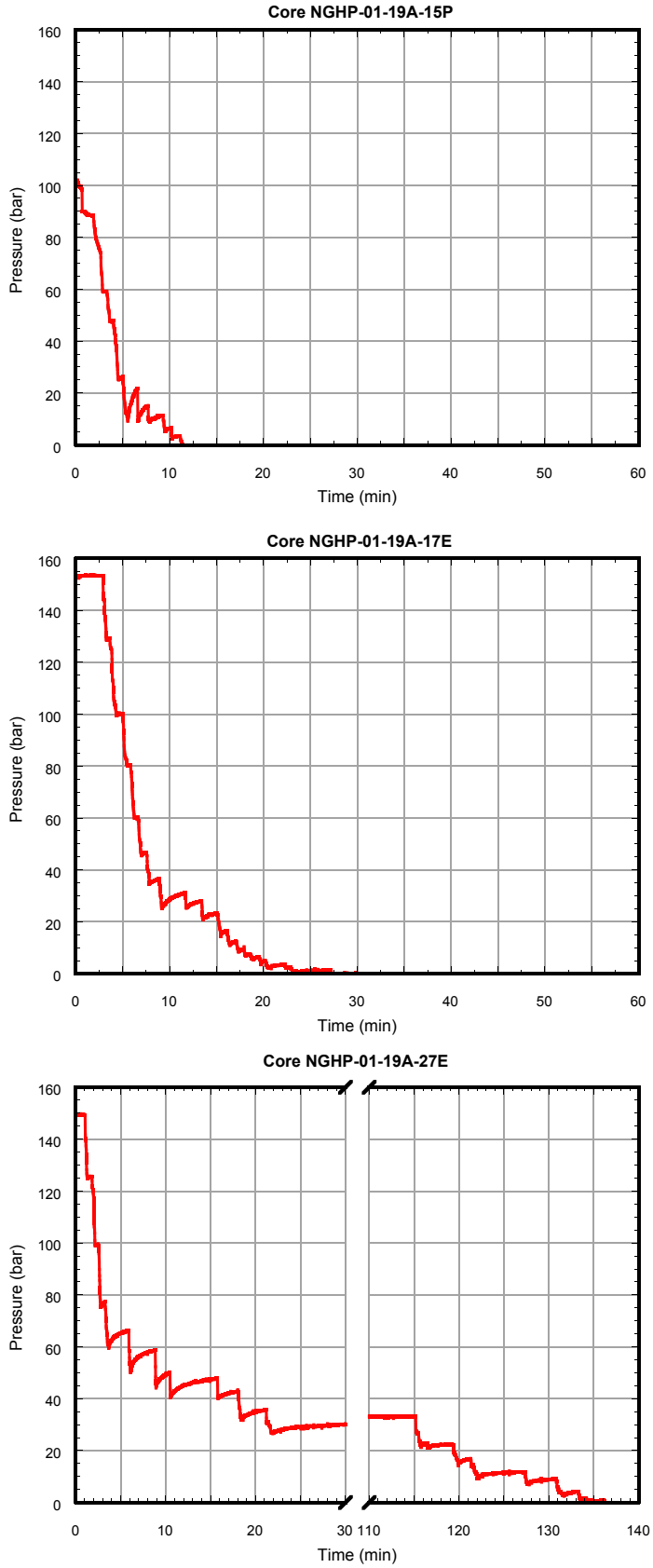


Figure 36. Pressure versus time for successful pressure cores. Note the multiple pressure rebounds during depressurization of Core NGHP-01-19A-27E.

Table 21. Methane-hydrate volume and concentration in pore space for successful pressure cores at Site NGHP-01-19. Values required for calculation of methane-hydrate concentration are also included.

Parameter	Units	NGHP-01-19A-15P	NGHP-01-19A-17E	NGHP-01-19A-27E
Core diameter	mm	43.2	51	51
Sediment length	cm	100	87	107
Sediment porosity	%	66	66	60
Pore volume	*liters*	*0.962*	*1.167*	*1.304*
Volume methane collected	*liters*	*1.64*	*3.16*	*8.78*
Methane concentration in pore fluids	mM	1.9	0.8	2.1
Total methane in core	*mmol*	*73.0*	*138.4*	*384.3*
In situ salinity	ppt	31.5	31.5	31.5
Methane saturation**	mM	84.7	85.4	118.8
Methane in pore fluids, assuming saturation	*mmol*	*81.5*	*99.6*	*155.0*
Excess methane	*mmol*	*–8.5*	*38.8*	*229.3*
Volume of methane hydrate	*ml*	*0.0*	*5.3*	*31.2*
*Methane hydrate, % of pore volume****	*%*	*0.0*	*0.5*	*2.4*

Notes:

Rows in *italics* are calculated parameters.

*Methane concentration (via headspace) was not measured on these cores. Zero concentration generates a conservative (minimum) estimate of gas hydate volume.

**Methane saturation calculated from Xu (2002, 2004) using a water depth of 1434 mbsl, the above salinities, and a thermal gradient of 52.3 °C/km and a seafloor intercept of 4.8 °C.

***Assuming all gas hydrate is evenly distributed throughout the pore space.

Core NGHP-01-19A-27E (195.3 mbsf) retrieved a full core (1.07 m) at pressure (table 20). This core was also taken with the new "Viking" auger bit, with the tool completing its coring stroke as observed by a pressure increase in the drill-pipe during coring. The core was transferred to the MSCL-P and X-ray images, gamma density data, and *P*-wave velocity measurements were collected (fig. 33B). Core NGHP-01-19A-27E showed a uniform density with some subtle structure in its velocity, but there was no compelling evidence for gas-hydrate-like structures. A large pebble-sized rock at the top of the core was clearly visible in all the records and probably fell from higher in the hole (see "Lithostratigraphy"). Core NGHP-01-19A-27E was depressurized in the MSCL-P, releasing 8.78 L of methane, corresponding to 31.2 mL of gas hydrate or 2.4 percent methane hydrate as a percent of pore volume (table 21). The core showed repeated pressure rebounds with time and an indication of a pressure plateau versus volume near 40 bar, consistent with small amounts of distributed gas hydrate as well as a very tightly sealed core (fig. 36). A final MSCL-P scan was collected at atmospheric pressure which showed an intact core with a few small voids (fig. 34C). Two chlorinity measurements were made on this core (498 mM, 33–43 cm; 541 mM, 76–88 cm). Both measurements were lower than the background chlorinity in nearby cores (550–560 mM); the upper sample contained 9.5 percent fresh water, equivalent to 11.8 percent gas hydrate as a percent of pore volume.

Gas-Hydrate Concentration, Nature, and Distribution from Pressure Coring

Three of the six pressure cores at Site NGHP-01-19 were recovered at sufficient pressures to accurately assess the total concentration of methane and to predict the amount of gas hydrate contained in the core. The calculated methane concentration for these cores is shown in figure 37 in relation to the phase boundaries for Structure I methane hydrate. Methane concentrations in pressure cores were near saturation in two cores in the middle of the gas-hydrate stability zone, with one core (Core NGHP-01-19A-15P) at 0.5 percent methane hydrate as a percent of pore space. One core near the BSR (Core NGHP-01-19A-27E) contained gas hydrate (2.4 percent of pore space). No cores were taken below the BSR or the base of gas hydrate stability, so the presence of free gas below the BSR or at depths equivalent to the nearby seismic reflectors could not be confirmed.

Pressure core gases and other gases (headspace, void gas) showed increased ethane and propane compared to all other sites drilled on NGHP Expedition 01 (see "Organic Geochemistry"). The ethane and propane content (up to 1,600 and 100 ppmV, respectively) in the gas-hydrate stability zone did not substantially affect the calculations used to estimate gas-hydrate stability. The propane content below the BSR increased to 250 ppm, but this concentration of propane was not enough to invoke Structure II mixed methane-propane hydrate. Core NGHP-01-19A-27E, collected near the BSR,

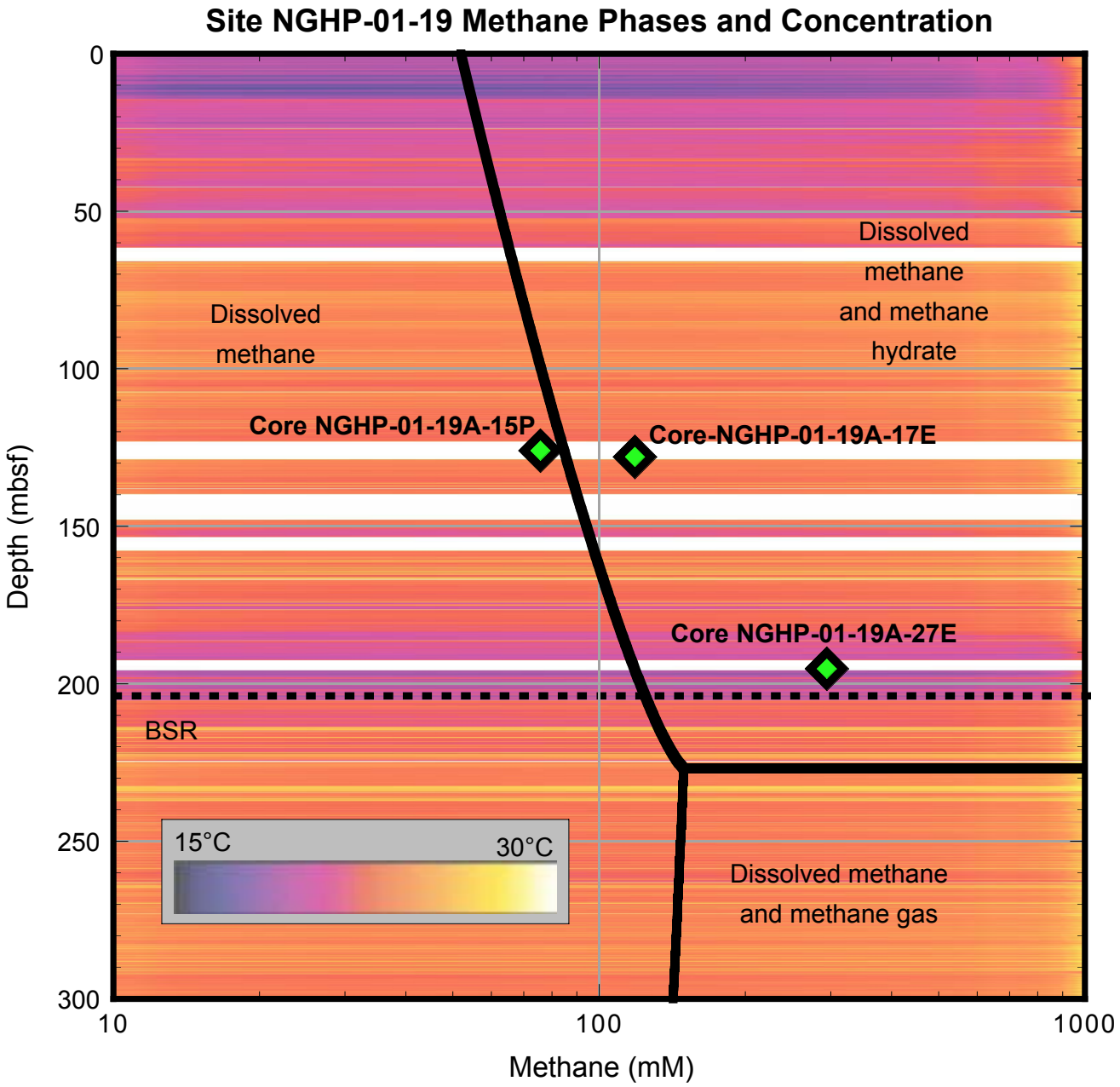


Figure 37. Methane phase diagram for Site NGHP-01-19, with total methane concentration measured from the three successful pressure cores at Site NGHP-01-19. The shipboard-calculated seafloor temperature (4.8 °C) and thermal gradient (52.3 °C/km) were taken from "Temperature Measurements" in "Physical Properties" (this chapter). The salinity was the average background salinity around the depths of the pressure cores (35 ppt; from table 4), and methane saturation was calculated according to Xu (2002, 2004). Background image is composite infrared thermal image (see "IR Imaging" in "Physical Properties"). [°C/km, degrees Celsius per kilometer; ppt, parts per thousand]

contained the highest concentration of ethane at Site NGHP-01-19A; concentrations were twice that of the average ethane content of void gases at Site NGHP-01-19A. Core NGHP-01-19A-27E contained 2.4 percent gas hydrate as a percent of pore volume, and ethane may have been preferentially concentrated within Structure I gas hydrate as seen at Hydrate Ridge on the Cascadia Margin (Tréhu and others, 2003). Enhanced concentrations of ethane were not seen in either of Cores NGHP-01-19A-15P or -17E, supporting the observation from depressurization experiments that these cores contained little or no gas hydrate.

The gas hydrate at Site NGHP-01-19 was believed to be concentrated in the zone of 177–204 mbsf (Cores NGHP-01-19A-23X to NGHP-01-19A-28X), based on IR imaging, chlorinity measurements, and methane mass balance from pressure cores. These cores were anomalously cold in the infrared images (see "IR Imaging" in "Physical Properties"). Porewater samples from these cores showed the only clustering of porewater freshening anomalies (except in the pressure cores higher in the sediment column; see below). Core NGHP-01-19A-27E (195.3 mbsf) was estimated to have 2.4 percent gas hydrate as a percent of pore volume. The gas composition of void gas from Core NGHP-01-19A-22X was enriched in ethane, similar to that collected in Core NGHP-01-19A-27E. However, the ethane content of voids in Cores NGHP-01-19A-23X and NGHP-01-19A-28X was not increased compared to the rest of the section (see "Organic Geochemistry").

The gas hydrate at Site NGHP-01-19A appeared to be finely distributed throughout the sections where it was found. Infrared anomalies were broad, with no defined shapes (see "Infrared Imaging" in "Physical Properties"). Core NGHP-01-19A-27E, which contained 2.4 percent methane hydrate, did not show any obvious gas-hydrate-related features in the X-ray image or density profile, and when the core was depressurized, gas was not apparently concentrated in any particular zone.

Though the gas hydrate in Core NGHP-01-19A-27E was finely distributed, it was not uniformly distributed. Of ten samples of porewater taken in the interval 177–204 mbsf (Cores NGHP-01-19A-23X to NGHP-01-19A-28X), five showed gas hydrate concentrations greater than 2 percent, based on porewater freshening, but two showed concentrations greater than 10 percent (background chlorinity assumed to be 558 mM). These data indicate that the gas hydrate was unevenly distributed at the sub-meter scale. The single pressure core taken in this gas hydrate bearing interval had a gas hydrate concentration of 2.4 percent of pore space, averaged over a meter of core. However, the variability of *P*-wave velocity in this core could not be correlated to density changes (fig. 33), suggesting that the gas-hydrate distribution could be quite variable on a centimeter scale.

Chlorinity measurements made on Cores NGHP-01-19A-15P and NGHP-01-19A-17E showed that the porewater in these cores was fresher than the surrounding cores, equivalent to 3–6 percent gas hydrate as a percent of pore space (see "Inorganic Geochemistry"). This does not agree with the methane-mass-balance calculations made using the released volumes of gas from these cores. While the PCS could possibly have been contaminated by fresh water during core extrusion, there was no simple explanation for the low chlorinities in the HRC core.

It is conceivable that there was a shift in the baseline chlorinity at this depth to slightly fresher values, but there is no geochemical or geological reason to suggest such an excursion.

Downhole Logging

Operations

Coring and temperature measurement operation at Hole NGHP-01-19A were completed at 0300 hr on 7 August. The initial plan was to log this hole with the triple combo, the FMS-sonic, and a VSP, but after failing to lower the triple combo tool string below 1,582 mbrf (148 mbsf), it was decided to drill a new hole to achieve the logging objectives of Site NGHP-01-19.

Hole NGHP-01-19B was drilled to the TD of 1,713 mbrf (280 mbsf) at 0000 hr on 8 August. The hole was then conditioned for logging: it was swept with 40 bbl of Sepiolite mud, displaced with 100 bbls of 10.5 ppg barite, and the pipe was pulled to logging depth of 1,495 mbrf (62 mbsf). At 0215, the wireline was spooled and the logging sheaves brought to prepare the rig floor for logging.

Assembly of the triple combo started at 0325 hr, was complete at 0350 hr and the tool was run into the hole (RIH) at 0410 hr. The bottom of the tool came out of the pipe (1,495 mbrf) without problem at 0510 hr, but could not pass 1,510 mbrf, with about 15 m still inside. After raising the pipe and circulating drilling mud, the tool string was in open hole at 0535 hr. It encountered some sticking at 1,565, 1,585, 1,607, 1,620 and 1,630 mbrf, but none of these required more than a few minutes to clear. The log up started at 0600 hr from the TD of 1,716 mbrf, and the HLDS caliper was closed at 0642 hr with the bottom of the tool at 1,527 mbrf before the cable head reached the bit at 1,489 mbrf. The first attempts to enter the pipe failed, and it proved necessary to rotate the drill string several times and to circulate at high pump rates to get the top of the tool inside the pipe. This occurred at 0705 hr.

The pass was concluded at 0723 hr, after the gamma ray log identified the seafloor at 1,436 mbrf. The triple combo was then brought back to the surface at 0820 hr and was rigged down at 0900 hr.

Because of the daylight requirements to operate the air gun for the VSP, the following run was the VSI. Considering the several tight spots that were encountered while lowering the triple combo, and the bad hole conditions shown by the caliper above 1,600 mbrf (167 mbsf), it was assumed that the light weight of the VSI would make it unlikely to pass some of these ledges, and we decided to lower the pipe to 1,610 mbrf to be able to record the VSP across the BSR. After adding four stands to the drill string, the VSI was rigged up at 1005 hr and RIH at 1035 hr. At 1155 hr, the tool could not pass below 1,594 mbrf (the tool was still inside the pipe about 16 m above the bit) and it was necessary to pump several times to get it to the bottom of the pipe and then in open hole at 1235 hr.

At 1245 hr, we could not go deeper than 1,697 mbrf, or ~17 m above TD, and at 1250 hr we decided to start the VSP from here, which was about 60 m below the estimated depth of the BSR (~1,635 mbrf, see "Background and Objectives"). The tool was anchored for the first station at 1,696 mbrf, and the first shot was fired at 1253 hr. Stations were attempted every 10 m, and at intermediate depths in case of failure, with the goal of acquiring about ten stations. The last shot was fired at 1440 hr, with the VSI at 1,631 mbrf after a total of 203 shots were fired. Out of the ten stations attempted, six provided adequate travel times after stacking more than five traces. The VSI was back inside the pipe without trouble at 1455 hr, on the rig floor at 1550 hr and checked and rigged down at 1620 hr.

The wireline and the logging sheaves were then moved aside again to pull the pipe back to its original logging depth of 1,495 mbrf. Rig up of the FMS-sonic started at 1710 hr, and the tool was RIH at 1800 hr. It passed the bit without problem at 1850 hr and reached the maximum depth of 1,701 mbrf after encountering only one significant obstacle a 1,605 mbrf, where the bottom of the pipe had been seating during most of the VSP. The log up started at 1930 hr with the following DSI modes: low frequency monopole, low frequency upper dipole, standard frequency lower dipole, and stoneley. At 2006 hr, with the bottom of the tool at 1,540 mbrf, the FMS calipers were closed and the WHC turned off. At 2010 hr the top of the tool was inside the pipe and the pass was stopped at 1,505 mbrf at 2017 hr, just short of bringing the FMS inside the pipe. The tool was sent back down for a second pass, which started at 2039 hr from the same maximum depth of 1,701 mbrf. The DSI modes were medium frequency monopole and cross dipole. At 2055 hr, the pipe was raised to 1,485 mbrf. At 2117 hr, the FMS calipers were closed at 1,529 mbrf, and the pass was complete at 2130 hr when the full tool string was inside the pipe. It was back on the floor at 2210 hr, checked, cleaned and rigged down at 2300 hr, and the rig floor was ready to operate at 2345 hr.

Logging Data Quality

Figure 38 shows the main logs recorded during the triple combo run in Hole NGHP-01-19B. The hole size calculated from the HLDS caliper (see "Downhole Logging" in the "Methods" chapter) shows that the hole was extremely irregular above ~170 mbsf. In addition to various washouts, a series of ledges apparent in this figure made it difficult to reach the bottom of the hole during most runs. However, the borehole wall was never beyond the reach of the caliper arm and the quality of most logging data was likely only moderately affected. Below 170 mbsf, except for one ledge at ~202 mbsf, the hole size remains very close to the bit size (11 7/16 in or 29 cm), indicating that the data should be of good quality near and below the predicted depth of ~190 mbsf for the BSR (see "Background and Objectives").

Over most of the interval logged, there is an almost constant offset between the spherically focused unaveraged resistivity log (SFLU) and the other resistivity curves, which stops abruptly at ~72 mbsf. While the SFLU is generally more sensitive to hole irregularities and invasion of the formation by the drilling fluids, these could not account for the almost uniform nature of this offset and its abrupt interruption, which suggest a tool malfunction and will require further investigation.

Despite the irregular hole size, the good agreement over most of the logged interval between the density log and the measurements made on core samples from Hole NGHP-01-19A shows that the logs were adversely affected in only a few short intervals, in particular between 80 and 90 mbsf and between 105 and 112 mbsf.

The density porosity was calculated from the density log and from the grain density measured on core samples from Hole NGHP-01-19A, by using at each depth the grain density from the closest sample. Hence the good agreement between the density-porosity log and the porosity measurements from core samples is a direct consequence of the good agreement in the density data. The neutron porosity is consistently higher than the other porosity estimates because of the influence of mineral-bound water in these clay-dominated sediments.

The hole size in figure 39 derived from the FMS calipers shows that by the time of the FMS-sonic run, the hole conditions remained stable to the time of the FMS-sonic run, but that most of the ledges were still present or slightly larger than during the first run. Only one new ledge had developed (at ~160 mbsf) where the bit had been located during the VSP. The strong amplitude and coherence of the monopole waveforms show that the P-wave velocity provides a reliable measurement of the velocity of the formation, and only minimal additional reprocessing was necessary. Weak amplitude and low coherence over most of the hole shows that dipole waveforms were seriously affected by the hole conditions and required additional reprocessing to derive reliable shear velocity values.

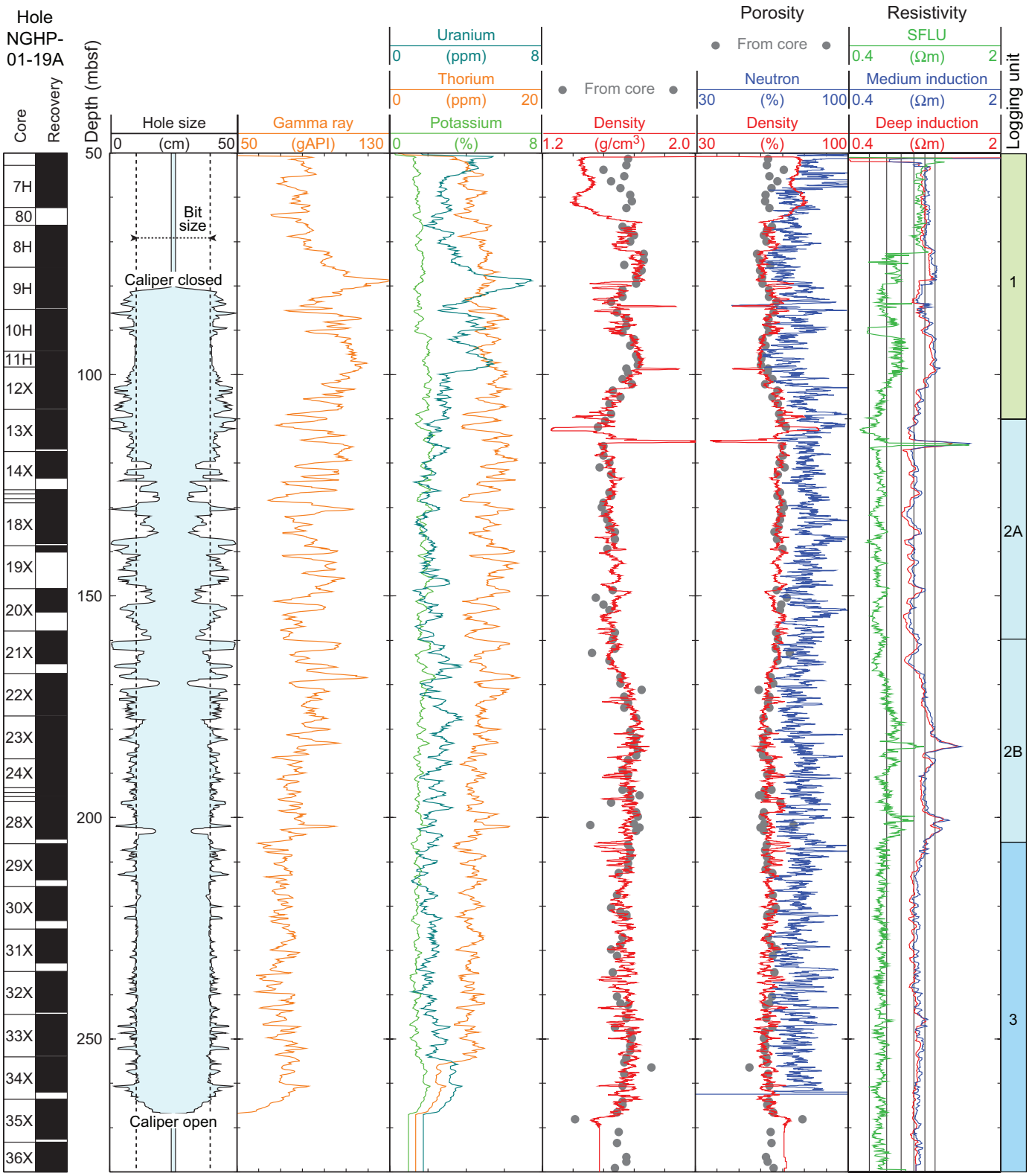


Figure 38. Summary of the wireline logs recorded during the two triple combo runs in Hole NGHP-01-19B. The hole size is calculated from the Hostile Litho Density Sonde (HLDS) caliper. The density and porosity measurements made on core samples from Hole NGHP-01-19A are shown for comparison. [SFLU, Spherically focused unaveraged resistivity]

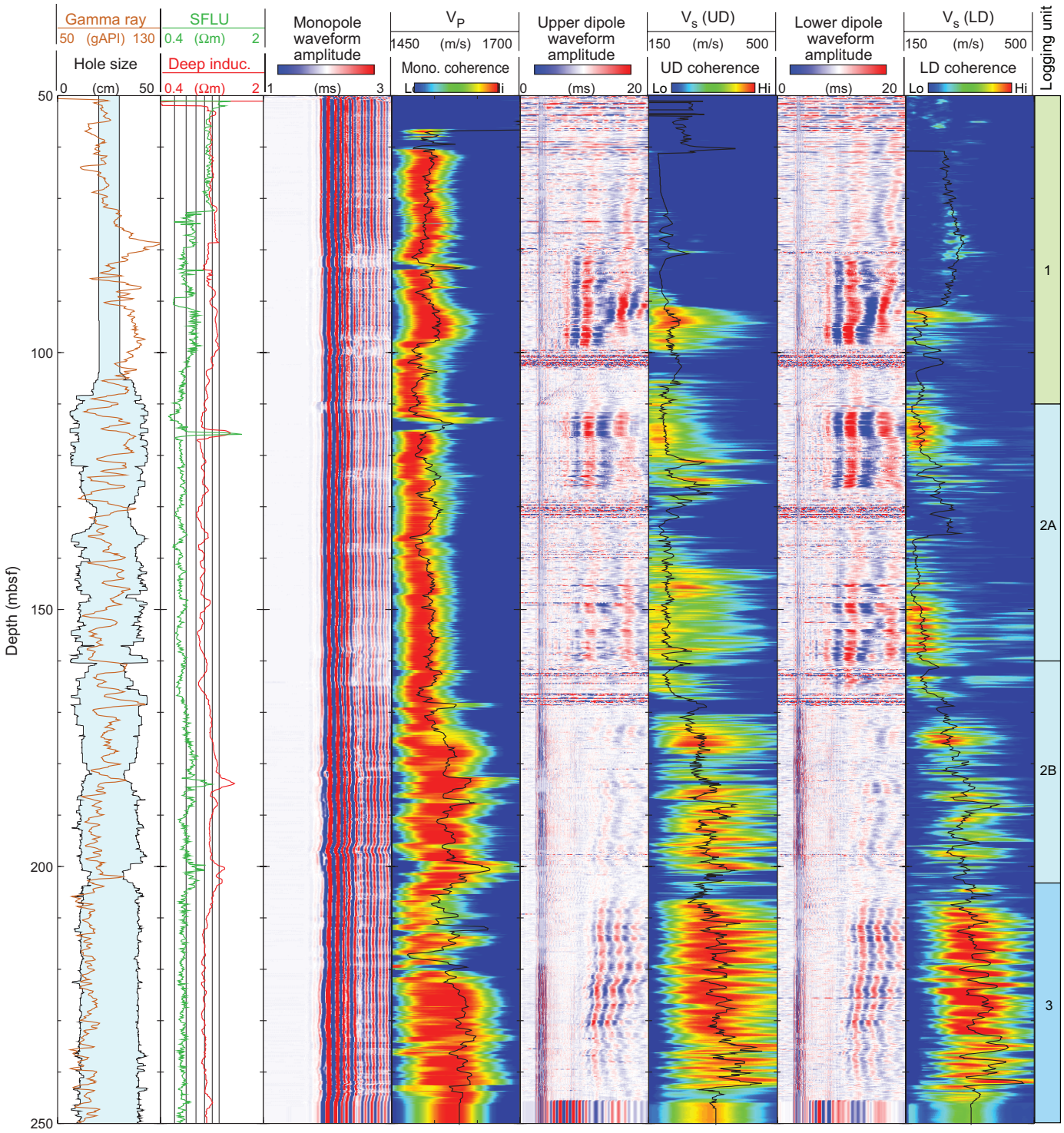


Figure 39. Sonic waveform amplitude and coherence data and velocity logs measured by the DSI in Hole NGHP-01-19B. The hole size, calculated from the FMS calipers, and the gamma ray and resistivity logs, are shown for quality control and correlation. [DSI, dipole sonic log; V_P, *P*-wave velocity; V_S, *S*-wave velocity; LD, Lower dipole; UD, Upper dipole; FMS, formation micro scanner]

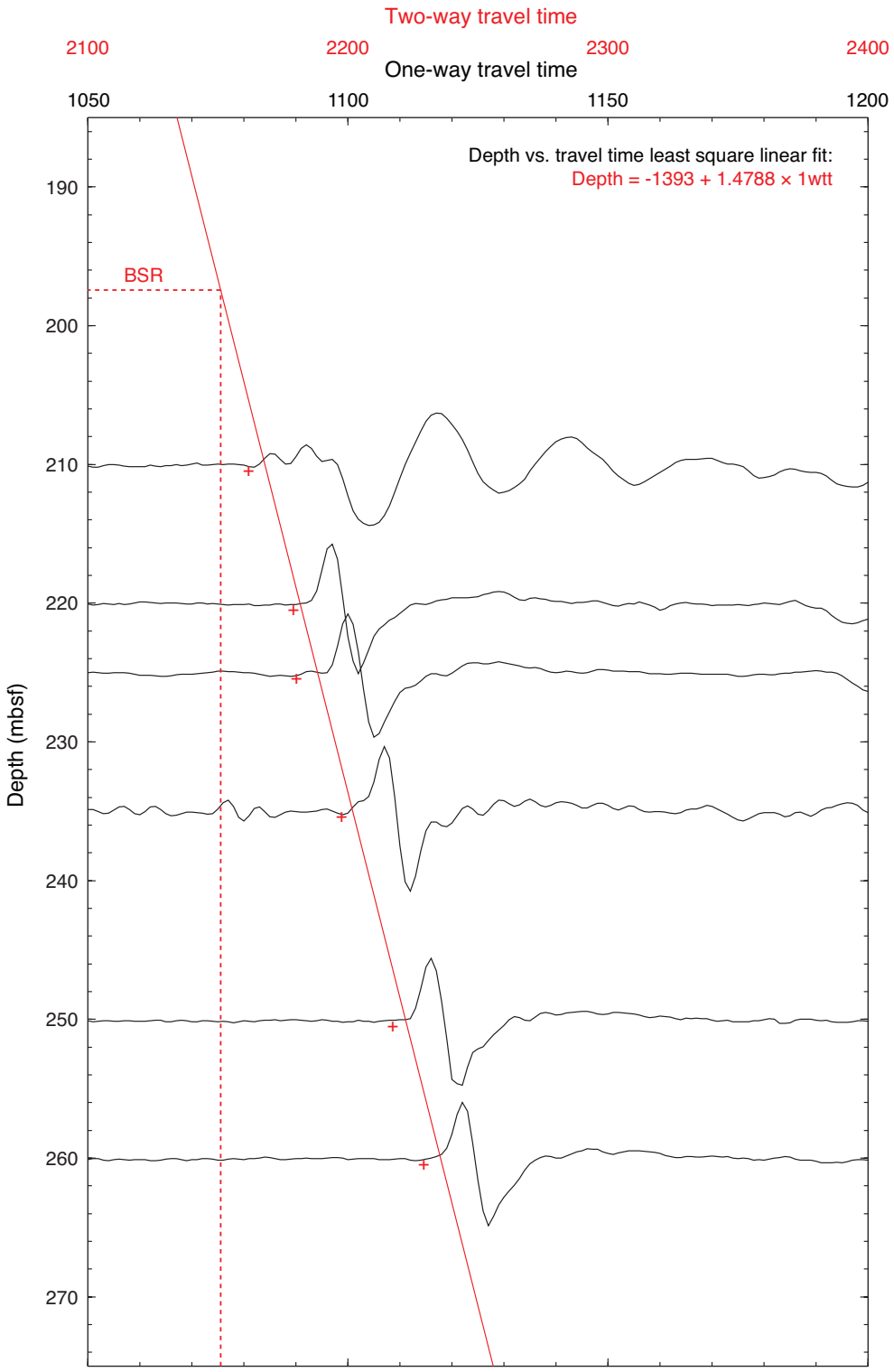


Figure 40. Preliminary stacks derived from the waveforms recorded during the VSP survey in Hole NGHP-01-19B. The automatic travel times picked at the time of the acquisition are shown (crosses), as well as the least square linear fit for the depth of the stations as a function of one-way travel time. [VSP, vertical seismic profile]

Considering the light weight of the VSI, and after encountering difficulties while lowering the triple combo through the various ledges (fig. 38), it was decided to lower the bit to 160 mbsf during the VSP, which prevented us from recording data above 180 mbsf (see "Operations"). Figure 40 shows all the preliminary stacks that were derived from the most reliable shots recorded in Hole NGHP-01-19B and the travel times picked from these stacks. Unfortunately, it was not possible to get sufficient coupling between the VSI and the formation for any of our attempts above the predicted depth of the BSR (~190 mbsf). However, extrapolation of the least-square linear fit for the six travel times, which indicates an average velocity of ~1,480 m/s below, suggests that the BSR, at a two-way travel time of 2,150 m/s, is at ~198 mbsf in this site, which is in reasonable agreement with the decrease in V_p shown at ~203 mbsf in figure 39.

Logging Units

The trends in the main logs displayed in figures 38 and 39 (particularly in the velocity, resistivity, and density logs) allow the definition of three logging units in Hole NGHP-01-19B.

Logging unit 1 (50–110 mbsf) is characterized by a slight increase with depth in density, resistivity, and compressional velocity until ~100 mbsf, and by a sharp decrease in these measurements for the rest of the unit. These trends are mostly following the gamma ray and the uranium content logs, indicating that they are the results of high variability of the clay-dominated lithology in this unit (see "Lithostratigraphy").

Logging unit 2 (110–205 mbsf) is also defined by an increase with depth in V_p, density, and resistivity, which remains subtle within Subunit 2A (101–160 mbsf) and has a more pronounced trend in Subunit 2B, below 160 mbsf. The top of logging unit 3 (205–280 mbsf) is defined most clearly by the drop in V_P that produces the BSR at this depth. It also coincides with a decrease in resistivity that marks the deepest occurrence of gas hydrate (see below). While the density, resistivity and most other logs are mostly constant over the rest of the unit, compressional velocity remains low between ~205 and 220 mbsf, before returning to normal values below 225 mbsf, indicating the likely presence of free gas in this interval, which is also suggested by the low coherence in the monopole waveforms.

Gas-Hydrate and Free Gas Occurrence

As previously discussed (see "Downhole Logging" in the "Methods" chapter), the presence of gas hydrate is generally identified by increases in electrical resistivity and acoustic velocity that are not accompanied by a corresponding density increase. No visible gas hydrate samples were recovered in Hole NGHP-01-19A, but the IR camera identified a steady decrease with depth in the temperature measured on the core liner above ~205 mbsf, which was interpreted as the indication for gas hydrate disseminated in the formation above the BSR (see "Physical Properties").

To make a quantitative estimate of the amount of gas hydrate present, we followed the procedure described in "Downhole Logging" in the "Methods" chapter by applying the Archie relationship to the resistivity and porosity logs recorded in Hole NGHP-01-19B. Because no LWD logs were recorded in this site, we used the wireline resistivity deep induction log (ILD) to make this estimate. The procedure and the results are illustrated in figure 41. The pore fluid resistivity (R_W) was estimated from Fofonoff (1985) using a temperature profile derived from a linear fit of the *in situ* temperature measurements at Site NGHP-01-19 (4.78 °C at the seafloor; gradient of 52.3 °C/km, see "Physical Properties") and the water salinity values measured on IW samples in this hole. The estimated value for m was derived from R_w, the porosity (φ) and resistivity (R_t) logs (mest= -logF/logφ, where $F=R_t/R_w$). As this relationship is defined for water-saturated sediments, the chosen value of m=2.4 is given by the baseline of this curve in the low-resistivity intervals where there is likely no gas hydrate. Using the porosity log and Archie's equation ($R_o = (a\ R_w)/\varphi m$), we derived the predicted resistivity of the water-saturated formation R_o. A qualitative influence of gas hydrate on the resistivity log is indicated by the difference between the R_o and the measured resistivity R_t. The estimated water saturation, assumed to be the numerical complement of the hydrate saturation, is $S_w = (R_o/R_t)^{1/n}$, where n=2 (Pearson and others, 1983). We used the density porosity and the deep induction resistivity log (ILD) to derive the results shown in figure 41.

The results indicate that gas hydrate could occupy about ~15 percent of the pore space in the ~25 m immediately above the BSR (180–205 mbsf). This coincides with the interval with the lowest IR temperature anomalies shown in the same figure (see "Physical Properties"). In addition, some thin intervals with smaller water saturation excursions could also coincide with discrete IR anomalies (at ~150 mbsf and 175 mbsf). The saturation values below the BSR could be associated with the presence of free gas that is suggested by low V_p values between 205 and 225 mbsf. Because of the irregular hole around ~110 mbsf and between 80 and 90 mbsf, the anomalously low density readings in these intervals generate unreliably high porosity values, and the saturation values are likely overestimated. These intervals are highlighted in grey in figure 41.

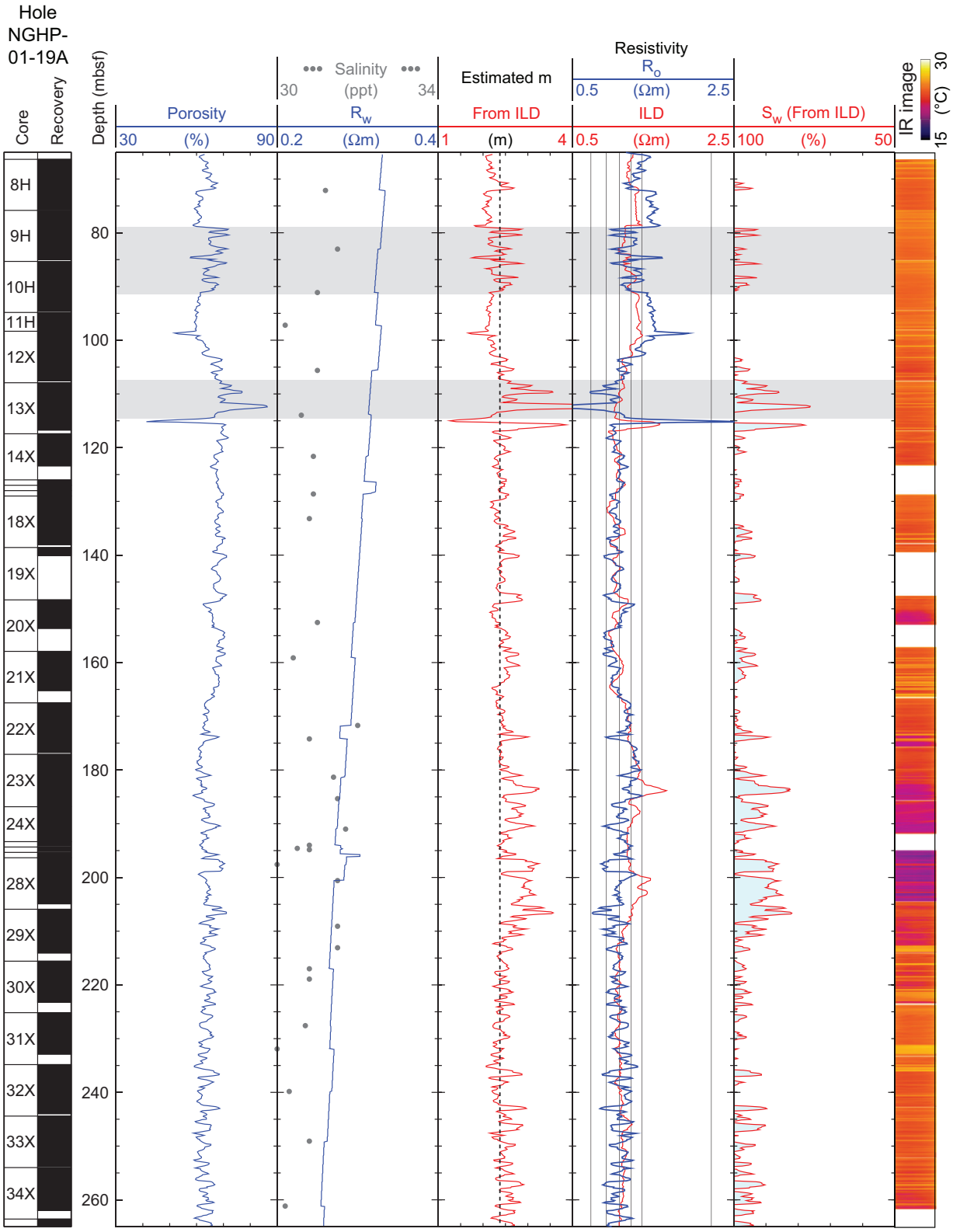


Figure 41. Water saturations from Archie's equation and wireline porosity and resistivity logs in Hole NGHP-01-19B. The gray area indicates degraded data quality. On the right track, a summary of the infrared (IR) images recorded on the cores recovered from Hole NGHP-01-19A shows the intervals where cold anomalies identify the presence of gas hydrate. [R_w, Formation water resistivity; R_o, Computed formation resistivity for 100 percent water saturation; R_t, Measured resistivity; S_w, water saturation; ILD, Deep induction resistivity log]

References Cited

Bjerrum, L., 1972, Embankments on soft ground, *in* ASCE Specialty Conference on Performance of Earth and Earth-Supported Structures, Lafayette, Ind., June 11–14, 1972, Proceedings: New York, American Society of Civil Engineers, v. 2, p. 1–54. [Held at Purdue University]

Clift, P.D., 2006, Controls on the erosion of Cenozoic Asia and the flux of clastic sediment to the ocean: Earth and Planetary Science Letters, v. 241, p. 571–580.

Davis, E.E., Hyndman, R.D., and Villinger, H., 1990, Rates of fluid expulsion across the northern Cascadia accretionary prism—Constraints from new heat flow and multichannel seismic reflection data: Journal of Geophysical Research, v. 95, p. 8869–8889.

Dickens, G.R., Owen, R.M., 1999, The latest Miocene-Early Pliocene biogenic bloom—A revised Indian Ocean perspective: Marine Geology, v. 161, p. 75–91.

Duan, Z., Møller, N., Greenberg, J., and Weare, J.H., 1992, The prediction of methane solubility in natural waters to high ionic strengths from 0° to 250 °C and from 0 to 1600 bar: Geochim. Cosmochim. Acta, v. 56, p. 1451–1460.

Fofonoff, P., 1985, Physical properties of seawater: Journal of Geophysical Research, v. 90, no. C2, p. 3332–3342.

Hesselbo, S.P., and Huggett, J.M., 2001, Glaucony in ocean-margin sequence stratigraphy (Oligocene-Pliocene, offshore New Jersey, U.S.A.; ODP Leg 174A): Journal of Geophysical Research, v. 71, p. 599–607.

Holtz, R.D. and Kovacs, W.D., 1981, An introduction to geotechnical engineering: Englewood Cliffs, New Jersey, Prentice-Hall, Inc., 733 p.

Hunt, R.E., 1984, Geotechnical engineering investigation manual: New York, McGraw-Hill Book Company, 983 p.

Kvenvolden, K.A., and Lorenson, T.D., 2000, Methane and other hydrocarbon gases in sediment from the southeastern north American continental margin, *in* Paull, C.K., Matsumoto, R., Wallace, P.J., and Black, N.R. and others, eds., Proceedings of the Ocean Drilling Program—volume 164 Scientific Results; gas hydrate sampling on the Blake ridge and Carolina rise; covering leg 164 of the cruises of the drilling vessel JOIDES resolution, Halifax, Nova Scotia, to Miami, Florida, sites 991–997, 31 October–19 December 1995: Proceedings of the Ocean Drilling Program, Scientific Results, v. 164, p. 29–36.

Kudrass, H.R., Hofmann, A., Doose, H., Emeis, K. and Erlenkeuser, H., 2001, Modulation and amplification of climate changes in Northern Hemisphere by Indian summer monsoon during the past 80 Ky: Geology, v. 29, p. 63–66.

Ladd, C.C., Foote, R., Ishihara, K., Schlosser, F., and Poulos, H.G., 1977, Stress-deformation and strength characteristics, state-of-the-art report *in* Ninth International Conference on Soil Mechanics and Foundation Engineering, Tokyo, 10–15 July 1977: Tokyo, Japan, International Conference on Soil Mechanics and Foundation Engineering, v. 2, p. 421–494.

Lambe, T. William, Whitman, Robert V., 1969, Soil mechanics: New York, John Wiley and Sons, 553 p.

Ninkovich, D., Shackleton, N.J., Abdel-Monem, A.A., Obradovich, J.D., and Izett, G., 1978, K-Ar age of the late Pleistocene eruption of Toba, north Sumatra: Nature, v. 276, p. 574–577.

Novosel, I., Winters, W.J., Boldina, O.M., Labails, C., and Geli, L., 2007, Thermal conductivity of sediment recovered from the IMAGES VIII/PAGE 127 Gas Hydrate and Paleoclimate Cruise on the R/V Marion Dufresne in the Gulf of Mexico, 2–18 July 2002, chap. 7 *of* Winters, W.J., Lorenson, T.D., Paull, C.K., eds., Initial report of the IMAGES VIII/PAGE 127 gas hydrate and paleoclimate cruise on the R/V Marion Dufresne in the Gulf of Mexico, 2–18 July 2002: U.S. Geological Survey Open-File Report 2004–1358, p. 1–5.

Pearson, C.F., Halleck, P.M., McGuire, P.L., Hermes, R., and Mathews, M., 1983, Natural gas hydrate deposits:—A review of *in situ* properties: Journal of Physical Chemistry, v. 87, p. 4180–4185.

Rose, W.I., Chesner, C.A., 1990, Worldwide dispersal of ash and gases from Earth's largest known eruption, Toba, Sumatra 75ka: Global and Planetary Change, v. 3, p. 269–275.

Sloan, E.D., 1998, Clathrate hydrates of natural gases (2d ed.): New York, Marcel Dekker, 705 p.

Tréhu, A.M., and others, 2004, Three-dimensional distribution of gas hydrate beneath southern Hydrate Ridge—Constraints from ODP Leg 204: Earth and Planetary Science Letters, v. 222, p. 845–862.

Tréhu, A.M., Bohrmann, G., Rack, F.R., Torres, M.E., and others, 2003, Proceedings of the Ocean Drilling Program—Volume 204 Initial Reports [CD-ROM]. Available from: Ocean Drilling Program, Texas A&M University, College Station, Tex. 77845-9547, USA.

Westgate, J.A., Shane, P.A.R., Pearce, N.J.G., Perkins, W.T., Korisettar, R., Chesner, C.A., Williams, M.A.J., and Acharyya, S.K., 1997, All Toba tephra occurrences across peninsular India belong to the 75,000 year before present eruption: Quaternary Research, vol. 50, no. 1, p. 107–112

Xu, W., 2002, Phase balance and dynamic equilibrium during formation and dissociation of methane gas hydrate, *in* 4th International Conference on Gas Hydrates, Yokohama, Japan, 19–23 May 2002, Proceedings: Yokohama, Japan, International Conference on Gas Hydrates, p. 195–200.

Xu, W., 2004, Modeling dynamic marine gas hydrate systems: American Mineralogist, v. 89, p. 1271–1279.